Study on ELF/VLF Emission in a Multicomponent Plasma Observed by the Akebono Satellite(Dissertation_全文)

AUTHOR(S):

Kasahara, Yoshiya

Study on ELF/VLF Emissions in a Multicomponent Plasma Observed by the Akebono Satellite

by

Yoshiya Kasahara

August, 1995

Study on ELF/VLF Emissions in a Multicomponent Plasma Observed by the Akebono Satellite

by

Yoshiya Kasahara

August, 1995

Preface

Plasma, which is the fourth state of matter, consists of mobile charged particles. It is space age now and many rockets and satellites have been launched into various part of outer space in order to explore the various kinds of physical phenomena, such as heating/acceleration of plasma, and generation/propagation of plasma waves. As the plasma waves have a lot of information on the media in which they propagate, it is essential to observe these waves and to clarify their characteristics in order to understand the physical phenomena occurring in outer space.

Especially the region so-called magnetosphere is the surrounding space of the Earth, filled with highly ionized plasmas and pervaded with the strong magnetic field of the Earth. The Akebono (EXOS-D) satellite was launched in 1989 for precise observations of the magnetosphere. Six years has passed after launching, however, the Akebono satellite is still alive and continues to obtain the observation data successfully. It is noted that the Akebono satellite was launched as the first satellite associated with ISTP (International Solar-Terrestrial Physics) project which was extensively organized internationally. Finally, more than 15 of scientific satellites will be launched in order to construct a network of satellites around the Earth, and the Akebono satellite is expected to make a significant contribution to this international collaboration.

The VLF instruments on board the Akebono satellite were designed to investigate the plasma waves in a ELF/VLF range. The instruments also have a function to determine the wave normal vector of these waves. In the present paper, we introduce the ELF/VLF phenomena observed by the VLF instruments. In order to understand the characteristics of the waves, propagation direction of the waves must be analyzed theoretically, which is carried out by a ray tracing method.

The outline of the present thesis is as follows. The analyses techniques developed for the present study is first described. In order to calculate the ray paths of the wave associated with ions, we developed a three-dimensional ray tracing program applicable to the case that the effects of ions are taken into account. We describe the ray tracing techniques both in cold and hot plasma models.

Another important technique used in the present study is a wave distribution function (WDF) method by which the wave normal direction of the plasma wave is determined from the observed wave data. As the solution given by the WDF method is calculated on the basis that the observed wave satisfies the dispersion relation of the plasma wave, we developed a WDF method, in which the effects of multicomponent ions are taken into account.

Using these techniques described above, we discuss the characteristics of several kinds of ELF/VLF wave phenomena observed by the Akebono satellite. First, we introduce ELF emis-

sions often observed in the vicinity of the geomagnetic equator. As the ELF range receiver on board the Akebono satellite covers local cyclotron frequencies of proton (H^+), helium (He^+), and oxygen (O^+) ions, those are considered to be associated with ion constituents. They are classified into two types. One is usually observed below the local proton cyclotron frequency (f_{cH^+}) with a clear cutoff above the local cyclotron frequencies of heavy ions such as helium or oxygen (type A). The other is observed not only below but also above the local proton cyclotron frequency, has a multiband structure in frequency, and has no dependence upon the local cyclotron frequencies (type B). Following the statistical studies such as spatial and time distribution and refractive index, the wave normal directions of both types are determined and the results are compared with those of three-dimensional ray tracing for ion mode waves.

Next, a typical VLF wave phenomenon, auroral hiss, observed in the polar region is studied. Auroral hiss is one of well-known phenomena and is studied by many scientists, however, so far no detailed observation for the wave normal direction has been done. In the present study, the wave normal vector directions are studied in detail and the frequency spectra of the emissions were also interpreted by ray tracing. We also introduce a conjunction study between two satellites; the Freja satellite, which is a joint Swedish and German scientific satellite, and the Akebono satellite. We show our ray tracing study is useful to estimate the three dimensional extent of the source region.

It should be emphasized that our contribution of the present study is not only clarifying the generation mechanism and propagation characteristics of ELF/VLF waves but also giving a clue to investigate the global plasma distribution especially for the plasma density distribution and ion constituents in the magnetosphere by using the propagation characteristics of the plasma wave in a multicomponent plasma. We hope our study will play a significant role for future studies.

Contents

List of Tables

List of Figures

Chapter 1

General Introduction

1.1 Introduction

It is well-known that space is extremely vast and the Earth is only a small star among many various stars. Almost all space is filled with plasmas which are the fourth state of matter. Especially the region so-called magnetosphere is the surrounding space of the Earth, filled with highly ionized plasmas and pervaded with the strong magnetic field of the Earth (Figure 1.1). The Sun is a main energy source which controls the environment of the magnetosphere. For example, the solar wind brings enormous energized particles from the Sun into the magnetosphere, where there take place heating and acceleration of plasma, various kind of plasma waves, wave-particle interactions, wave-wave interactions and so on.

Many rockets and satellites have been launched into various part of the magnetosphere in order to explore mysterious phenomena. As a result, we have rapidly increased our knowledge about extraterrestrial environment, although more and more questions about it come out one after another. As for the plasma wave phenomena of VLF range, for example, Omega signals, whistlers and hiss are well-known. The behavior of such plasma waves is much different from that of the waves in free space on the ground. Therefore, it is useful and necessary both to observe these waves and to clarify their characteristics to know the structure of the magnetosphere.

In 1981, the DE 1 satellite was launched into a semi-polar orbit in the altitude range between 675 km and 23,000 km and revealed detailed information especially on the energization mechanism in the auroral region (e.g. *Menietti and Burch,* [1985]). On board the DE 1 satellite, *Gurnett et al.* [1983] observed funnel-shaped auroral hiss emissions at a radial distance between about 2 and 5. They suggested that the radial distance of the low-altitude boundary of the source is between 1.7 and 1.9 R_E and the hiss is propagating upward. The frequency spectra

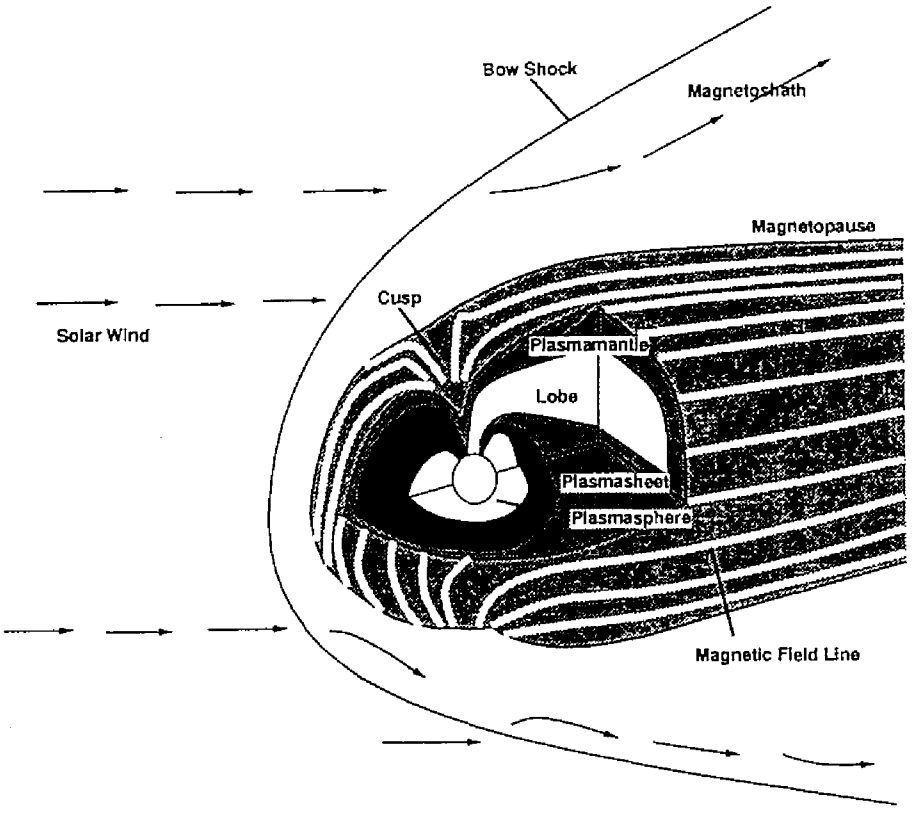

Figure 1.1: Overview of the Earth's magnetosphere.

of the emissions were interpreted by ray tracing as upgoing coherent Cérenkov radiation due to an upgoing beam of low-energy electrons.

In 1986, the Swedish satellite named Viking was launched into a semi-polar orbit in the altitude range between 817 km to 13,530 km [*Hultqvist*, 1987] and measurements of particles, waves and so on were made for about 1 year. *André et al.* [1987] discussed the relation between ion beams and electrostatic hydrogen cyclotron waves, and *Koskinen et al.* [1987] introduced ion cyclotron harmonic waves discovered around the equatorward border of the morning side auroral field lines.

In Japan, a series of EXOS satellites had been planned and launched in order to observe the exosphere. Namely the EXOS-A satellite nicknamed "Kyokko" was launched in February 1978, and the EXOS-B satellite nicknamed "Jikiken" was launched in September 1978. A lot of valuable observation data were taken by them (e.g. *Matsumoto et al.*, 1981a; 1981b; *Kimura et al.*, 1983) As for plasma wave observations, they observed various wide-band wave spectra

and achieved good results, but they did not have a function to determine the wave normal vector of the observed waves.

The EXOS-D satellite which was nicknamed "Akebono" after launch was planned and launched for more precise observations of the magnetosphere. The orbit of the EXOS-D satellite was similar to those of the DE 1 and Viking satellites, but the data quality is much higher than the previous satellites. Moreover the EXOS-D satellite is still alive and continues to obtain the observation data successfully although more than six years have passed after launching, therefore it is even possible to make a statistical study on a phenomenon related to the solar cycle.

The VLF instruments on board the EXOS-D satellite were designed to investigate the plasma waves in a ELF/VLF range. The instruments also have a function to determine the wave normal vector of these waves. There have already appeared many reports for observed results including the one presented by the VLF project team [*Kimura et al.*, 1990]. In the present paper, we introduce the ELF/VLF phenomena observed by the VLF instruments.

Besides, the EXOS-D satellite was launched as the first satellite associated with ISTP (International Solar-Terrestrial Physics) project which was extensively organized internationally. The GEOTAIL satellite, which investigates the geomagnetic tail region of the magnetosphere, is also one of the satellites associated with ISTP and launched as a joint program of ISAS (The Institute of Space and Astronautical Science) and NASA (National Aeronautics and Space Administration) in 1992. Finally, more than 15 of scientific satellites will be launched in order to construct a network of satellites around the Earth. The EXOS-D satellite is expected to make a significant contribution to this international collaboration. As a study of the collaborative observation between multi-satellites, we introduce conjunction study between the Akebono satellite and a joint Swedish and German scientific satellite "Freja" in the present paper.

On the other hand, from the view of theoretical studies, owing to the recent computer technology, computer simulations and numerical calculations have been done and theoretical interpretations have been made for the observed results. In this paper, as a theoretical method, a three-dimensional ray tracing technique is used. Ray tracing is a method of tracing the propagation direction of a wave in an inhomogeneous medium and the obtained pass of the wave is called a ray path [*Haselgrove*, 1955; *Kimura*, 1966]. The propagation characteristics of the waves can be examined by ray tracing method, and it is also useful for determining the origin of the wave and for knowing the structure of the magnetosphere. Our three-dimensional ray tracing is applicable to the case that the effects of ions are taken into account and to the case that the plasma model is assumed either cold or hot plasma model. The techniques are described in

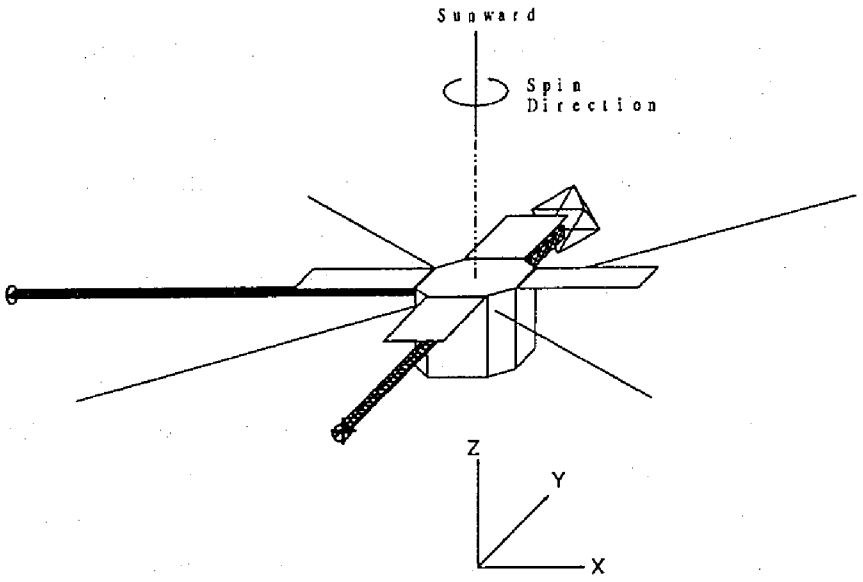

Figure 1.2: The EXOS-D(Akebono) satellite, in-flight configuration.

the following chapter.

1.2 Akebono satellite

1.2.1 Overview of the Akebono satellite

The EXOS-D (Akebono) satellite was designed in order to investigate energy flow from the magnetospheric tail to the auroral region. The configuration of the EXOS-D satellite is shown in Figure 1.2. The EXOS-D satellite is equipped with four solar paddles, two sets of 60 m tip-to-tip wire antennas, orthogonally crossed three loop antennas installed at the tip of a 1.5 m mast, and orthogonally crossed three search coils at the tip of a 3 m mast.

The EXOS-D satellite was launched on February 22, 1989 into a semi-polar orbit with an initial perigee and apogee of 274 km and 10,500 km, respectively, and an inclination of 75°, and was nicknamed "Akebono". The Akebono satellite carries eight scientific instruments:

a) Electric field detectors (EFD)

b) Magnetic field detectors (MGF)

Table 1.1: Locations of the tracking stations for the Akebono satellite.

Station		Location (Geographic Coordinate)	
KSC	(Kagoshima Space Center)	131.1°E	31.3°N
PA	(Prince Albert)	105.9°W	53.2°N
ESR	(Esrange)	20.2°E	67.8°N
ASB	(Antarctic Syowa Base)	39.6°E	69.0°S

c) Very low frequency plasma wave detectors (VLF)
d) Plasma wave detectors in high frequency range and sounder experiments (PWS)
e) Low energy particle spectra analyzer (LEP)
f) Superthermal ion mass spectrometer (SMS)
g) Temperature and energy distribution of plasma (TED)
h) Auroral television camera (ATV)
As for the VLF instruments, Professor Kimura in Kyoto University is the principle investigator (PI) and in charge of the observation of wave phenomena in the frequency range of ELF and VLF [*Kimura et al.*, 1990]. The author is included in a science team for the VLF instruments.

Observed data are transmitted through a PCM telemetry and an analog telemetry and archived at four tracking ground stations, i.e. Kagoshima Space Center (KSC) in Japan, Prince Albert (PA) in Canada, Esrange (ESR) in Sweden and Antarctic Syowa Base (ASB). The locations of these stations are listed in Table 1.1.

The observed PCM data are stored in a large data base system called SIRIUS (Scientific Information Retrieval and Integrated Utilization System) at ISAS in Sagamihara city in Kanagawa prefecture. The volume of PCM data observed by the Akebono satellite is about 33 Mbytes per hour in the high (H) bit rate mode (64 kbps). We can access to the data in SIRIUS through international network from Kyoto University (Figure 1.3). However, since the transmission rate of the network is too small for the volume of the PCM data to be analyzed in Kyoto University, we copy the PCM data from SIRIUS into 8 mm video cassette tapes and preserve these cassette tapes. When we analyze the PCM data, they are loaded into a file system of the work stations from the cassette tapes. The PCM data consist of many blocks. One block corresponds to 0.5 second in the H bit rate mode, and consists of 32 frames. One frame consists of 144 words and 1 word consists of 1 octet.

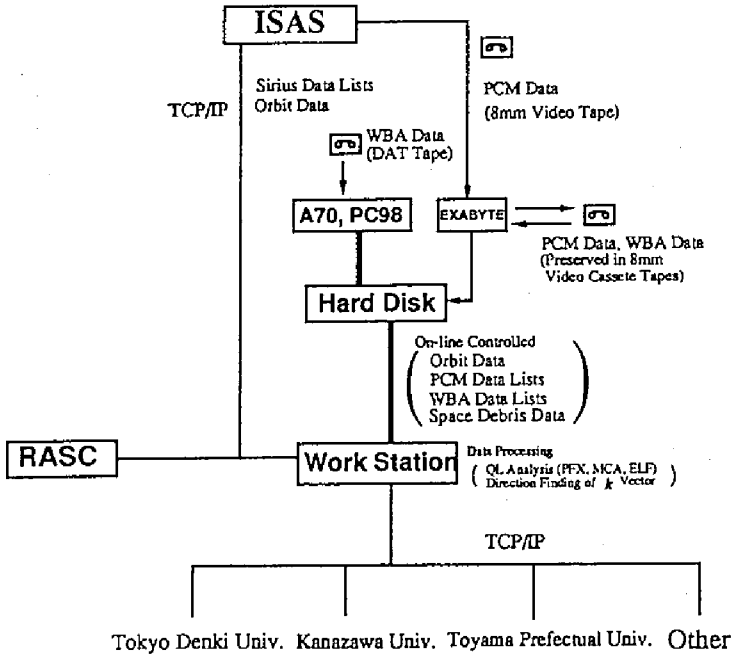

Figure 1.3: Block diagram of computers and network system for the Akebono VLF data analyses.

1.2.2 VLF instruments

The VLF instruments were designed to investigate the behavior of plasma waves associated with accelerated auroral particles, wave-particle interaction mechanisms and propagation characteristics of whistler mode, ion cyclotron mode and electrostatic mode waves in the magnetospheric plasma.

Specific wave phenomena of interest in the frequency range of ELF and VLF in the auroral region are: i) Auroral hiss, ii) Saucers and iii) Broad-band electrostatic noise. As for the wave-particle interaction phenomena, triggered emission events generated by e.g. Omega navigational signals and intense flux of resonant electrons are well-known and such kinds of phenomena are called ASE (artificially stimulated emissions).

In order to clarify these wave characteristics, the determination of the wave normal direction and the direction of the Poynting flux directions are essential in addition to their dynamic spectra. Our VLF instruments are designed to satisfy such requirements.

The VLF instruments are responsible for the frequency range below 17.8 kHz down to 3.16 Hz. The frequency range above tens of kHz is covered by PWS, which are the other

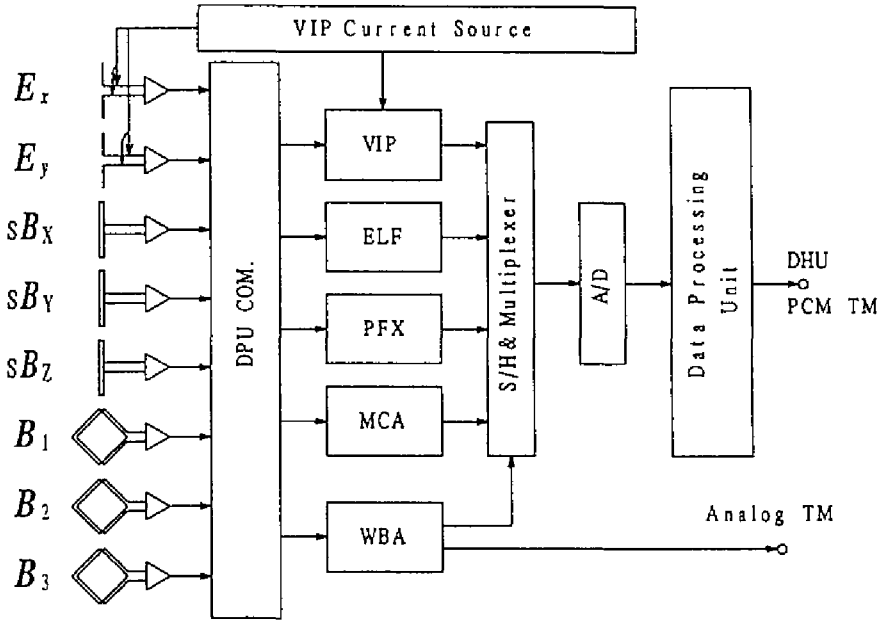

Figure 1.4: Block diagram of the VLF instruments.

wave instruments of the Akebono satellite for high frequency plasma wave phenomena. The block diagram of the VLF instruments is shown in Figure 1.4. They are composed of several subsystems, dipole wire antennas (WAT), loop antennas (LPA), search coils (SC), and common preamplifiers so-called DPU COM (Data Processing Unit Common) directly connected between the sensors and subsystems.

Wave sensors and coordinate systems

To detect the electric field component of plasma waves, a pair of crossed dipole wire antennas, 60 m tip-to-tip shielded for 3 m nearest to the spacecraft, are used. For the magnetic field sensors, orthogonal three open loop antennas installed on the tip of a 1.5 m mast are used for frequencies higher than 800 Hz. For frequencies lower than this frequency limit, three orthogonal search coils are used, which are mounted on the tip of the 3 m mast.

The coordinate systems for the wire antennas, loop antenna and search coils are shown in Figure 1.5. The spin axis of the satellite is always directed to the sun, and is taken to be the Z axis. The mast with the loop antennas is directed in the positive Y direction and the other two

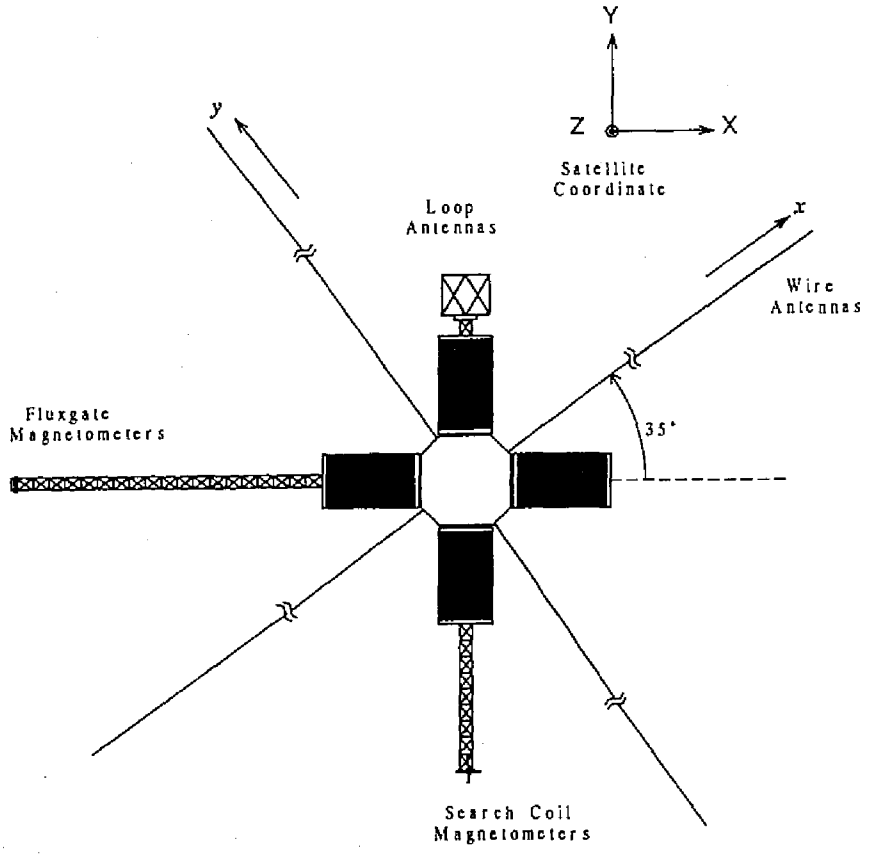

Figure 1.5: Configuration of wave sensors and coordinate systems of the Akebono satellite.

masts of 3 m and 5 m for magnetic flux gate magnetometers and search coils are directed in the $-$X and $-$Y directions respectively as shown in Figure 1.5.

The search coils measure the X, Y, and Z components of magnetic wave field in the above so-called satellite coordinate system. The outputs of the three search coils are named sB_X, sB_Y and sB_Z. The plane normal directions for the three loop antennas are orthogonal to each other, but are directed in different directions from the X, Y, and Z axes so that the outputs of the loop antennas are called B_1, B_2 and B_3. The directions of the crossed dipole wire antennas are directed about 35° off from the X and Y directions and the two components of the electric fields are called E_x and E_y where the positive x and positive y axes are in the first and second quadrants in the X-Y plane with the x axis 35° off from the X axis. In order to convert the outputs of (B_1, B_2, B_3) and (E_x, E_y) into (B_X, B_Y, B_Z) and (E_X, E_Y), respectively, which are defined in the satellite

coordinate system, the following equations are used;

$$\begin{pmatrix} B_X \\ B_Y \\ B_Z \end{pmatrix} = \begin{pmatrix} -\frac{1}{\sqrt{2}} & \frac{1}{\sqrt{2}} & 0 \\ -\frac{1}{\sqrt{3}} & -\frac{1}{\sqrt{3}} & \frac{1}{\sqrt{3}} \\ \frac{1}{\sqrt{6}} & \frac{1}{\sqrt{6}} & \frac{2}{\sqrt{6}} \end{pmatrix} \begin{pmatrix} B_1 \\ B_2 \\ B_3 \end{pmatrix}, \tag{1.1}$$

$$\begin{pmatrix} E_X \\ E_Y \end{pmatrix} = \begin{pmatrix} \cos\theta_{WAT} & -\sin\theta_{WAT} & 0 \\ \sin\theta_{WAT} & \cos\theta_{WAT} & 0 \end{pmatrix} \begin{pmatrix} E_x \\ E_y \end{pmatrix}, \tag{1.2}$$

where θ_{WAT}= 35°.

PFX (Wave normal and Poynting flux analyzers)

The PFX subsystem measures two components of electric field (E_x and E_y) and three components of magnetic field (B_1, B_2, and B_3, or sB_X, sB_Y, and sB_Z) with an output band-width of 50 Hz in a frequency range from 100 Hz to 12.75 kHz. The center frequency of the PFX is either automatically stepped by the minimum step of 50 Hz or kept fixed at a constant frequency, and mode selection described above can be operated by command from KSC. The observed wave data are sampled by 320 Hz with a 12 bit-word and then log-compressed to an 8 bit-word.

The gain of each channel (two for electric field and three for magnetic field) of the PFX subsystem is changed independently in 25 dB steps from 0 dB up to 75 dB by checking the averaged signal level every 0.5 second. This procedure is automatically executed by the WIDA (Wide dynamic range amplifier) hybrid IC. By using three WIDA IC's for each channel, the dynamic range of the PFX subsystem is more than 80 dB. Using these five components of wave data, we can determine the wave normal direction and Poynting vector by the ground data processing.

MCA (Multi-channel analyzers)

The MCA subsystem measures one component of each electric (E_x or E_y; selectable by command) and magnetic field (chs. 1-10 for sB_Y and chs. 11-16 for B_2) with 16 channels of band-pass filters. It covers a frequency range from 3.18 Hz to 17.8 kHz with 500 msec time resolution. The center frequency for each channel is 3.16, 5.62, 10.0 and 17.8 [Hz] ×1, ×10, ×100 and ×1,000 with a band width of 30% of each center frequency. Three WIDA IC's are also installed for each channel, then the dynamic range of the MCA subsystem is more than 80 dB.

ELF (Extra low frequency range analyzers)

The ELF range receiver can be operated in either 4 channel mode (narrow mode) or 2 channel mode (wide mode), selectable by command.

In the narrow mode, waves in a frequency range less than 80 Hz are observed and are sampled by 160 Hz to 8 bit words. The four channels are composed of Ch.1; E_x or E_y (selectable by command), Ch.2; sB_X, Ch.3; sB_Y and Ch.4; sB_Z. With the data observed in this mode, the wave normal direction can be calculated by the ground data processing. In the wide mode, the upper limit frequency is increased up to 160 Hz, but only two components, selected by command, can be observed with a sampling frequency of 320 Hz with 8 bit resolution. The two channels are composed of Ch.1; E_x or E_y, Ch.2; one of the three components; sB_X, sB_Y or sB_Z. By using the three WIDA IC's, the dynamic range for either mode is more than 80 dB.

VIP (Vector impedance probe)

In order to determine the electric field intensity of a signal as accurately as possible, the antenna impedance must be known. The VIP subsystem is installed for the purpose of measuring the antenna impedance.

WBA (Wide band analyzer)

One component of electric or magnetic field in a frequency range less than 15 kHz is measured. The received data are transmitted directly to the ground by analog telemetry. The raw wave data is recorded into a DAT (digital audio tape) at the tracking stations. The data is reproduced from the DAT and are frequency-analyzed by fast Fourier transform (FFT) in Kyoto University.

1.3 Contribution of the present work

In Chapter 2, we describe analysis techniques developed for the present study. In order to calculate the ray paths of the wave associated with ions, we developed a three-dimensional ray tracing program applicable to the case that the effects of ions are taken into account. We describe the ray tracing techniques both in cold and hot plasma models in section 2.1.

In section 2.2, the techniques to calculate the absolute intensities and phase of electric and magnetic fields of ELF and VLF waves from raw data observed by the Akebono satellite are described. Furthermore, as the Akebono satellite is spin-stabilized by making the direction of the spin axis pointing towards the sun, it is necessary to convert the raw wave data observed by

the satellite into the Earth's coordinate system in order to determine the absolute direction, such as wave normal vector. We also describe the relation of the attitude of the Akebono satellite to the Earth's coordinate system.

The study of the wave normal vector is important to identify the mode of the waves and interpret the propagation characteristics of them. In section 2.3, we describe the technique to determine the wave normal direction from the observed wave data. If there exists only a plane electromagnetic wave, we can determine the direction of the wave normal vector easily by determining the polarization plane of the wave magnetic field. However, in case there are multiple waves coexisting we must analyze the wave normal direction without one plane wave assumption. Therefore we adopt the wave distribution function (WDF) method [*Storey and Lefeuvre* 1979; 1980], which is derived from the concept that observed signals consist of a number of elementary plane waves. As the solution given by the WDF method is calculated on the basis that the observed wave satisfies the dispersion relation of the plasma wave, we developed a WDF method, in which the effects of multicomponent ions are taken into account. Finally the performance of the WDF method using two different methods, the maximum entropy method (MEM) and the Phillips-Tikhonov regularization method (PTM), was evaluated by computer simulation.

We introduce several kinds of ELF/VLF wave phenomena observed by the Akebono satellite in Chapter 3,4 and 5. It should be noted that our contribution of the present work is not only clarifying the characteristics of ELF/VLF wave phenomena but also blazing a trail to investigate the structure of the magnetosphere because the waves have a lot of information on the media in which they propagate.

In Chapter 3, and 4, we introduce ELF emissions which are often observed by the Akebono satellite. Using the ELF instrument, various kinds of wave phenomena were observed. Especially in the vicinity of the geomagnetic equator, bands of electromagnetic ELF emissions were often observed. The frequency range of the ELF instrument covers the local cyclotron frequencies of proton (H^+), helium (He^+), and oxygen (O^+) ions, and most of these wave phenomena are considered to be associated with ion constituents. These ELF emissions are classified into two types. One is usually observed below the local proton cyclotron frequency (f_{cH^+}) with a clear cutoff above the local cyclotron frequencies of heavy ions such as helium or oxygen (type A). The other is a multiband structured emission which is observed not only below but also above the local proton cyclotron frequency (type B). Type B emission has no dependence upon the local cyclotron frequencies.

In Chapter 3, we focus on the type A emissions. From statistical study and estimation of the

refractive index of the emissions, the wave mode of type A emission is identified as ion cyclotron waves. The wave normal direction of the emission is determined and the result is compared with those of three-dimensional ray tracing for ion mode waves using both a cold and a hot plasma model. Propagation characteristics, spatial distribution, and growth rates of the emissions are clarified by our ray tracing with reference to the generation mechanism of the emissions.

In Chapter 4, we discuss the characteristics of type B emission. Following the statistical studies such as spatial and time distribution and refractive index, the wave normal direction of the emission is determined by using the WDF method. Their propagation characteristics are also examined by a three-dimensional ray tracing method.

In Chapter 5, auroral hiss which is a typical wave phenomenon in the auroral region is studied. By frequent passages above the auroral zone, the Akebono satellite has provided us with ample data of wave and particles around the region. The auroral hiss is thought to be generated by Cérenkov radiation and coherent amplification mechanism by beaming electrons [*Maggs*, 1976; 1978; *Yamamoto*, 1979; *Lotko and Maggs*, 1979; 1981; *Maggs and Lotko*, 1981]. The wave normal direction at the source point is therefore considered to be directed to the resonance cone angle, however, so far no detailed observation for their wave normal direction has been done. In order to confirm the above mechanism, the wave normal vector directions are studied in detail. The frequency spectra of the emissions were also interpreted by ray tracing.

It is difficult to tell a physical phenomenon from observed data by one satellite whether it is a temporal change, a spatial change or mixture of them. In order to study the spatial structure of the magnetosphere, simultaneous observation by multi-satellites is indispensable. In the last section in Chapter 5, we discuss the conjunction study between two satellites; the Freja satellite, which is a joint Swedish and German scientific satellite, and the Akebono satellite. There are nearly 10 conjunction passes between the Akebono satellite and the Freja satellite in 1993. We introduce two conjunction cases, in which fine structured V-shaped hiss were observed both by the Akebono and Freja satellites.

In Chapter 6, we summarize major contribution of our work and give conclusions obtained by the present study. Finally, we give suggestions for the further work.

Chapter 2

Development of Analysis Techniques in a Multicomponent Plasma Model

2.1 Three dimensional ray tracing

We have developed a three-dimensional ray tracing program for waves associated with ions [*Kasahara*, 1989] . The propagation characteristics of ion mode waves can be examined by this ray tracing program. In this section, we will present the techniques of three-dimensional ray tracing for ion mode waves both in cold and hot plasma model.

2.1.1 Fundamental equations

First, we will describe the fundamental equations of ray tracing which were derived by *Haselgrove* [1955] and *Kimura* [1966].

When spatial and time variations of medium parameters are enough small within the wavelength and time period of the wave which propagates in the medium, WKB approximation can be applied, and the next dispersion relation must be constant along a ray path:

$$D(t, r, \omega, k) = \text{constant}, \tag{2.1}$$

where t is the propagation time, r is the coordinate vector on the ray path, ω is the angular frequency of the wave and k is the wave normal vector. Then, we can obtain the following three differential equations which represent the ray path as the fundamental equations for ray tracing

$$\frac{\mathrm{d}r}{\mathrm{d}\tau} = \frac{\partial D}{\partial k}, \tag{2.2}$$

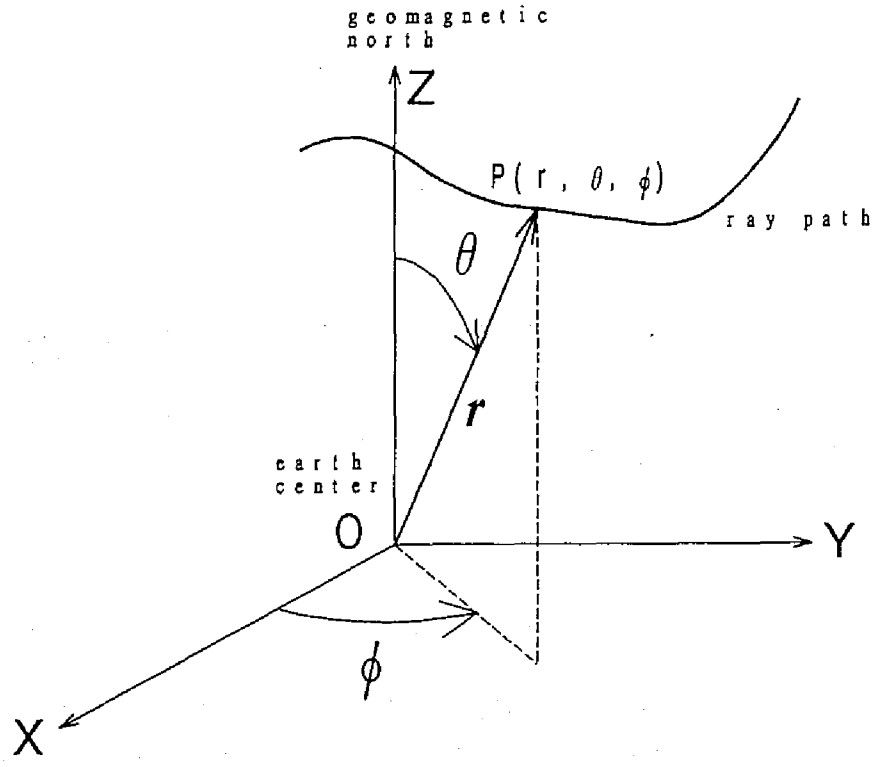

Figure 2.1: Coordinate system for representing the ray path.

$$\frac{dk}{d\tau} = -\frac{\partial D}{\partial r}, \tag{2.3}$$

$$\frac{dt}{d\tau} = -\frac{\partial D}{\partial \omega}, \tag{2.4}$$

where τ is the phase propagation time, which is related to the real propagation time t by (2.4). These equations show that if we can calculate numerically the deviatives of the dispersion relation D with respect to k, r and ω at an arbitrary point of the ray path, then the next r, k and t can be determined by integrating the right-hand sides of these equations, that is, we can solve these equations numerically as an initial value problem for a set of ordinary differential equations.

In the present paper, we perform three-dimensional ray tracing, so that both r and k should be three-dimensional values. In our three-dimensional ray tracing programs, we use spherical coordinate systems shown in Figure 2.1. The ray paths are represented by (r, θ, ϕ), where r, θ, ϕ are the geocentric distance, the geomagnetic colatitude and the geomagnetic longitude in

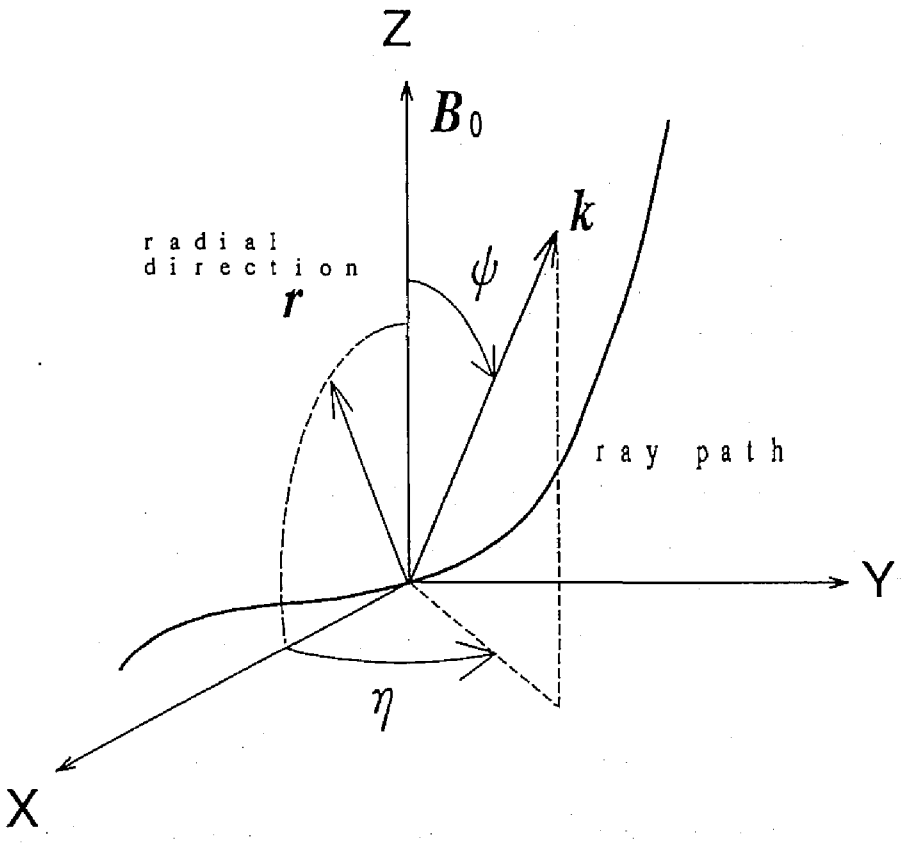

Figure 2.2: Coordinate system for representing the wave normal vector.

a dipolar spherical coordinate system, respectively. k is represented by (k_r, k_θ, k_ϕ) which are three components of the wave normal vector along the r, θ, ϕ directions respectively. In this coordinate system, the fundamental equations for ray tracing become

$$\frac{\mathrm{d}r}{\mathrm{d}\tau} = \frac{\partial D}{\partial k_r}, \tag{2.5}$$

$$\frac{\mathrm{d}\theta}{\mathrm{d}\tau} = \frac{1}{r}\frac{\partial D}{\partial k_\theta}, \tag{2.6}$$

$$\frac{\mathrm{d}\phi}{\mathrm{d}\tau} = \frac{1}{r\sin\theta}\frac{\partial D}{\partial k_\phi}, \tag{2.7}$$

$$\frac{\mathrm{d}k_r}{\mathrm{d}\tau} = \left(-\frac{\partial D}{\partial r} + k_\theta\frac{\mathrm{d}\theta}{\mathrm{d}\tau} + k_\phi\sin\theta\frac{\mathrm{d}\phi}{\mathrm{d}\tau}\right), \tag{2.8}$$

$$\frac{dk_\theta}{d\tau} = \frac{1}{r}\left(-\frac{\partial D}{\partial \theta} - k_\theta \frac{dr}{d\tau} + r k_\phi \cos\theta \frac{d\phi}{d\tau}\right), \tag{2.9}$$

$$\frac{dk_\phi}{d\tau} = \frac{1}{r\sin\theta}\left(-\frac{\partial D}{\partial \phi} - k_\phi \sin\theta \frac{dr}{d\tau} - r k_\phi \cos\theta \frac{d\theta}{d\tau}\right). \tag{2.10}$$

In order to express the direction of the wave normal vector k, we use the coordinate system represented by (ψ, η) shown in Figure 2.2 instead of (k_r, k_θ, k_ϕ), where ψ is a polar angle from the geomagnetic field direction and η is an azimuthal angle from the geomagnetic meridian plane, with $\eta = 0$ for the radially outward direction and positive η being measured clockwise (eastward) for the geomagnetic field direction.

2.1.2 Dispersion relation of plasma wave

We describe the dispersion relation including the effects of ions. In the present study, the wave amplitude is assumed to be very small and has no effect on the dispersion relation, that is, the dispersion relation should be linear.

In order to get the dispersion relation in a plasma, we use the Vlasov equation and Maxwell's equation. The Vlasov equation is

$$\frac{\partial f_i}{\partial t} + (v \cdot \nabla) f_i + \frac{q_i}{m_i}(E + v \times B) \cdot \frac{\partial f_i}{\partial v} = 0, \tag{2.11}$$

where $f_i = f_i(t, r, v)$ indicates the velocity distribution function of i-th species of the charged particles. E, B, v, q_i and m_i are electric field, magnetic field, particle velocity, charge and mass respectively. On the other hand, Maxwell's equations are

$$\nabla \times E = -\frac{\partial B}{\partial t}, \tag{2.12}$$

$$\nabla \times B = \frac{1}{c^2}\frac{\partial E}{\partial t} + \mu_0 J, \tag{2.13}$$

where μ_0 is the permeability of free space and J is conduction current density of plasma given by the following equation:

$$J(t, r) = \sum_i q_i \int f_i(t, r, v) v dv. \tag{2.14}$$

Then we assume that f_i, E and B are the sums of zero-order terms and first-order terms which change in space and time by the term $\exp\{j(k \cdot r - \omega t)\}$, we can linearize these equations. Using equations (2.11), (2.12) and (2.13), the following equation concerning to E is obtained:

$$k \times (k \times E) + \left(\frac{\omega}{c}\right)^2 K \times E = 0, \tag{2.15}$$

where K is a dielectric tensor.

In a cold plasma approximation, we can get the following double quadratic equation for refractive index $\mu(= kc/\omega)$ from (2.15) [*Kimura*, 1966; *Maeda and Kimura*, 1984],

$$A\mu^4 + B\mu^2 + C = 0, \tag{2.16}$$

where A, B and C are determined by the plasma frequency f_{pi} and the cyclotron frequency f_{ci} of the i-th species of charged particle in the plasma, and the angle ψ between k and B. Therefore, the effects of the ions are involved in the quantity μ. Especially f_{pi} and f_{ci} of ions are much smaller than those of electron, the effects of ions are the most effective in the frequency range around f_{pi} or f_{ci} of ions.

When we use the refractive index μ in the cold plasma approximation, the dispersion relation D satisfies the following equations:

$$\frac{\partial D}{\partial \alpha} = -\frac{1}{\mu}\frac{\partial \mu}{\partial \alpha} \quad (\alpha = r, \theta, \phi), \tag{2.17}$$

$$\frac{\partial D}{\partial \rho_\alpha} = \frac{1}{\mu^2}\left(\rho_\alpha - \mu\frac{\partial \mu}{\partial \rho_\alpha}\right), \tag{2.18}$$

where $\rho_r, \rho_\theta, \rho_\phi$ are r, θ, ϕ components of the refractive index vector ρ (ρ // k, $|\rho| = \mu$).

In a hot plasma in which thermal velocities of the particle are taken into account, assuming that the bi-Maxwellian distribution are used as a zero-order velocity distribution function, we can get the following equations from (2.15) [*Miyamoto*, 1980; *Sawada*, 1988]:

$$D = \begin{vmatrix} F_{xx} - k^2 + (\omega/c)^2 & F_{xy} & F_{xz} \\ F_{yx} & F_{yy} - k^2\cos^2\psi + (\omega/c)^2 & F_{yz} + k^2\sin\psi\cos\psi \\ F_{zx} & F_{yz} + k^2\sin\psi\cos\psi & F_{zz} - k^2\sin^2\psi + (\omega/c)^2 \end{vmatrix} = 0, \tag{2.19}$$

$$\boldsymbol{F} = \sum_i \left(\frac{\Pi_i}{c}\right)^2 \sum_{n=-\infty}^{+\infty} [\zeta_0 Z(\zeta_n) - (1 - A_i)\{1 + \zeta_n Z(\zeta_n)\}]\mathrm{e}^{-b}\boldsymbol{X}_n + \sum_i \left(\frac{\Pi_i}{c}\right)^2 \eta_0^2 \frac{2}{A_i}\boldsymbol{L}, \tag{2.20}$$

$$\boldsymbol{X}_n = \begin{pmatrix} \frac{n^2}{b}I_n(b) - 2b\{I_n'(b) - I_n(b)\} & in\{I_n'(b) - I_n(b)\} & -i\eta_n\alpha\sqrt{\frac{2}{A_i}}\{I_n'(b) - I_n(b)\} \\ -in\{I_n'(b) - I_n(b)\} & \frac{n^2}{b}I_n(b) & -\eta_n\frac{n}{\alpha}\sqrt{\frac{2}{A_i}}I_n \\ i\eta_n\alpha\sqrt{\frac{2}{A_i}}\{I_n'(b) - I_n(b)\} & -\eta_n\frac{n}{\alpha}\sqrt{\frac{2}{A_i}}I_n & \eta^2\sqrt{\frac{2}{A_i}}I_n \end{pmatrix}, \tag{2.21}$$

where

$$\alpha = k\rho_i\sin\psi \quad , \quad b = \alpha^2, \tag{2.22}$$

$$\eta_n = \sqrt{\frac{A_i}{2}}\frac{\omega/\Omega_i + n}{k\rho_i\cos\psi} \quad , \quad \zeta_n = \eta_n - \sqrt{\frac{A_i}{2}}\frac{V_i}{\rho_i\Omega_i}, \tag{2.23}$$

where Π_{i_α}, Ω_{i_α}, ρ_i, V_i and A_i are the plasma angular frequency, the cyclotron angular frequency, the Larmor radius, the drift velocity and the temperature anisotropy defined by $T_{i\perp}/T_{i//} = (v_{i\perp}/v_{i//})^2$ of the velocities of the i-th species of charged particles. ($v_{i\perp}$ and $v_{i//}$ are thermal velocities perpendicular and parallel to the magnetic field). $Z(\zeta_n)$ is the so-called plasma dispersion function, $I_n(b)$ is the modified Bessel function of order n with the argument of b, and L is a tensor, in which all elements except L_{zz} are zero.

In these equations, for $\psi \sim 0°$ or $\psi \sim 90°$, $1/\alpha$ or ζ_n respectively goes to infinity, so that expansions of the functions of $Z(\zeta_n)$ and $I_n(b)$ are used.

2.1.3 Models of the magnetosphere

Model of geomagnetic field

In the present paper, the so-called dipole model are used for geomagnetic field model. In the dipole geomagnetic field model, the geomagnetic field is approximated by a dipole magnet located at the center of the Earth, and geomagnetic field is represented by the function of only r and θ. That is,

$$B_r = -2B_0\frac{\cos\theta}{r^3} \quad (B_0 = \text{constant}), \tag{2.24}$$

$$B_\theta = -B_0\frac{\sin\theta}{r^3}, \tag{2.25}$$

$$B_\phi = 0. \tag{2.26}$$

Model of plasma density profiles

In order to use the ray tracing method, a model of plasma density profiles must be given by analytic continuous functions. In our calculation, we used the Aikyo-Ondoh model [*Aikyo and Ondoh*, 1971], which can simulate the presence of the plasmapause by connecting the diffusive equilibrium (DE) model for the inside of the plasmapause and the collisionless (CL) model [*Eviatar et al.*, 1964] for the outside of the plasmapause.

The DE model is based on the physical process that the thermal diffusion of plasma has to be balanced with the gravity force along each magnetic field line [*Angerami and Thomas*, 1964]. In the DE model, the electron density is given by the following equations:

$$N_{de} = n_0\sqrt{\sum_i \eta_i \exp\left(-\frac{z}{H_i}\right)} \quad (i = H^+, He^+, O^+), \tag{2.27}$$

$$z = \frac{r_0}{r}(r - r_0) \ , \ H_i = \frac{kT_i}{m_i g(r_0)}, \tag{2.28}$$

where n_0 and η_i are the electron density and the relative constituent of the i-th species of ion respectively at a reference geocentric distance r_0. z is the geopotential height and H_i is the scale height of the i-th ion. k, T_i, m_i and $g(r_0)$ represent the Bolzman constant, the ion temperature, the ion mass and the gravitational acceleration respectively at the reference distance r_0 .

In the CL model, the electron density is given by the following equation:

$$N_{\rm cl} = N_{\rm de}\left\{1 - \sqrt{1 - \frac{B}{B_0}}\exp\left(-\frac{z}{2H_{\rm H^+}} \cdot \frac{B}{B_0 - B}\right)\right\}, \tag{2.29}$$

where B is the geomagnetic intensity at a given point, $H_{\rm H^+}$ is the scale height of H^+ in the collisionless region and B_0 is the geomagnetic field intensity of the bottom of the collisionless region following from the given point along the geomagnetic field line.

In the Aikyo-Ondoh model, the electron density is given by the following equations:

$$N_{\rm e} = F_{-1}(L) \cdot N_{\rm de} + F_{+1}(L) \cdot N_{\rm cl}, \tag{2.30}$$

$$F_{\pm 1}(L) = \frac{1}{2} \pm \frac{1}{\pi}\tan^{-1}\left(\frac{L - \xi_L}{\varepsilon_L}\right), \tag{2.31}$$

where the function $F_{\pm 1}(L)$ is introduced in order to connect the DE model with the CL model smoothly. L is L-value at the given point, and ξ_L and ε_L are the location of the plasmapause and its halfwidth represented by L-value.

In the altitude range below the peak density altitude in the ionosphere, a following function which decreases with decreasing altitudes should be multiplied to $N_{\rm de}$,

$$N_{\rm l} = 1 - \exp\left\{-\left(\frac{r - 6460}{140}\right)^2\right\}. \tag{2.32}$$

In this way, the models of geomagnetic field and plasma density profiles are given by the functions of only r and θ and do not depend on ϕ. Therefore if a ray tracing is started with an initial wave normal direction in the geomagnetic meridian plane, the ray paths do not deviate from the same geomagnetic meridian plane.

2.2 Techniques for the data analyses of the Akebono satellite

2.2.1 Calculation of the intensities of electric and magnetic fields

In this section the techniques to calculate the absolute intensities of electric and magnetic fields of ELF and VLF waves from raw data observed by the Akebono satellite are described.

The wave form data observed by the PFX subsystem of the Akebono VLF-ELF instruments [*Kimura et al.*, 1990] have originally 12 bit resolution and are compressed into 1 word data which consists of 8 bit in the PCM data. On the other hand, the wave form observed by the ELF have 8 bit resolution and directly recorded into 1 word. The full scale for the output signal of both the PFX and the ELF subsystem is 1 V_{rms}. Therefore the output amplitude (V_{out}) of the PFX and ELF is given by the following equations.

$$V_{out} = \frac{\sqrt{2}}{2^{(n-1)}} \cdot D_{out} \ (\mathrm{V}), \tag{2.33}$$

$$-2^{(n-1)} \leq D_{out} \leq 2^{(n-1)} - 1, \tag{2.34}$$

where D_{out} is a digital data with 12 bit resolution for the PFX (8 bit for the ELF) restored from the PCM data for each channel, and the parameter n in the equations equals to 12 for the PFX and 8 for the ELF.

Next, the gain of the amplifier must be considered. As was described in the previous section, the WIDA (wide dynamic range amplifier) IC's are installed in each channel for the PFX and ELF subsystem and they change the gain of the receiver automatically every 0.5 seconds. Every channel of the PFX and ELF has three WIDA IC's and the WIDA IC's execute independently with every channel. When we define the WIDA status W_s as the number of the executing WIDA IC's, the input amplitude to the PFX or ELF subsystem, which equals to the output amplitude from the DPU COM, i.e. V_{DPU}, is given as follows:

$$V_{DPU} = V_{out} - 25 \cdot W_s \ (\mathrm{dBV}). \tag{2.35}$$

The WIDA status of the every channel is recorded in the PCM data every 0.5 seconds, that is, every 1 block, and every WIDA status is valid for last 0.5 sec data of the channel from the location where the WIDA status is recorded. It should be noticed that the maximum output level from the PFX or ELF subsystem is 1 V_{rms}, if too large input signal suddenly comes into

the subsystem the WIDA IC's cannot follow that kind of sudden change and the signal may be possibly saturated. From equations (2.33), (2.34) and (2.35), we can get the raw input signal to each channel of the PFX or ELF subsystem (the output signal from the DPU COM).

For the next step, the intensities of electric and magnetic fields are calculated from the raw output signal from the DPU COM. As shown in Figure 1.4, each subsystem of the VLF instruments is connected to the electric and magnetic sensors through the DPU COM. Therefore, in order to get the absolute intensities of the electric and magnetic fields of the waves observed by the sensors, we must consider the gains of the DPU COM and the effective length of the sensors. As for the gains of the DPU COM, the gains for electric $G_{\mathrm{E-DPU}}$ and magnetic field $G_{\mathrm{B-DPU}}$ are as follows: $G_{\mathrm{E-DPU}}$= 20 dB, and $G_{\mathrm{B-DPU}}$= 30 dB for the loop antennas and 25 dB for the search coils.

In order to determine the electric field intensity of a signal as accurately as possible, the antenna impedance must be known. The VIP subsystem, one of the VLF instruments, measure the impedance of the wire antennas. The principle of the VIP subsystem is reported in detail by *Kimura et al.* [1990]. On the other hand, the effective length of a pair of wire antennas is assumed to be half of the wire length, that is,

$$h_{\mathrm{eff}} = 2 \times 30/2 = 30 \quad (\mathrm{m}). \tag{2.36}$$

When we define $V_{\mathrm{E-DPU}i}$ as the output amplitude from the DPU COM concerning to the observed electric field E_i (where i = x, y), the relation between $V_{\mathrm{E-DPU}i}$ and E_i is as follows [*Ito*, 1990]:

$$V_{\mathrm{E-DPU}i} = E_i \cdot h_{\mathrm{eff}} \cdot \left| \frac{Z_{\mathrm{in}}}{Z_{\mathrm{WAT}} + Z_{\mathrm{in}}} \right| \cdot G_{\mathrm{E-pre}} \cdot G_{\mathrm{E-DPU}} \quad (i = \mathrm{x}, \mathrm{y}), \tag{2.37}$$

where Z_{WAT} and Z_{in} are the impedance of the wire antenna and the preamplifier, and $G_{\mathrm{E-pre}}$is a gain of the preamplifier and the DPU COM for the wire antennas ($G_{\mathrm{E-pre}}$= $-2.1 \sim -2.2$ dB).

In the same way, the relation between $V_{\mathrm{B-DPU}i}$ defined as the output amplitude for magnetic component of the DPU COM and the observed magnetic field B_i (where i = X, Y, Z) for loop antenna (or sB_i (i = X, Y, Z) for search coil) is given as follows:

$$V_{\mathrm{B-DPU}i} = \frac{Z_0 \cdot B_i}{\mu_0} \cdot l_{\mathrm{eff}} \cdot G_{\mathrm{B-DPU}} \quad (i = X, Y, Z), \tag{2.38}$$

where Z_0 is the characteristic impedance in vacuum, μ_0 is the permeability of free space and l_{eff} is the effective length of a search coil. In Figure 2.3, the frequency dependence of the effective lengths of electric and magnetic sensors including the gains of preamplifiers.

In the analyses, after getting a time series of $V_{\mathrm{DPU}}(t)$, an FFT processing is made and the effective length given by Figure 2.3 is multiplied to the $V_{\mathrm{DPU}}(f)$ with every frequency components,

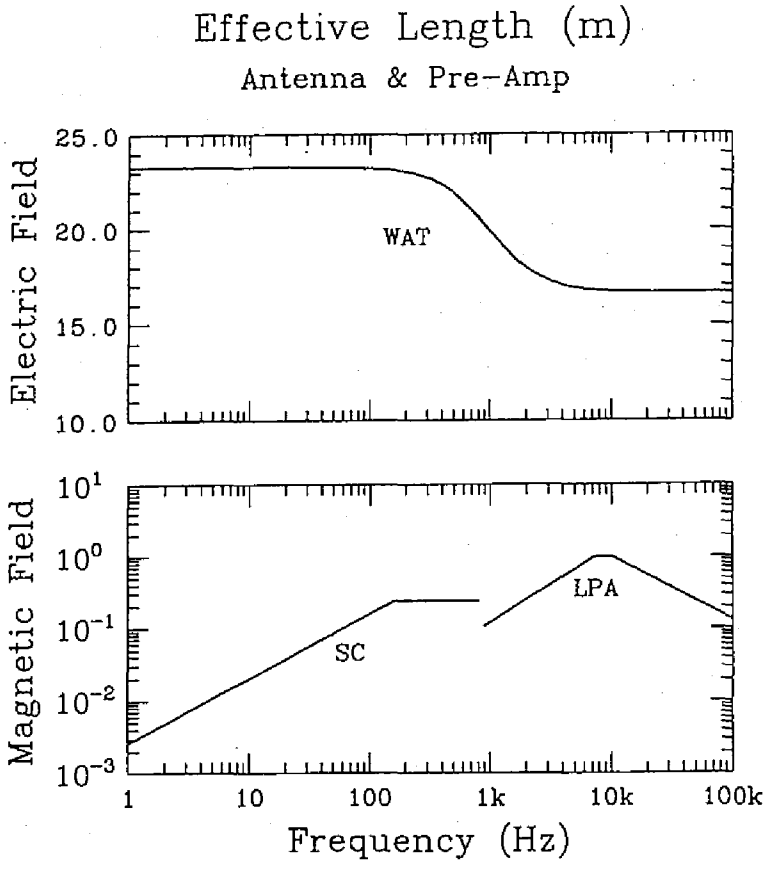

Figure 2.3: Frequency dependences of the effective lengths of electric and magnetic sensors.

where $V_{DPU}(f)$ is a frequency series given by the FFT processing. Thus the absolute intensities of electric and magnetic fields can be calculated.

2.2.2 Compensation for the spin motion

The Akebono satellite is spin-stabilized by making the direction of the spin axis pointing towards the sun with a period of nearly 8 seconds, and the wave data are converted from the satellite coordinate system (X, Y, Z) which is spinning with the satellite to the non-spinning coordinate system (X_o, Y_o, Z_o) referred to the direction of the geomagnetic field and the direction of the sun. The relation between both coordinate systems is shown in Figure 2.4. As shown in this figure, the direction of Z_o in the non-spinning coordinate system is the same as the direction of Z in the satellite coordinate system. The precession of the satellite is not taken into account.

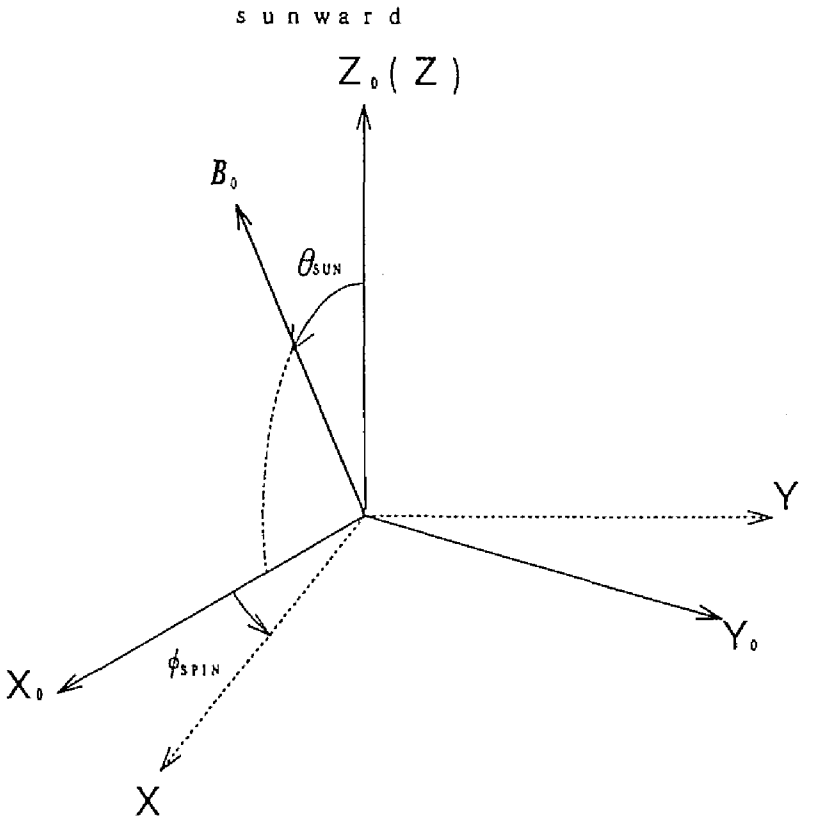

Figure 2.4: Relation between the satellite coordinate system (X, Y, Z) and the non-spinning coordinate system (X_0, Y_0, Z_0).

In order to convert the wave data from the satellite coordinate system to the non-spinning coordinate system, three components of the geomagnetic field data observed by the MGF instruments are referred. The main subjects of the MGF instruments are to observe vectorially the intensity of the geomagnetic field and the structures of field-aligned currents (FAC) in the polar region [*Fukunishi et al.*, 1990]. The MGF instruments include a triaxial fluxgate magnetometer which has four automatically switchable ranges from ± 1024 to ± 65536 nT (full scale) to measure the geomagnetic field. The coordinate system is the same as that of the triaxial search coil magnetometer. The observed data are sampled by 32 Hz and converted to 16 bit words. We can determine the attitude of the Akebono satellite with the help of these geomagnetic field data. The accuracy of the attitude of the Akebono satellite is within 1°. As the spin axis (Z axis) is always directed to the sun with an accuracy within 2.5° and the MGF data are sampled by

32 Hz, the geomagnetic field is assumed to be constant for 1 period of the satellite spin and the spin phase is determined by the variations of X and Y components of the geomagnetic field.

When the geomagnetic field B_0 observed by the MGF instruments in the satellite coordinate is defined by (B_{mX}, B_{mY}, B_{mZ}), the spin phase ϕ_{SPIN} of the satellite is given as follows:

$$\phi_{SPIN} = \arg(B_{mX} - jB_{mY}). \tag{2.39}$$

That is, when B_{mX} is maximum and $B_{mY}= 0$, ϕ_{SPIN} is equal to 0.

Using the spin phase ϕ_{SPIN}, the conversion from (X, Y, Z) in the satellite coordinate system to (X_o, Y_o, Z_o) in the non-spinning coordinate system is given as follows:

$$\begin{pmatrix} X_o \\ Y_o \\ Z_o \end{pmatrix} = \begin{pmatrix} \cos\phi_{SPIN} & -\sin\phi_{SPIN} & 0 \\ \sin\phi_{SPIN} & \cos\phi_{SPIN} & 0 \\ 0 & 0 & 1 \end{pmatrix} \begin{pmatrix} X \\ Y \\ Z \end{pmatrix}. \tag{2.40}$$

2.2.3 Determination of the absolute direction

As a next step, we have to determine the absolute aspect of the satellite, in order to determine the absolute direction, such as the wave normal vector, in the Earth's coordinate system. The absolute aspect of the satellite is determined by assuming that the direction of the geomagnetic field observed by the MGF instruments is identical to that calculated by the IGRF(International Geomagnetic Reference Field) model. A plausible error by this assumption is within 1°.

The relation between the non-spinning coordinate system (X_o, Y_o, Z_o) and the Earth's coordinate system (U, V, W) is shown in Figure 2.5. Since the spin axis points towards the sun and the geomagnetic field B_0 is always in the X_oZ_o plane, the conversion from (X_o, Y_o, Z_o) in the non-spinning coordinate system to (U, V, W) in the Earth's coordinate system is given as follows:

$$\begin{pmatrix} U \\ V \\ W \end{pmatrix} = \begin{pmatrix} u_{X_o} & u_{Y_o} & u_{Z_o} \end{pmatrix} \begin{pmatrix} X_o \\ Y_o \\ Z_o \end{pmatrix}, \tag{2.41}$$

where u_{X_o}, u_{Y_o}, u_{Z_o} are unit vectors of the directions of X_o, Y_o and Z_o respectively represented in the Earth's coordinate system (U,V,W), and are given by

$$u_{Z_o} = s = \begin{pmatrix} s_U \\ s_V \\ s_W \end{pmatrix}, \tag{2.42}$$

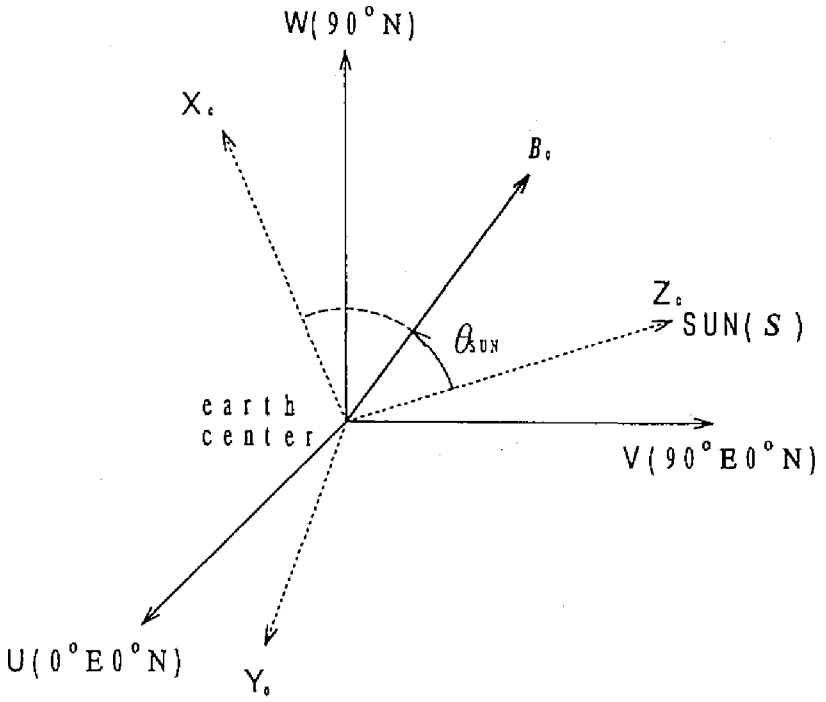

Figure 2.5: The relation between the non-spinning coordinate system (X_o, Y_o, Z_o) and the Earth's coordinate system (U, V, W).

$$u_{X_o} = \frac{B_{0X_o}}{|B_{0X_o}|}, \quad \text{where } B_{0X_o} = B_0 - (B_0 \cdot u_{Z_o}) \cdot u_{Z_o}, \tag{2.43}$$

$$u_{Y_o} = u_{Z_o} \times u_{X_o}, \tag{2.44}$$

where s= (s_U, s_V, s_W) is a unit vector of the sunward direction represented in the Earth's coordinate system.

In the analysis, as far as there is no intense fluctuation in the geomagnetic field, the accuracy of the absolute aspect of the satellite deduced as mentioned above is within 5° [*Ito*, 1990].

2.3 Determination of wave normal direction

The study of the wave normal vector is important to identify the mode of the waves and interpret the propagation characteristics of them. In this section, the technique for analyzing the wave normal vector is described.

2.3.1 Spectral matrix

First, we will describe the spectral matrix which is used in the analysis of the wave normal vector. We define functions $g_i(t)$ (where i = 1, 2, 3, 4, 5, 6) from analytic representations of the measured electric and magnetic field of the wave $E_{x,y,z}$ and $B_{x,y,z}$, respectively, in the time domain in a three dimensional coordinate system (x,y,z).

$$g_{1,2,3}(t) = E_{x,y,z}(t), \tag{2.45}$$

$$g_{4,5,6}(t) = Z_0 \cdot B_{x,y,z}(t), \tag{2.46}$$

where Z_0 is the space impedance in free space. Using those functions $g_i(t)$, the six-dimensional covariance matrix is given by the following equation,

$$J = \begin{vmatrix} \langle g_1(t)g_1^*(t)\rangle & \langle g_1(t)g_2^*(t)\rangle & \cdots & \langle g_1(t)g_6^*(t)\rangle \\ \langle g_2(t)g_1^*(t)\rangle & \langle g_2(t)g_2^*(t)\rangle & \cdots & \langle g_2(t)g_6^*(t)\rangle \\ \vdots & \vdots & & \vdots \\ \langle g_6(t)g_1^*(t)\rangle & \langle g_6(t)g_2^*(t)\rangle & \cdots & \langle g_6(t)g_6^*(t)\rangle \end{vmatrix}, \tag{2.47}$$

where $g_i^*(t)$ (i = 1, 2, 3, 4, 5, 6) indicates the complex conjugate function of $g_i(t)$. However, the generation of the covariance matrix in the time domain is complicated, since the generation of the analytic representation of a real function involves a convolution integral. Then by using the generalized power theorem:

$$\int_{-\infty}^{\infty} g(t)h^*(t)\mathrm{d}t = \int_{-\infty}^{\infty} G(f)H^*(f)\mathrm{d}f, \tag{2.48}$$

we can extend the definition of the covariance matrix to the frequency domain. That is,

$$S = \begin{vmatrix} \{G_1(f)G_1^*(f)\} & \{G_1(f)G_2^*(f)\} & \cdots & \{G_1(f)G_6^*(f)\} \\ \{G_2(f)G_1^*(f)\} & \{G_2(f)G_2^*(f)\} & \cdots & \{G_2(f)G_6^*(f)\} \\ \vdots & \vdots & & \vdots \\ \{G_6(f)G_1^*(f)\} & \{G_6(f)G_2^*(f)\} & \cdots & \{G_6(f)G_6^*(f)\} \end{vmatrix}, \tag{2.49}$$

where the braces represent the average over all the positive frequencies and the functions $G_i(f)$ (i = 1, 2, 3, 4, 5, 6) are the Fourier transforms of the corresponding time functions. Since the functions $G_i(f)G_j^*(f)$ (i, j = 1, 2, 3, 4, 5, 6) give the distribution of the covariance with respect to frequency, we can use the spectral matrix (2.49) as a function of frequency.

2.3.2 Determination methods under plane wave approximation

Several methods have been developed for determining the direction for wave normal vector by many authors [*Means*, 1972; *Samson and Olson*, 1980; *Sakamoto et al.*, 1995; *Storey and Lefeuvre*, 1979; 1980]. It is easily derived from the Maxwell's equations that a direction of wave normal vector is always perpendicular to the polarization plane of the wave magnetic field. Therefore, if there exists only a plane electromagnetic wave, we can determine the direction of the wave normal vector by determining the polarization plane of the wave magnetic field. In this section, we will introduce some methods which are useful for the case that only one plane wave exists.

1. **Means' Method** [*Means*, 1972]

   From the definition of the covariance matrix or spectral matrix mentioned above, each element of the matrix includes the information of the phase difference between one component of wave form and another. If the off-diagonal elements of the matrix are nonzero, the components of the signals are at least partly coherent and the imaginary part of the matrix represents the signals with components in quadrature to one another. Thus if a wave is propagating as a single plane wave, the wave normal direction k can be determined from imaginary part of the spectral matrix calculated by three components of magnetic wave field as follows:

$$k \;//\; \begin{pmatrix} \mathrm{Im}(S_{56}) \\ \mathrm{Im}(S_{64}) \\ \mathrm{Im}(S_{45}) \end{pmatrix}, \tag{2.50}$$

   where the double slash indicates that these two vectors are parallel to each other and Im (S_{ij}) $(i,j = 4, 5, 6)$ indicates the imaginary part of ijth element of the spectral matrix. We must notice that the wave normal direction has an ambiguity of 180°, since only magnetic field components are used in (2.50). In order to determine the absolute sense of the direction, we use the phase information of electric field components in a way that the refractive index μ of the wave calculated by the following equation becomes positive:

$$\mu = \frac{cB_Z}{u_{kY}E_Y - u_{kY}E_X}, \tag{2.51}$$

   where u_{kY} and u_{kY} are the X and Y components of unit vector of wave normal direction.

   Because this technique is simple and reduces the computation time for the determination of wave normal vector, in the study so far made, we have analyzed the wave normal and

Poynting flux directions of the Omega signals observed by the PFX subsystem by the Means' method. Omega signals are VLF signals for radio navigation and are transmitted from eight stations in the world. Because the band width of the signal is very narrow and we can identify the transmitting station of these Omega signals by referring to the time format of the signal which is different for each station, the signals observed by the Akebono satellite can be analyzed as one plane wave.

2. **Eigen Vector Method** [*Samson and Olson*, 1980]
   The Means' method is a simple method, but has some restriction to be used for the analysis. That is, the Means' method shown by (2.50) is valid for a plane polarized wave. *Samson* and *Olson* [1980] suggested the eigen vector method.

   We define the eigenvalues of three-dimensional spectral matrix calculated from three components of wave magnetic field as λ_m (where $m = 1, 2, 3$), and corresponding eigenvectors as u_m. If there are not more than two nonzero eigenvalues, the number of the nonzero eigenvalues corresponds to the number of the waves. If there are three eigenvalues, we can't distinguish there are three waves or more. According to the eigen vector method, the wave normal direction k is given by the following equation when the spectral matrix has only one non-zero eigenvalue λ_1:

$$k \;//\; \mathrm{Re}(u_1) \times \mathrm{Im}(u_1), \tag{2.52}$$

   where "Re" and "Im" indicate real and imaginary part of the eigenvector, respectively.

3. **Amplitude Method** [*Sakamoto et al.*, 1995]
   The two methods introduced as above are both using the phase information concerning the wave magnetic field. Amplitude method was developed by our group [*Sakamoto et al.*, 1995], which is a geometrical method to determine the direction of wave normal vector. The merit of the method is that information of relative phase between one component of wave field and another is not necessary, that is, this method is applicable even when only the information of amplitude of three components of wave magnetic field and two components of wave electric field. The validity of this method is guaranteed under the condition that the wave is circularly polarized. This assumption is well satisfied for a wide range of wave normal angle for the whistler wave mode, except very close to the resonance cone angle.

In the present study, however, we have to analyze the wave normal direction of natural emissions whose band width is relatively wide. That is, we may observe waves with a finite

bandwidth and with different directions at the same time. In case there are multiple waves coexisting, it has been known that the methods for determination of the wave normal direction introduced above are not always correct. Therefore we must analyze the wave normal direction without one plane wave assumption. In that case, the wave distribution function (WDF) method, introduced by *Storey and Lefeuvre* [1979; 1980], described in the next subsection is useful.

2.3.3 Wave distribution function method

The WDF is derived from the concept that observed signals consist of a number of elementary plane waves and can be defined as the distribution of the wave energy density relative to the angular frequency ω and to the variables ψ and η. Calculating a spectral matrix composed from the autospectra and cross spectra of the electric and magnetic wave field components S_{ij}, the WDF is related to the spectral matrix by the following equation,

$$S_{ij} = \frac{\pi}{2} \int_0^{2\pi} \int_0^{\pi} a_{ij}(\omega, \psi, \eta) F(\omega, \psi, \eta) \sin\psi \mathrm{d}\psi \mathrm{d}\eta, \quad (i, j = 1, 2, 3, 4, 5, 6) \tag{2.53}$$

where $a_{ij}(\omega, \psi, \eta)$ are integration kernels introduced by *Storey and Lefeuvre* [1980], and $F(\omega, \psi, \eta)$ is the distribution function for a wave with its frequency ω and the wave normal direction (ψ, η). Knowing the integration kernels a_{ij} and the calculated S_{ij}, we can estimate the function F by solving the set of integral equations (2.53).

In the present study, we have taken account of the effects of multicomponent ions in the integration kernels a_{ij} in order to study the effect of multicomponent ion constituents. Integration kernels a_{ij} are determined by the propagation mode, plasma frequencies, and cyclotron frequencies of electron and ion frequencies, that is, a_{ij} is derived from refractive index of the wave (μ calculated by (2.16)) in which the effects of ions are involved.

As S_{ij} and a_{ij} are the elements of Hermitian matrix, equations (2.53) can be transformed into more simple equation as follows:

$$P_k(\omega) = \frac{\pi}{2} \int_0^{2\pi} \int_0^{\pi} q_k(\omega, \psi, \eta) F(\omega, \psi, \eta) \sin\psi \mathrm{d}\psi \mathrm{d}\eta, \quad k = 1, 2, \cdots, 36) \tag{2.54}$$

where

$$\begin{aligned} P_1 &= \mathrm{Re}(S_{11}) = S_{11}, \quad P_2 = \mathrm{Re}(S_{12}), \quad P_3 = \mathrm{Im}(S_{12}), \quad \cdots, \quad P_{36} = \mathrm{Re}(S_{66}) = S_{66} \\ q_1 &= \mathrm{Re}(a_{11}) = a_{11}, \quad q_2 = \mathrm{Re}(a_{12}), \quad q_3 = \mathrm{Im}(a_{12}), \quad \cdots, \quad q_{36} = \mathrm{Re}(a_{66}) = a_{66} \end{aligned} \tag{2.55}$$

Solving equations (2.53) or (2.54) is a so-called ill-posed problem and the solution is not determined uniquely. In order to solve (2.53) or (2.54), we must assume an adequate model as

a solution. Several kind of models are suggested by many authors, e.g. [*Buchalet and Lefeuvre*, 1981], and we applied two different methods in the present study: One is a maximum entropy method (MEM) [*Lefeuvre and Delannoy*, 1979; *Lefeuvre et al.*, 1981], and the other is a Phillips-Tikhonov regularization method (PTM) [*Yamaguchi et al.*, 1992; 1993].

In the MEM, the entropy of the function F can be expressed as the following equation,

$$H(F) = \int_0^{2\pi} \int_0^{\pi} F \log \frac{1}{F} \mathrm{d}\psi \mathrm{d}\eta. \tag{2.56}$$

When the entropy $H(F)$ takes its maximum subject to the constraints of (2.54), the solution F becomes as follows,

$$F(\psi, \eta) = \exp\left(-1 + \sum_{i=1}^{N} \mu_i q_i(\psi, \eta)\right), \tag{2.57}$$

where the parameters μ_i are Lagrange multipliers and N is the number of available projection data. Obtaining the solution of the Lagrange multipliers μ_i, F can be determined.

On the other hand, in the Phillips-Tikhonov regularization method (PTM), an optimum solution is supposed to be sufficiently smooth. This method was first applied for the ground-based direction finding of the magnetospheric VLF/ELF radio wave by *Yamaguchi et al.* [1992; 1993]. Therefore they assumed wave distribution function F on a plane rectangular area in the ionosphere. As our observation is made in the magnetosphere and wave distribution function F is defined in a spherical surface (ψ, η), we modified their method for our purpose. We introduce an objective function $R(F)$ as follows,

$$R(F) = \iint |\nabla^2 F(\psi, \eta)|^2 \sin\psi \mathrm{d}\psi \mathrm{d}\eta. \tag{2.58}$$

The solution is obtained by minimizing equation (2.58) subject to the constraints of (2.54).

In order to solve the problem algebraically, we divide the reconstruction area of the distribution function into $k_\psi \times k_\eta$ pixels, where k_ψ and k_η are the number of strips on the spherical surface represented by (ψ, η). Using the Laplacian matrix C, the problem is solved by minimizing the following equation,

$$R(\boldsymbol{f}) = |C\boldsymbol{f}|^2, \tag{2.59}$$

subject to

$$\frac{1}{N}|\boldsymbol{p} - Q\boldsymbol{f}|^2 \leq \epsilon^2, \tag{2.60}$$

where $\boldsymbol{f}$ is a column vector whose element is a quantity of wave distribution function F in each pixel, $\boldsymbol{p}$ is a column vector whose elements are P_k, Q is a matrix corresponding to the

integration kernel, and ϵ is the limit of error. This procedure is equivalent to the minimization of the following quantity,

$$J(f) = \gamma|Cf|^2 + \frac{1}{N}|p - Qf|^2, \tag{2.61}$$

and the solution is expressed as follows:

$$f = |Q^tQ + N\gamma C^tC|^{-1}Q^tp \tag{2.62}$$

where γ is so-called the regularization parameter. If γ is large the image of the solution becomes smooth but decreases spatial resolution, while the smaller γ causes the solution more unstable because of the effect of noise. In order to choose the optimum value for the parameter γ, we refer to a criterion such as PRESS (PREdiction Sum of Square), or its generalized version GCV (Generalized Cross Validation) [*Yamaguchi et al.*, 1992; 1993].

2.3.4 Simulation of wave distribution function method

Using computer-generated spectral matrix S_{ij} which was calculated from given wave distribution function $F(\omega, \psi, \eta)$ by (2.53), the performance of the wave distribution function (WDF) method using two different methods, the maximum entropy method (MEM) and the Phillips-Tikhonov regularization method (PTM), was evaluated.

In order to compare the merits and demerits of the MEM and the PTM, several cases were examined by varying the distribution of wave source. The source wave is assumed to be whistler mode wave with the frequency of 10 kHz, and plasma frequency and cyclotron frequency of electron are 350 kHz and 450 kHz, respectively. Ion constituents were assumed to be (80% H^+, 15% He^+, 5% O^+), but it should be noticed that the effect of ion constituents is negligible in the present simulation because the wave mode is whistler mode. As for the effects of ion constituents on the solution of the WDF, we will mention in Chapter 3 and 4. Furthermore, we used only three components of magnetic wave field, thus a spectral matrix is composed of 3×3 components and the wave distribution reconstructed by the WDF method has an ambiguity of 180°.

One point source

Wave source is assumed to be a single point source located at (ψ, η)=(60°, 120°). Figures 2.6 (a) and (b) show the reconstructed wave distribution using the MEM and the PTM, respectively. In the figure, the polar angle ψ is shown by the radius of the circle, and the azimuthal angle η is measured peripherally counterclockwise from the reference radial axis of the polar angle.

It is found that the wave distribution is successfully reconstructed by the MEM. As for the wave distribution reconstructed by the PTM, the location of the peak is correctly reconstructed, but the image is widely distributed. The reconstructed image by the PTM becomes sharper if the size of pixels for the reconstruction area of the distribution function is reduced. However, computation time and memory increase in exponential. In the present study, we divided the reconstruction area with $(\Delta\psi, \Delta\eta) = (7.5°, 15°)$ in order to make time for computation comparable to one by the MEM. In the figure, the reconstructed image is still more widely distributed than the resolution of reconstruction area. This comes from the principle of the PTM that an optimum solution is supposed to be sufficiently smooth.

Two point sources

Wave source is assumed to be two point sources located at (ψ, η)=(60°, 120°) and (60°, 270°). The intensities of two point source are same. Figures 2.7 (a) and (b) show the reconstructed wave distribution using the MEM and the PTM, respectively. In Figure 2.7 (a), the locations of two peaks are almost correctly estimated, however, the reconstructed shapes of wave distribution are elongated elliptically. The closer the locations of the two point sources, the more conspicuous this tendency becomes, and finally estimated image becomes only one elliptical source (not shown here). On the other hand, the wave distribution estimated by the PTM method (Figure 2.7 (b)) is almost correctly reconstructed except the fact that the reconstructed image is widely distributed. In case two point sources is more closely located, the image becomes a coupled two wave sources with gourd shaped and finally becomes one distribution, however, the shape of solution is never elongated elliptically (not shown here).

One extended source

The performances of two methods for the extended wave source were evaluated. Figure 2.8 (a) shows an extended wave source approximated by a Gaussian distribution having its peak located at (ψ, η)=(60°, 120°). The width at half maximum is assumed to be 30°. Figures 2.8 (b) and (c) show the wave distribution reconstructed by the MEM and the PTM, respectively. The image is almost correctly reconstructed by the MEM although the wave distribution shape is a little narrow and distorted. The image reconstructed by the PTM is also almost correctly reconstructed.

Two extended sources

Figure 2.9 (a) shows two extended wave source approximated by a Gaussian distribution with their center separately located at (ψ, η)=(60°, 120°) and (60°, 270°), whose intensities are same and widths of half maximum are both 20°. Figures 2.9 (b) and (c) show the reconstructed wave distribution using the MEM and the PTM, respectively. We find that both methods can almost correctly reconstruct the wave distribution, although there exist a little error in azimuthal direction η for both method. The closer the locations of the two point sources, the image reconstructed by the MEM becomes worse than that by the PTM, which is the same tendency as the case for two point sources described before.

Effect of S/N ratio

An effect of signal-to-noise (S/N) ratio is taken into account in the simulation. A single wave point source is located at (ψ, η)=(60°, 120°), and randomly distributed noise, whose bandwidth is the same as the wave source and intensity is 10 dB weaker, is added to the wave distributions function. Figures 2.10 (a) and (b) show the reconstructed wave distribution using the MEM and the PTM, respectively. It is found that the wave distribution estimated by the MEM is sensitive to the noise, whereas the result by the PTM is correctly reconstructed.

Summary

In conclusion, the MEM is more suitable than the PTM for the estimation of sharply distributed wave source, e.g. a point source. Because of the principle of the PTM that an optimum solution is supposed to be sufficiently smooth, reconstructed image by the PTM becomes dull. In addition, computation time and memory increase in exponential for the PTM when the size of pixels for the reconstruction area of the distribution function is reduced. Therefore there is a limitation of resolution for the PTM. However, the PTM can be efficiently used for the extended wave source.

The effect of signal-to-noise ratio for two methods is also examined. The MEM is more sensitive to the noise than the PTM. This may be explained that the regularization parameter γ is taken into account in the PTM in order to make the effect of noise as small as possible, whereas the MEM has no such kind of objective index.

In the simulation, we have confirmed that our results deduced from these two methods whose principles are quite different are almost agreeable. However, both methods do not always perfectly reconstruct the true image for all cases. Therefore we must notice the merits and demerits of the MEM and PTM and select more optimum method.

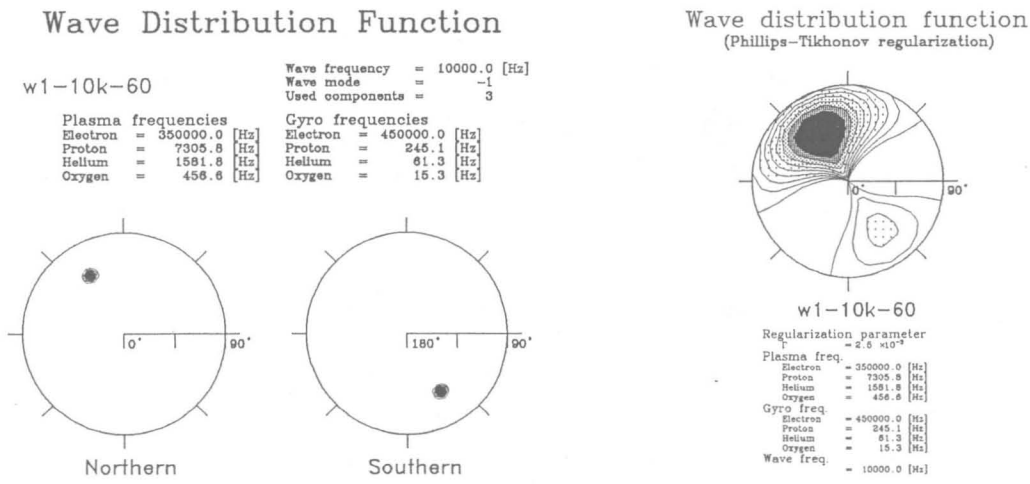

Figure 2.6: Wave distribution reconstructed by (a) the MEM and (b) the PTM, when wave source is assumed to be a single point source located at $(\psi, \eta) = (60°, 120°)$.

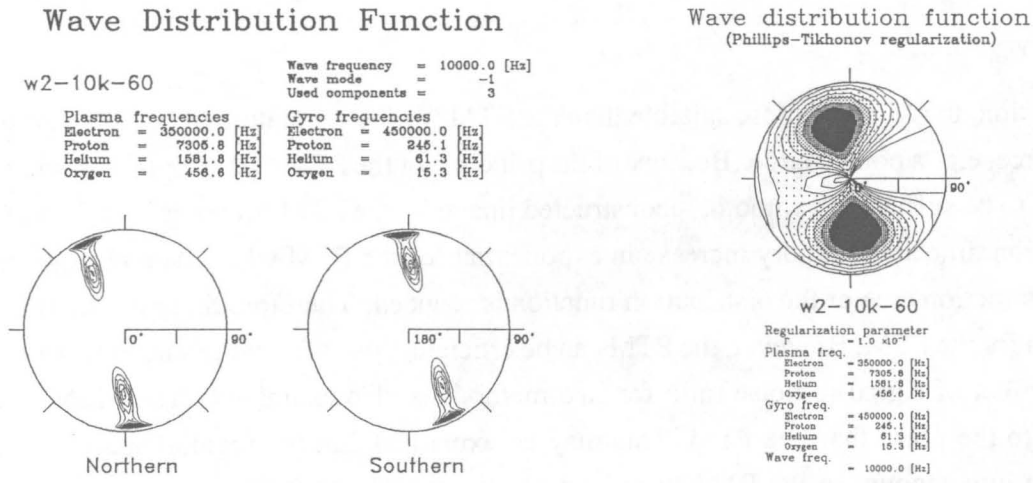

Figure 2.7: Wave distribution reconstructed by (a) the MEM and (b) the PTM, when wave sources are assumed to be two point sources located at $(\psi, \eta) = (60°, 120°)$ and $(60°, 270°)$, where their intensities are same.

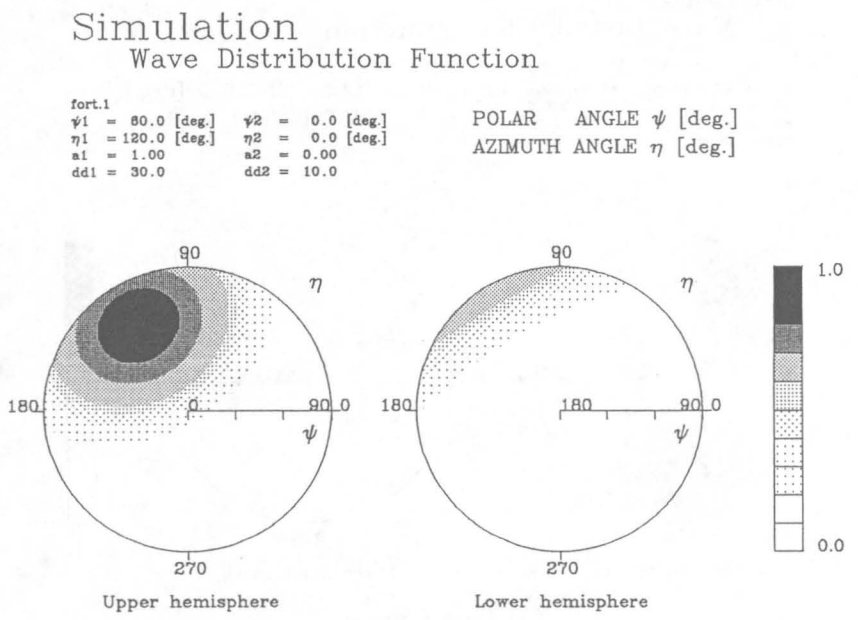

(a) True Source

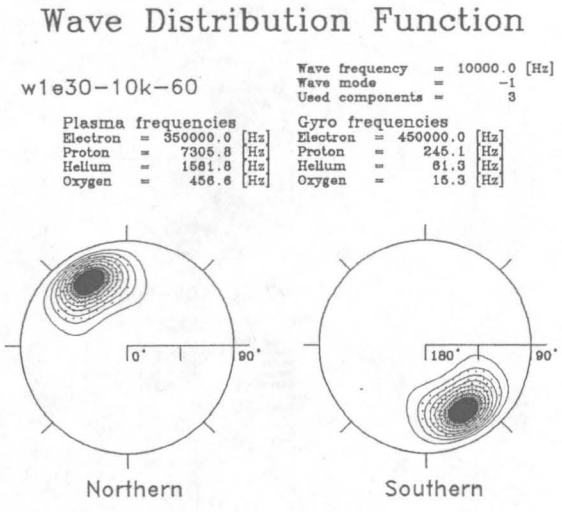

(b) MEM

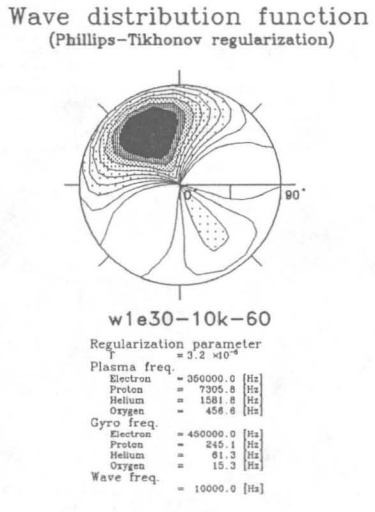

(c) PTM

Figure 2.8: (a) One extended wave source approximated by a Gaussian distribution having its peak located at (ψ, η)=(60°, 120°) and half width of 30°. (b) and (c) show the wave distribution reconstructed by the MEM and the PTM, respectively.

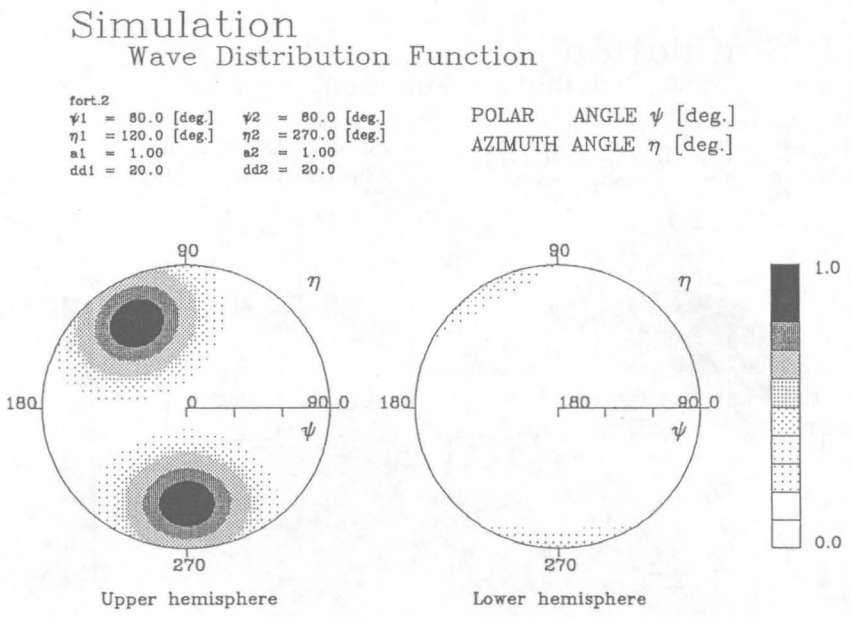

(a) True Source

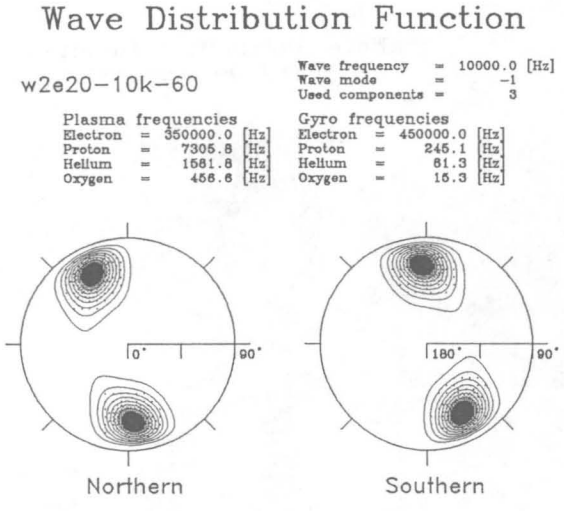

(b) MEM

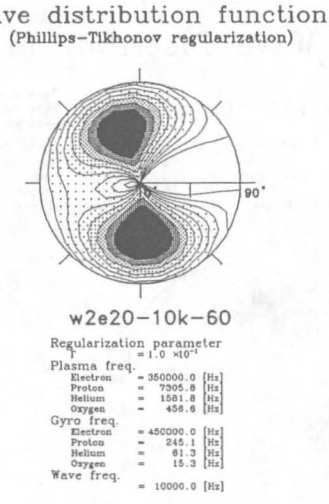

(c) PTM

Figure 2.9: (a) Two extended wave sources approximated by Gaussian distributions having their peaks located at (ψ, η)=(60°, 120°) and (60°, 270°). Their intensities at peak points are same and the widths at half maximum are both 30°. (b) and (c) show the wave distribution reconstructed by the MEM and the PTM, respectively.

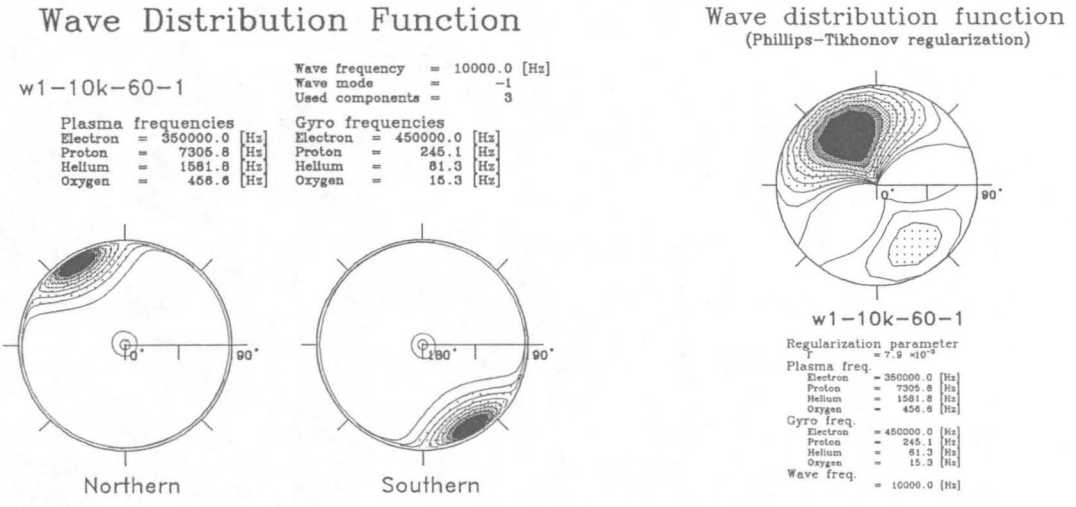

Figure 2.10: Wave distribution reconstructed by (a) the MEM and (b) the PTM, when the S/N ratio equals to 10 dB. A single point wave source is assumed to be located at (ψ, η) = (60°, 120°).

Chapter 3

Ion Cyclotron Wave in the vicinity of the Magnetic Equator

3.1 Introduction

Using the ELF instrument, various kinds of wave phenomena have been observed. Especially in the vicinity of the geomagnetic equator, bands of electromagnetic ELF emissions were often observed. The frequency range of the ELF instrument covers the local cyclotron frequencies of proton (H^+), helium (He^+), and oxygen (O^+) ions, and most of these wave phenomena are considered to be associated with ion constituents. These ELF emissions observed by the Akebono satellite around the geomagnetic equator are classified into two types. One is usually observed below the local proton cyclotron frequency (f_{cH^+}) with a clear cutoff above the local cyclotron frequencies of heavy ions such as helium or oxygen (type A). The other is observed not only below but also above the local proton cyclotron frequency, has a multiband structure in frequency, and has no dependence upon the local cyclotron frequencies (type B).

In the past, several observations by other satellites have been reported for emissions similar to those observed by the Akebono satellite in the frequency ranges near the local ion cyclotron frequencies around the geomagnetic equatorial region, although most of their locations of observation and their absolute frequency ranges are greatly different from ours. By the GEOS 1 and 2 satellites, measurements of ULF-ELF waves were made near the plasmapause and ULF-ELF emissions in a frequency range near the local cyclotron frequencies of H^+ and He^+ ions ($0.4 \sim 2$ Hz) were observed around the geomagnetic equatorial region [*Young et al.*, 1981]. Similar emissions were also observed by the ATS-6 satellite [*Mauk et al.*, 1981]. They were interpreted as ion cyclotron waves (ICW) associated with the existence of He^+ ions [*Young et al.*, 1981;

Mauk et al., 1981; *Roux et al.*, 1982]. The propagation characteristics of these ELF emissions were confirmed by ray tracing in a cold plasma model [*Rauch and Roux*, 1982]. Several studies have been made for the wave-particle interaction between ICW and multicomponent ions by using analytical results and simulation techniques [*Gendrin et al.*, 1984; *Omura et al.*, 1985; *Gomberoff and Vega*, 1987; *Omura et al.*, 1988].

On the other hand, observations by the OGO 3 satellite have revealed the existence of the ELF noise in frequencies between 1 and 1000 Hz near the geomagnetic equator [*Russell et al.*, 1970]. They proposed that these waves were propagating nearly perpendicular to the geomagnetic field. By the IMP 6 and the Hawkeye 1 satellites, a band of intense electromagnetic noise is frequently observed near the magnetic equatorial plane at radial distance from about 2 to 5 R_E (R_E is the radius of the Earth, that is, $\simeq$ 6,370 km) [*Gurnett*, 1976]. *Perraut et al.* [1982] reported a detailed analysis of that kind of waves in the frequency range from 0.2 Hz to 12 Hz observed by the GEOS 1 and 2 satellites in the vicinity of the geomagnetic equator at all L-values between 4 and 8. These waves are mainly polarized along the geomagnetic field with a right-handed polarization. They have frequencies above the cyclotron frequency of proton and a harmonic structure. *Perraut et al.* [1982] designated these waves as magnetosonic waves (MSW) propagating in a direction perpendicular to the geomagnetic field.

As for the observation by the Akebono satellite, type A emission is very similar to ion cyclotron waves observed by the GEOS 1 and 2 satellites and the ATS-6 satellite, and type B emission is similar to the ones introduced by *Russell et al.* [1970] and *Gurnett* [1976]. In the present chapter, we introduce the characteristics of type A emissions observed by the Akebono satellite, in a manner similar to that of *Young et al.* [1981] and *Roux et al.* [1982]. As for type B emissions, we will discuss in the next chapter.

An outline of the present chapter is as follows. In the next section the results of data analyses of the ELF waves observed by the Akebono satellite are presented. In section 3.3, with reference to the generation mechanism of the emissions, we will present the results of three-dimensional ray tracing for ion mode waves using both a cold and a hot plasma model. Propagation characteristics, spatial distribution, and growth rates of the emissions are clarified by our ray tracing. Finally, a summary and discussions are added in the last section.

3.2 Observation

3.2.1 General characteristics

At first we will introduce the typical spectra of type A emissions observed by the Akebono satellite in the vicinity of the geomagnetic equator.

Figure 3.1 shows an example of type A emissions observed from 0342 to 0358 UT on May 27, 1989, when the Akebono satellite was tracked from Kagoshima Space Center (KSC) in Japan. ALT, MLT, and MLAT stand for altitude (kilometers), magnetic local time, and magnetic latitude, respectively, of the trajectory of the Akebono satellite. The vertical dashed line indicates the location of the geomagnetic equator. The thick solid lines indicates the local He^+ cyclotron frequency (f_{cHe^+}), and O^+ cyclotron frequency (f_{cO^+}), respectively. The thin solid line indicates a half of the local H^+ cyclotron frequency (f_{cH^+}). The Akebono satellite was traversing from the southern hemisphere to the northern hemisphere. The telemetry reception was terminated on this orbit nearly at the geomagnetic equator for the sake of ranging the Akebono satellite.

In the figure a band of emissions were observed for the geomagnetic latitude range from $-28°$ to nearly $0°$. It is clearly seen that the frequencies of the emissions are always above the local f_{cHe^+}, and there is a sharp gap between the bottom of the emissions and the f_{cHe^+}. It is distinctive that these emissions have magnetic field components, so that these are identified as one of the electromagnetic ion cyclotron modes. A dark horizontal band around 32 Hz, most apparent in the magnetic field components, is caused by interference.

Figure 3.2 illustrates the frequency dependence at 0358:00 UT of E_y and B after a fast Fourier transform (FFT) analysis, where

$$B = \sqrt{sB_X{}^2 + sB_Y{}^2 + sB_Z{}^2}. \tag{3.1}$$

The frequency resolution is 1.25 Hz, and dashed lines in the figure represent the threshold levels for electric field and magnetic field channels respectively. The internal interference around 32 Hz, seen in Figure 3.1, has been removed in Figure 3.2. From the figure the maximum electric and magnetic fields around 55 Hz are 60 μV/m and 14 pT, respectively.

Figure 3.3 shows an event observed from 1034 to 1047 UT on July 14, 1989, in which two bands of emissions coexist, one above f_{cHe^+} (the upper thick solid line in the figure) and the other one above f_{cO^+} (the lower thick solid line) although the frequency of the lower band emission becomes a little less than f_{cO^+} in the higher altitude range. It should be noticed that

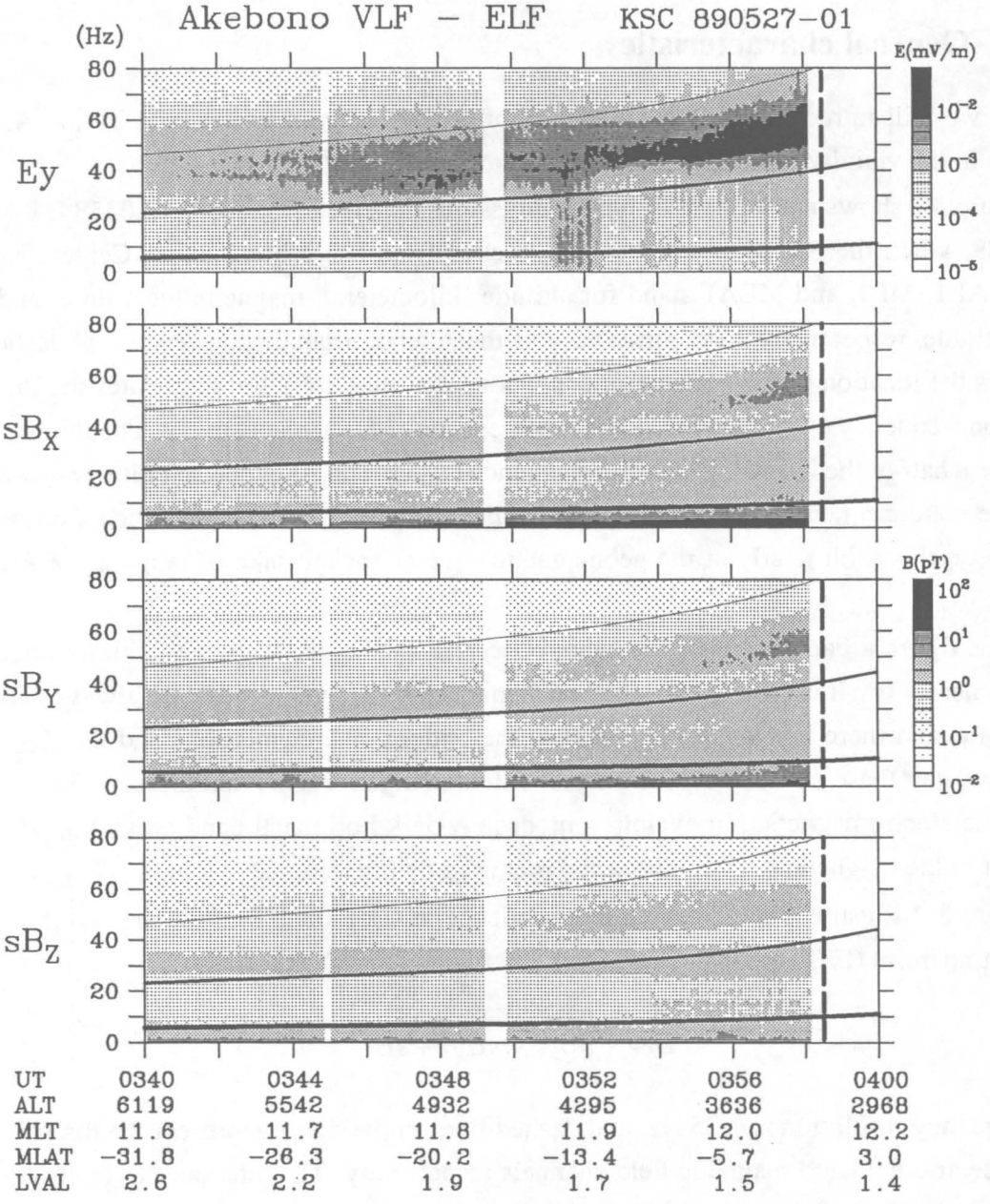

Figure 3.1: An f-t diagram of the ELF emissions observed on May 27, 1989. The vertical dashed line indicates the location of the geomagnetic equator. The thick solid lines indicates the local He^+ cyclotron frequency (f_{cHe^+}), and O^+ cyclotron frequency (f_{cO^+}), respectively. The thin solid line indicates a half of the local H^+ cyclotron frequency (f_{cH^+}).

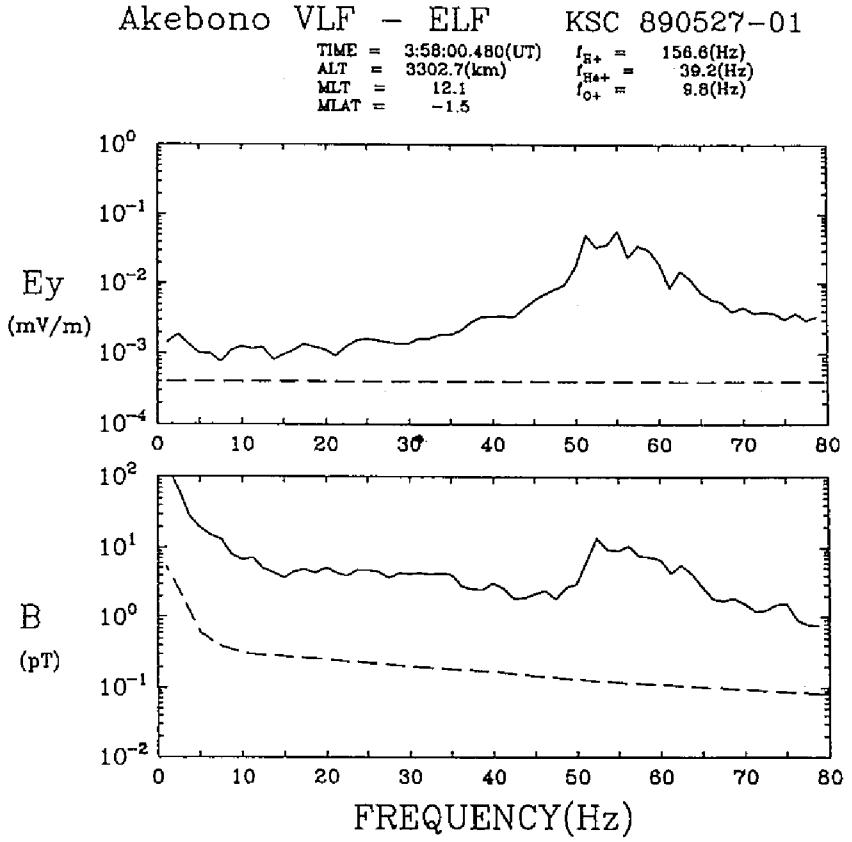

Figure 3.2: Frequency dependence of the electric and magnetic intensity of the ELF emissions observed on May 27, 1989. The dashed lines represent the threshold levels for electric field and magnetic field channels respectively.

the geomagnetic latitude range where the lower band emissions were observed is wider than the range of the upper band emissions.

In this figure, because the intensities of the electric components are very weak (the peak intensities of both emissions are about 1.5 μV/m) in comparison with the case on May 27, 1989, the magnetic components were under the threshold noise level and were not identified. In some cases with two emission bands coexisting. However, the magnetic field component is also identified. Therefore these ELF emissions are considered to be one of the electromagnetic ion cyclotron modes.

These examples indicate that the frequencies of these waves are dependent on the local cyclotron frequencies of ions, that is, they are closely connected with the presence of He^+ and O^+

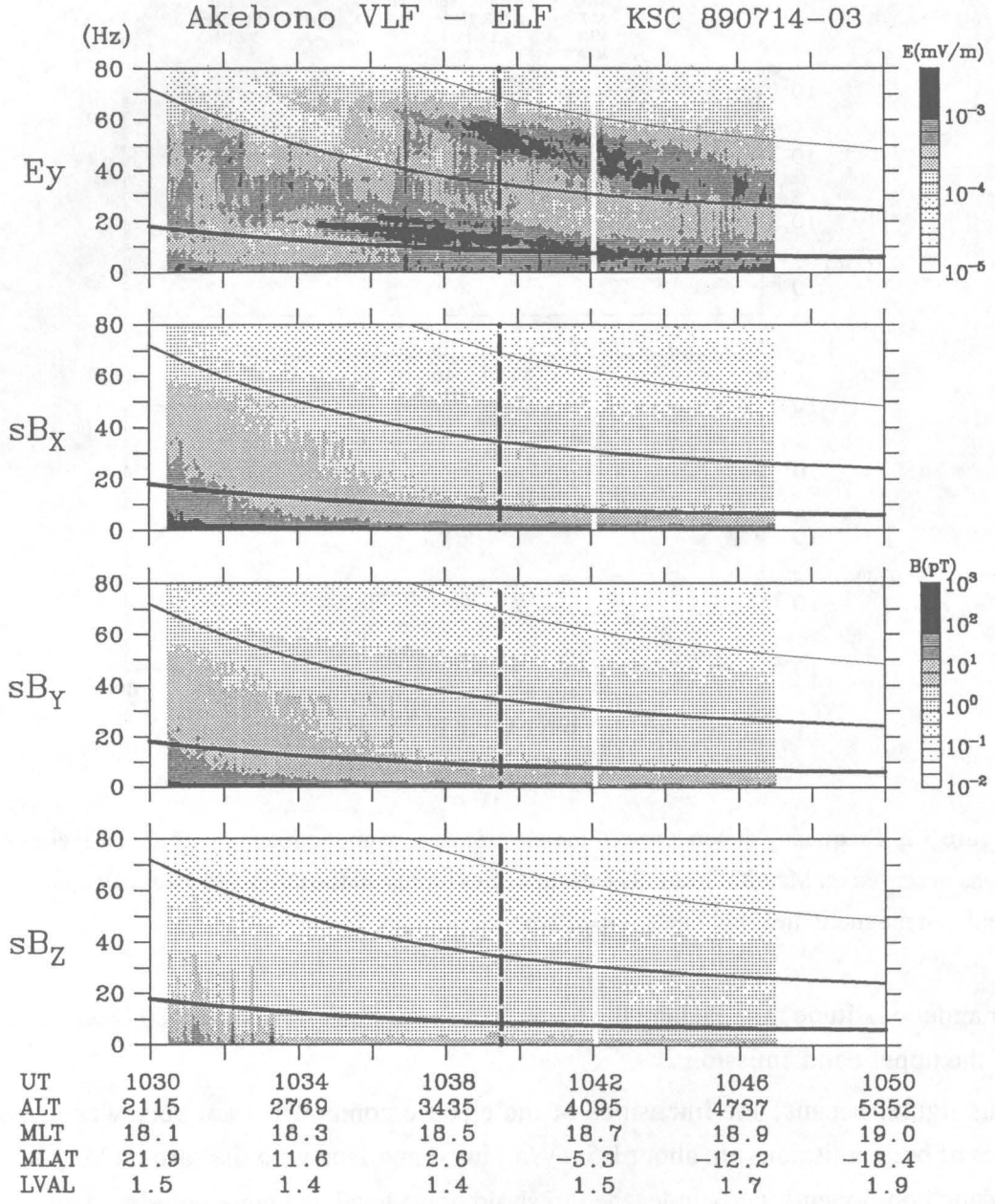

Figure 3.3: An f-t diagram of the ELF emissions observed on July 14, 1989. The vertical dashed line indicates the location of the geomagnetic equator. The thick solid lines indicates the local f_{cHe^+} and f_{cO^+}, respectively. The thin solid line indicates $0.5 f_{cH^+}$.

ions in addition to H^+ ions in the magnetospheric plasma. In this paper we propose that these ELF emissions are electromagnetic ion cyclotron waves (ICW) trapped along the magnetic field lines around the geomagnetic equatorial region. The details of the ICW mode will be discussed in the following sections. The generation mechanism of these emissions will be discussed in section 3.3. In the following we will call the upper band of emissions above f_{cHe^+} the H^+ mode, and the lower band of emissions above f_{cO^+} the He^+ mode.

3.2.2 Statistical study

In this section we will show the results of the statistical analyses of type A emissions which we observed. In general, the characteristics of the H^+ mode emissions are very similar to those of the emissions observed by the GEOS 1 and 2 satellites [*Young et al.*, 1981], though the absolute frequencies observed by us were much higher than those observed by the GEOS 1 and 2 satellites, since the locations of our observations are much lower than the GEOS observations. On the other hand, there have been no previous observation reports of emissions similar to the He^+ mode emissions revealed by our observation using the Akebono satellite.

Spatial and time distribution

We have analyzed the data of 775 orbits tracked at KSC, Prince Albert (PA) in Canada and Esrange (ESR) in Sweden from April 1989 to November 1990, although we have not yet completed the examination of all the data in this term. In the analyses we have found 81 H^+ mode emissions and 48 He^+ mode emissions, in which we do not count emissions whose mode is not clearly identified. For 48 passes in which the He^+ mode emissions were observed the H^+ mode emissions were simultaneously observed. On the other hand, there are some cases when those emissions were observed in 1994 and 1995, although the frequency of observation around the geomagnetic equator is fewer compared with 1989 or 1990.

The trajectories of the Akebono satellite while the H^+ mode emissions were observed are shown in Figure 3.4, which includes the cases where the H^+ mode and He^+ mode emissions were simultaneously observed. On the other hand, the trajectories for the He^+ mode emissions are shown in Figure 3.5. In Figure 3.4 and Figure 3.5 the left panels show the projections of the trajectories on the geomagnetic meridian plane and the right panels show their projections on the geomagnetic latitude-longitude plane.

In these figures we can find that most of the H^+ mode emissions were observed in a region lower than 20° in geomagnetic latitude. It is interesting to note that the observed region of

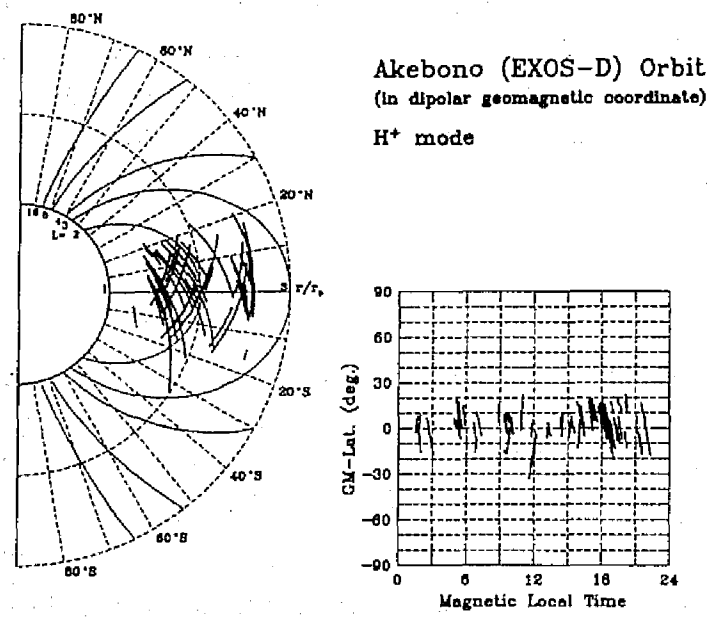

Figure 3.4: Trajectories of the Akebono satellite where the H^+ mode emissions were observed.

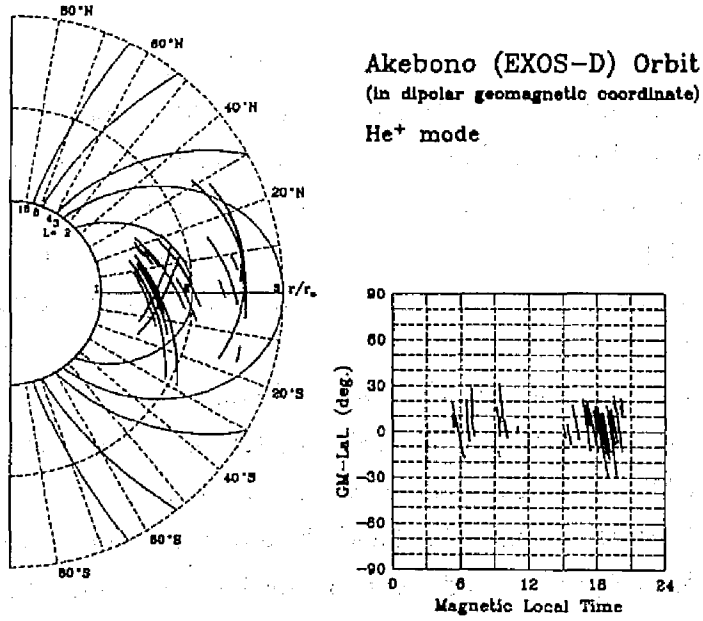

Figure 3.5: Trajectories of the Akebono satellite where the He^+ mode emissions were observed.

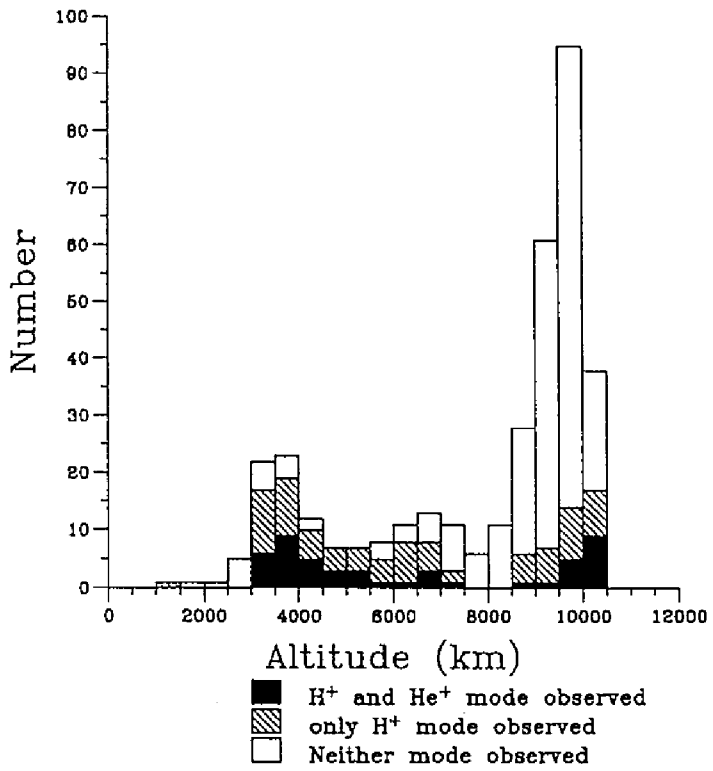

Figure 3.6: Altitude dependence of the occurrence probabilities of the H^+ mode and the He^+ mode emissions.

the He^+ mode emissions is wider in latitudes than the region of the H^+ mode emissions. The trajectories of the Akebono satellite range in altitudes from about 1,000 km to the apogee of about 10,000 km in these 2 years. It is remarkable that both the H^+ mode and He^+ mode emissions were observed even at altitudes as high as 10,000 km (nearly the apogee altitude). These observations suggest that considerable quantity of He^+ and O^+ ions exist at such high altitudes.

Figure 3.6 is a histogram of the occurrence number of the emissions versus altitude. The vertical axis indicates the number of trajectories when the ELF instrument was operating around the geomagnetic equator. The horizontal axis indicates the altitude of the Akebono satellite passing through the geomagnetic equator. The cross-hatched region indicates the number of trajectories when two bands emissions of H^+ mode and He^+ mode coexist. The single-hatched region indicates those in which one band emissions, that is, only the H^+ mode emissions were observed during the trajectory. The blank region indicates none of the emissions was observed around the geomagnetic equator even through the ELF instrument was in operation.

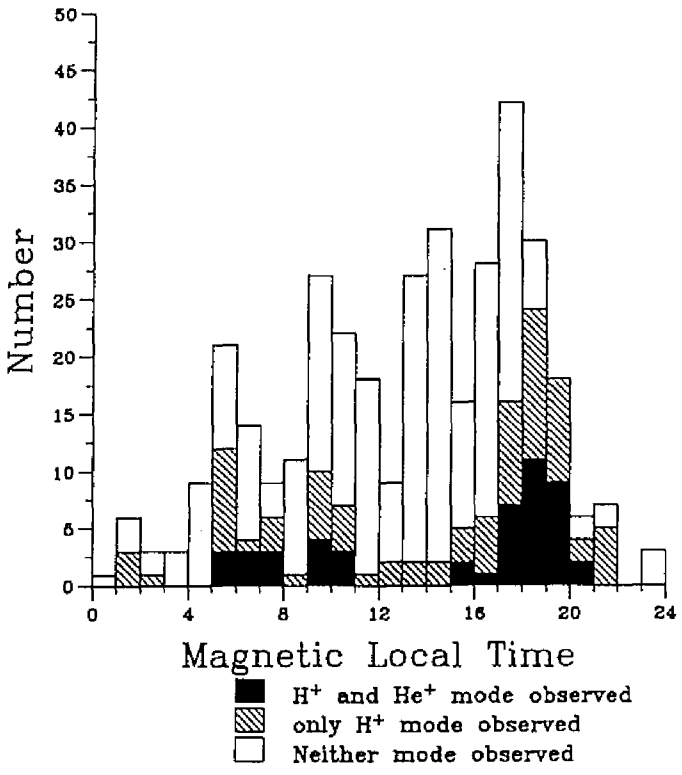

Figure 3.7: Magnetic local time dependence of the occurrence probabilities of the H^+ mode and the He^+ mode emissions.

As shown in Figure 3.6, the H^+ mode emissions were observed very frequently in the altitude range from 3,000 to 7,000 km. Especially in the altitude range from 3,000 to 5,500 km, two-band emissions, that is, H^+ mode and He^+ mode coexist with a very high occurrence probability. In the higher-altitude range around 10,000 km, the occurrence probabilities of the emissions decrease, but some emissions were observed because there are very many orbits in such a high-altitude range. One band, that is, only H^+ mode emissions are likely to occur more frequently than two-band emissions.

In the same way, Figure 3.7 is a histogram of occurrence number of the emissions versus the magnetic local time of the trajectories. The horizontal axis indicates the magnetic local time when the Akebono satellite has passed through the geomagnetic equator. Both modes (especially the He^+ mode) emissions were often observed in the eveningside. On the other hand, the H^+ mode emissions were also observed in the morning to the dayside. Since the observational coverage from the nightside to the morningside are insufficient, occurrence characteristics in

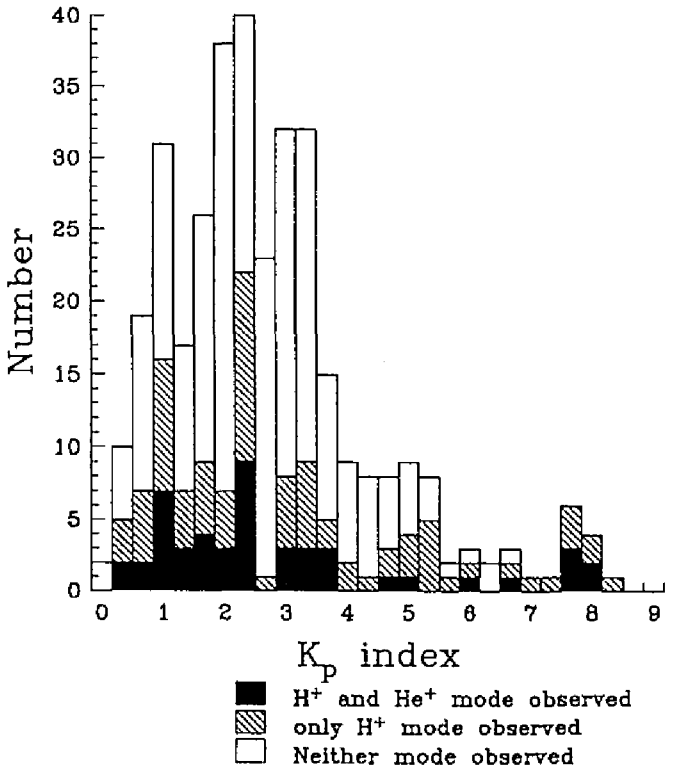

Figure 3.8: Relation between the K_p index and the occurrence probabilities of the H^+ mode and the He^+ mode emissions.

such a region are not clear at present.

Relationship with K_p index

We have surveyed the relationship between K_p indexand the emissions. Figure 3.8 is a histogram which indicates this relationship. The vertical axis is the same as in Figure 3.6 and Figure 3.7 and the horizontal axis indicates the K_p index when the Akebono satellite passed through the geomagnetic equator. It is evident from this figure that when the geomagnetic activity was high, these emissions were observed with a high occurrence probability. However, even during the time periods when the geomagnetic activity was very quiet these emissions were also observed. There is no clear difference in the relationship with magnetic activity between one-band case and two-band case.

3.2.3 Refractive index

The refractive index μ of each mode was roughly estimated, by using the observed one component of electric field and three components of magnetic field, i.e., by the following equation:

$$\mu \simeq \frac{cB}{E_i} \quad (i = \text{x or y}), \tag{3.2}$$

where c is the light velocity and B is calculated by (3.1). However, it should be noticed that error range of estimation by this equation becomes larger as the angle between the geomagnetic field line and the wave normal direction approaches to perpendicular.

In the case of Figure 3.2 observed on May 27, 1989, the refractive index calculated by (3.2) is of the order of 100 in the frequency range from 45 to 60 Hz. In general, the quantity of the refractive index of the H^+ mode determined by (3.2) at the altitude range from 3,000 to 4,000 km is from 100 to 200, and the one of the He^+ mode is 400 to 600.

3.2.4 Dispersion relation

Condition of the plasmasphere

As mentioned in section 3.2, the existence of H^+ and He^+ mode emissions suggests a relatively high content of He^+ and O^+ ions at altitudes as high as 10,000 km.

Figure 3.9 shows the electron temperature observed by the TED (temperature and energy distribution of plasma) instruments on board the Akebono satellite in the equatorial region on May 31, 1989, when the H^+ mode emissions were observed (private communication, *Oyama and Abe*). Figure 3.10 shows the electron temperature observed on July 12, 1989, when two-band emissions were observed. In those figures, GLON, GLAT, and ILAT stand for geographic longitude, geographic latitude, and invariant latitude, respectively. It is remarkable that the electron temperature is very high around 4,500° to 6,000°. According to the temperature observations by the TAIYO satellite during the rather low solar activity period of 1975, the electron temperature was around 2,500° for L = 1.3 to 1.7 [*Oya and Oyama*, 1985]. Five thousand degrees is a very high temperature, maybe due to a high solar activity in 1989. Although it is not certain that the magnetospheric plasma is in perfect thermal equilibrium with the same temperature for electron and ions, such a high temperature is favorable to explain the existence of heavy ions such as He^+ and O^+ in high altitudes based on the DE density model.

To theoretically clarify our observed results of the emissions, we have to know the relative concentration of He^+ and O^+ ions, and the flux of nonthermal H^+ ions. However, because the

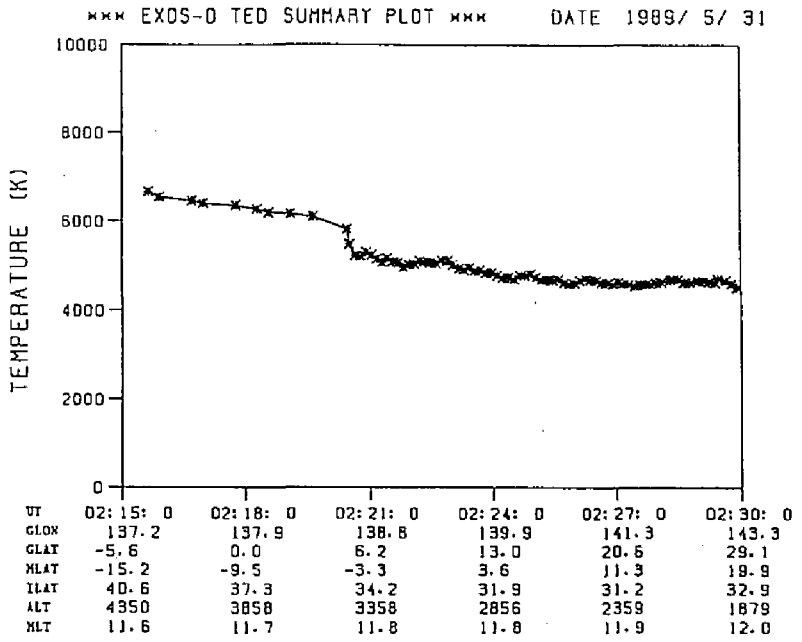

Figure 3.9: Electron temperature observed by the TED instruments while both the H^+ mode and the He^+ mode emissions were observed on July 12, 1989.

trajectories of the Akebono satellite are within the inner radiation belt, the ion mass spectrometer and low-energy particle analyzer on board the Akebono satellite cannot measure these quantities correctly. We therefore assume the following plasma parameters in the DE model: 44% of H^+, 8% of He^+, 48% of O^+, 1.5×10^4 cm^{-3} of the electron density at the reference altitude of 1,100 km, and the ion temperature of 5,000°. Since we do not have any information of the relative constituents of ions by the Akebono satellite around the geomagnetic equator, the relative constituents of ions were referred to the data observed by the ISS-b satellite [*Radio Research Laboratories, Ministry of Posts and Telecommunications*, 1985].

Dispersion curve of ion mode waves

In the presence of H^+, He^+, and O^+ ions in the magnetospheric plasma an ω-k diagram in the frequency range around their ion cyclotron frequencies is as shown in Figure 3.11. In this ω-k diagram, ω is normalized by Ω_{H^+}, and k is normalized by Ω_{H^+}/V_A, where V_A is the Alfven

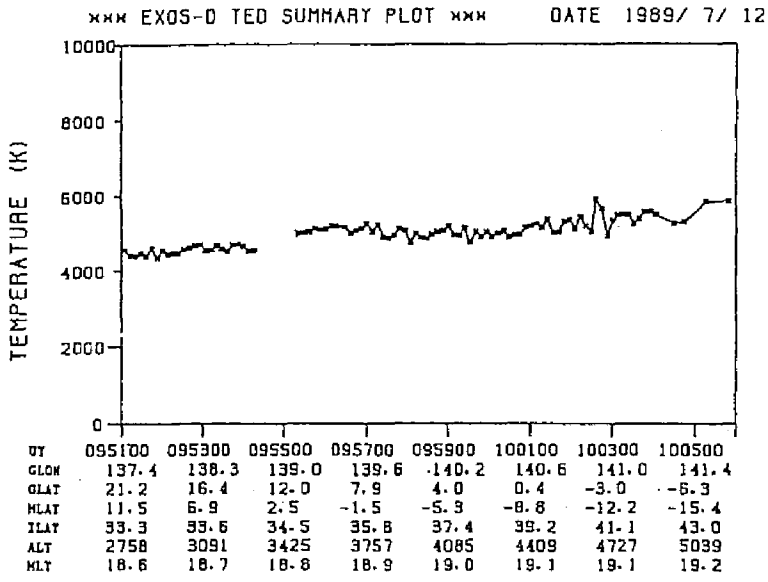

Figure 3.10: Electron temperature observed by the TED instruments while both the H^+ mode and the He^+ mode emissions were observed on July 12, 1989.

velocity given by

$$V_A = \frac{c}{\sqrt{\Sigma(\Pi_{i_\alpha}/\Omega_{i_\alpha})^2}}, \tag{3.3}$$

where $i = H^+$, He^+ and O^+. The solid lines and dashed lines in the figure correspond to the wave normal angle ψ of 0° and 90°, respectively. The finely hatched region corresponds to the region of left-handed polarization and the coarsely hatched region corresponds to that of right-handed polarization. At the boundary of two different modes and at $\psi \simeq 90°$, the polarization is almost linear.

In the presence of H^+, He^+, and O^+ ions, there are three characteristic regions of ICW modes indicated by the symbols "H^+," "He^+," and "O^+" and the electron mode connected to the whistler mode is indicated by the symbol "e." There are cutoff frequencies and crossover frequencies. It is very important to note that there are two band gaps between Ω_{He^+} and Ω_{LHR2}, and between Ω_{O^+} and Ω_{LHR3}, where Ω_{LHRi} denotes the ith lower hybrid resonance (LHR) angular frequency. Ω_{LHR2} and Ω_{LHR3} are approximated by the following equations,

$$\Omega_{LHR2} = \frac{b + \sqrt{b^2 - 4ac}}{2a}\Omega_{H^+}, \tag{3.4}$$

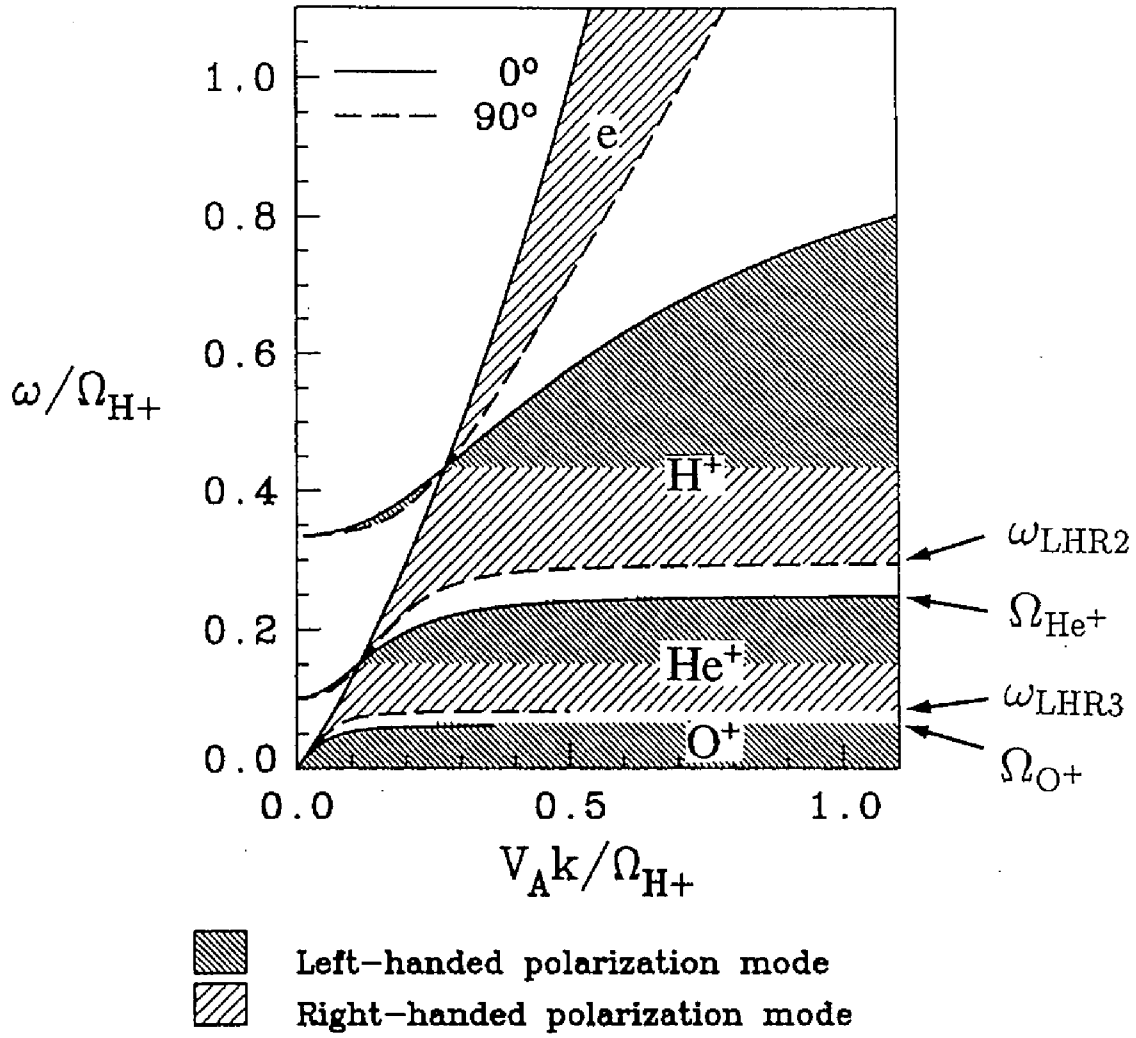

Figure 3.11: Dispersion curve for the electromagnetic ion mode waves in the presence of H^+, He^+ and O^+ ions. The relative constituents of ions there are H^+: 85.0%, He^+: 9.0%, and O^+: 6.0%.

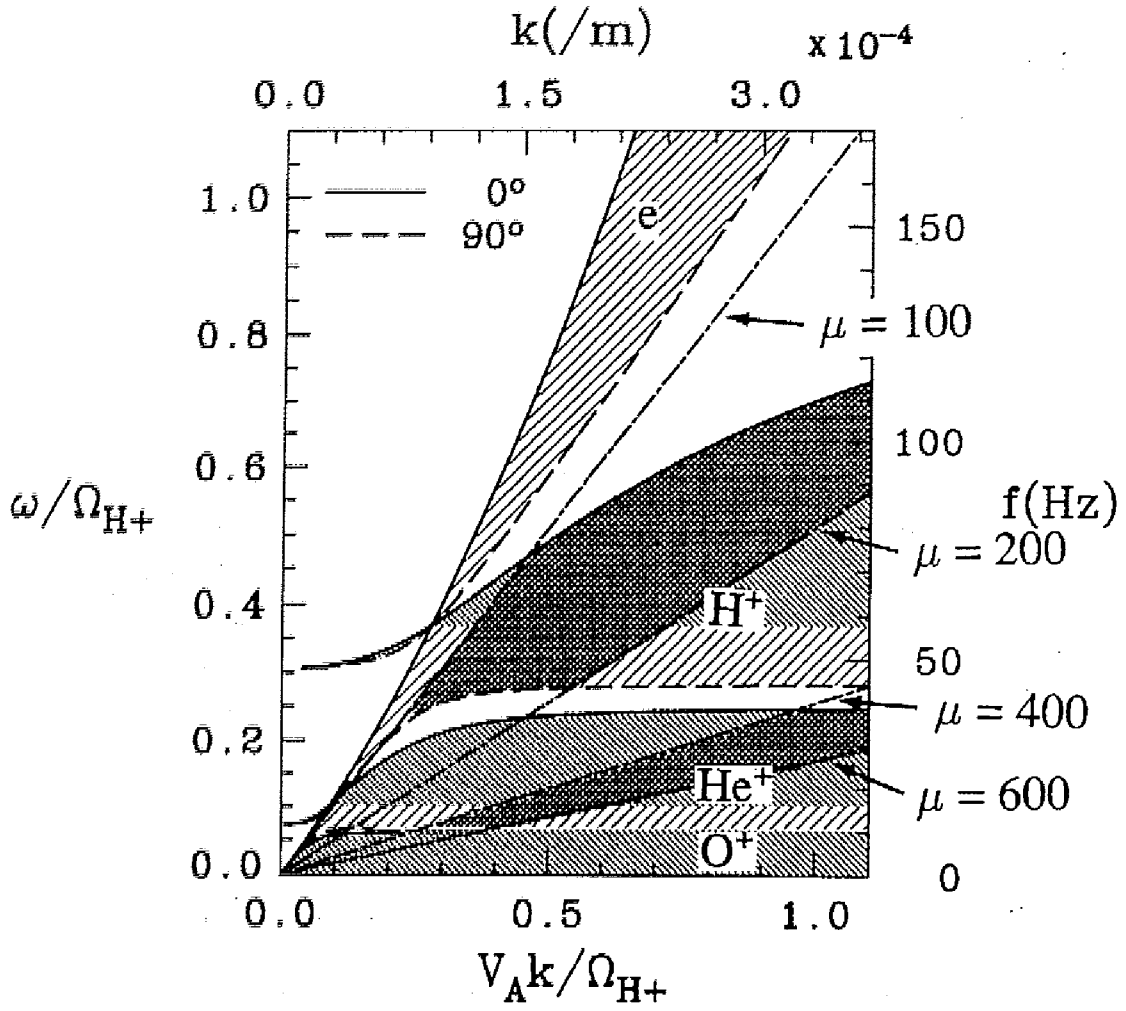

Figure 3.12: Dispersion curve at an altitude of 1.5 R_E on the geomagnetic equator in the DE model. The relative constituents of ions there are H^+: 91.5%, He^+: 7.1%, and O^+: 1.4%.

$$\Omega_{\mathrm{LHR3}} = \frac{b - \sqrt{b^2 - 4ac}}{2a}\Omega_{\mathrm{H^+}}, \tag{3.5}$$

$$a = 64C_{\mathrm{H^+}} + 16C_{\mathrm{He^+}} + 4C_{\mathrm{O^+}}, \tag{3.6}$$

$$b = (4 + 1/4)C_{\mathrm{H^+}} + (16 + 1/16)C_{\mathrm{He^+}} + (4 + 1/4)C_{\mathrm{O^+}}, \tag{3.7}$$

$$c = 1/64C_{\mathrm{H^+}} + 1/16C_{\mathrm{He^+}} + 1/4C_{\mathrm{O^+}}, \tag{3.8}$$

where

$$C_{\mathrm{H^+}} + C_{\mathrm{He^+}} + C_{\mathrm{O^+}} = 1, \tag{3.9}$$

where $C_{\mathrm{H^+}}$, $C_{\mathrm{He^+}}$, and $C_{\mathrm{O^+}}$ are the relative constituents of H^+, He^+, and O^+ ions, respectively. In this dispersion diagram the H^+ mode emissions correspond to the region indicated by the symbol "H^+" and the He^+ mode emissions correspond to the region indicated by the symbol "He^+." It should be remembered that the band gap between H^+ and He^+ mode waves cannot exist without a sufficient content of He^+ ions, at least, more than a few percent. In the same way, the band gap between He^+ and O^+ mode waves cannot exist without a sufficient content of O^+ ions.

Figure 3.12 is an ω-k diagram which is calculated by using the relative constituents of ions; H^+: 91.5%, He^+: 7.1% and O^+: 1.4%. These percentages correspond to those at an altitude of 1.5 R_{E} on the geomagnetic equatorial plane, according to the DE density model with the parameters mentioned previously. The axes on the right and on the top indicate the real wave frequency and $|k|$ respectively at an altitude of 1.5 R_{E} on the geomagnetic equatorial plane.

In subsection 3.2.3, we roughly estimated the refractive indices of H^+ mode and He^+ mode by (3.2) and found that the refractive index of H^+ mode is from 100 to 200 and that of He^+ mode is 400 to 600 at an altitude range from 3,000 to 4,000 km. In the ω-k diagram a refractive index is indicated by the gradient of a line passing through the origin. Considering the refractive indices and frequency range of the observed emissions, we can presume that these emissions are located in the cross-hatched regions.

3.2.5 Determination of wave normal direction

The study of the wave normal vector is important to identify the mode of the waves and to interpret the propagation characteristics of them. Using three components of wave magnetic fields observed by search coils on board the Akebono satellite, the wave normal directions were determined.

As was mentioned in section 2.3.2, the number of the nonzero eigenvalues in the spectral matrix corresponds to the number of the waves coexisting [*Samson and Olson*, 1980]. We then calculate the spectral matrix elements and eigenvalues. In the analyses, wave magnetic field

data of the emissions are frequency-analyzed by fast Fourier transform (FFT) with a frequency resolution of 0.16 Hz, and the spectral matrix elements are calculated from these frequency components. When the ratio of the smallest eigenvalue to the largest one exceeds the threshold level (= 0.01), we assume that there are more than three waves. In the same way, when the ratio of the second largest to the largest exceeds the threshold level, there exist two waves.

For the spectral matrix of H^+ mode waves observed from 0350:00 to 0358:20 UT on May 27, 1989 (see Figure 3.1), which is composed of 32 frequency components of 0.16-Hz resolution around 50 Hz, 5.9% of all spectral matrices have only one eigenvalue, 74.8% and 19.2% of them have two and three eigenvalues, respectively. Especially in the case of two eigenvalues, 36.2% of them are nearly the same order of eigenvalues. This fact implies that multiple waves usually coexist around the geomagnetic equatorial region.

As the next step, the wave normal directions were determined by means of the wave distribution function (WDF) method. In the analyses, the electron density and the geomagnetic field intensity are provided by the PWS instruments [*Oya et al.*, 1990] and IGRF 1985 model [*IAGA*, 1985], respectively. Since we have used only magnetic wave field components, the wave normal direction has an ambiguity of 180°.

To solve the WDF solution we use both maximum entropy method (MEM) and Phillips-Tikhonov regularization method (PTM). We will show the results obtained for the wave normal direction of emissions observed on May 27, 1989. As for the ion constituents, data of the ion mass spectrometer and low-energy particle analyzer on board the Akebono satellite are not available because the trajectories of the Akebono satellite are within the inner radiation belt. We therefore examine for four sets of ion constituents, that is, (1) (95% H^+, 4% He^+, 1% O^+); (2) (91% H^+, 7.5% He^+, 1.5% O^+); (3) (86% H^+, 11% He^+, 3% O^+); and (4) (86% H^+, 9% He^+, 5% O^+).

Figures 3.13 (a) -(d) show the wave normal directions estimated by the maximum entropy method (MEM) around 0357:56 UT, when the frequency of the maximum intensity of the emission was 52.3 Hz. In these figures, an energy peak is located on the meridian plane. However, the wave normal angle is different depending on the ion constituents. Figures 3.14 (a) -(d) show the wave normal directions estimated by the Phillips-Tikhonov method (PTM). These results are very similar to those estimated by the MEM.

The reason why the wave normal angle depends on the ion constituents is explained as follows. As shown in Figure 3.11, there exist additional lower hybrid resonance (LHR) frequencies of Ω_{LHR2}, and Ω_{LHR3} approximated by (3.4) and (3.5) in the presence of H^+, He^+, and O^+ ions. Therefore the LHR frequency of H^+ mode (Ω_{LHR2}) for each set of ion consitituents is (a) 40.8 Hz,

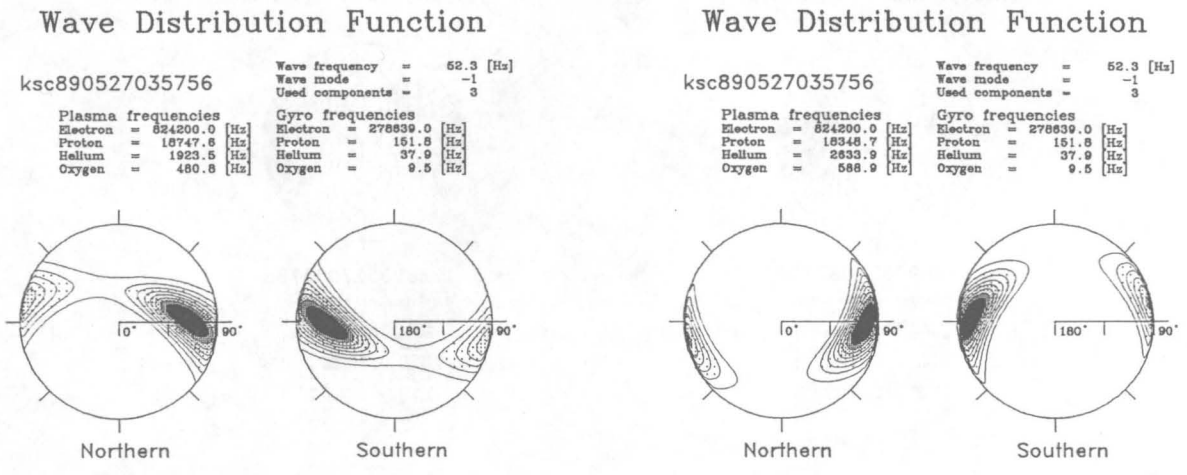

Figure 3.13: Wave normal directions estimated by MEM for the emissions around the frequency of 50 Hz 035756:00-0358:28 UT on May 27, 1989, with H^+: He^+: O^+= (a) 95:4:1, (b) 90:8:2, (c) 86:11:3, and (d) 86:9:5.

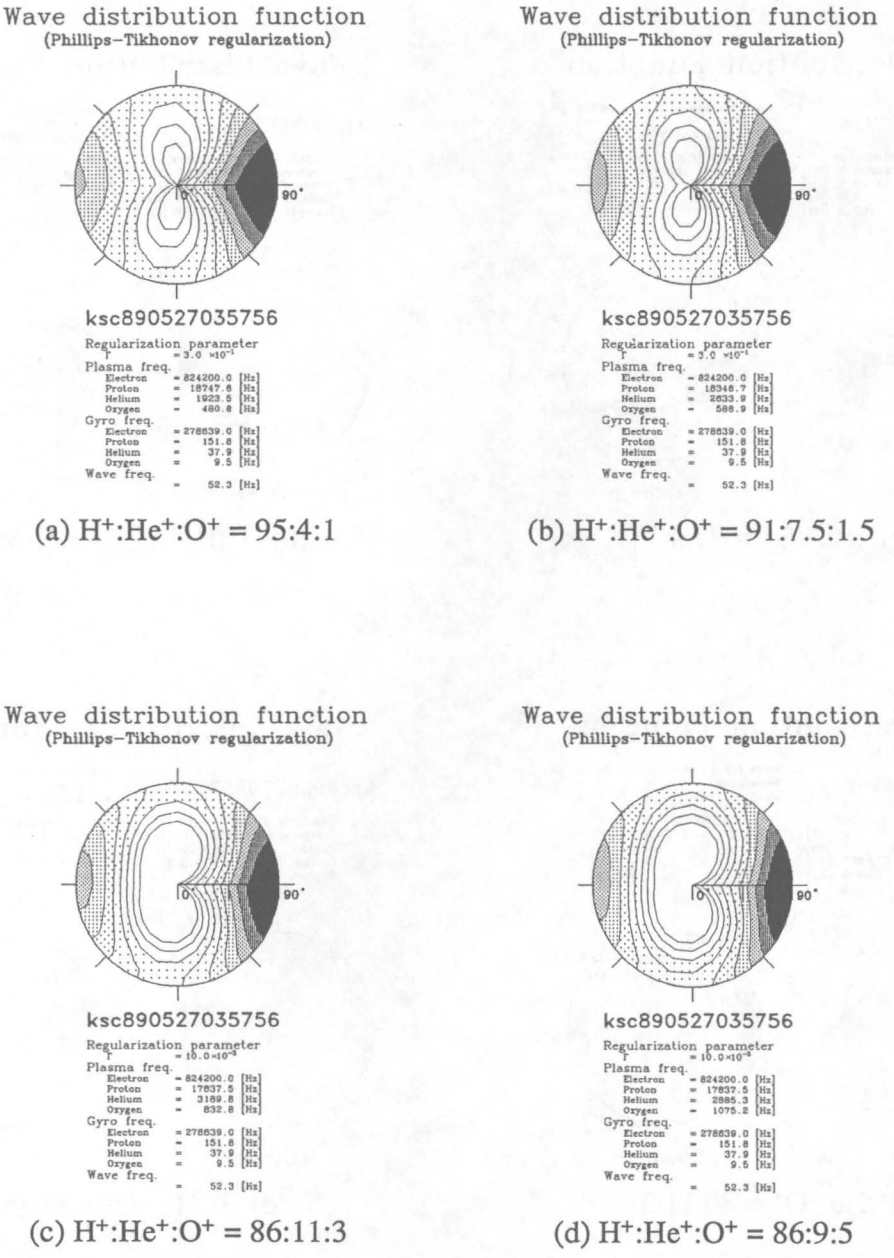

Figure 3.14: Wave normal directions estimated by the PTM for the emissions around the frequency of 50 Hz 035756:00-0358:28 UT on May 27, 1989, with H^+: He^+: O^+= (a) 95:4:1, (b) 90:8:2, (c) 86:11:3, and (d) 86:9:5.

(b) 43.3 Hz, (c) 46.0 Hz, and (d) 44.8 Hz. The larger the LHR frequency, the wave frequency is close to the LHR frequency, so that the estimated wave normal direction becomes nearly perpendicular to the geomagnetic field line. In Figures 3.13, the maximum peaks of wave distribution estimated by the MEM are located at (ψ,η) = (a) (61.3°, 4.0°), (b) (76.2°, 356.0°), (c) (84.1°, 356.0°), and (d) (83.1°, 356.0°), respectively. On the other hand, there is a limitation of resolution for the PTM as was discussed in subsection 2.3.4. Therefore the maximum peaks estimated by the PTM are (ψ,η) = (90.0°, 0.0°) for all cases from (a) to (d). However, we can find similar tendency, that is, the reconstructed images in cases (a) and (b) are distributed in smaller ψ region than the cases of (c) and (d).

3.3 Ray path calculations

The propagation characteristics of the ICW mode emissions can be examined by ray tracing. In this section we will present the results of three-dimensional ray tracing for ion mode waves both in cold and hot plasma model.

As for the geomagnetic field, a dipole model is adopted. For the plasma density profile in the magnetosphere a diffusive equilibrium (DE) model [*Angerami and Thomas*, 1964] is used. Therefore if a ray tracing is started with an initial wave normal direction in the geomagnetic meridian plane, the ray paths do not deviate from the same geomagnetic meridian plane. We have, however, found that when the initial wave normal direction deviates from a geomagnetic meridian plane, we have found that the ray path first deviates from the initial meridian plane and is finally trapped in a different meridian plane. In the following the ray tracing results are those obtained by the two-dimensional ray tracing in a geomagnetic meridian plane.

3.3.1 Estimation of growth rate of the emissions

At first, the generation mechanism of the emissions is discussed. According to *Roux et al.* [1982], the ICW mode waves which they observed by the GEOS 1 and 2 satellites near the plasmapause are assumed to be generated by the ion cyclotron resonant instability caused by a temperature anisotropy of hot H^+ ions around the geomagnetic equatorial plane. On the other hand, our observations have been made within the inner radiation belt, so that we can expect a possible existence of an abundant energy source for the ICW mode waves which we observed in the area. In this paper we assume that these ICW mode emissions are generated by the ion cyclotron resonant instability similar to the generation mechanism suggested by *Roux et al.*

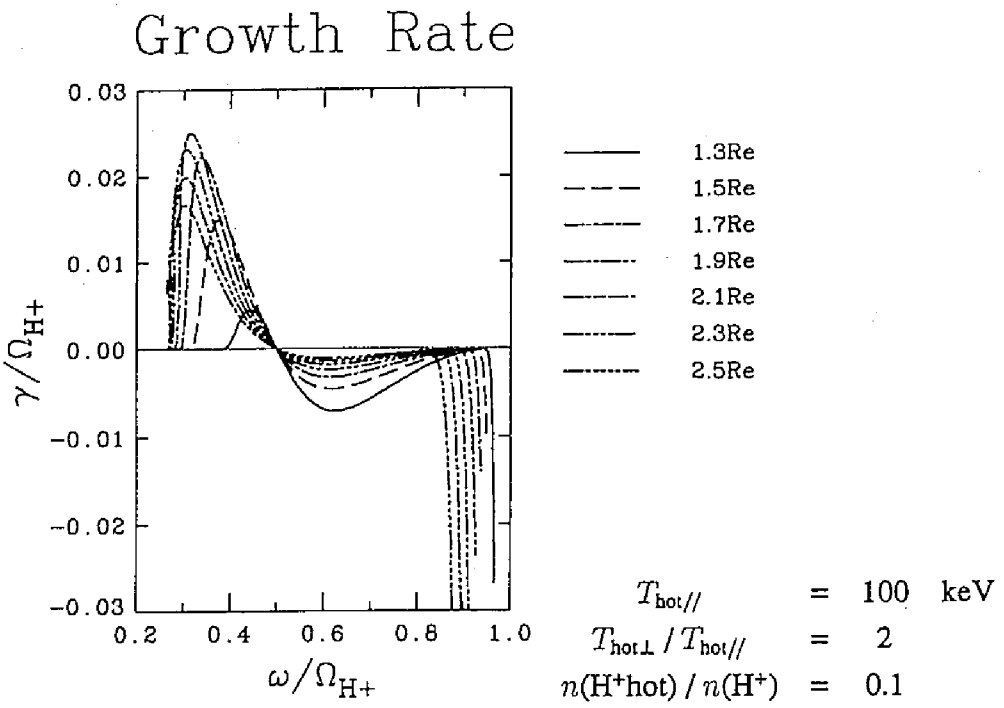

Figure 3.15: Growth rate γ versus real part ω_r of the ICW mode waves caused by a temperature anisotropy of the hot H^+ ions. The angle ψ is assumed to be 0°.

[1982].

By the ion cyclotron instability due to the temperature anisotropy of the hot H^+ ions, the ICW mode waves are generated in the following process. When the velocity of ions parallel to a geomagnetic field line satisfies the resonance condition:

$$v_{i//} = v_R = (\omega - \Omega_{i_\alpha})/k_{//}, \tag{3.10}$$

they can strongly interact with circularly polarized waves, where v_R is the resonance velocity and Ω_{i_α} is the angular cyclotron frequency of the ion. In that condition, the Doppler-shifted frequency of such a circularly polarized wave is equal to the ion cyclotron frequency. Thus the electric field of that wave rotates in phase with ions that satisfy the matching condition $v_{i//} = v_R$, resulting in an efficient energy exchange. Depending upon the slope of ion distribution function along diffusion curves [*Gendrin*, 1981], the wave will either be amplified or damped. If the ion velocity perpendicular to the geomagnetic field $v_{i\perp}$ is larger than the parallel ion velocity $v_{i//}$, the energy of the perpendicular velocity of ions is used for the growth of the wave.

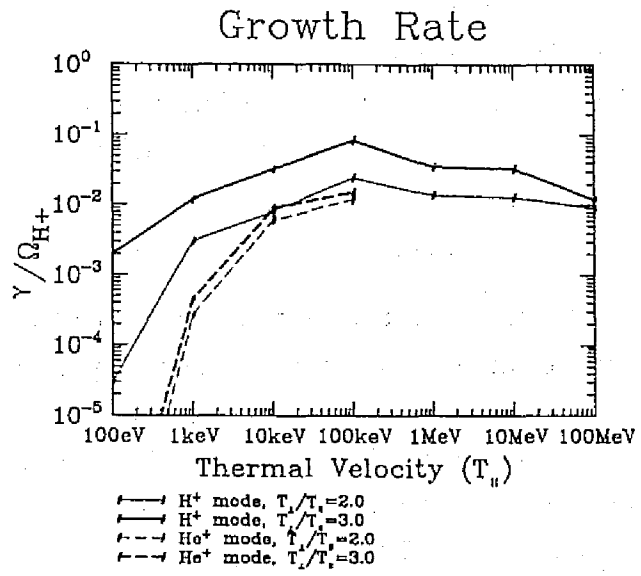

Figure 3.16: Growth rate γ of the ICW mode waves caused by a temperature anisotropy of the hot H^+ ions. The horizontal axis indicates $T_{hot//}$ of the hot H^+. The angle ψ is assumed to be 0°.

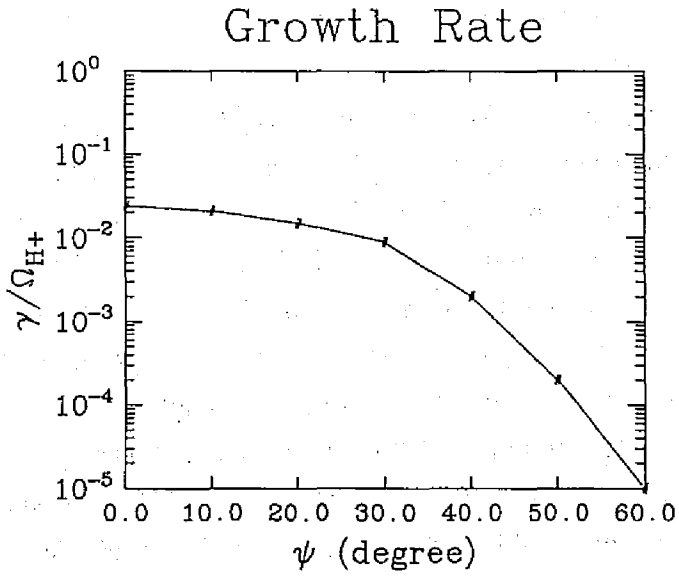

Figure 3.17: Relation between the growth rate γ of the H^+ mode wave and the angle ψ, where $T_{hot//}$ = 100 keV and $T_{hot\perp}/T_{hot//}$ = 2.

The growth rates of the ICW mode waves in a hot plasma are estimated numerically [*Gendrin et al.*, 1984]. As mentioned in section 2.1.2, we have assumed that the first-order terms of E and $B \propto \exp\{\mathrm{j}(k \cdot r - \omega t)\}$ in deriving the dispersion relation in a hot plasma model. When the wave normal vector k of the wave is treated as a real number, the angular frequency ω is in general a complex value composed of a real part ω_r and an imaginary part γ, that is, $\omega = \omega_r + \mathrm{j}\gamma$. Then,

$$E, B \propto \exp\{\mathrm{j}(k \cdot r - \omega_r t) + \gamma t\}. \tag{3.11}$$

From (3.11), the growth rates of the waves are determined by γ under the condition $\omega_r \gg \gamma$.

In order to estimate the growth rate of the wave quantitatively, we need to know velocity distribution of energetic particles as well as relative constituents of ions. However, as was mentioned before, the ion mass spectrometer and low-energy particle analyzer on board the Akebono satellite cannot measure these quantities correctly because the trajectories of the Akebono satellite are within the inner radiation belt. There is another instrument named radiation monitor (RDM) on board the Akebono satellite, which measures energetic particles in the energy range of MeV. Because this instrument is installed originally not for scientific purpose, comparing these data with wave data is now left as a future work.

In our calculations the relative constituents of ions at 1.5 R_E as mentioned before are used, and particle temperatures are assumed as follows; 10% of H^+ ions are hot with an anisotropy of $T_{hot\perp}/T_{hot//} > 1$, and He^+, O^+ and 90% of H^+ ions are background particles with an energy of 1.5 eV. As for the hot H^+, we have calculated for $T_{hot//}$ from 100 eV to 100 MeV, with two temperature anisotropy cases; $T_{hot\perp}/T_{hot//} = 2$ and $T_{hot\perp}/T_{hot//} = 3$.

Figure 3.15 shows the growth rate γ (imaginary part of ω) versus ω_r (real part of ω) of H^+ mode. The angle ψ is assumed to be 0°. We can find that the frequency at which the ion cyclotron resonant instability has the maximum growth rate is from $0.3 f_{cH^+}$ to $0.4 f_{cH^+}$.

Figure 3.16 shows the growth rate γ normalized by Ω_{H^+} of the ICW mode waves, versus the thermal energy of the hot H^+ ions ($T_{hot//}$) parallel to the geomagnetic field line, calculated by using the parameters mentioned above. The wave normal angle ψ is assumed to be 0°. In this figure the growth rates of H^+ mode and He^+ mode wave are shown. However, for He^+ mode wave the growth rate is not plotted for $T_{hot//}$ larger than 100 keV because the real part ω_r and the imaginary part γ become comparable and the growth rate is meaningless in the linear theory. From this figure it is seen that the hot H^+ ions with $T_{hot//}$ of 100 keV are most effective for the growth of the H^+ mode waves. It is because the Alfven velocity is of the same order as the thermal velocity of $T \simeq 100$ keV.

Figure 3.17 shows the dependency of the growth rate of the H^+ mode waves on the wave

normal angle ψ , where the thermal velocity of the hot H^+ is assumed to be 100 keV and the temperature anisotropy $T_{hot\perp}/T_{hot//}$ is 2. As shown in this figure, the ICW mode waves interact most closely with the hot H^+ when the wave normal direction is parallel to the geomagnetic field line.

In the following subsections, we will examine the propagation characteristics of the ICW waves and estimate their growth rate along their ray paths using ray tracing technique on the assumption that the temperature anisotropy of the hot H^+ ions causes the generation of the ICW mode wave. As a case study, we use an above mentioned plasma parameters for the ray path calculation, that is, 10% of H^+ ions are hot whose thermal velocity of parallel component is 100 keV and the temperature anisotropy $T_{hot\perp}/T_{hot//}$ of 2.

3.3.2 Results of cold plasma ray tracing

In this section we will show the ray paths for the H^+ and He^+ mode waves calculated by ray tracing in a cold plasma model and discuss the general propagation characteristics of the emissions and the spatial distribution where they were observed.

As mentioned in subsection 3.3.1, we have studied that the ICW mode emissions can be generated by ion cyclotron resonant instability caused by a temperature anisotropy of hot H^+ ions around the geomagnetic equatorial region. We have also learned that most favorable wave normal angle with a geomagnetic field line for the ion cyclotron resonant instability is nearly zero. We therefore start our ray tracing at the geomagnetic equatorial region with $\psi = 0°$. The plasma parameters used in the DE model are the same as those mentioned in subsection 3.3.1. Each ray path is initiated from the geomagnetic equatorial plane at an L-value from 1.4 to 2.9 with a frequency at which the ion cyclotron resonant instability has the maximum growth rate at the start point where the thermal velocity of the hot H^+ is assumed to be 100 keV and the temperature anisotropy $T_{hot\perp}/T_{hot//}$ is 2.

Figure 3.18 (a) shows the ray paths calculated for the H^+ mode waves, and Figure 3.18 (b) shows those for the He^+ mode waves. The arrows along each ray path represent the wave normal directions. As shown in these figures, H^+ mode and He^+ mode waves propagate along the geomagnetic field lines, and are reflected back at the lower hybrid resonance condition. Once reflected, these waves propagate back and forth along almost the same ray paths nearly along a geomagnetic field line and are trapped within a limited geomagnetic latitude range. From these two figures it is evident that He^+ mode waves can propagate over a wider range in latitude than H^+ mode waves.

Figure 3.19 shows the related quantities calculated along a ray path when the H^+ mode wave

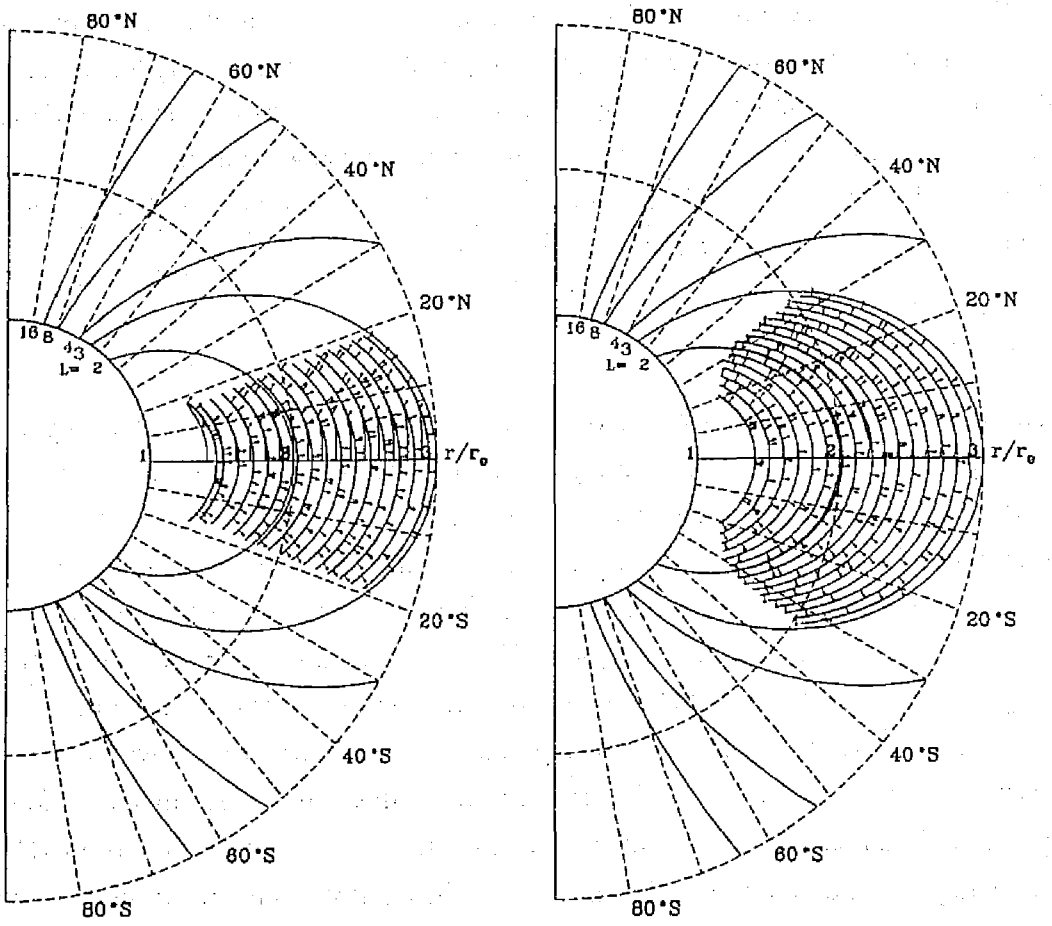

Figure 3.18: Ray paths of the ICW calculated by ray tracing method in cold plasma model. Each ray path is initiated from the geomagnetic equatorial plane at an L-value from 1.4 to 2.9 with a frequency of maximum growth rate at the start point where $T_{hot//} = 100$ keV and $T_{hot\perp}/T_{hot//} = 2$.

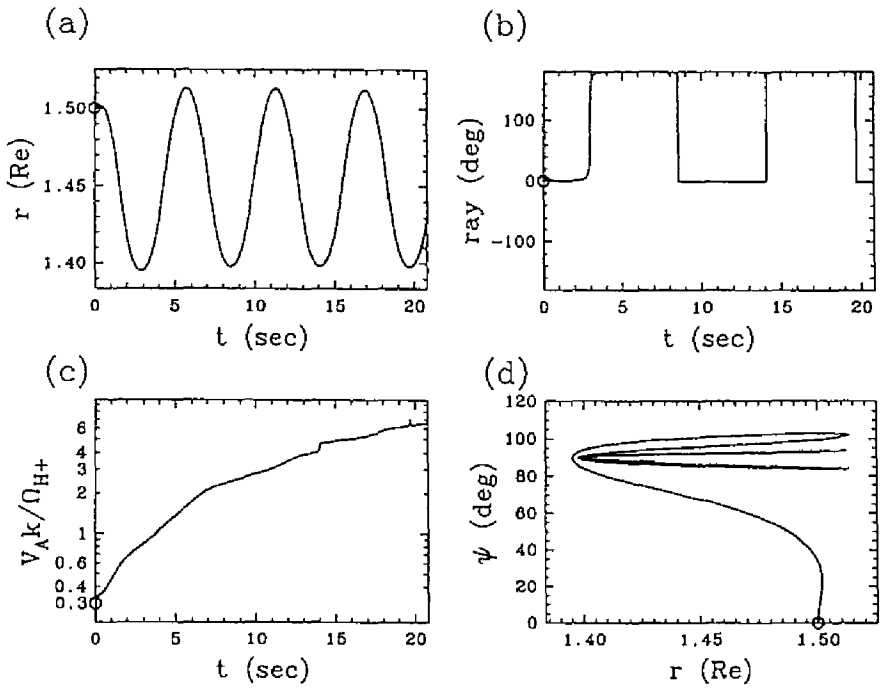

Figure 3.19: Parameters of the H^+ mode wave along the ray path. The wave is initiated from the geomagnetic equator at an L-value of 1.5 with its wave normal parallel to the geomagnetic field with a frequency of maximum growth rate at the start point where $T_{hot//} = 100$ keV and $T_{hot\perp}/T_{hot//} = 2$.

is initiated from the geomagnetic equator at an L-value of 1.5. In the figure the symbol "o" indicates the initial point of the ray path. In Figure 3.19 (a), r indicates the radial position of the ray path and t is the propagation time. We can find that the wave bounces with periodic trajectory of about every 5.5 s. In Figure 3.19 (b), "ray" indicates the ray direction with respect to the geomagnetic field line. It is evident that the H^+ mode wave is trapped on a same geomagnetic field line. Figure 3.19 (c) shows the variation of the wave number along the ray path, and Figure 3.19 (d) shows the relation between r and ψ . It turns out that the wave normal angle gradually increases and turns to a direction nearly perpendicular to the geomagnetic field line. That is, the wave gradually changes to be electrostatic.

Figure 3.20 shows the similar quantities along the ray path of He^+ mode started at an L-value of 1.5. As shown in Figure 3.20 (a), the He^+ mode wave stays as long as about 15 s around the geomagnetic equatorial region and bounces back from the reflecting point very quickly,

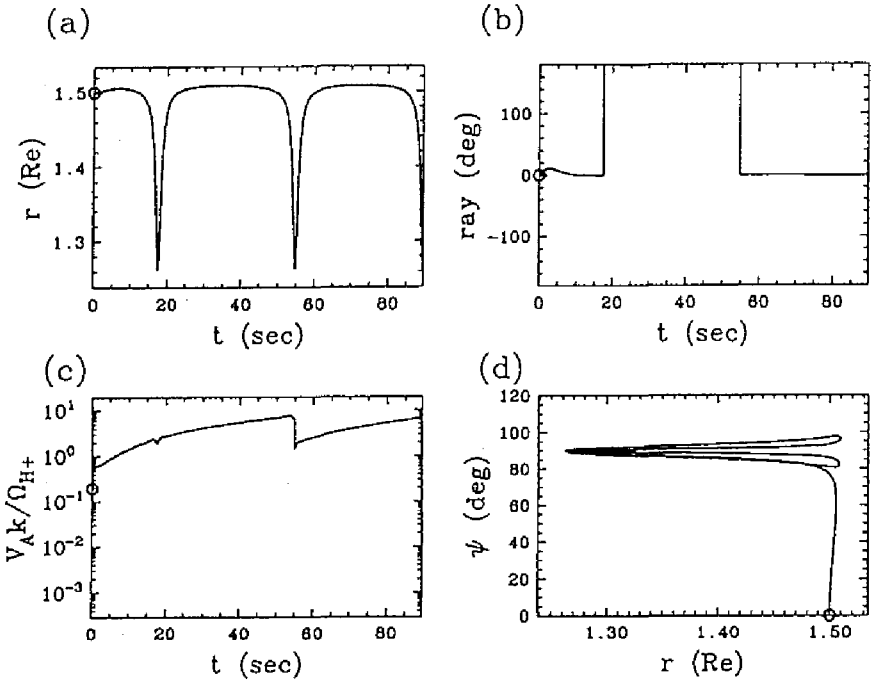

Figure 3.20: Parameters of the He^+ mode wave along the ray path. The wave is initiated from the geomagnetic equator at an L-value of 1.5 with its wave normal parallel to the geomagnetic field with a frequency of maximum growth rate at the start point where $T_{hot//} = 100$ keV and $T_{hot\perp}/T_{hot//} = 2$.

the interval of bouncing back to the geomagnetic equatorial plane is about 36 s. The other propagation characteristics of the He^+ mode wave are similar to those of H^+ mode wave, that is, the wave propagates along almost the same geomagnetic field line, the wave normal gradually increases and approaches perpendicular to the geomagnetic field line and the wave gradually changes to be electrostatic.

Thus the ray tracing in a cold plasma model has clarified that the latitudinal range of the observed emissions. The azimuthal direction of the wave normal represented by η was not mentioned in the above discussion, because the wave normal direction stays in the same meridian plane (i.e., $\eta = 0°$) in the dipole magnetic field model, due to the assumption that the initial wave normal is directed along the geomagnetic field line. It has been found that even if a ray tracing is started with an initial wave normal direction off from the geomagnetic meridian plane the ray paths finally follow nearly along one meridian plane, though such ray paths are not shown

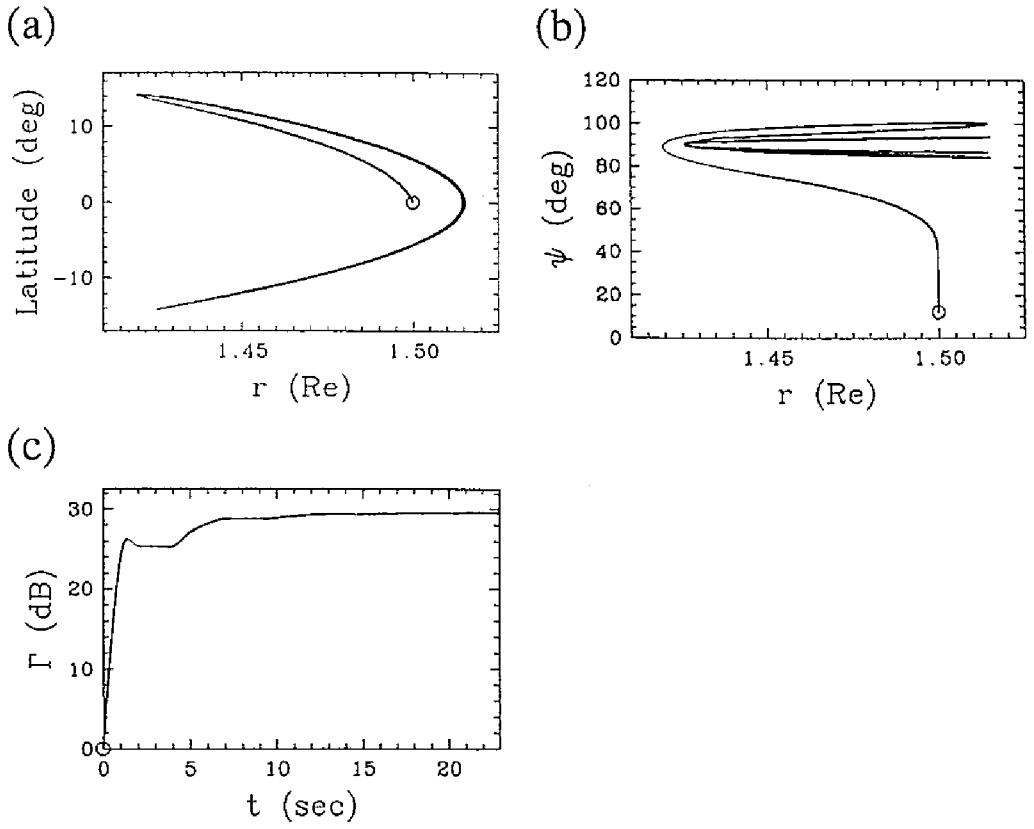

Figure 3.21: Ray path and parameters of the H^+ mode wave along the ray path. The wave is initiated from the geomagnetic equator at an L-value of 1.5 with its wave normal parallel to the geomagnetic field with a frequency of maximum growth rate at the start point where $T_{hot//} = 100$ keV and $T_{hot\perp}/T_{hot//} = 2$.

here. To determine the three-dimensional effect, we have to use the international geomagnetic reference field model (IGRF) for ray tracing.

3.3.3 Results of hot plasma ray tracing

In this section we will show the ray paths calculated in a hot plasma. For ray tracing in a hot plasma we have extended our hot plasma ray tracing program [*Hashimoto and Kimura*, 1973; *Hashimoto et al.*, 1977; 1987] to the case where the effects of ions are included. By this ray tracing we can calculate the total growth and damping along the ray paths.

In our hot plasma ray tracing the angular frequency of the wave ω is treated as a real number,

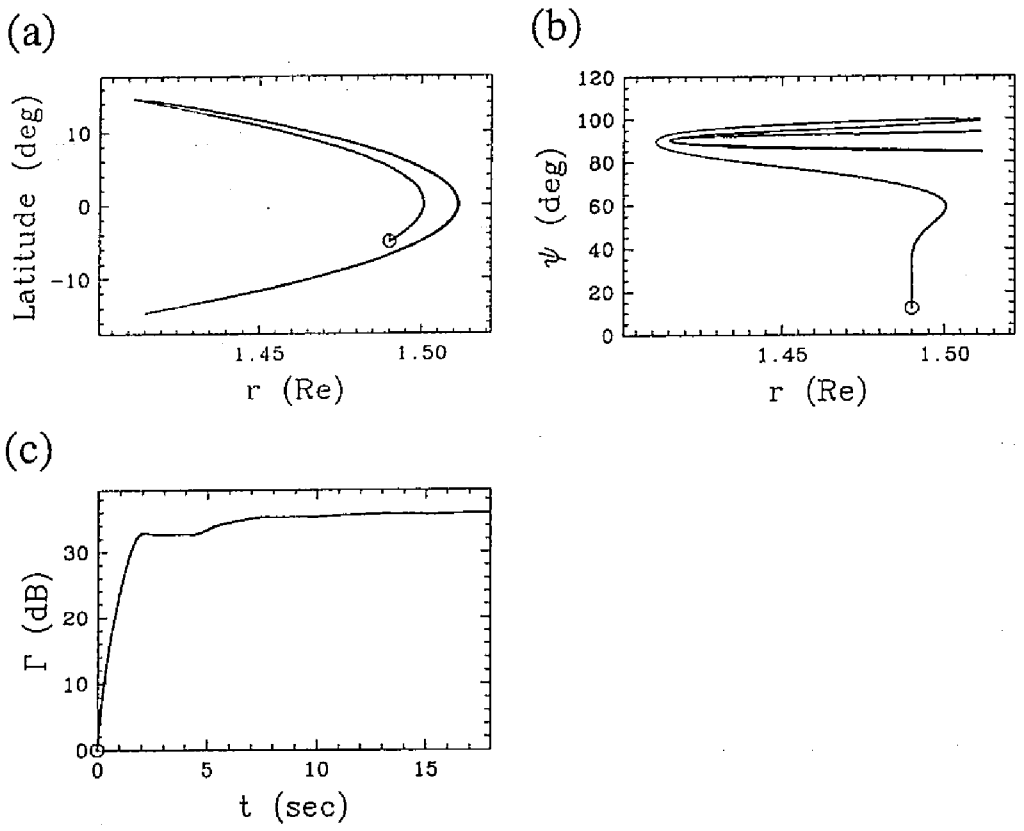

Figure 3.22: Ray path and parameters of the H^+ mode wave along the ray path. The wave is initiated from the geomagnetic latitude of 5°at an L-value of 1.5 with its wave normal parallel to the geomagnetic field with a frequency of maximum growth rate at the start point where $T_{hot//}$ = 100 keV and $T_{hot\perp}/T_{hot//}$ = 2.

and the wave vector k is regarded as a complex number, that is, $k = k_r + jk_i$. Then,

$$E, B \propto \exp\{j(k_r \cdot r - \omega t) - k_i \cdot r\}. \tag{3.12}$$

Therefore the imaginary part $-k_i$ indicates the growth rate of the wave under the condition $|k_r| \gg |k_i|$, and total integrated growth along the ray path is calculated by the following integrations:

$$\begin{aligned} \Gamma &= -\int_{path} k_i \cdot dr &&= -\int_{path} k_i \cdot v_g dt \\ &= -\int_{path} k_i \cos\alpha dr &&= -\int_{path} k_i v_g \cos\alpha dt, \end{aligned} \tag{3.13}$$

where α is an angle between k and v_g. In the actual ray tracing we have imposed a condition

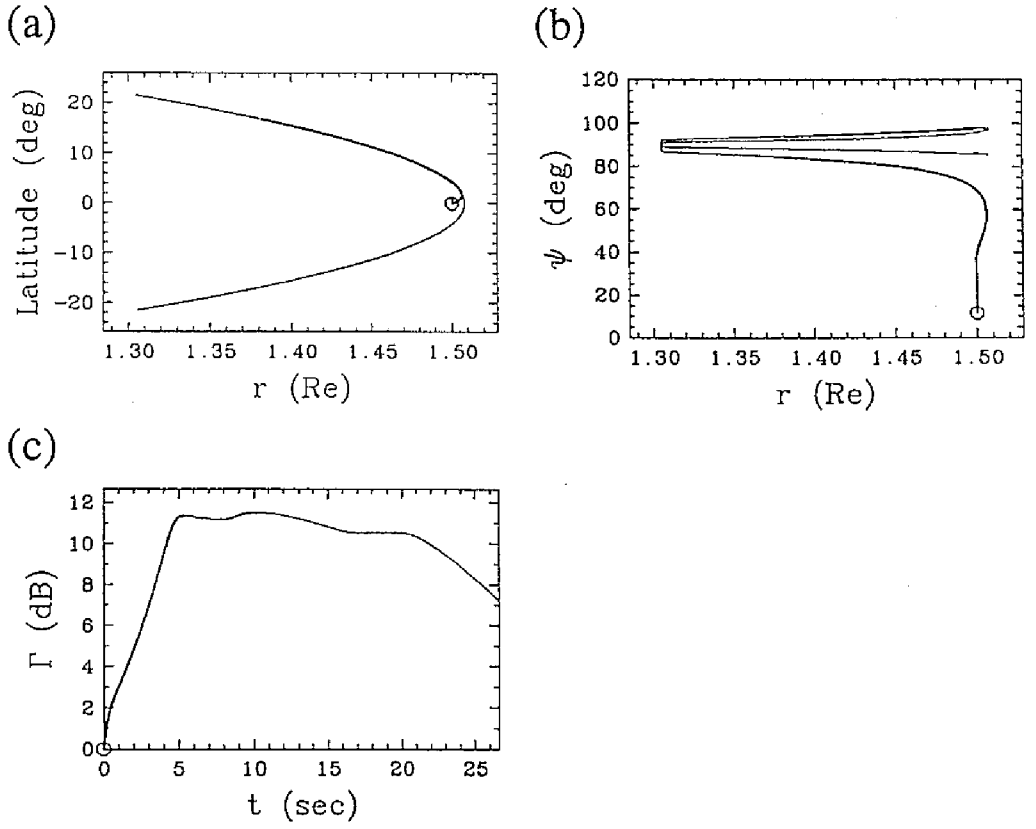

Figure 3.23: Ray path and parameters of the He^+ mode wave along the ray path. The wave is initiated from the geomagnetic equator at an L-value of 1.5 with its wave normal parallel to the geomagnetic field with a frequency of maximum growth rate at the start point where $T_{hot//} = 100$ keV and $T_{hot\perp}/T_{hot//} = 2$.

that the ratio of $|k_i|$ to $|k_r|$ is required to be less than 0.1, and the ray tracing was terminated when this condition is not satisfied. It is because for a relatively large $|k_i|$ condition the ray path obtained by ray tracing becomes meaningless.

Figure 3.21 shows the results of the ray tracing for the H^+ mode wave, which is initiated from the geomagnetic equator at an L-value of 1.5 with its wave normal direction along the geomagnetic field line, using the plasma model with 10% of hot H^+ ions, whose thermal velocity is assumed to be 100 keV and the temperature anisotropy $T_{hot\perp}/T_{hot//}$ is 2, all along the ray paths. Figures 3.21 (a)-(c) show the ray path, the variation of the wave normal angle ψ, and the total integrated growth Γ along the ray path, respectively. In the figures the thick lines indicate the parts where the wave is growing.

In general, the propagation characteristics of the wave is very similar to those shown by the cold plasma ray tracing method. As shown in Figure 3.21 (b), since the angle ψ gradually turns to a direction perpendicular to the geomagnetic field line, the wave grows at first and then stops growing. In this case the wave grows up to nearly 30 dB in two bounces. The region where the wave grows is within the geomagnetic latitude of $\pm 10°$.

We have tried to do the ray tracing of the H^+ mode wave by starting from various geomagnetic latitude at an L-value of 1.5 with its wave normal direction along the geomagnetic field. Figure 3.22 shows the results that the wave can grow over most part of the ray path. In this case the wave is initiated from the geomagnetic latitude of 5°, and the wave grows up to 36 dB. After many ray tracing analyses we have found that the H^+ mode waves which are initiated from the geomagnetic latitude range within 10° can efficiently grow and propagate in the magnetosphere.

On the other hand, the results of ray tracing for the He^+ mode wave is shown in Figure 3.23. The ray path is also initiated from the geomagnetic equator at an L-value of 1.5. In comparison with the results of the H^+ mode wave, this wave does not grow so much (up to 11.5 dB at most), and is damped quickly after a couple of bouncing. In the present paper we showed only one case study using a set of plasma parameters, and more detailed study will be needed to investigate the plasma condition which makes He^+ mode wave sufficiently enhanced.

3.3.4 Comparison with the observation results

In the previous subsection, we assumed that the waves are generated by ion cyclotron resonant instability caused by a temperature anisotropy of hot H^+ ions around the geomagnetic equatorial plane. It is also clarified from our ray tracing study that these ion cyclotron waves of both H^+ mode and He^+ mode propagate back and forth along nearly the same geomagnetic field lines. Therefore, if our assumption is true, the frequencies of the waves observed by the satellite must be same along the geomagnetic field line, that is, the frequencies of the observed waves depend on the L-value.

Figure 3.24 shows the L-value dependence of the frequency of H^+ mode emissions. In the figure, we picked up the frequencies of the peak magnitude in the band of emissions of H^+ mode, for the typical 11 trajectories. We can find that the relation between the frequency and the L-value is almost confined within the region between f_{cHe^+} and $0.5 f_{cH^+}$, and the frequencies of the observed waves in general depend on the L-value regardless of the latitude. The line of $0.35 f_{cH^+}$ is also plotted as a reference because the ion cyclotron resonant instability has the maximum growth rate around $0.35 f_{cH^+}$ according to our thoretical study. Frequency of maximum growth rate, of cource, depends on the plasma parameters such as thermal energy and tempera-

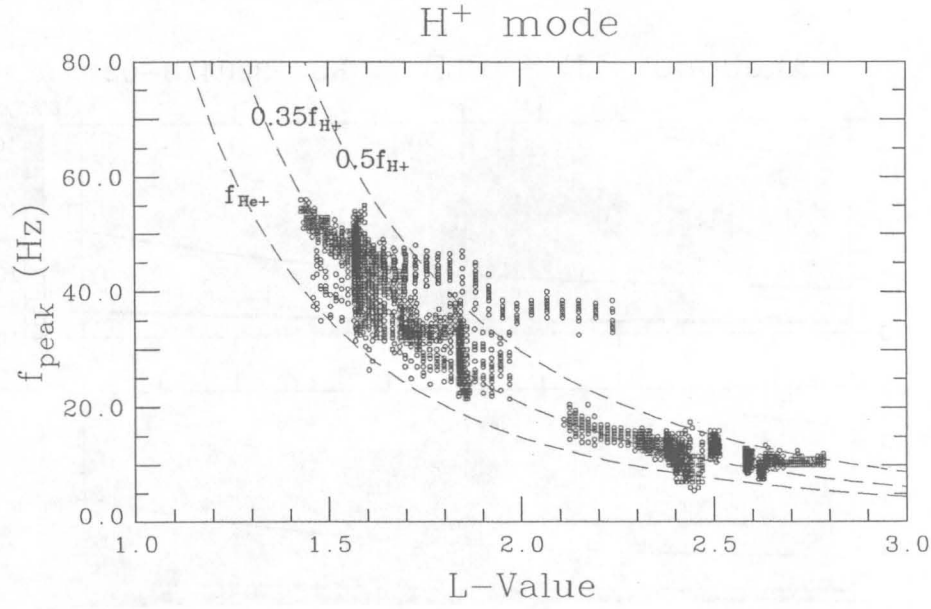

Figure 3.24: L-value dependence of the observed frequency of the H^+ mode emissions.

ture anisotropy of ions, but the observation result shows a good correlation with $0.35 f_{cH^+}$ line.

3.4 A different type of ion cyclotron wave

In this section, we will introduce a new type of emissions which is rarely observed and also assumed to be ion cyclotron wave. Figure 3.25 shows an f-t diagram obseved on April 18, 1989. In the figure, the thick solid lines indicates the local f_{cHe^+} and f_{cO^+}, respectively, and the thin solid line indicates $0.5 f_{cH^+}$. It is interesting that we can find a band of emissions just above the thin solid line ($0.5 f_{cH^+}$) around the geomagnetic equator. Figure 3.26 is another example, where two bands of emissions coexist. The lower band of emission is assumed to be H^+ mode wave, and the upper band of emission has a cuttoff just above $0.5 f_{cH^+}$. We found the new type of emissions for 16 trajectories shown in Table 3.1.

These examples suggest that they are related to ions such as dueteron (D^+) or alpha (He^{++}) particle, whose cyclotron frequencies are both $0.5 f_{cH^+}$. Properly speaking, there should be a band gap between the lower cutoff of the emission and $0.5 f_{cH^+}$ if there are sufficient content (more than a few percents) of such ions in a plasma, but they are such minor ions compared with H^+, He^+ or O^+ that the band gap may become so small. It is difficult to differentiate these

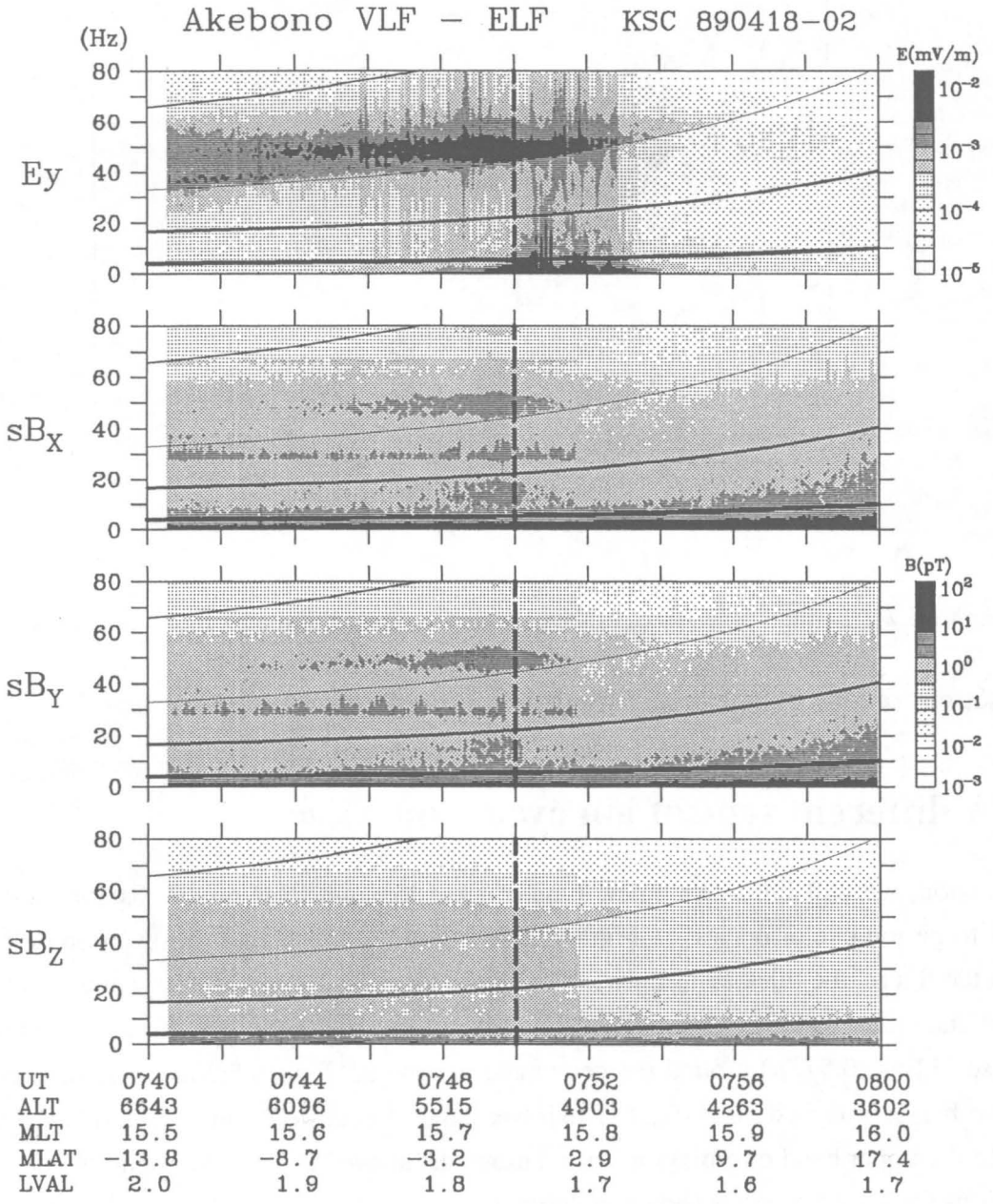

Figure 3.25: An f-t diagram of the ELF emissions observed on April 18, 1989. The vertical dashed line indicates the location of the geomagnetic equator. The thick solid lines indicates the local f_{cH^+}, f_{cHe^+} and f_{cO^+}, respectively. The thin solid line indicates $0.5 f_{cH^+}$.

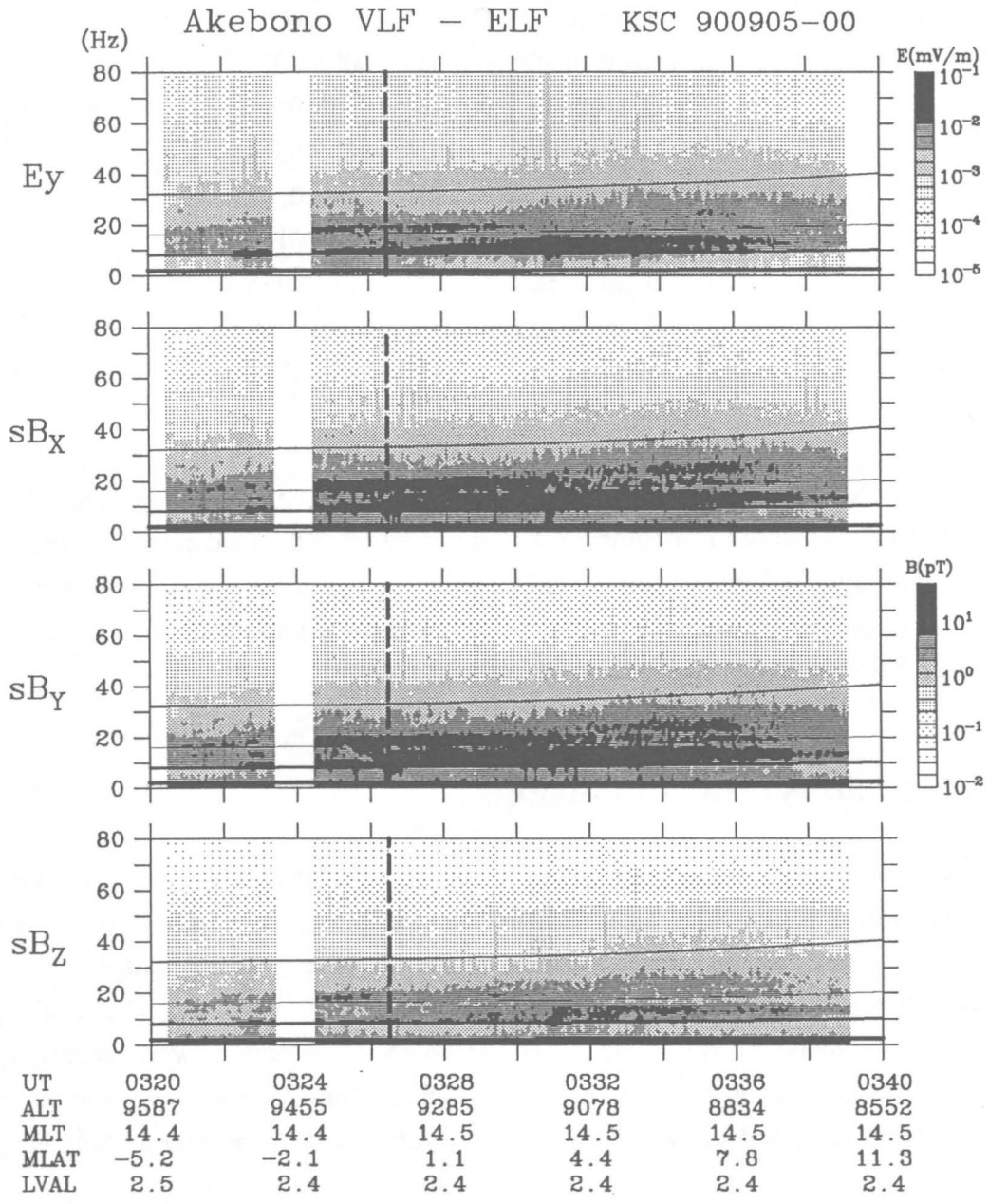

Figure 3.26: An f-t diagram of the ELF emissions observed on September 5, 1990. The vertical dashed line indicates the location of the geomagnetic equator. The thick solid lines indicates the local f_{cH^+}, f_{cHe^+} and f_{cO^+}, respectively. The thin solid line indicates $0.5 f_{cH^+}$.

Table 3.1: Lists of trajectries when a band of emissions which have a cutoff just above $0.5 f_{cH^+}$.

Date	Time (UT)	Date	Time (UT)
890418	0740-0756	901009	0006-0024
890717	0816-0832	901024	0158-0218
890810	0558-0609	910129	0506-0514
900412	0740-0750	910301	0142-0147
900627	1240-1249	910306	0102-0111
900905	0320-0338	910308	2243-2258
900907	0554-0600	910309	0155-0200
900922	0152-0216	910324	2254-2259

two particles by observation. However, it is possible to make a distinction between them by their origins, that is, dueteron is assumed to be originated from the ionosphere whereas alpha particle is mainly involved in the solar wind. Considering that these observations were made in a high solar activity, it is reasonable that alpha particles came into the plasmasphere and ion cyclotron waves related to alpha particle were generated.

3.5 Discussions and conclusions

Our ELF observations by the Akebono satellite have revealed that bands of electromagnetic emissions which have a frequency dependence on the local cyclotron frequencies of ions are often observed in the vicinity of the geomagnetic equatorial region in a wide range of altitudes. They are identified as electromagnetic ion cyclotron waves (ICW) which might have been generated in the geomagnetic equatorial plane. The wave normal directions were determined by means of the wave distribution function (WDF) method. It is found that the wave normal vector is in the meridian plane, and the wave normal angle between the geomagentic field is rather large.

In particular, the existence of the lower band emissions, which we call the He^+ mode, requires an existence of rather high concentration of O^+ ions. This fact may be due to the low altitude of the Akebono satellite. In any case, over the region where the He^+ mode emissions are observed the concentration of O^+ ions should be high.

The high electron temperature (4,000 $\sim$ 5,000 K) observed by the TED instruments [*Abe et*

al., 1990] in 1989 may be due to a high solar activity. Although it is not certain that the magnetospheric plasma is in perfect thermal equilibrium with an equal temperature for electrons and ions, such a high temperature is favorable to explain the existence of the ICW mode emissions. Decreasing the occurrence probabily of the emission in 1994 and 1995 is also explained by the lower solar activity. In order to confirm the reason of less occurrence probability in 1994 and 1995, it is necessary to examine electron temperature in the period.

In addition to the H^+ and He^+mode wave, ion cyclotron wave which may be related to alpha particles was also observed. This fact reflect a high solar activity in 1989 and 1990 and a strong evidence that a lot of alpha particle originated from the solar wind were pervaded into the magnetosphere.

The ray tracing method for ion mode waves has been applied to the observed emissions for both cold and hot plasma models. We have found that these ICW mode waves propagate along the geomagnetic field lines, and are trapped within a limited geomagnetic latitude range with multiple bounces by the LHR reflection. In the process of multiple bounces the wave gradually turns out to be electrostatic with its wave normal increasing and turning nearly perpendicular to the geomagnetic field line. The wave normal directions deduced from the WDF analyses are consistent with the ray tracing results.

The total integrated growth Γ along the ray path is estimated with hot plasma ray tracing method, on the assumption that the ion cyclotron resonant instability due to the temperature anisotropy of the hot H^+ ions causes the generation of the ICW mode wave. We have found that these waves can grow sufficiently when they are initiated around the geomagnetic equator with their wave normal vector parallel to the geomagnetic field line. Since the trajectories of the Akebono satellite around the geomagnetic equator is within the inner radiation belt, an abundant energy source for the ion cyclotron resonant instability may possibly exist. According to the PWS (plasma waves and sounder experiments) measurement for frequencies from 20 kHz to 5 MHz, upper hybrid resonance (UHR) emissions are sharply intensified strictly at the magnetic equator [*Oya et al.*, 1990]. This fact implies that an energy source for wave generation is always present there. Although the ion mass spectrometer and low-energy particle analyzer could not have measured particle distribution correctly in the equatorial region, radiation monitor (RDM) on board the Akebono satellite was measuring energetic particles in the energy range of MeV and comparison these data with wave data is left as a future study.

In conclusion, the generation mechanism of these emissions is considered as follows. That is, the source region of the H^+ and He^+ mode emissions is within the geomagnetic latitude of 10° and the energy source is a temperature anisotropy of the hot H^+ which exists within the inner

radiation belt. In that condition these emissions can be generated and grow while bouncing back and forth, and then they gradually turn out to be electrostatic and are damped. In this way the back and forth waves can coexist around the geomagnetic equatorial region. However, as was mentioned before, the growth rate for the He^+ mode was not large enough in our estimation. Is may be because only one case study was made in the present paper. More detailed discussion will be needed to investigate the plasma condition which makes He^+ mode wave sufficiently enhanced, for example, in the cases that anisotropy of He^+, more thermal and/or anisotropic H^+ are taken into account.

Finally, it should be emphasized that our contribution of the present study is not only clarifying the generation mechanism and propagation characteristics of ICW observed by the Akebono satellite but also giving a clue to investigate the global plasma distribution especially for the ion constituents in the plasmasphere. For example, relative ion constituents may be theoretically estimated from the lower cutoff of the ICW, and the plasma density and temperature may also be estimated using ray tracing technique. Such kind of point of views will be important as a future study.

Chapter 4

Multiband Structured Emission in the vicinity of the Magnetic Equator

4.1 Introduction

As was introduced in the previous chapter, two kinds of ELF emissions are observed in the vicinity of the geomagnetic equator; type A and type B. In the present chapter we will discuss the characteristics of type B emission.

In the past, there is one short report on the analysis for the characteristics of the type B emissions observed by the Akebono satellite [*Kokubun et al.*, 1991], although detailed study of these waves has not yet been undertaken. Their suggestion is constructed in similar line with the observation results of the GEOS 1 and 2, IMP 6 and Hawkeye satellites [*Russell et al.*, 1970; *Gurnett*, 1976; *Perraut et al.*, 1982], that is, the wave is generated as magnetosonic wave (MSW) and propagates nearly perpendicular to the geomagnetic field. *Kokubun et al.* [1991] investigated the spectra of type B emissions observed by the Akebono satellite and pointed out that each band of the emissions are harmonically related. They supposed that the emissions were of distant origin and their source region was located at L-values greater than 3, on the basis that the frequency interval in multiband structure of the emission should be the proton cyclotron frequency at the wave source.

On the other hand, *Laakso et al.* [1990] investigated the characteristics of these waves observed by the GEOS 2 satellite with regard to polarization, propagation direction, and refractive index in detail by taking account of the electric field. As a result of their analysis, they concluded that the waves have right-handed polarization, with their magnetic components strongly field aligned, and are propagating azimuthally, that is, perpendicular to the meridian plane. In

comparison with the reports by *Laakso et al.* [1990] and *Kokubun et al.* [1991], there is a conflict in the argument for the propagation direction of the emission.

In the present study, the wave normal direction of the emission is determined by using the wave distribution function (WDF) analysis technique, and their propagation characteristics are examined by a three-dimensional ray tracing method [*Kasahara et al.*, 1994]. An outline of the present chapter is as follows. In the next section, statistical studies of the MSW waves observed by the Akebono satellite are given, that is, the spatial and time distribution and refractive index. In the following section, the wave normal directions of the emissions are presented. Then we will present the results of three-dimensional ray tracing in a cold plasma model including the effects of ions. Finally, a summary and discussions are added in the last section.

4.2 Observation

4.2.1 General characteristics

In order to clarify the spectral difference between type A and type B emissions, the typical spectra of type B emissions is introduced. Figure 4.1 shows an example of type B emissions observed 0638-0710 UT on September 26, 1990. In this case, multiband emissions were observed within magnetic latitude $\pm 18°$ in the frequency range around f_{cH^+} (top of the thick solid line). The most remarkable characteristics of these emissions are that the frequency of each band and its spacing are almost constant and do not depend on the local cyclotron frequencies, that is, they do not depend on the local geomagnetic field intensity. Figure 4.2 shows another example observed 1032-1048 UT on August 20, 1990. Here we can find the emissions which have broadband spectra above f_{cH^+}(top of the thick solid line) and do not depend on the local cyclotron frequencies. The duration for type B emissions to exist around the magnetic equatorial region are usually a few days and several weeks at the longest. The number of harmonics of the emission sometimes changes within a few hours, and in some cases the fundamental frequency changes within such a short duration. Although the observed location differs greatly, the type B emissions are similar to those reported by *Gurnett* [1976] and *Perraut et al.* [1982], and these waves may be interpreted as MSW, in which electric and magnetic field components coexist.

4.2.2 Spatial and time distribution

We have examined ELF wave data of 221 orbits tracked at KSC from April 1989 to October 1990 which cover latitudinal regions around the geomagnetic equator, although we have not yet

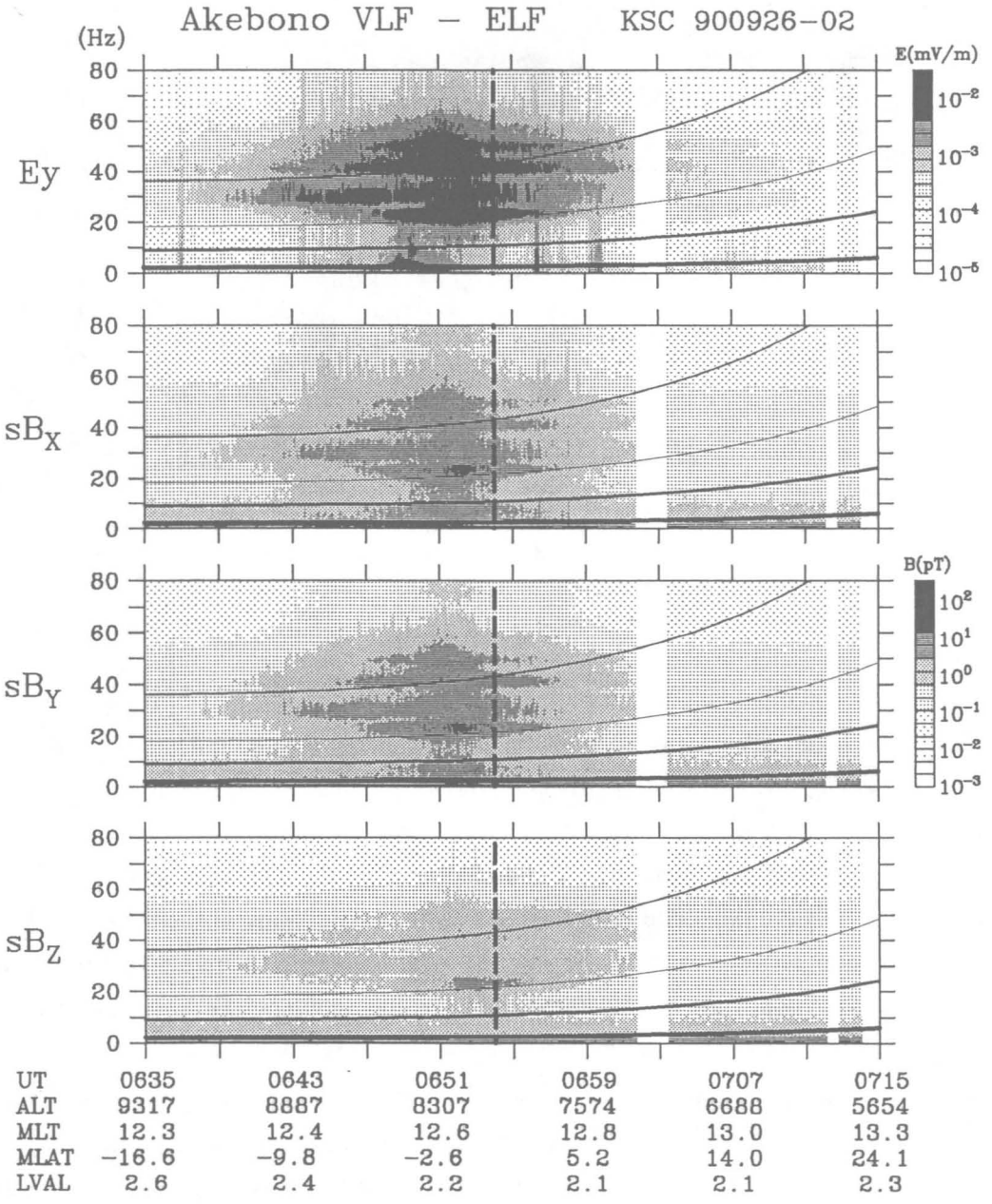

Figure 4.1: An f-t diagram of the ELF emissions observed on September 26, 1990. The vertical dashed line indicates the location of the geomagnetic equator. The thick solid lines indicate the local f_{cH^+}, f_{cHe^+} and f_{cO^+}, respectively. The thin solid line indicates $0.5 f_{cH^+}$.

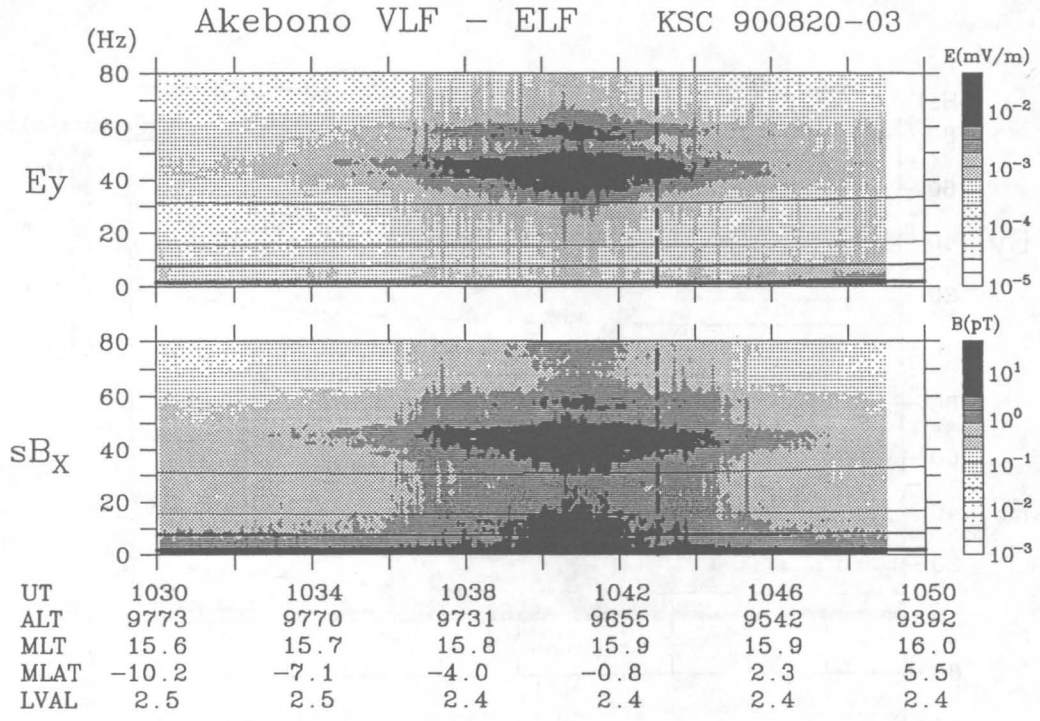

Figure 4.2: An f-t diagram of the ELF emissions observed on August 20, 1990. The vertical dashed line indicates the location of the geomagnetic equator. The thick solid lines indicate the local f_{cH^+}, f_{cHe^+} and f_{cO^+}, respectively. The thin solid line indicates $0.5 f_{cH^+}$.

analyzed all of the data in this term. The 221 trajectories of the Akebono satellite mentioned above are shown in Figure 4.3. The left panel shows the projections of the trajectories on the geomagnetic meridian plane, and the right panel shows the relation between geomagnetic latitude versus magnetic local time of the trajectories. In the analyses, we have found 77 orbits in which type B emissions were observed. Figure 4.4 indicates the trajectories of the Akebono satellite while the type B emissions were observed. Compared with the spatial distribution of type A emissions (Figure 3.4 and Figure 3.5), type B emissions were observed only in the region where L is greater than 2.0, whereas type A emissions were observed at all ranges in altitudes from the perigee of about 1,000 km to the apogee of about 10,000 km.

Figure 4.5 is a histogram of occurrence number of type B emissions versus the magnetic local time of the trajectories. The horizontal axis indicates the magnetic local time when the Akebono satellite has passed through the geomagnetic equator. The emissions have no dependence on magnetic local time.

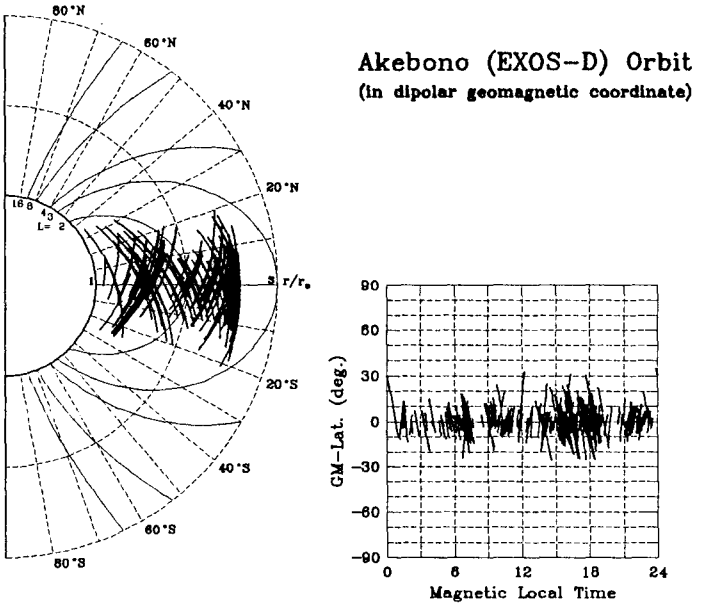

Figure 4.3: The 221 trajectories of the Akebono satellite in which we have examined the ELF wave data.

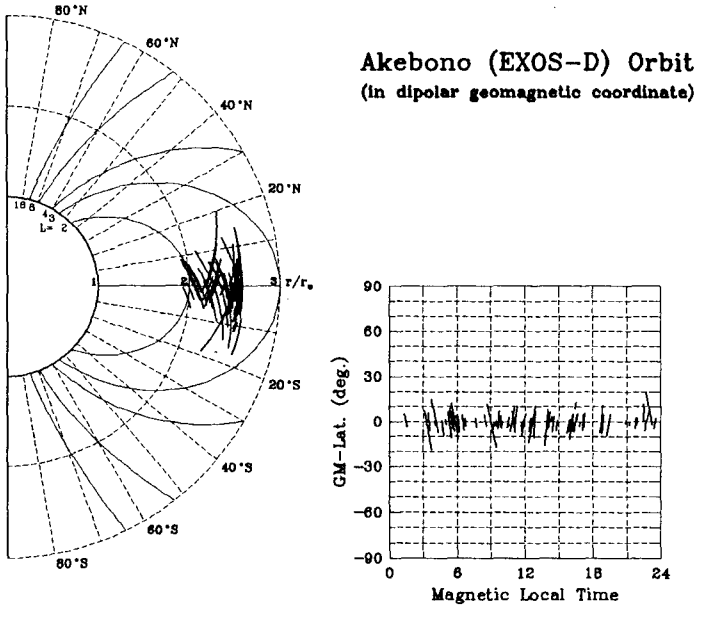

Figure 4.4: Trajectories of the Akebono satellite where the type B emissions were observed.

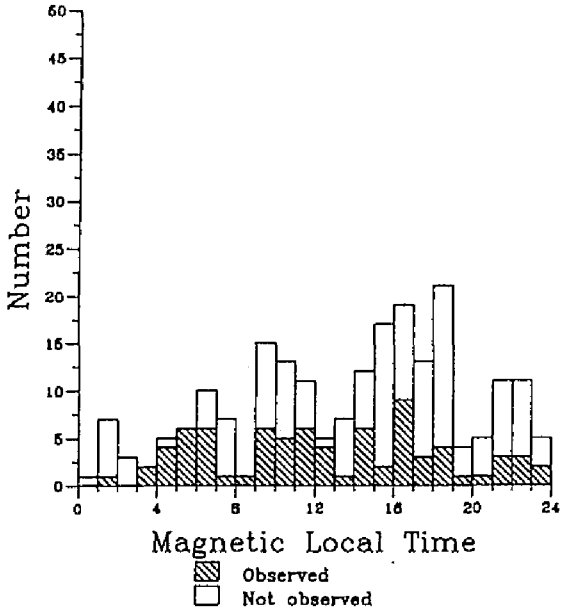

Figure 4.5: Magnetic local time dependence of the occurrence probabilities of the type B emissions.

4.2.3 Refractive index

The refractive index μ of MSW was roughly estimated, by using one component of the electric field observed by a 60-m tip-to-tip wire antenna and three components of the magnetic field observed by three orthogonal search coil antennas extended from the Akebono satellite by (3.2). As mentioned in the previous chapter, we must notice that error range of the refractive index estimated by this equation becomes larger as the angle between the geomagnetic field line and the wave normal direction approaches to perpendicular.

We assume that the frequency range $f \ll f_{\mathrm{LHR}}$ in a cold plasma which consists of electrons and pure hydrogen ions, where $f_{\mathrm{LHR}} = (f_{\mathrm{ce}} f_{\mathrm{cH^+}})^{1/2}$ is the lower hybrid resonance (LHR) frequency and f_{ce} is the electron cyclotron frequency. *Laasko et al.* [1990] investigated the ratio between electric and magnetic field amplitude of MSW. According to their study, the following equation is valid in a cold plasma approximation,

$$V_{\mathrm{A}} \leq \frac{E}{B} \leq V_{\mathrm{A}} \sqrt{1 + \left(\frac{f}{f_{\mathrm{cH^+}}}\right)^2}, \tag{4.1}$$

where V_{A} is the Alfven velocity. In the present paper, we consider MSW as a whistler mode wave under the cold plasma approximation, so that the refractive index calculated by (3.2) is

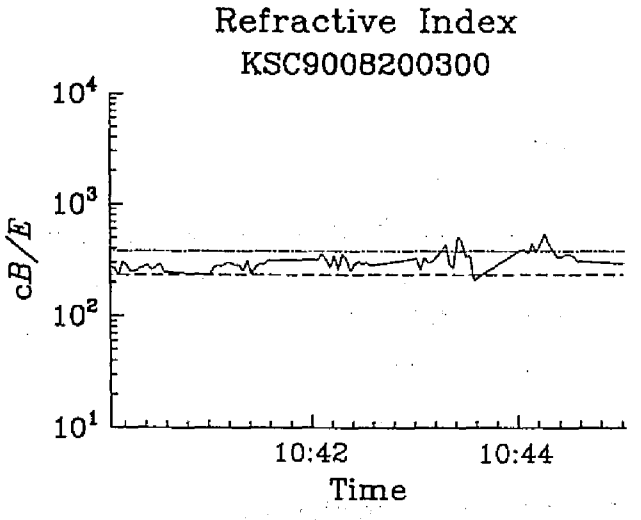

Figure 4.6: Refractive index for the emissions in the frequency ranges from 40 Hz to 60 Hz observed 1040-1045 UT on August 20, 1990. The dashed line and dot-dashed line indicate $R^{1/2}$ and $(RL/S)^{1/2}$, respectively.

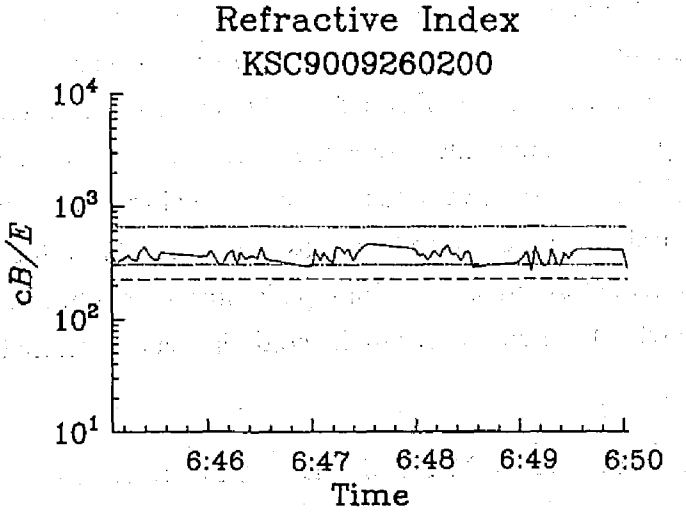

Figure 4.7: Refractive index for the emissions in the frequency ranges from 35 Hz to 40 Hz observed 0645-0650 UT on September 26, 1990. The dashed line, dot-dashed line, and two-dot-dashed line indicate $R^{1/2}$, $(RL/S)^{1/2}$ and $L^{1/2}$, respectively.

expected to satisfy the following equation,

$$R \leq \mu^2 \leq RL/S, \tag{4.2}$$

where R, L, and S are those defined by *Stix* [1962]. R and RL/S correspond to whistler mode waves propagating along and perpendicular to the geomagnetic field line, respectively. In the frequency range much below f_{LHR}, RL/S nearly equals c^2/V_A. In order to calculate the parameters R, L, and S, the cyclotron frequencies and the plasma frequencies of the particles are needed. In the present paper, the electron cyclotron frequency (f_{ce}) given by the International Geomagnetic Reference Field (IGRF) 1985 model [*IAGA*, 1985] was used, and the electron plasma frequency (f_{pe}) was determined from the upper hybrid resonance frequency $f_{UHR} = (f_{ce}^2 + f_{pe}^2)^{1/2}$, which could be observed by the plasma wave instruments (PWS) [*Oya et al.*, 1990] on board the Akebono satellite.

Figure 4.6 shows the refractive index, indicated by the solid line, for the emissions in the frequency ranges from 40 Hz to 60 Hz observed 1040-1045 UT on August 20, 1990. The dashed line and dot-dashed line indicate $R^{1/2}$ and $(RL/S)^{1/2}$, respectively (using the parameters of $f_{ce} \simeq$ 60 kHz, $f_{pe} \simeq$ 500 kHz). It turns out that the estimated refractive index satisfies the relation indicated by (4.2).

The emissions, whose frequency is below f_{cH^+}, were also examined. Figure 4.7 shows the refractive index for the emissions in the frequency ranges of 35-40 Hz ($f_{cH^+} \simeq$ 40 Hz) observed 0645-0650 UT on September 26, 1990. Defined by *Stix* [1962] and corresponding to ion cyclotron mode wave propagating along the geomagnetic field, $L^{1/2}$ is also indicated by two-dot-dashed line in Figure 4.7. The refractive index is almost equal to $(RL/S)^{1/2}$, that is, the wave normal angle of the emission is assumed to be almost perpendicular to the magnetic field line. In general, it is found that the refractive index for type B emissions is between 100 and 300, and these emissions are the whistler mode waves in the cold plasma approximation.

4.3 Measurements of wave normal directions

4.3.1 Results of the wave normal direction measurements

The wave normal directions of the emissions were estimated by wave distribution function (WDF) method. In the present study we have regarded the emissions as whistler mode. As for the ion constituents, we examined for three sets of ion constituents, that is, (1) (100% H^+, 0% He^+, 0% O^+); (2) (90% H^+, 9% He^+, 1% O^+); and (3) (70% H^+, 20% He^+, 10% O^+). We have

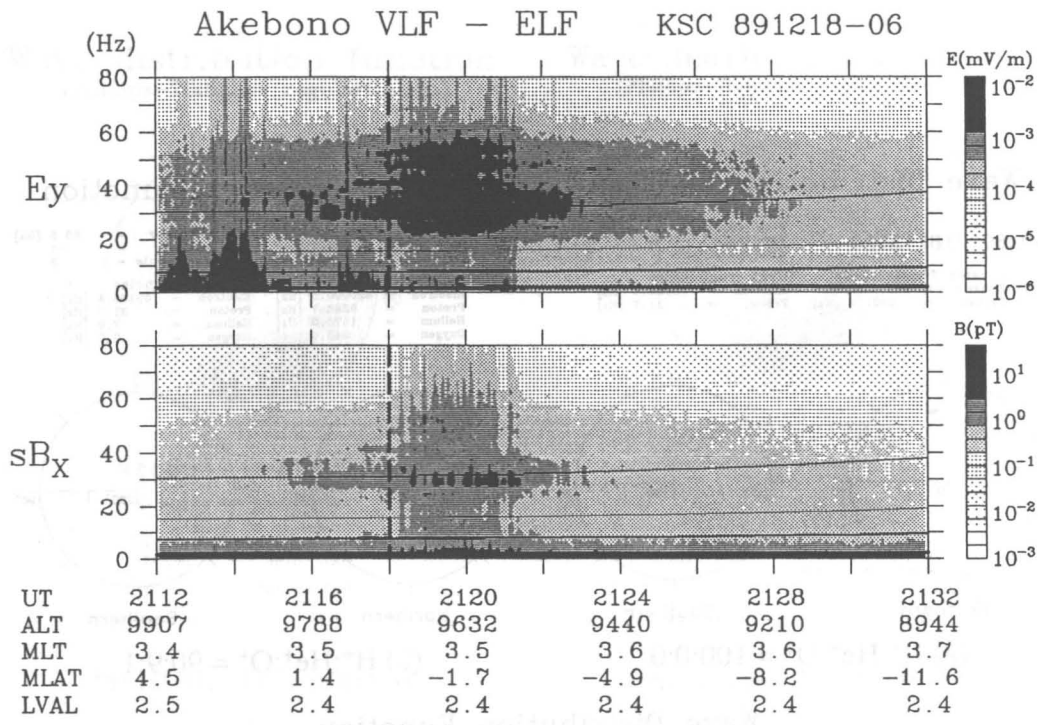

Figure 4.8: An f-t diagram of the ELF emissions observed on December 18, 1989. The vertical dashed line indicates the location of the geomagnetic equator. The thick solid lines indicate the local f_{cH^+}, f_{cHe^+} and f_{cO^+}, respectively. The thin solid line indicates $0.5 f_{cH^+}$.

used only magnetic field components, therefore the wave normal direction has an ambiguity of 180°.

December 18, 1989

We will show the results obtained for the wave normal direction of the emissions observed 2112-2130 UT on December 18, 1989 (see Figure 4.8). As the bandwidth of the emissions is wide, the spectral matrix was produced for a bandwidth of 4 Hz extracted from the emissions after the FFT analyses, which are composed of 25 frequency components of 0.16-Hz resolution around the frequency of the maximum signal intensity ~55 Hz.

Figures 4.9 (a)-(c) show the wave normal directions of the emissions between 2120:20 and 2120:52 UT estimated by the maximum entropy method (MEM). Regardless of the ion constituents, the polar angles ψ are around 70°, and the azimuthal angles η are around 90° and 270° that are nearly perpendicular to the geomagnetic meridian plane.

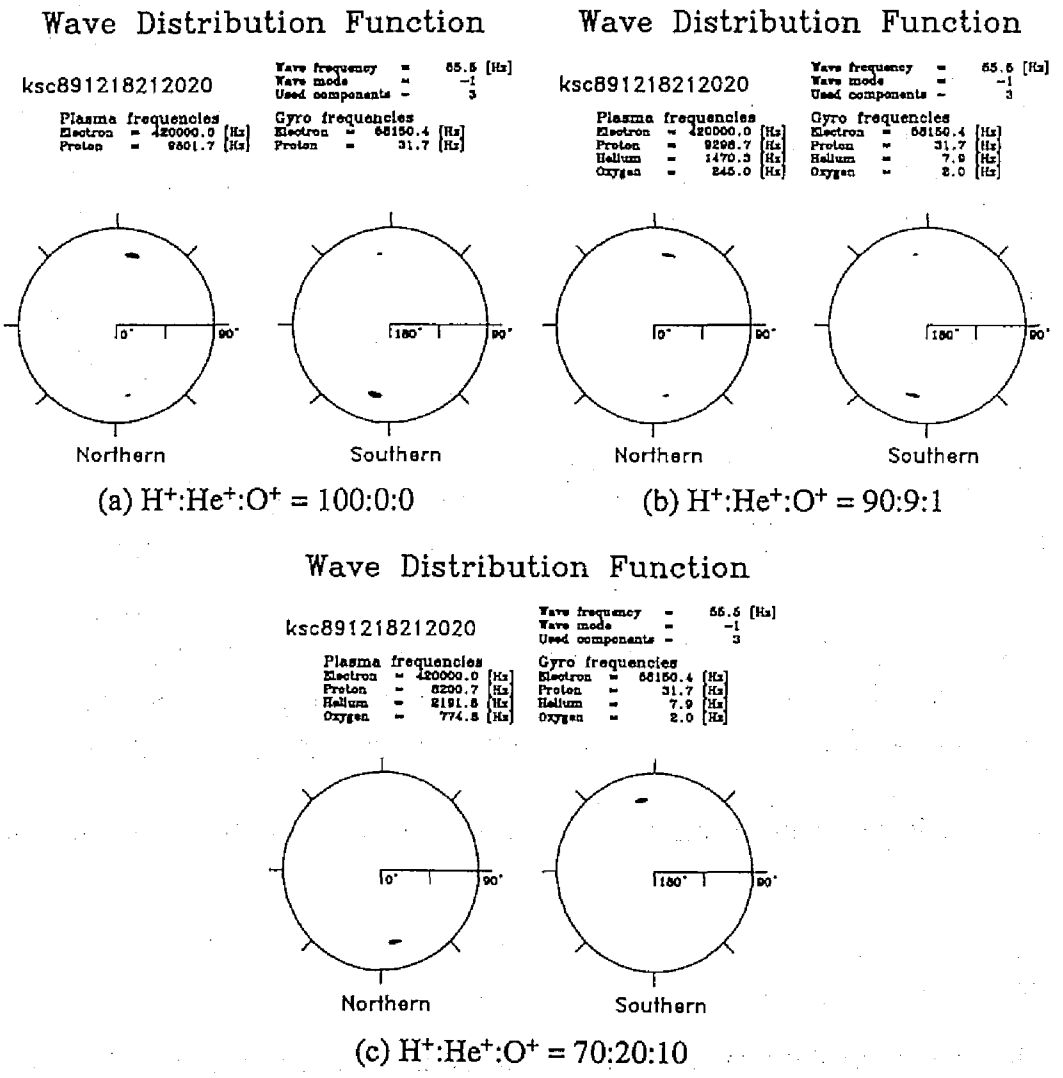

Figure 4.9: Wave normal directions estimated by the MEM for the emissions around the frequency of 45 Hz 2120:20-2120:52 UT on December 18, 1989, with H^+: He^+: O^+= (a) 100:0:0, (b) 90:9:1, and (c) 70:20:10.

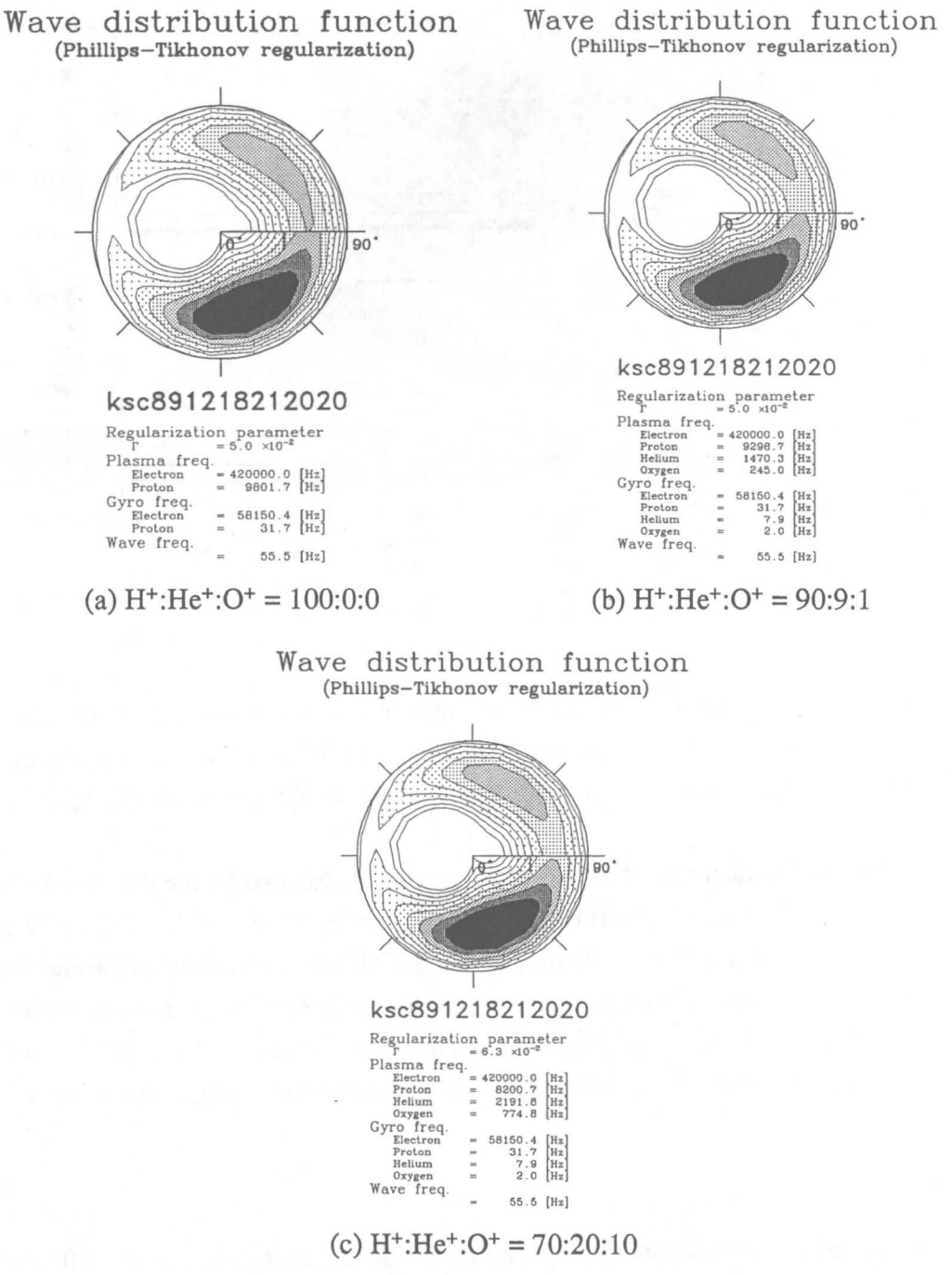

Figure 4.10: Wave normal directions estimated by the PTM for the emissions around the frequency of 45 Hz 2120:20-2120:52 UT on December 18, 1989, with H^+: He^+: O^+= (a) 100:0:0, (b) 90:9:1, and (c) 70:20:10.

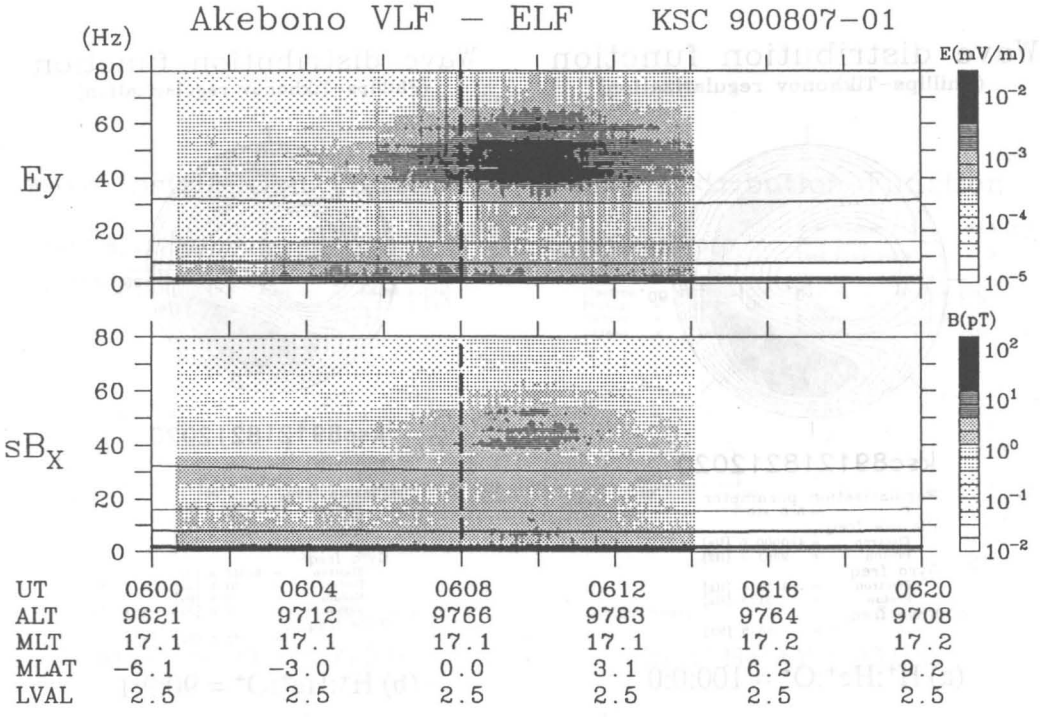

Figure 4.11: An f-t diagram of the ELF emissions observed on August 7, 1990. The vertical dashed line indicates the location of the geomagnetic equator. The thick solid lines indicate the local f_{cH^+}, f_{cHe^+} and f_{cO^+}, respectively. The thin solid line indicates $0.5 f_{cH^+}$.

Figures 4.10 (a)-(c) indicate the wave normal directions estimated by the Phillips-Tikhonov reguralization method (PTM). We can find two energy peaks at $(\psi, \eta) = (70°, 280°), (70°, 80°)$. These results are very similar to those estimated by the MEM. We also calculated the eigenvalues from the spectral matrix, and it is found that the ratio of the second largest to the largest was equal to 0.17, and the ratio of the smallest to the largest was equal to 4.8×10^{-2} . It is not contradictory against the results derived by the WDF that two waves coexist at that time.

August 7, 1990

The wave normal directions obtained by the MEM for the emissions observed 0606-0614 UT on August 7, 1990 (see Figure 4.11), are presented in Figures 4.12 (a)-(c).

The spectral matrix was calculated for a bandwidth of 1 Hz in a frequency ~60 Hz between 0608:48 and 0609:20 UT. Figures 4.13 (a)-(c) indicate the wave normal directions estimated by the PTM.. We can also find from both results that there were two waves propagating quasitrans-

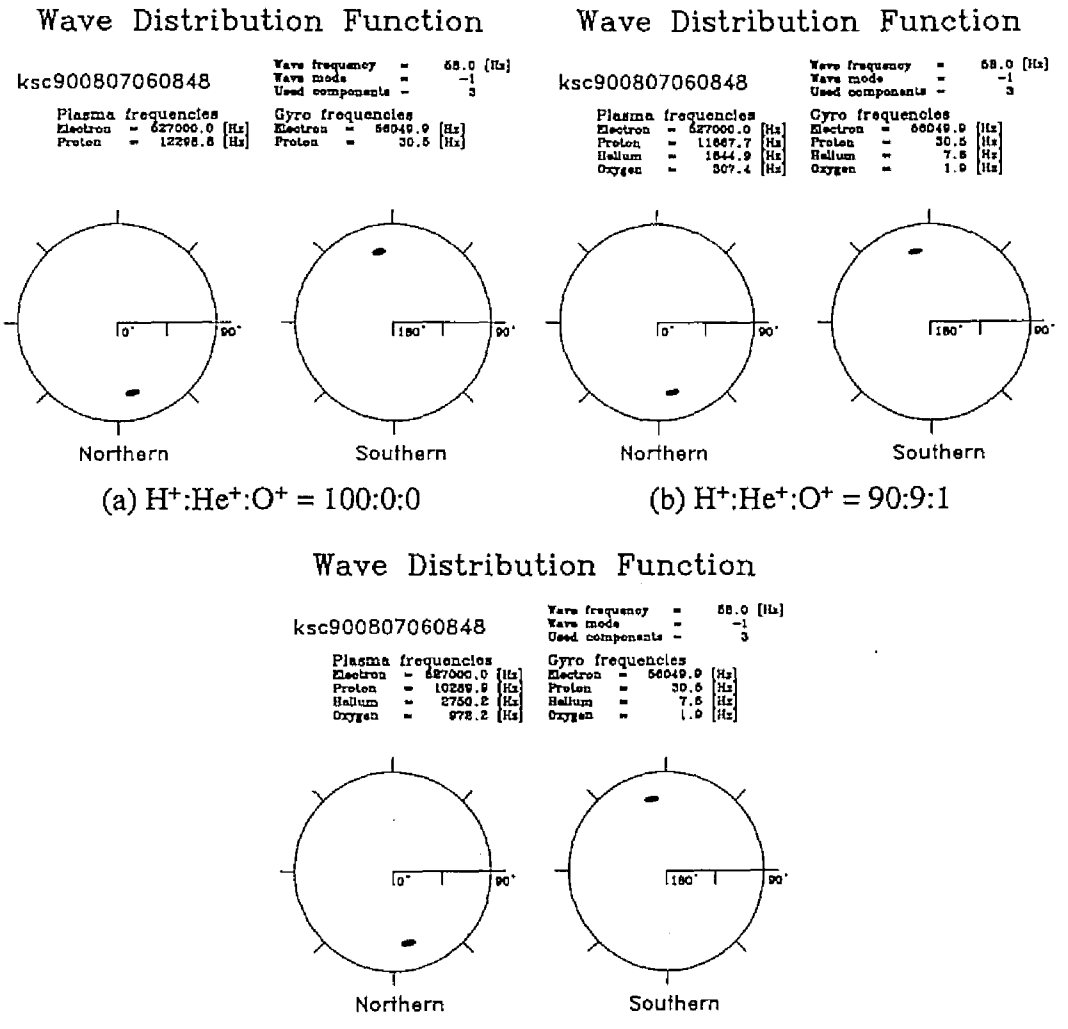

Figure 4.12: Wave normal directions estimated by the MEM for the emissions around the frequency of 60 Hz 0608:48-0609:20 UT on August 7, 1990, with H^+: He^+: O^+= (a) 100:0:0, (b) 90:9:1, and (c) 70:20:10.

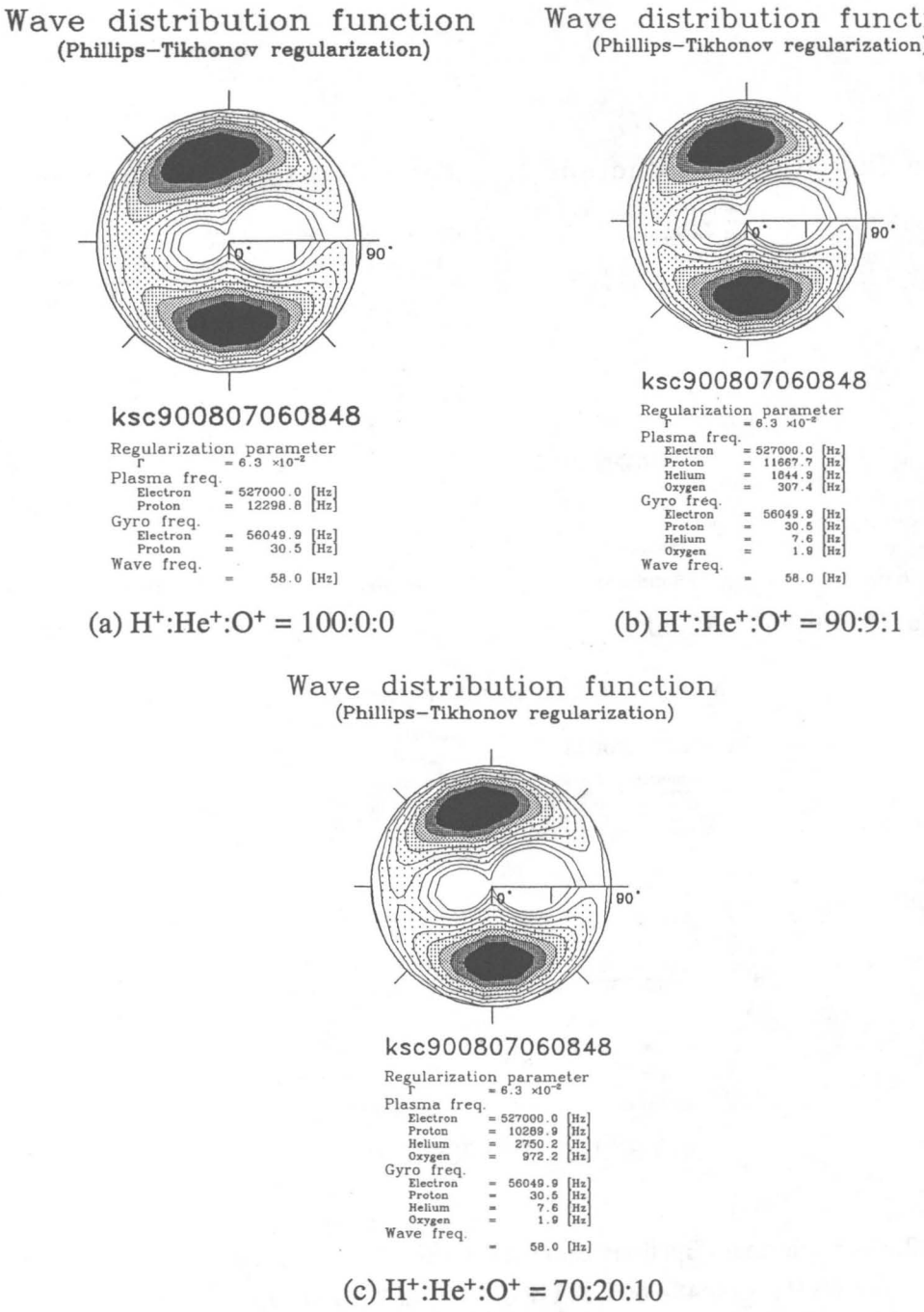

Figure 4.13: Wave normal directions estimated by the PTM for the emissions around the frequency of 60 Hz 0608:48-0609:20 UT on August 7, 1990, with H^+: He^+: O^+= (a) 100:0:0, (b) 90:9:1, and (c) 70:20:10.

verse ($\psi \simeq 70°$) with their azimuthal angles nearly perpendicular to the geomagnetic meridian plane. As for the eigenvalues calculated by the spectral matrix, the ratio of the second largest to the largest and the smallest to the largest was equal to 0.38 and 4.9×10^{-2}, respectively.

Propagation characteristics

Here we will summarize the propagation characteristics derived from the wave normal directions determined by the WDF method.

1. The waves were propagating quasi-transverse. Their polar angles ψ were not smaller than 45°.

2. The wave normal directions were nearly perpendicular to the geomagnetic meridian plane, which suggests an azimuthal propagation.

3. Multiple (more than two) waves with different wave normal directions often coexisted.

These results show good agreement with the suggestions given by *Laakso et al.* [1990] that the MSW observed by GEOS 2 was propagating toward the azimuthal direction, the magnetic component of the wave was strongly field aligned, and the main axis of the electric field wave polarization ellipse was close to the azimuthal direction.

4.4 Ray path calculations

A three-dimensional ray tracing study was made for the whistler mode waves calculated in a cold plasma model including the effects of multicomponent ions such as protons and helium and oxygen ions. The propagation characteristics of the emissions are discussed to confirm the spatial distribution where they were observed and our results of wave normal direction analysis.

4.4.1 Three-dimensional ray tracing including the effect of steep density gradient

In the past, the propagation characteristics of the ULF waves in the presence of helium ions were investigated by ray tracing in a cold plasma model [*Rauch and Roux*, 1982]. They traced the ray paths of three modes (class I, II, and III in their paper) and concluded that class II wave, that is, essentially a whistler mode wave, is unguided along the geomagnetic field line regardless of the wave normal direction and propagates outward from the Earth. In their calculation, however, they used plasma density profile in the magnetosphere in which the cold plasma density smoothly decreases as the radial distance increases. Such an approximation is not appropriate for us to

understand the mechanism of the emissions because the existence of the steep density gradient such as plasmapause may affect the results of ray tracing.

Our three-dimensional ray tracing program is also applicable to ion cyclotron modes and a whistler mode including the effects of multicomponent ions [*Kasahara et al.*, 1992]. As for the geomagnetic field, a dipole model was adopted. In order to include the effect of the steep density gradient, the Aikyo-Ondoh model [*Aikyo and Ondoh*, 1971] was used for the plasma density profile in the magnetosphere. In the ray tracing study, the plasmapause was located at an L-value of 3.0 and the width of the plasmapause was varied from 0.1 to 0.5 R_E.

In the Aikyo-Ondoh model, a diffusive equilibrium (DE) model [*Angerami and Thomas*, 1964] was used inside the plasmapause. The DE model is a typical analytical model of ion and electron densities inside the plasmapause, and it is parameterized by the relative abundances of, for example, hydrogen, helium, and oxygen ions, the temperature of each ion constituent, and the electron density N_0 at a reference altitude. We assumed the following plasma parameters in the DE model: 44% of H^+, 8% of He^+, 48% of O^+, 1.5×10^4 cm^{-3} of the electron density at the reference altitude of 1100 km, and the particle temperature of 5000°. They were the same parameters used in the previous ray tracing study of the ICW observed by the Akebono satellite described Chapter 2 or reported by *Kasahara et al.* [1992].

It is necessary to check that the WKB approximation is valid for the plasmapause where the density gradient is large along the radial direction, that is, the following equation is valid for each integration step,

$$\lambda \frac{1}{\mu} \cdot \frac{\mathrm{d}\mu}{\mathrm{d}s} \ll 1, \tag{4.3}$$

where λ is the wave length and s is the distance along the ray path. As the rough estimation for the whistler mode wave with the frequency of 30 Hz, the refractive index takes the quantity from 100 to 300, and therefore the wave length λ is from 30 to 100 km, while the width of the plasmapause assumed in the present study is not less than $0.1 R_E (\simeq 637$ km). It is evident that our ray tracing calculation satisfies the WKB approximation.

4.4.2 Results of the ray tracing

Wave normal direction

Kokubun et al. [1991] suggested that if the fundamental frequencies for harmonically related band structures of the emissions were the proton cyclotron frequencies in the source regions, the source region might be located at L-values greater than 3. Therefore ray paths were initiated in the vicinity of the geomagnetic equatorial plane at L-values around 3 with various frequencies

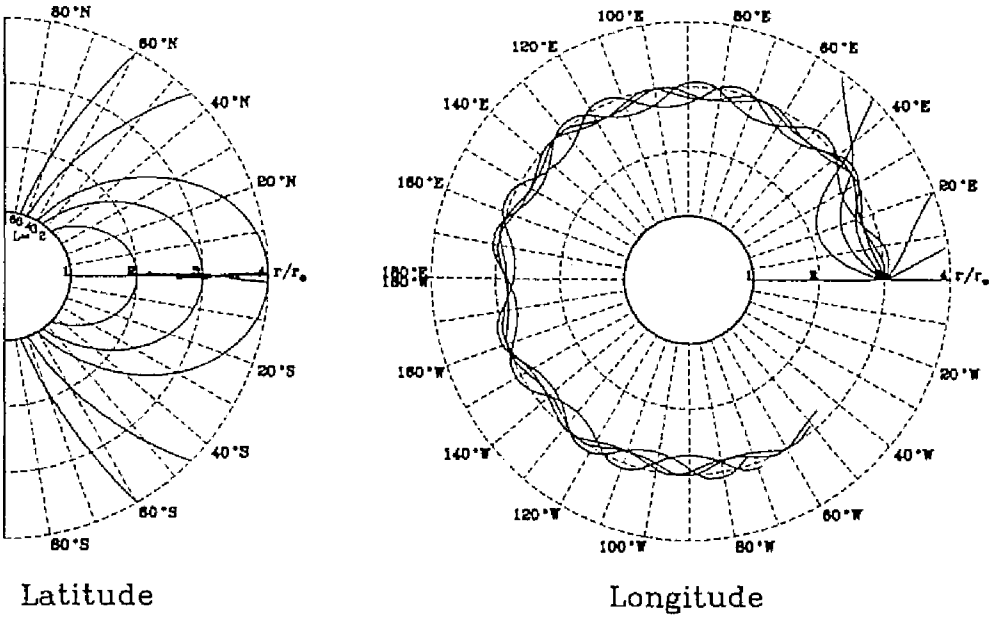

Figure 4.14: Ray paths calculated by ray tracing method. Each ray path is initiated from the geomagnetic equator at an L-value of 3.0 with its azimuthal angle η varied from 0° to 180°and polar angle $\psi \simeq 90°$. The frequency of the wave is equal to the proton cyclotron frequency at the start point.

and wave normal directions. We must pay attention that the plasmapause was also located at an L-value of 3.0.

When ray paths are initiated from the geomagnetic equator with various wave normal directions, the waves deviate outward from the Earth in general as reported by *Rauch and Roux* [1982]. However, it was found that there are some exceptions if the initial wave normal directions are nearly perpendicular to the geomagnetic meridian plane (Figure 4.14). In Figure 4.14, the left panel shows the projection of the ray paths on the geomagnetic meridian plane, and the right panel shows the projection on the geomagnetic equatorial plane. Each ray path was initiated from the geomagnetic equator at an L-value of 3.0 with its azimuthal angle η varied from 0° to 180°and polar angle $\psi \simeq 90°$. In addition, we assumed that the frequency of the wave was equal to the proton cyclotron frequency at the start point. It is remarkable that the waves can propagate around the plasmapause if their azimuthal angles of the wave normal directions are initiated in the range from 60° to 120°. This tendency can take place because the wave tends to propagate inward to the Earth in the density gradient region of the plasmapause and, consequently, is trapped around the plasmapause. We have also varied the initial polar angle of the

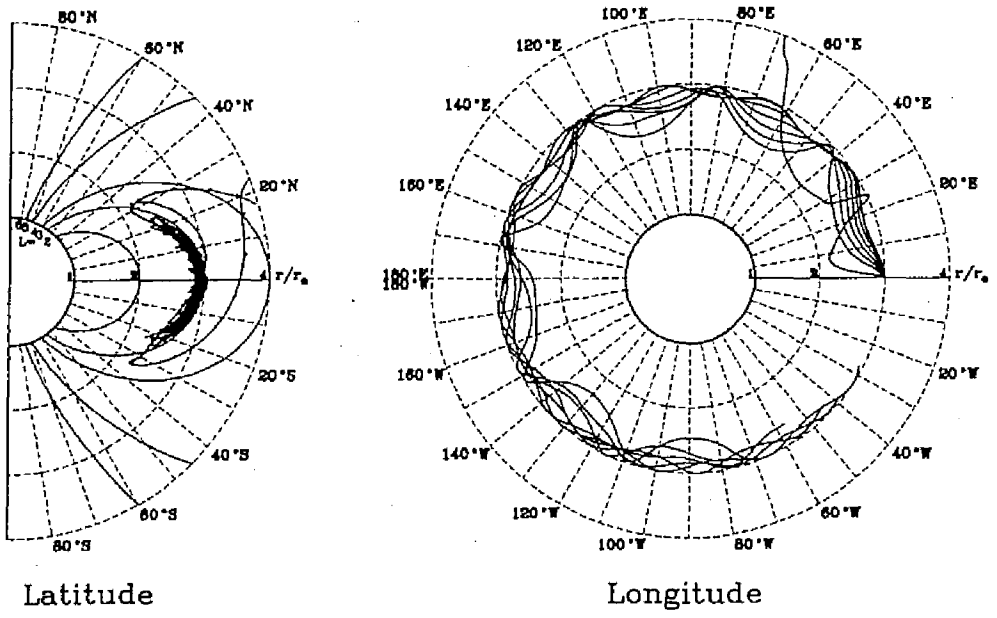

Figure 4.15: Ray paths calculated by ray tracing method. Each ray path is initiated from the geomagnetic equator at an L-value of 3.0 with its azimuthal angle $\eta \simeq 90°$ and polar angle $\psi \simeq$ varied from 0° to 90°. The frequency of the wave is equal to the proton cyclotron frequency at the start point.

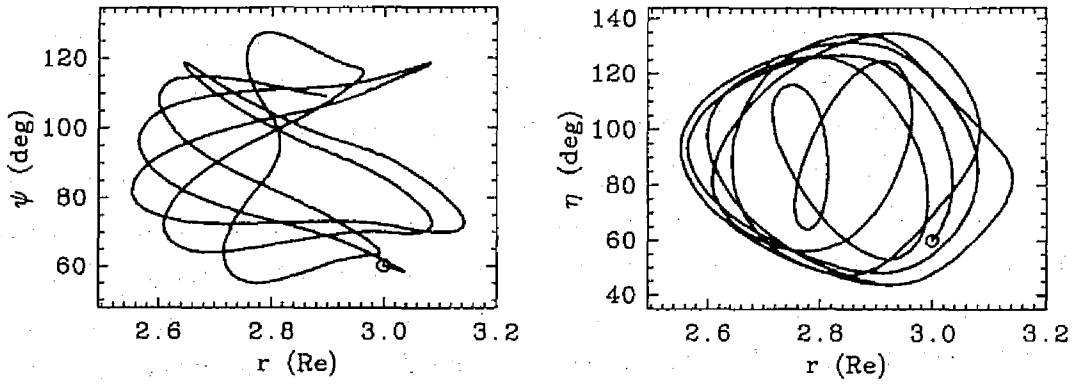

Figure 4.16: Parameters calculated along a ray path when the wave is initiated from the geomagnetic equator at an L-value of 3.0 with its wave normal direction $(\theta, \phi) = (60°, 60°)$.

wave normal direction and found that the waves are also trapped around the plasmapause if their polar angles are larger than 30°.

In Figure 4.15, each ray path was initiated from the geomagnetic equator at an L-value of 3.0 with its azimuthal angle $\eta \simeq 90°$ and polar angle ψ varied from 0° to 90°. It is found that the waves with their initial polar angle between 30° and 90° are trapped along the plasmapause. It should be noted that the latitude range of propagation region is also restricted around the equatorial region (in this case, less than 22°).

Figure 4.16 shows the related quantities calculated along a ray path when the wave is initiated with wave normal direction $(\theta, \phi) = (60°, 60°)$. In the figure, the symbol "o" indicates the initial point, and the transverse axis r indicates the radial position of the ray path. It turns out that the polar angle ψ takes the value from 50° to 130° and the azimuthal angle η from 40° to 140°. These are consistent with the wave normal directions deduced from the WDF analyses for the data observed by the Akebono satellite.

Frequency dependence

The observed emission consisted of several bands with harmonically related frequencies. Propagation characteristics for several different frequencies were also examined by ray tracing. We started our ray tracing from the geomagnetic equator at an L-value of 3.0 with the wave normal direction nearly perpendicular to the geomagnetic meridian plane. The propagation characteristics change when the frequency is above the LHR frequency f_{LHR}; the wave energy propagates along the geomagnetic field line. The LHR frequency f_{LHR} is much higher than the proton cyclotron frequency $f_{\mathrm{cH^+}}$ ($f_{\mathrm{LHR}} \simeq 42.8 f_{\mathrm{cH^+}}$ in our model), and it is found that the ray paths whose frequencies are less than $20.0 f_{\mathrm{cH^+}}$ are the same as those illustrated in Figure 4.14.

Trapping conditions

Now we will discuss the plasma conditions in which the waves are trapped around the plasmapause. In the ray tracing calculation, the width of the plasmapause was varied from 0.1 to 0.5 R_{E}. Figure 4.17 shows the plasma density profile along the geomagnetic equator. In the figure, the solid line and dashed line indicate the plasma density profiles when the width of the plasmapause is 0.5 R_{E} and 0.1 R_{E} respectively. It is found that the waves can be trapped around the plasmapause when the width of the plasmapause is less than 0.5 R_{E}, that is, the density gradient is larger than 1.1 cm^{-3}/km.

Figure 4.18 shows the ray paths when each wave is initiated with its wave normal direction

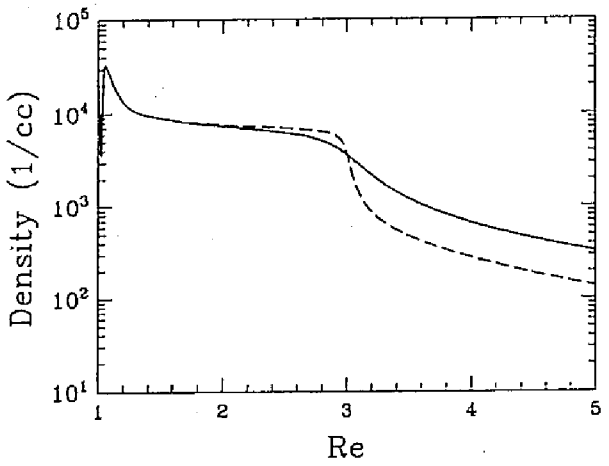

Figure 4.17: Plasma density profile along the geomagnetic equator. The solid line and dashed line indicate the plasma density profiles when the width of the plasmapause is 0.5 R_E and 0.1 R_E respectively.

nearly perpendicular to the geomagnetic meridian plane from the geomagnetic equatorial plane at an L-value from 2.6 to 3.5 with a proton cyclotron frequency at the start point, while the width of the plasmapause is assumed to be $0.2R_E$. The wave initiated at an L-value from 2.7 to 3.2 is trapped around the plasmapause, in other words, the waves initiated between the inner and outer edge of the plasmapause can be trapped around the plasmapause. It is emphasized that the wave generated just outside the plasmapause is possibly observed around the apogee of the Akebono satellite ($\simeq 2.7\ R_E$) if the plasmapause is located at $L \simeq 3$.

Propagation mechanism

The propagation mechanism for a wave to be trapped around the plasmapause nearly in the equatorial plane can be stated as follows. In general, a whistler mode wave, whose frequency is much lower than the LHR frequency, propagates outward from the Earth. If there is a steep density gradient such as plasmapause, the wave tends to propagate toward denser plasma area like a ducted propagation. Two effects keep balance and the wave propagates along an almost constant L line, nearly on the equatorial plane, surrounding the Earth. The above propagation mechanism satisfies all observational facts; the wave was observed in the plasmasphere, the wave normal direction is nearly perpendicular to the geomagnetic meridian plane, and the source region should be located at the L-value greater than 3.

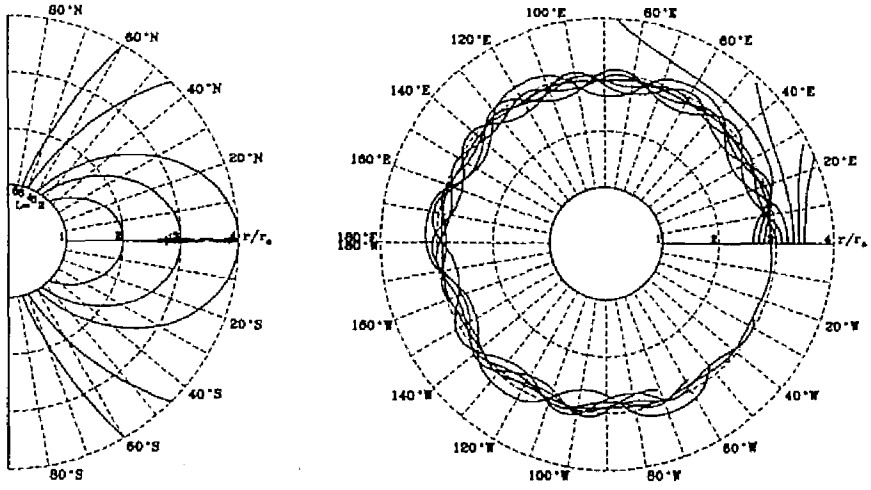

Figure 4.18: Ray paths calculated by ray tracing method. Each ray path is initiated from the geomagnetic equator at an L-value from 2.6 to 3.5 with its wave normal direction nearly perpendicular to the geomagnetic meridian plane, while the width of the plasmapause is assumed to be $0.2R_{\mathrm{E}}$. The frequency of the wave is equal to the proton cyclotron frequency at the start point.

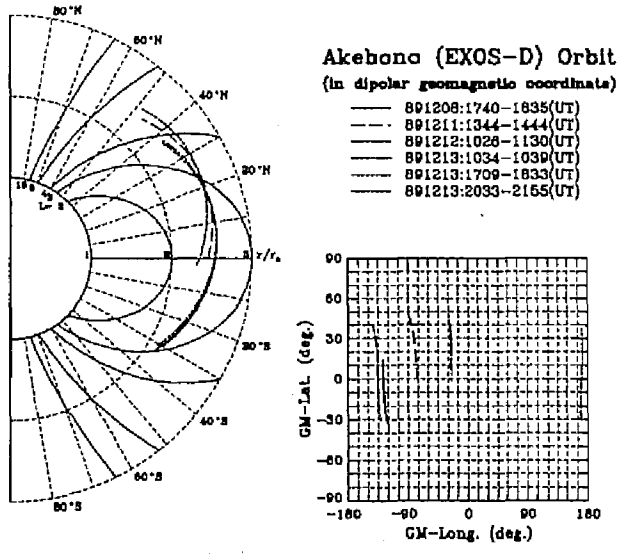

Figure 4.19: Six trajectories of the Akebono satellite from December 8 to 13, 1989.

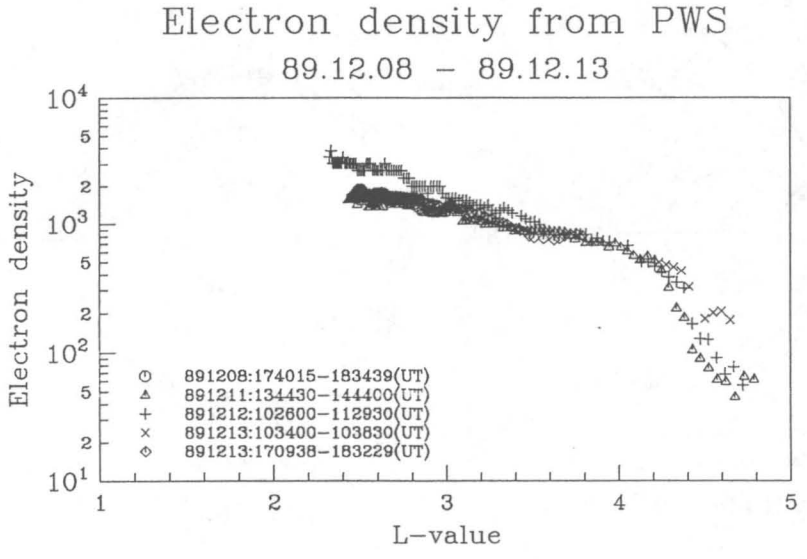

Figure 4.20: Electron density versus L-value observed along the 5 trajectories of the Akebono satellite indicated in Figure Figure 4.19

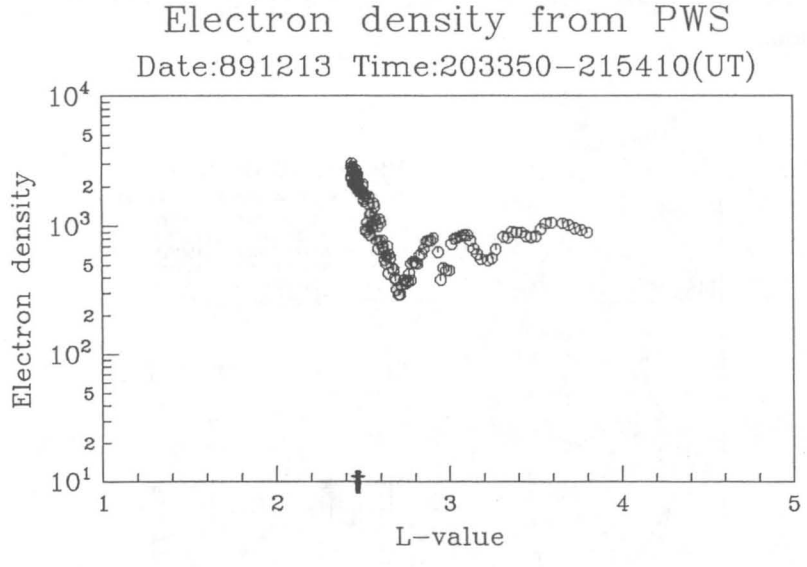

Figure 4.21: Electron density versus L-value observed along the trajectory of the Akebono satellite from 2033 to 2155 UT on December 18, 1989. The dagger mark on the transverse axis indicates the location where the ELF emissions were simultaneously observed.

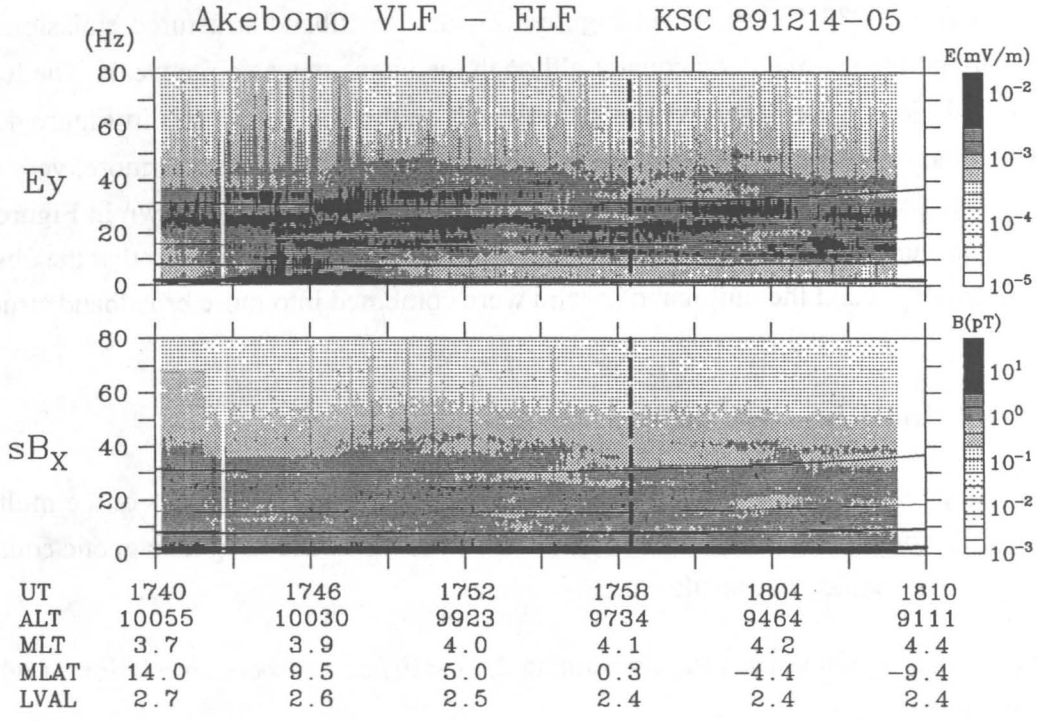

Figure 4.22: An f-t diagram of the ELF emissions observed on December 14, 1989. The vertical dashed line indicates the location of the geomagnetic equator. The thick solid lines indicates the local f_{cH^+}, f_{cHe^+} and f_{cO^+}, respectively. The thin solid line indicates $0.5 f_{cH^+}$.

In order to confirm this mechanism, it is necessary to investigate the relation between the occurrence probability of the emissions and the location of the plasmapause or an existence of sharp density gradients at the L-value around 3 in the equatorial region. We have not yet study the relation statistically, but here we show one observational example which supports our suggestion.

Figure 4.19 shows 6 trajectories of the Akebono satellite from December 8 to 13, 1989. It is found that the Akebono satellite was orbiting along the nearly the same trajectory at an altitude around 10,000 km for these days. Figure 4.20 shows in-situ electron densities versus L-value of the observation point along the former 5 trajectories and Figure 4.21 shows electron density for the last trajectory from 2033 to 2155 UT on December 13, 1989. In Figure 4.20, it is found that electron densities for those passes are almost same and smoothly decreases as L-value increases. As for the ELF data observed during this period, no ELF emission was observed around the geomagnetic equator for these passes. However, just two hours after the last pass

(1709 - 1833 UT on December 13 in Figure 4.20), electron density profile suddenly changes for the orbit from 2033 UT shown in Figure 4.21, and multiband structured emissions were observed around the geomagnetic equator although the intensity was quite weak. The location where the emissions were observed is also indicated on the transverse axis in Figure 4.21. It is important that the location is just inside the steep density gradient. Furthermore, very strong and complicated structured emissions were observed on the next day as shown in Figure 4.22. The emissions were still observed on December 18 (see Figure 4.8) in the way that the observed region was localized and the multiband spectra were combined into more broadband structure.

4.5 Discussions and conclusions

In the present paper, we have studied in detail the propagation characteristics of the multiband structured emission, often observed by the Akebono satellite around the geomagnetic equatorial region. Here we conclude our results.

1. The refractive index was roughly estimated. It satisfies a dispersion relation of whistler mode wave.

2. Wave normal directions were determined by the WDF method. Is was found that more than two waves often coexisted, and their wave normal directions were nearly perpendicular to the geomagnetic meridian plane. That is, they were propagating in the azimuthal direction nearly on the equatorial plane.

3. In order to support the observational results, a three-dimensional ray tracing study was made in a cold plasma model including the effects of multicomponent ions. We suggest that a propagation perpendicular to the geomagnetic meridian plane is possible as a result of a density gradient such as plasmapause. Around the plasmapause region, waves with their frequencies below f_{LHR} are trapped between the edges of a density gradient and propagate around the plasmapause in a low latitude region.

The generation mechanism of the emissions must be discussed. *Perraut et al.* [1982] suggested that the energy source is the 5 to 30 keV ion portion of the plasma sheet, or ring current. On the other hand, *Curtis and Wu* [1979] discussed that several kinds of MeV ions such as H^+, He^+, O^+, O^{2+}, and O^{3+} in the plasmasphere which have strong pitch angle anisotropy can give rise to emissions at frequencies near the harmonics of the ion cyclotron frequencies. In addition, they proposed that the emissions are confined just below the ion cyclotron harmonics, and the

growth rate is so small that the waves must travel a significant distance for reasonable amplification to take place under the condition of constant geomagnetic field intensity. In this sense, the most favorable propagation condition is an azimuthal propagation. The scenario discussed by *Curtis and Wu* [1979] appears to show a good agreement with our result.

In order to confirm our suggestion further, statistical study on the relation between the plasma profile and occurrence probability of the emissions are required. Although the ion mass spectrometer and low-energy particle analyzer could not have measured particle distribution correctly in the equatorial region, radiation monitor (RDM) on board the Akebono satellite was measuring energetic particles in the energy range of MeV and comparison these data with wave data is left as a future study. For the generation mechanism, ray tracing study in a hot plasma model will be also useful.

Chapter 5

VLF Emissions Observed in the Polar Region

5.1 Introduction

By frequent passages above the auroral zone, the Akebono satellite has provided us with ample data of wave and particles around the region [*Kimura et al.*, 1990]. A typical wave phenomenon, auroral hiss, has been studied in relation to the precipitating electrons by many authors (cf. appropriate review of hiss phenomena was recently made by *Sazhin et al.*, [1993]).

Occurrence map of the auroral hiss observed by ISIS satellite was studied by *Ondoh* [1988], and the contour map of the occurrence rate is found to be very similar to the occurrence location of inverted-V electron precipitation; the low-latitude boundary and axial symmetry of the 10-22 hour geomagnetic local time meridian [*Ondoh*, 1990]. In this chapter, a similar statistics are made for V-shaped hiss and saucer emissions using the data obtained by the Akebono satellite and their propagation characteristics are discussed [*Kasahara et al.*, 1995].

The auroral hiss is thought to be generated by Cérenkov radiation and coherent amplification mechanism by beaming electrons and correlation between VLF wave and energetic electrons are discussed using observed data or computer simulations by many authors [*Kimura*, 1971; *Maggs*, 1976; 1978; *Yamamoto*, 1979; *Kumagai et al.*, 1980; *Matsumoto et al.*, 1981; *Lotko and Maggs*, 1981; *Maggs and Lotko*, 1981]. When considering low energy (< 1 keV) electron interaction with whistler mode waves, the mechanism described above appears to be dominant with respect to the instabilities corresponding to higher cyclotron harmonics as in the case of incoherent whistler mode radiation. It was assumed that the wave normal angle of a propagating wave lies close to the resonance cone angle where the Cérenkov interaction between electrons and

whistler mode wave is most effective. In order to confirm the above mechanism, it is necessary to observe their wave normal vector directions. However, so far no detailed observation has been done for their wave normal direction although upward or downward direction of Poynting flux for V-shaped hiss and saucer emission was identified by Injun-5 [*Gurnett et al.*, 1971]. They found that downgoing V-shaped hiss and upgoing saucer emissions were observed at an altitude of 2,000 km. As for the observation by the S-310JA-5 rocket, it is found that auroral hiss observed at an altitude between 200 km and 230 km was propagating downward with a large wave normal angle to the geomagnetic field line [*Kimura et al.*, 1981; *Kimura and Matsuo*, 1982]. On the other hand, on board the DE 1 satellite, *Gurnett et al.* [1983] observed funnel-shaped auroral hiss emissions at a radial distance between about 2 and 5. They suggested that the radial distance of the low-altitude boundary of the source is between 1.7 and 1.9 R_E and the hiss is propagating upward. The frequency spectra of the emissions were interpreted by ray tracing as upgoing coherent Cérenkov radiation due to an upgoing beam of low-energy electrons.

5.2 Occurrence probability of auroral hiss

Figure 5.1 shows one example of V-shaped hiss observed by a wide band analyzer (WBA) on board the Akebono satellite on September 9, 1990, when WBA was measuring magnetic field. A sharp cutoff above 11 kHz on the figure is due to a low pass characteristics of WBA. According to the observation by the PWS instrument [*Oya et al.*, 1990]., the frequency of this V-shaped hiss extended up to a few hundreds kHz (private communication, *Oya et al.*).

For a statistical study of the occurrence rate of the V-shaped hiss, we have used 696 passes, tracked at Prince Albert, Canada, over one year of 1992, when the WBA was measuring electric field by a 60 m tip-to-tip wire antenna. The WBA data of magnetic field data were not used for the statistical study because the auroral hiss is quasi-electrostatic and therefore the magnetic wave field has often only comparable intensity with the noise level of the WBA. Figure 5.2 illustrates the occurrence rate of the V-shaped hiss as functions of observed altitude and magnetic local time for three geomagnetic latitude ranges; lower than 55°, between 55° and 70°, and above 70°from the top to the bottom. The darkest region corresponds to an occurrence probability of more than 50%. The completely white region corresponds to where the number of orbits passing there is less than 5.

Comparing this figure with the occurrence map for ISIS reported by *Ondoh* [1990] and a map of Inverted-V events after *Hoffman and Lin* [1981], a similar feature is seen; especially for the latitudes higher than 70°, one occurrence peak is around 8 hrs to 10 hrs and the second after

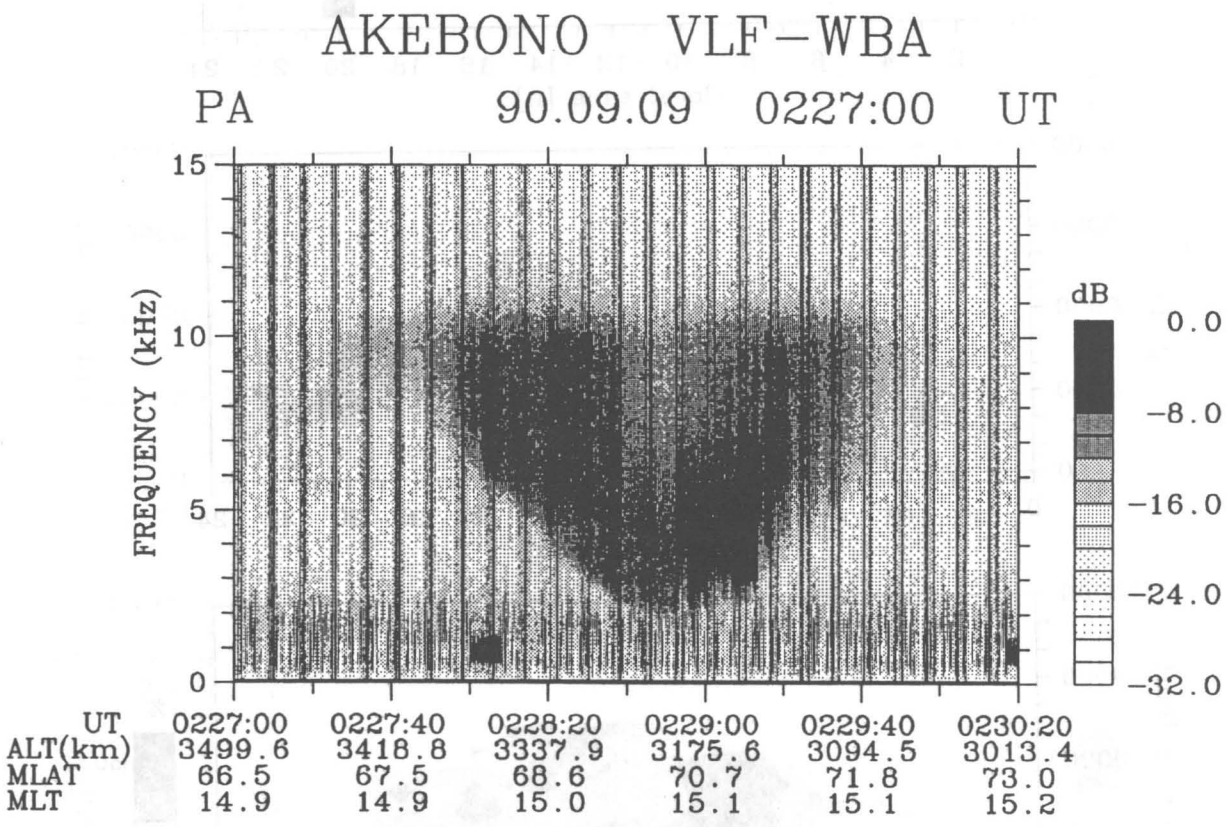

Figure 5.1: One typical example of dynamic spectrum of V-shaped hiss observed on September 9, 1990 (0 dB = 1.88 pT).

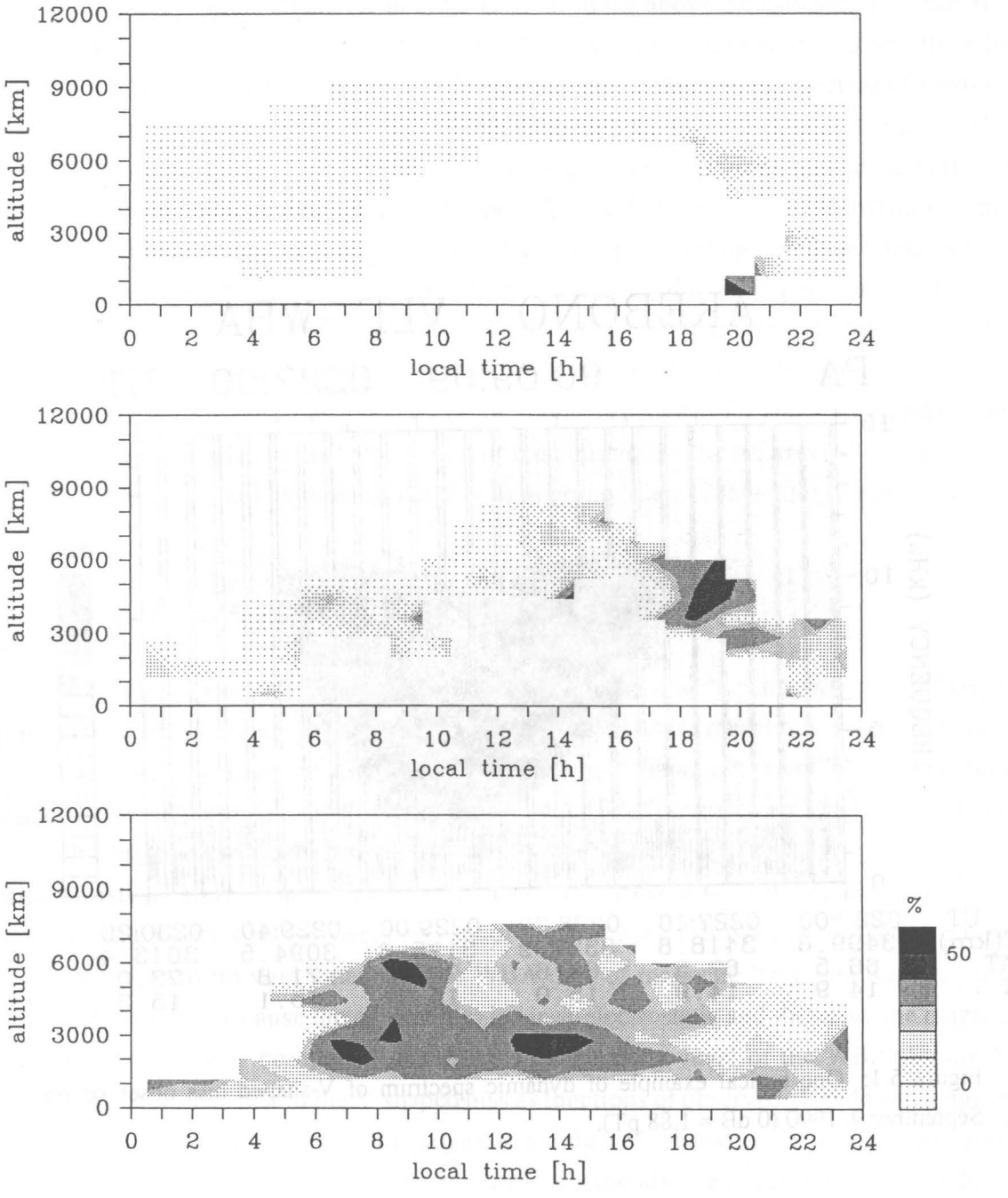

Figure 5.2: Occurrence rate of V-shaped hiss as functions of observed altitude and magnetic local time for three geomagnetic latitude ranges; from the top to the bottom, below 55°, between 55 and 70°, and above 70°, respectively.

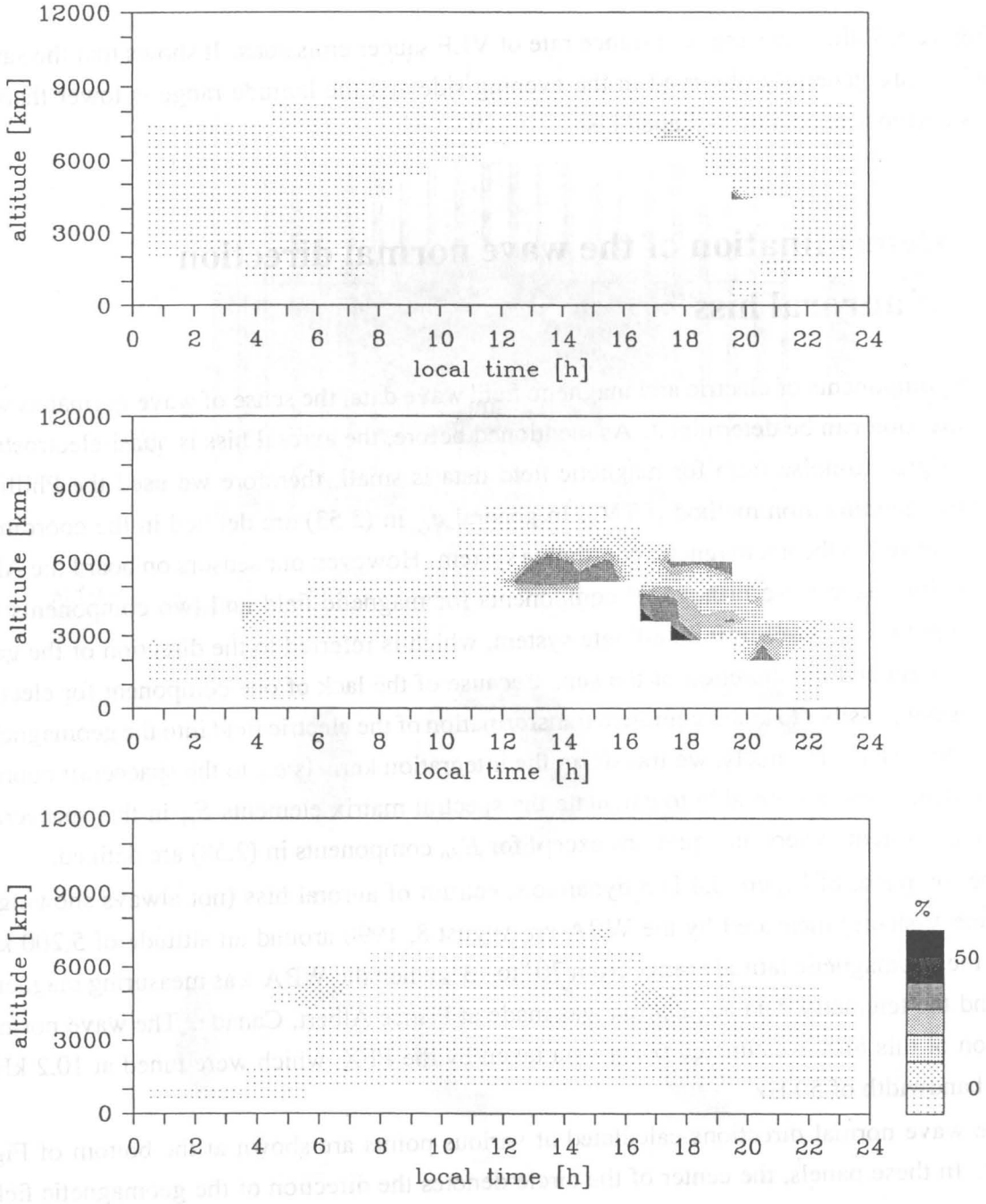

Figure 5.3: Occurrence rate of saucer emissions as functions of observed altitude and magnetic local time for three geomagnetic latitude ranges; from the top to the bottom, below 55°, between 55 and 70°, and above 70°, respectively.

13 hrs.

Figure 5.3 illustrates the occurrence rate of VLF saucer emissions. It shows that the saucer emissions are generally observed in the evening side and the latitude range is lower than the high occurrence region of V-shaped hiss.

5.3 Determination of the wave normal direction of auroral hiss

Using 5 components of electric and magnetic field wave data, the sense of wave normal as well as the direction can be determined. As mentioned before, the auroral hiss is quasi-electrostatic and the signal-to-noise ratio for magnetic field data is small, therefore we used the Phillips-Tikhonov reguralization method (PTM). In general a_{ij} in (2.53) are defined in the coordinate system referred to the geomagnetic coordinate system. However, our sensors on board the Akebono satellite have three orthogonal components for magnetic field and two components for electric field in the spacecraft coordinate system, which is referred to the direction of the geomagnetic field and the direction of the sun. Because of the lack of one component for electric field, it is not possible to attain complete transformation of the electric field into the geomagnetic coordinate system. Inversely, we transform the integration kernels a_{ij} to the spacecraft coordinate system. Now we are able to calculate the spectral matrix elements S_{ij} in this spacecraft coordinate system, where all equations except for E_{Z_0} components in (2.58) are defined.

The top panel of Figure 5.4 is a dynamic spectrum of auroral hiss (not always showing a complete V-shape) measured by the WBA on August 8, 1990 around an altitude of 5,200 km and in the geomagnetic latitude range from 70° to 73°, when the WBA was measuring magnetic field and the telemetry data acquisition was made at Prince Albert, Canada. The wave normal direction of this hiss is estimated using data taken by the PFX, which were tuned at 10.2 kHz with a bandwidth of 50 Hz.

The wave normal directions calculated at various points are shown at the bottom of Figure 5.4. In these panels, the center of the circle denotes the direction of the geomagnetic field and the wave normal angle (ψ) is shown by a radial distance from the center (0° to 90°), and the azimuthal angle (η) is shown along the periphery of the circle.

It is interesting to note in Figure 5.4 that the wave normal direction is downgoing in the northern hemisphere, that the wave normal angle is always close to 90°, and that the wave normal vector is directed radially outward in the geomagnetic meridian plane before the location of the

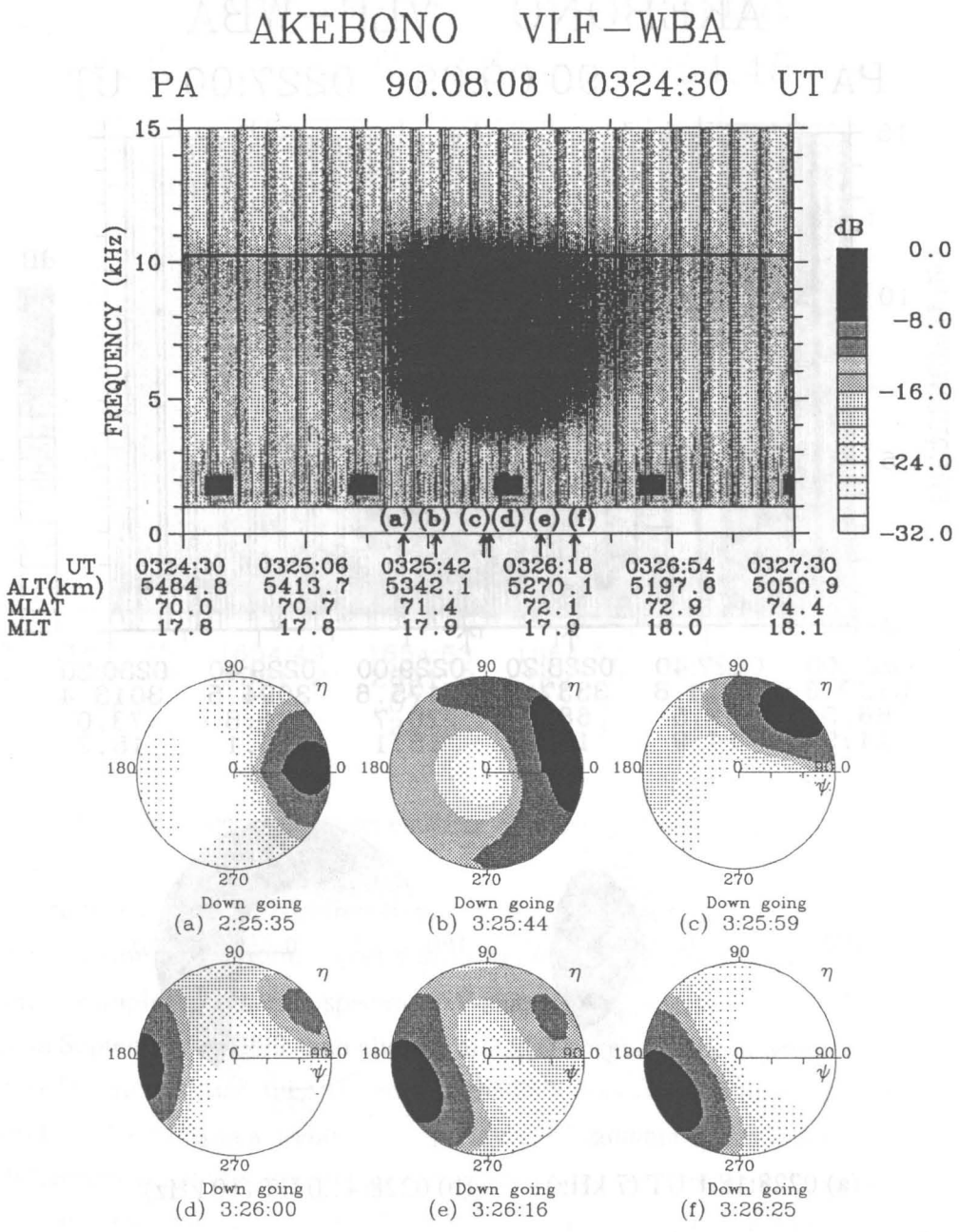

Figure 5.4: The top panel shows a dynamic spectrum of V-shaped hiss observed on August 8, 1990 (top panel: 0 dB = 1.88 pT). The wave normal directions at 6 different instants from (a) to (f) at 10.2 kHz (the solid line in the top panel) are shown in the bottom panels.

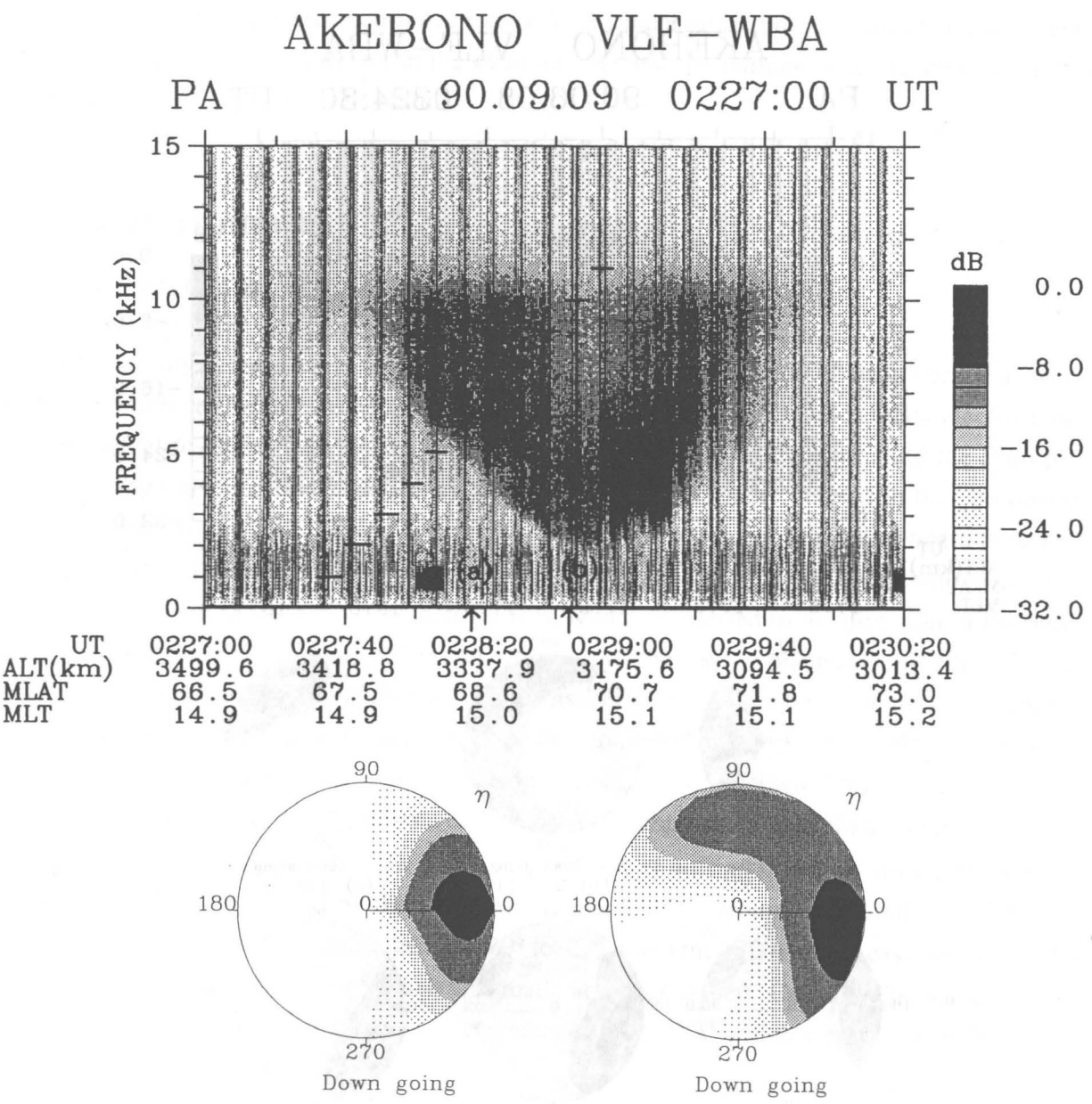

(a) 0228:18.1 UT (7 kHz) (b) 0228:41.0 UT (10 kHz)

Figure 5.5: A dynamic spectrum of V-shaped hiss observed on September 9, 1990 (same as Figure 1: 0 dB = 1.88 pT) and the wave normal directions at two different instants (a) and (b) observed on September 9, 1990 are shown in the two bottom panels. The solid lines in the top panel show the tuned frequencies of the PFX.

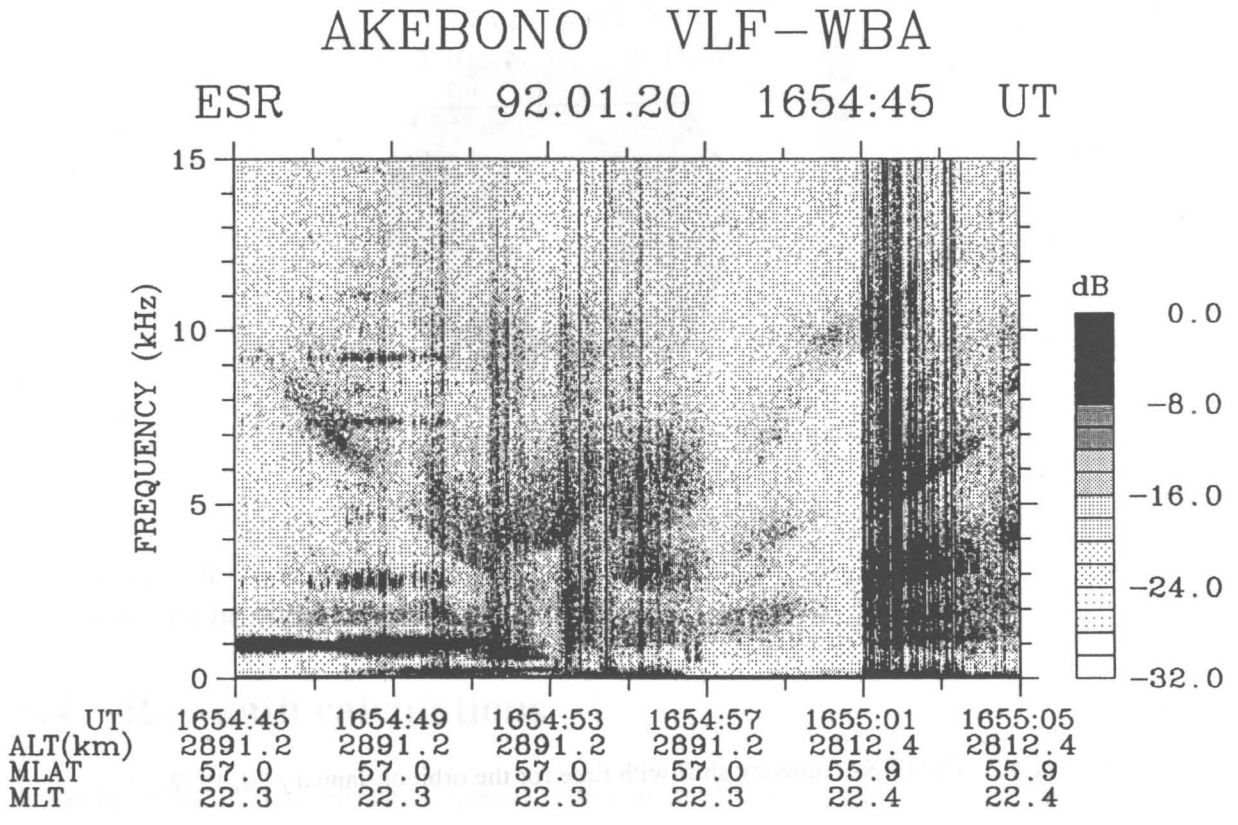

Figure 5.6: A dynamic spectrum of saucer emission observed on January 20, 1992 (0 dB = 2.0 mV/m).

V-shaped frequency minimum (corresponding to the lower latitude side) and after this location (higher latitude side) wave normal vector turns to the radially inward direction.

Another example of dynamic spectra of V-shaped hiss is shown in Figure 5.1, which was observed on September 9, 1990 at an altitude of 3,200 km and in the geomagnetic latitude range from 68° to 71°. In this case, the frequency of the PFX was swept in time like a staircase with a 1 kHz step from 1 kHz to 11 kHz as shown in Figure 5.5 with the dynamic spectrum of V-shaped hiss, each frequency staying constant for 7.5 seconds. The wave normal directions at 7 kHz and 10 kHz are analyzed in the same way as mentioned above. The direction of wave normal is displayed in the lower part of Figure 5.5 for these two frequencies. These two frequency points are located before the location of the V-shaped frequency minimum. The wave normal vector is also all directed in the vicinity of resonance cone angle and radially outward almost in the geomagnetic meridian plane. This direction of wave normal vector is identical with the first half of the August 8 event (Figure 5.4).

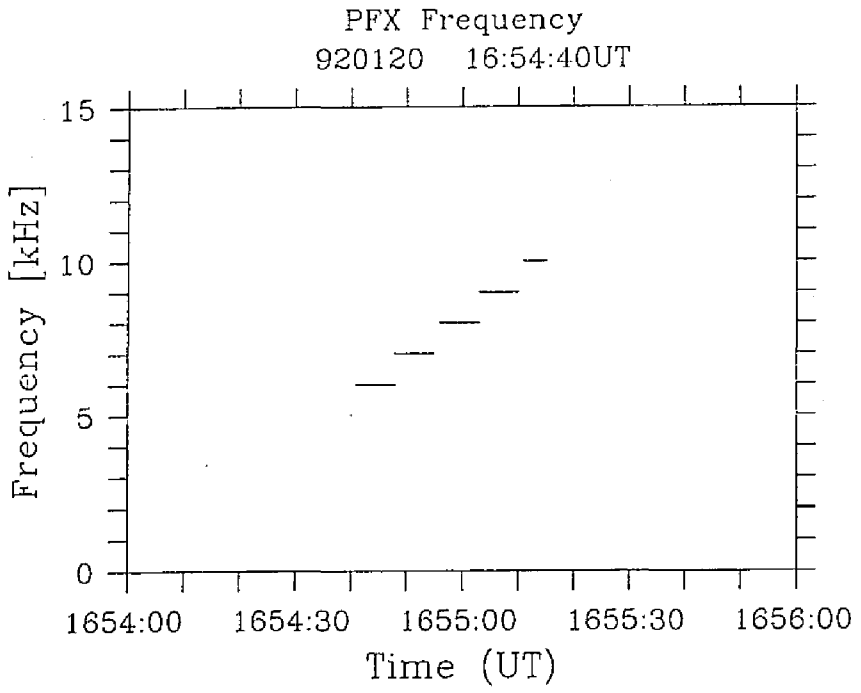

Figure 5.7: The PFX frequency shift with time for the orbit on January 20, 1992.

We examined the wave normal vector of the V-shaped hiss in several cases observed in the altitude range from 3,000 km to 5,000 km, and found that their wave normal directions were all downgoing. This characteristic feature will be studied by ray tracing in the later section.

Figure 5.6 shows a WBA dynamic spectrum of saucer emission observed on January 20, 1992 at an altitude of 2,890 km, when the WBA was measuring electric field. The frequency of the PFX on this event was changed like a staircase from 6 kHz to 10 kHz with a 1 kHz step (Figure 5.7). Figure 5.8 illustrates the diagram of wave normal vector for 1654:48 UT, when the tuned frequency of the PFX was 7 kHz. The center of the circle indicates the opposite direction of geomagnetic field, so that the corresponding wave normal angle is from 90° to 180°, which means that the wave normal vector appearing on this circle plane is going upward in the northern hemisphere.

From this example together with other examples not shown here, it was found that the wave normal vector of saucer emissions at the Akebono trajectory around 2,000 km are all directed upward with a large wave normal angle near the resonance cone angle. This feature is consistent with the previous results (e.g. *Gurnett et al*, [1971]; *Gurnett and Frank*, [1972]).

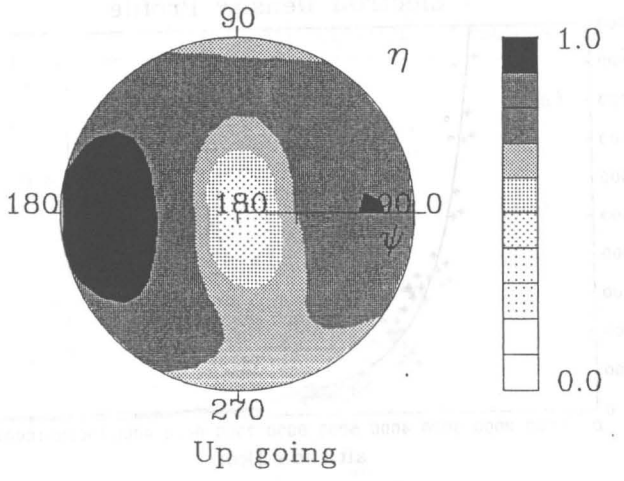

Figure 5.8: The wave normal direction of saucer emission at 1654:48 UT January 20, 1992, when the tuned frequency of the PFX was 7 kHz.

5.4 Ray path calculations

It has been found that the wave normal vector of the V-shaped hiss is radially outward in the lower latitude side with respect to the location of the V-shaped frequency minimum, whereas it is radially inward in the higher latitude side. Now we try to do ray tracing starting from the source region down to the Akebono trajectory, in order to see such a feature can be realized.

As to the electron density profile to be used for ray tracing, we have made a profile as shown in Figure 5.9. In the figure, the symbols "o" indicate in-situ electron density provided by the PWS instrument (private communication, *Oya et al.*) for several trajectories in the geomagnetic latitude range between 60° and 70° in the magnetic local time range between 6 hrs and 18 hrs. The symbols "+" added to "o" indicate electron densities observed on September 9 event. A smooth solid curve in the figure is a profile which is fitted by the collisionless (CL) model.

5.4.1 Ray tracing for the V-shaped hiss emissions

As was suggested by *Gurnett et al.* [1983] (see Fig.10 in their paper), auroral hiss propagates along almost a geomagnetic field line especially in the lower frequency range, we assumed that the source region was located at somewhere along a geomagnetic field line on which the V-shaped frequency minimum was observed by the satellite. As the V-shaped hiss was assumed

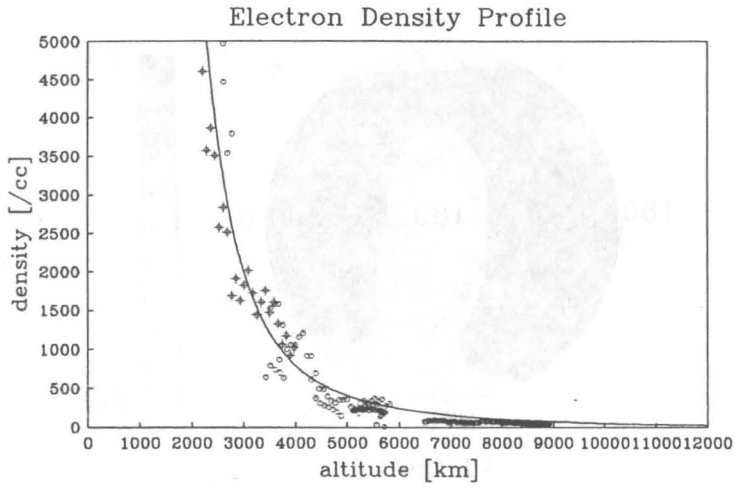

Figure 5.9: The electron density profile used for ray tracing is shown by a solid line. The symbols "o" indicate in-situ electron densities for several trajectories of the Akebono satellite in the geomagnetic latitude between 60° and 70° and in the magnetic local time between 6 hrs and 18 hrs. The symbols "+" show the electron densities observed on September 9, 1990.

to be propagating downward from the results of the WDF analysis, we changed initial altitude for ray tracing by a 1,000 km step and examined a frequency versus time curve to be observed along the Akebono trajectory for each case. In this way, we can estimate the upper altitude limit of the source region of the V-shaped hiss because ray paths for higher frequency range deviate from the geomagnetic field line at the source point and therefore the width of V-shape depends on the altitude of the source.

At first, the best fit ray tracing result for the V-shaped hiss observed on September 9, 1990 is represented. The three dimensional ray tracing of the V-shaped hiss for September 9 event was performed from an altitude of 12,000 km and geomagnetic latitude of 62.1° with initial wave normal vector being directed circularly symmetric with respect to the geomagnetic field line, the wave normal angle is set to be the resonance cone angle there and the azimuthal angle is distributed from 0° to 360° by a 3° step. A result of the ray tracing is shown in Figures 5.10 (a)-(c). Figure 5.10 (a) indicates a frequency versus time curve to be observed along the Akebono trajectory on September 9, which was located at an altitude around 3,200 km. The result shows a good agreement with the lower bound frequency of the V-shaped hiss shown in Figure 5.1 or Figure 5.5.

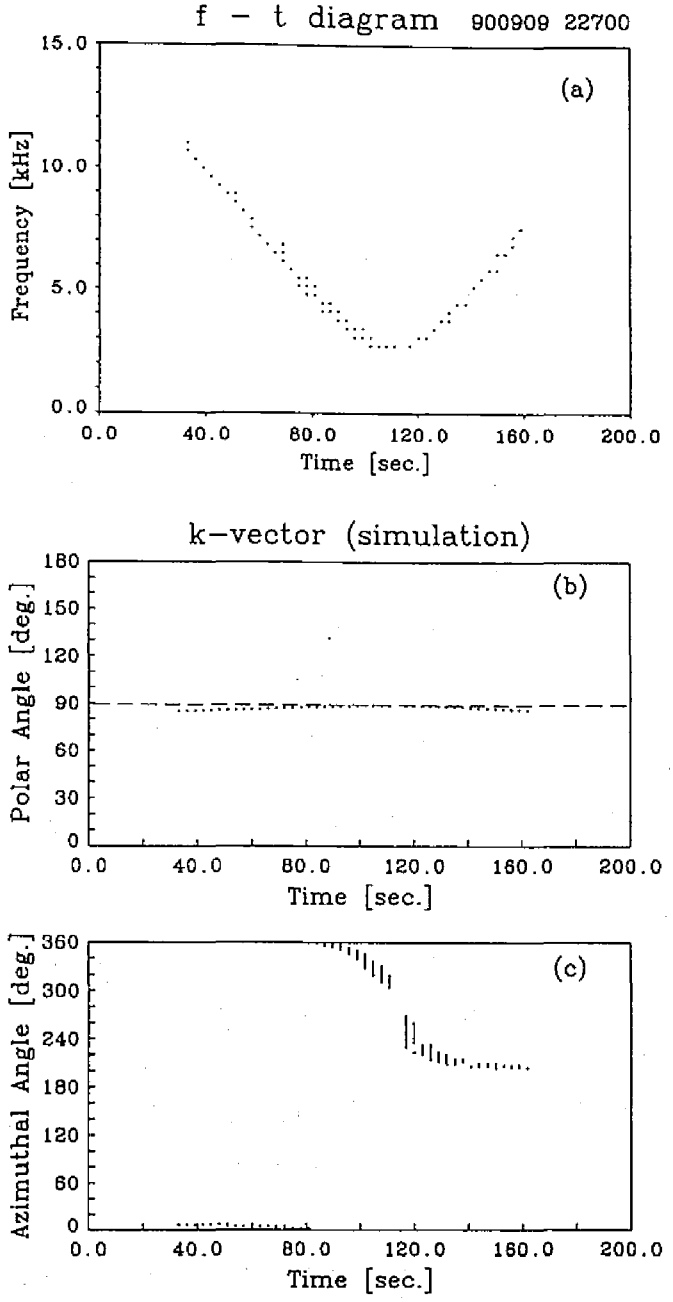

Figure 5.10: The results of ray tracing for the V-shaped hiss observed on September 9, 1990. (a) Frequency versus time curve to be observed along the Akebono orbit (at an altitude around 3,200 km). (b) (c) Polar and azimuthal angle of the wave normal direction along the orbit.

Figures 5.10 (b) and (c) show the polar angle (i.e. wave normal angle) and the azimuthal angle of wave normal vector along the trajectory. The polar angle is nearly the resonance cone angle, and the azimuthal angle of wave normal vector is directed radially outward in the first half, which corresponds to the lower latitude side with respect to the V-shaped frequency minimum, and radially inward in the second half of the trajectory.

The next example of ray tracing shown in Figures 5.11 (a)-(c) is made to simulate the August 8 event (Figure 5.4), which does not show a sharp V-shape as compared with the September 9 event (Figure 5.5). The location of the wave source is located at an altitude of 11,500 km and the source meridian is deviated by 1.5° from the spacecraft meridian at the time when the emission frequency shows minimum. (We changed the source meridian by a 0.5° step to investigate the best fit for the observation spectrum.) The observation points are assumed to be along the Akebono trajectory on August 8, which is located at an altitude around 5,200 km. It is evident that the V-shape of Figure 5.11 (a) also shows a good agreement with the envelope of dynamic spectrum of Figure 5.4. The longer is the deviation distance from the spacecraft meridian to the source, the larger the non-sharpness of the V-shape results in.

The wave normal direction obtained by ray tracing in this case is shown in Figures 5.11 (b) and (c). The characteristic features of the polar angle and azimuthal angle are the same as those shown in Figures 5.10 (b) and (c) from the point of view that wave normal vector is always downward in the hemisphere, and is directed radially outward in the first half, corresponding to lower latitude side, whereas it is directed radially inward in the second half, corresponding to the higher latitude side.

It is also important to note that the width of the V-shape, that is, the duration of the emissions shown in Figure 5.11 (a) is almost the same as Figure 5.10 (a), although the altitude of the observation point is about 2,000 km higher than the former case. It is because the ray path mostly deviates from the geomagnetic field line at the higher altitude where less electron density exists. That is, the extent of width of V-shape almost depends on the electron density near the wave source.

The above characteristics are obtained for a fixed source altitude, e.g. 12,000 km. In the most actual dynamic spectra of V-shaped hiss the inside of the lower frequency bound of the V-shaped envelope is completely filled by emissions. This feature can be realized when a line source from the top continuously down to the spacecraft location exists, and we can get a similar characteristics of wave normal vector shown in Figures 5.10 (b) and (c) or Figures 5.11 (b) and (c), though the width of the V-shape becomes narrower when the source approaches the observation point. These facts will conclude that the wave normal direction actually observed

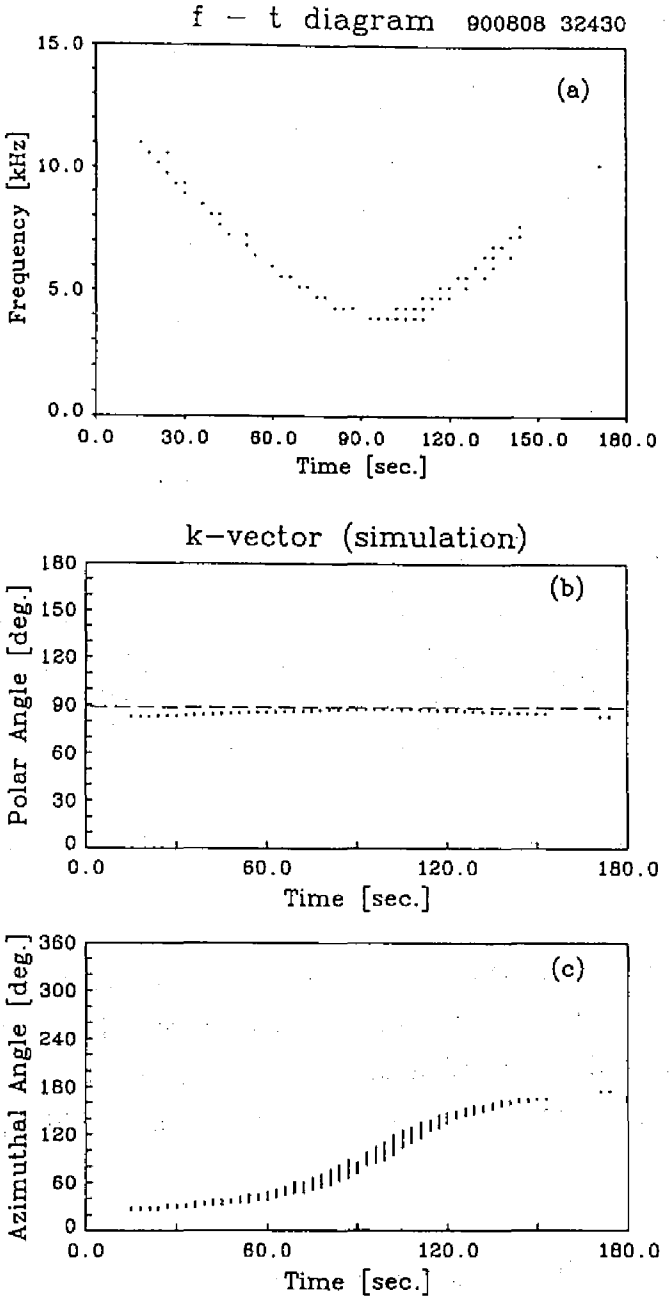

Figure 5.11: The results of ray tracing for another V-shaped hiss observed on August 8, 1990. (a) Frequency versus time curve to be observed along the Akebono orbit (at an altitude around 5,200 km). (b) (c) Polar and azimuthal angle of the wave normal direction along the orbit.

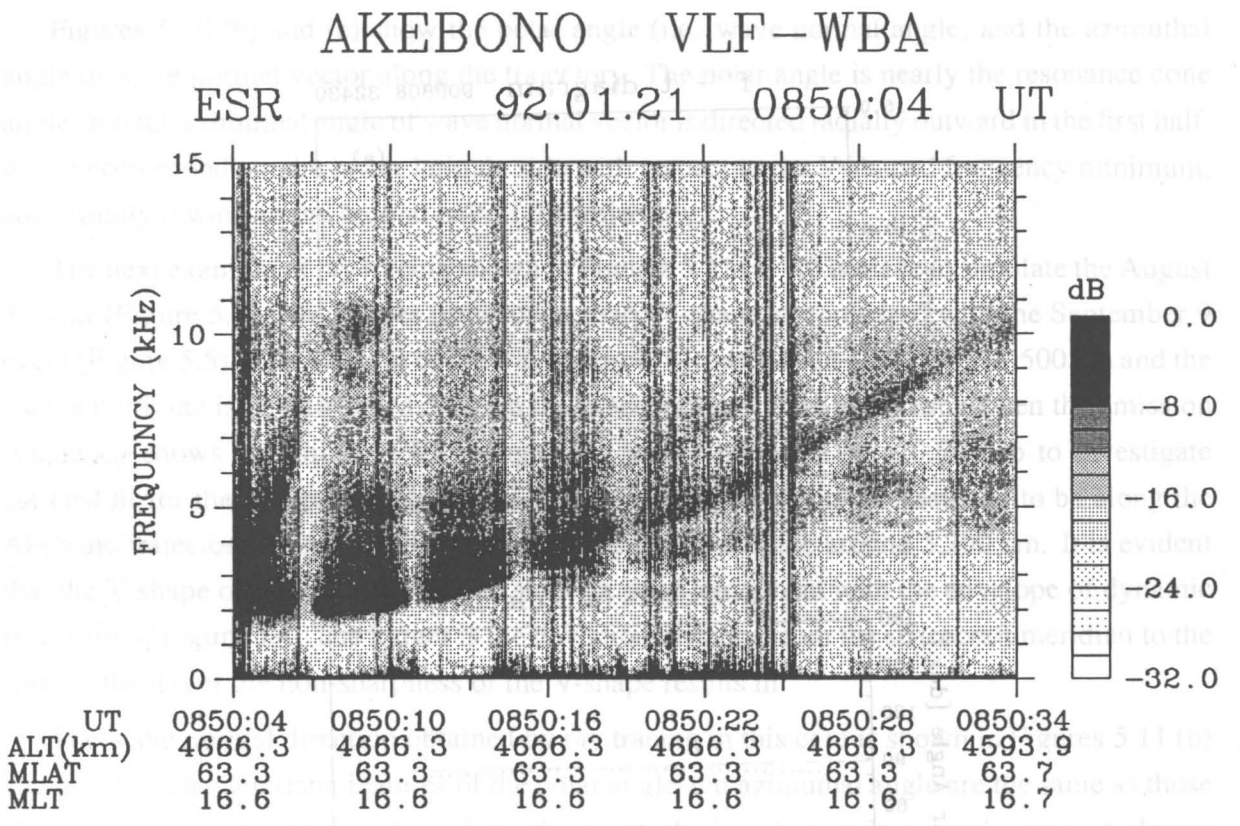

Figure 5.12: A dynamic spectrum of saucer emission observed on January 21, 1992 (0 dB = 2.0 mV/m).

at a constant frequency (say 10.2 kHz) shows a similar trend of change of wave normal vector in time shown in Figure 5.4. The observed wave normal vector and ray tracing can confirm the mechanism that the V-shaped hiss emissions are generated from an electron beam in the altitude range from more than 10,000 km down to a few 1,000 km, radiated initially with the resonance cone angle.

5.4.2 Ray tracing for the saucer emissions

In some saucer emissions the band width of the emission is larger in lower frequency (Figure 5.12). This characteristics can be realized if a line source is located across the spacecraft trajectory as shown in Figure 5.13, where the propagation region for a low frequency and a high frequency is represented by the small and large circles respectively. If a line source is extended from S_1 to S_2, the lower frequency component (denoted by B) can be observed over a wider area

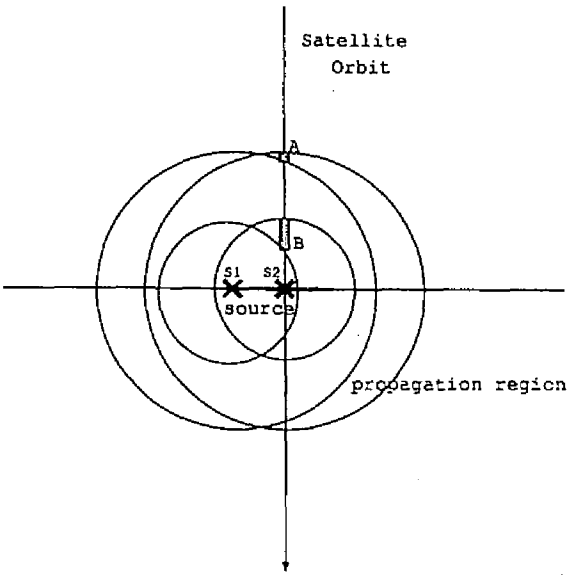

Figure 5.13: The saucer emission to be observed along a satellite trajectory when a horizontal line source is present. The thick solid line indicate the source region of saucer emission and the small and large circles indicate the propagation regions of lower and higher frequencies, respectively.

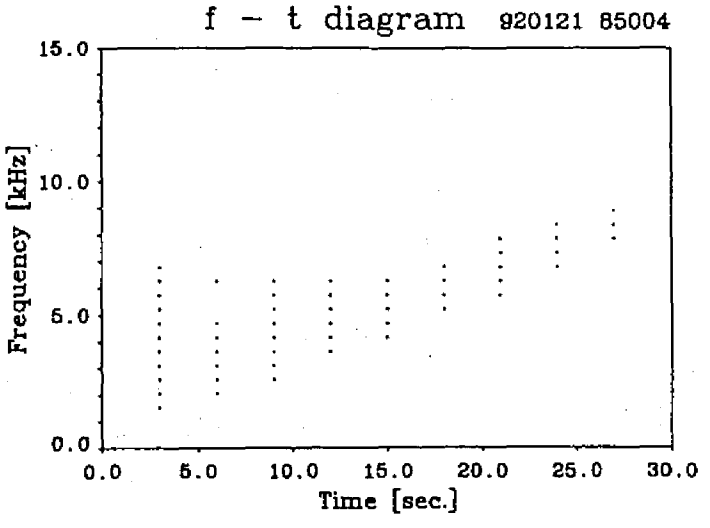

Figure 5.14: Frequency versus time curve to be observed along the orbit as a results of ray tracing for the saucer emission observed on January 21, 1992.

than the higher frequency component (denoted by A).

Figure 5.14 is a result of the ray tracing, which is started from an altitude of 2,090 km (constant) and the source is distributed in latitude from 66.6° to 67.3° in geomagnetic, for a spacecraft trajectory almost perpendicular to this line source at an altitude around 4,600 km.

5.5 Relationship of auroral hiss with low energy electrons

One example of correlation diagram is shown in Figure 5.15, between the wave measured by the multi channel analyzer (MCA) [*Kimura et al.*, 1990] and energetic electrons (energy versus time) measured by the low energy particle instrument (LEP) [*Mukai et al.*, 1990] on board the Akebono, corresponding to the August 8 event.

Just around the time from 0325:30 UT to 0326:30 UT when the frequency of lower bound of the emissions becomes minimum and where the spacecraft is supposed to pass through the region nearest from the source field line, precipitating electron beams with energies at least from a few tens to a few hundreds eV can be seen on the diagram. This is consistent with the Injun-5 observation [*Gurnett and Frank*, 1972]. Resonance condition between wave and electron is roughly estimated. The refractive index of whistler mode wave calculated by cyclotron frequency and plasma frequency at the observation point becomes a order of several hundreds if its wave normal angle is 1° less than resonance angle, therefore the wave can sufficiently resonate with precipitating electrons in the energy range between a few tens and a few hundreds eV.

As to the saucer emissions, we are not able to find any upgoing electron beam in the energy range above a few tens eV. Figure 5.16 illustrates the electron E-t diagram with the MCA wave data on January 21, 1992, when the saucer emission (Figure 5.12) was observed. This fact suggest that the electrons with energy less than a few eV may be responsible to saucer emissions, which is the same result reported by *James* [1976]. However there still remains a possibility that the saucer emissions might be generated by electrons with energies higher than a few tens of eV which were, by chance, not detected, because the source region is too small and the Akebono satellite crossed for a short time above the region as shown in Figure 5.13, or passed a little bit away from the source field line. The time resolution of the LEP instrument is 8 seconds.

5.6 Akebono-Freja conjunction study

It is difficult to tell a physical phenomenon from data observed by one satellite whether it is a temporal change, a spatial change or mixture of them. In order to study the spatial structure of the

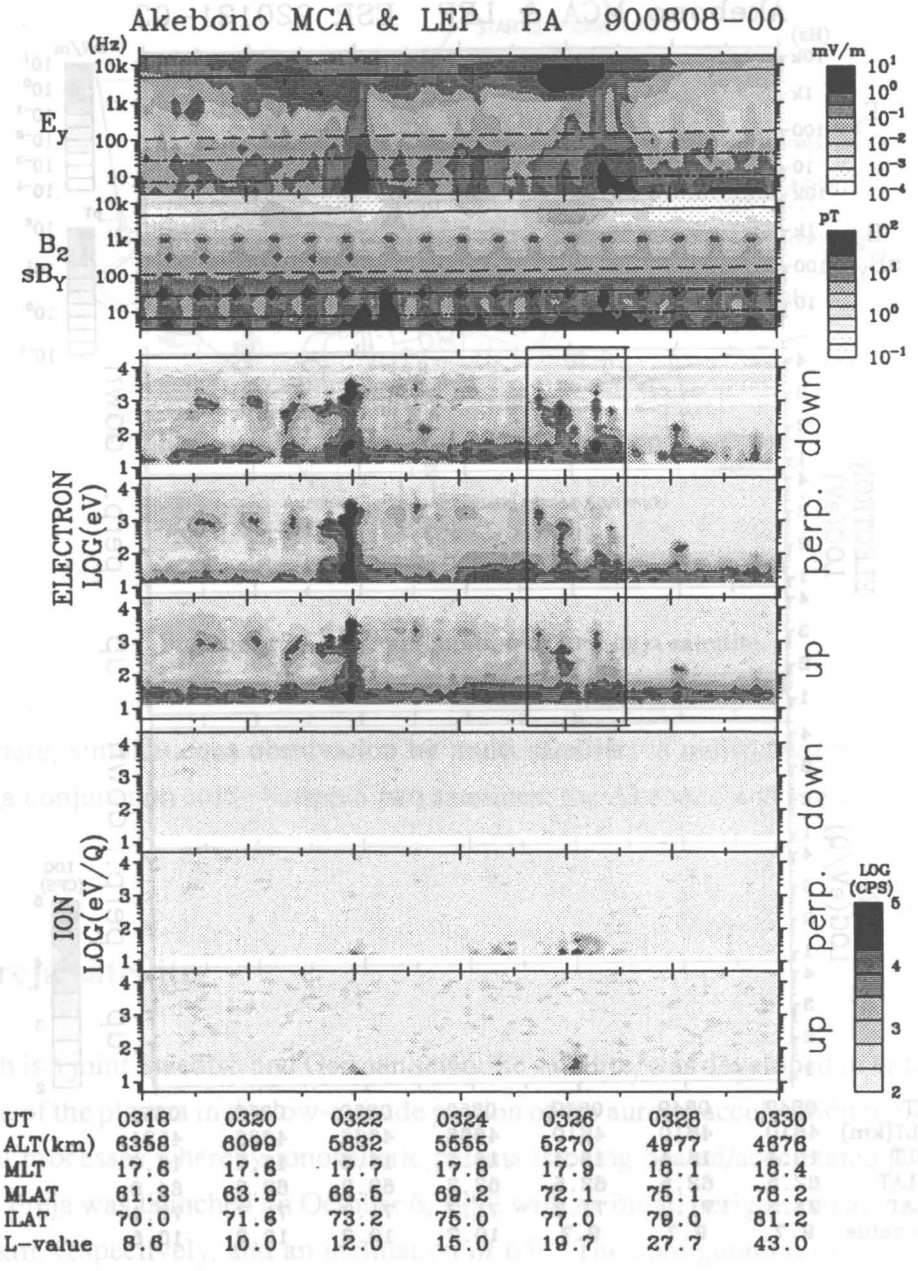

Figure 5.15: Relationship between V-shaped hiss and low energy particles observed on August 8, 1990. The top two panels show the electric and magnetic field wave spectrum. The next three panels and the bottom three panels show the pitch-angle sorted energy spectrum of electron and ion, respectively. Those panels are sorted by pitch-angle range of 0°-60° (up), 60°-120° (perp.) and 120°-180° (down).

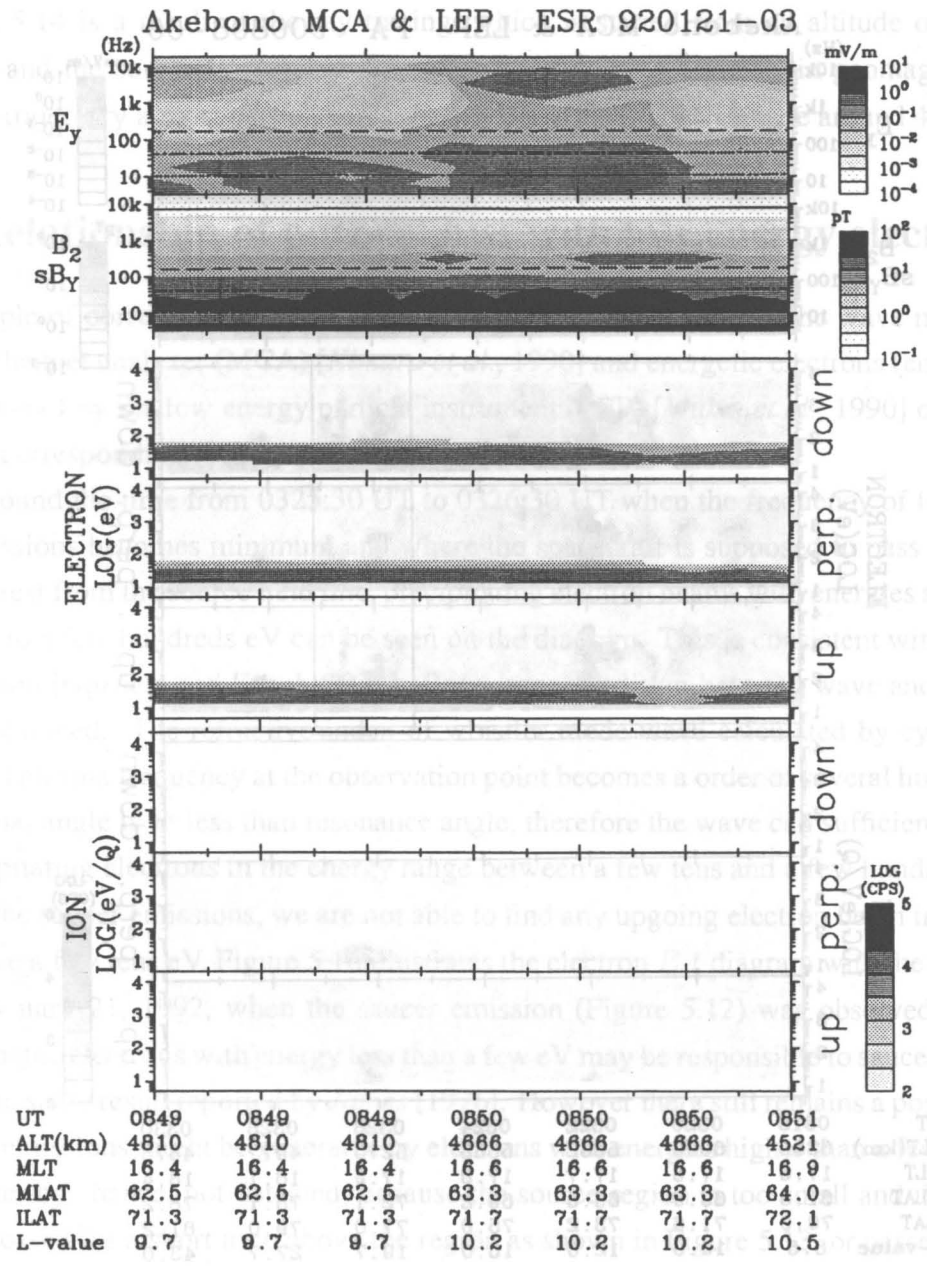

Figure 5.16: Relationship between saucer emission and low energy particles observed on January 21, 1992. The top two panels show the electric and magnetic field wave spectrum. The next three panels and the bottom three panels show the pitch-angle sorted energy spectrum of electron and ion, respectively. Those panels are sorted by pitch-angle range of 0°-60° (up), 60°-120° (perp.) and 120°-180° (down).

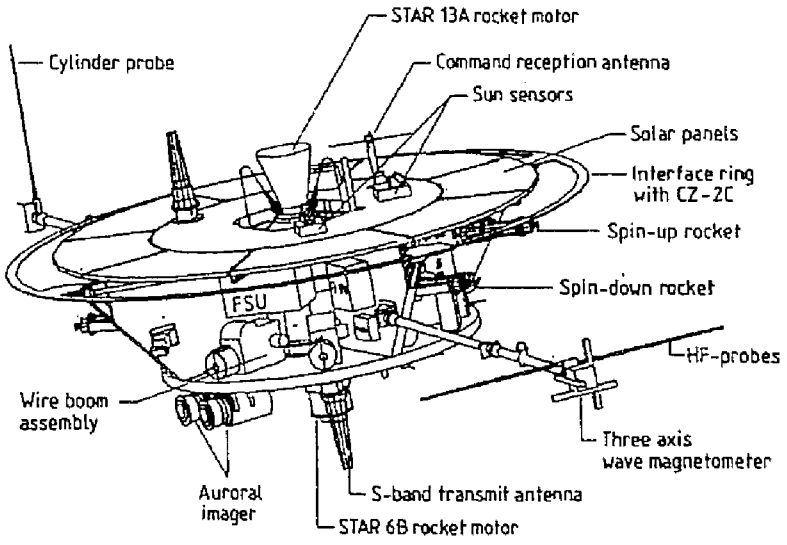

Figure 5.17: The configuration of the Freja satellite.

magnetosphere, simultaneous observation by multi-satellites is indispensable. In this section, we discuss a conjunction study between two satelliites; the Akebono and Freja satellites.

5.6.1 Freja satellite

Freja, which is a joint Swedish and German scientific satellite, was developed in order to explore the structure of the plasma in the low-altitude portion of the auroral acceleration region and study the physical processes whereby ionospheric plasma is being heated/accelerated [*Lundin et al.*, 1994]. The Freja was launched on October 6, 1992 with an initial perigee and apogee of 601 km and 1,756 km, respectively, and an inclination of 63°. The configuration of the Freja satellite is shown in Figure 5.17. The Freja satellite carries the similar instruments as those on board the Akebono satellite, such as electric and magnetic field detectors, plasma wave instruments, particle analyzers and an auroral imager.

The Freja satellite is mainly orbiting the lower part of the auroral acceleration region, whereas the observation region of the Akebono satellite is much higher, that is, in the main part of the auroral acceleration region.

Wave instruments [*Holback et al.*, 1994]

The wave instruments on board the Freja satellite (F4: Wave Experiment) is designed to measure the electric wave fields up to 4 MHz, the magnetic wave fields up to 16 kHz and the plasma density and its relative variations up to 2 kHz. Six wave signals and four density probe signals can be measured simultaneously. A distinctive feature of the instruments is that they obtain wave forms and transmit them to the ground. As the capacity of the telemetry is limited, measurements are normally made in snapshots of various intervals dependent on sampling frequency.

Particle instruments [*Eliasson et al.*, 1994; *Boehm et al.*, 1994]

In the present study, we refer the data observed by two kinds of instruments on board the Freja satellite, F3H: Hot Plasma Experiment and F7: Two-dimensional Electron Spectrometer (TESP). The F3H measures electron distributions in the energy range from 0.1 keV to 100 keV and positive ion distributions with mass identification in the energy range from 0.5 eV to 5 keV. The F7 measures two dimensional electron distribution in the energy range from 0.01 keV to 20 keV.

Using the observation data observed by the Akebono and Freja satellites, the characteristics of the V-shaped hiss are discussed in detail in the next section.

5.6.2 Observation results

There are nearly 10 conjunction passes between the Akebono and Freja satellites in 1993. Among those, 5 passes are identified as interesting events with sufficient large wave and particle activities. The locations of the two satellites are both in the northern hemisphere, and the Akebono satellite is at the higher altitude than the Freja satellite for the 3 passes. For the other 2 passes, the Akebono satellite is in the southern hemisphere and the Freja satellite is in the northen hemisphere. We introduce two cases in this section, in which fine structured V-shaped hiss were observed both by the Akebono and Freja satellites.

March 3, 1993

Figure 5.18 shows the trajectories of the Akebono and Freja satellites from 0608 UT to 0615 UT on March 3, 1993. The conjunction time when both the satellites were on the nearest magnetic field line was 0609 UT. The Akebono satellite was orbiting along the geomagnetic meridian

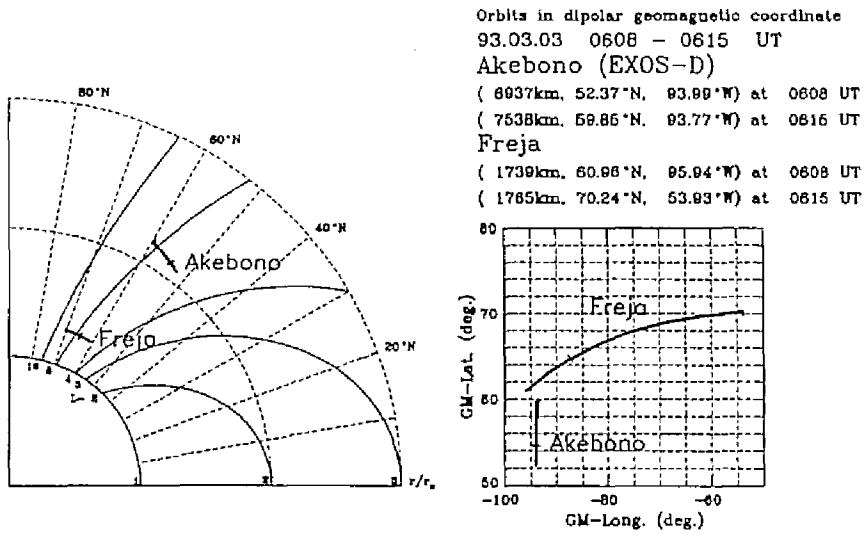

Figure 5.18: Trajectories of the Akebono satellite and the Freja satellite on March 3, 1993.

plane from lower latitude to higher latitude at an altitude of 7,300 km and the Freja satellite was orbiting across the geomagnetic meridian plane from dusk to midnight at an altitude of 1,750 km. The magnetic local time was from 19 hrs to 20 hrs.

Wave spectrum observed by the MCA and energetic particles observed by the LEP on board the Akebono satellite is shown in Figure 5.19. In Figure 5.19, a V-shaped hiss was observed from 0609 UT to 0614 UT, when the Akebono satellite was orbiting in the magnetic latitude range from 53.5° to 58.8° and the magnetic longitude range from 94.0° to 93.8°. The minimum frequency of the V-shaped hiss was about 0.5 kHz at 0612 UT. As for the particle data, energetic electrons in the energy range around a few keV, which are assumed to be accelerated by potential structure, were simultneously observed.

Figure 5.20 shows the wave spectrum of electric field observed by the Freja satellite. In Figure 5.20, we can find that a V-shaped hiss was also observed from 0608 UT to 0612 UT, when the Freja satellite was orbiting in the magnetic latitude range from 61.0° to 67.8° and the magnetic longitude range from 95.9° to 75.9°. The minimum frequency of V-shape was about 2 kHz at 0610 UT. This V-shaped hiss is assumed to be propagating from the same origin with that observed by the Akebono satellite. Comparing with the trajectories of the Akebono and Freja satellites, it is found that the observed region of the V-shaped hiss is located at eastern side of the Akebono trajectory, thus the source region is assumed to be located at eastern side of the Akebono trajectory.

Figure 5.21 shows the energetic particles corresponding to the V-shaped hiss observed by

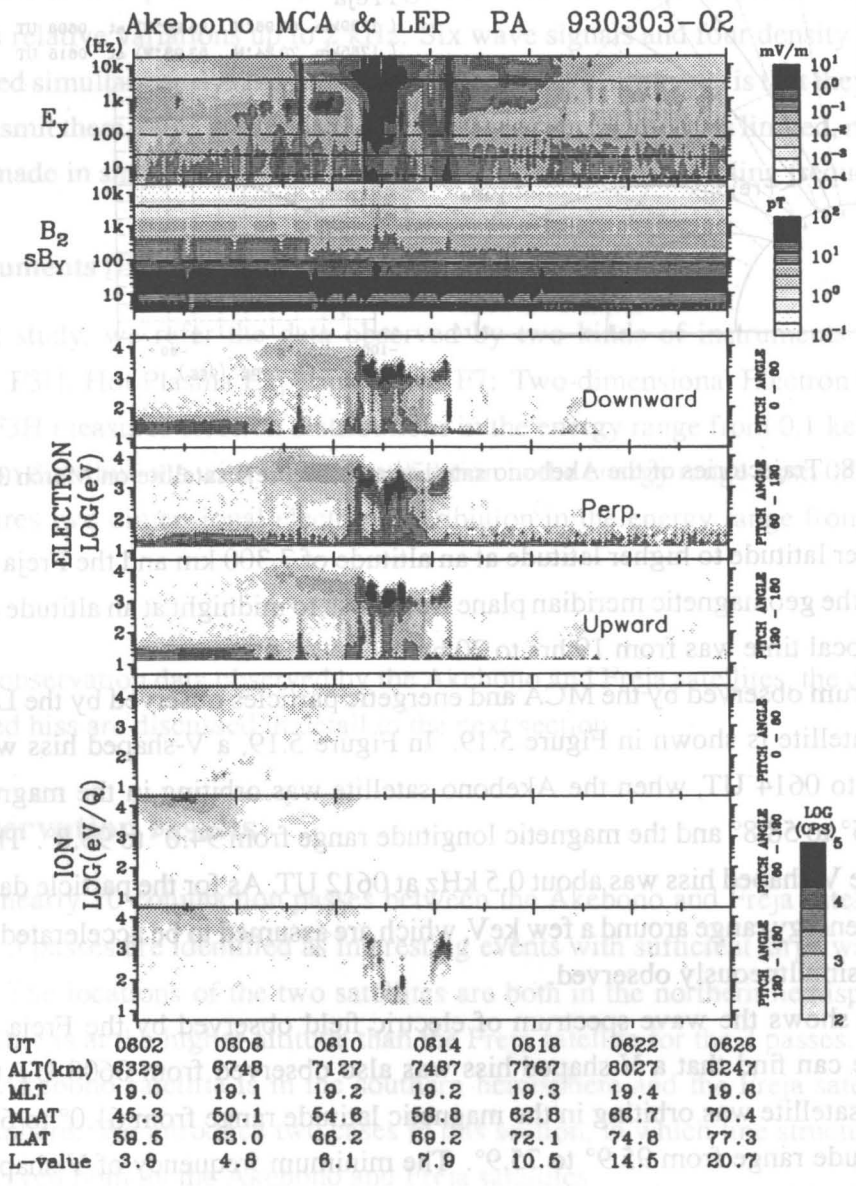

Figure 5.19: An f-t diagram of the V-shaped hiss and an E-t diagram of low energy particles observed by the Akebono satellite on March 3, 1993.

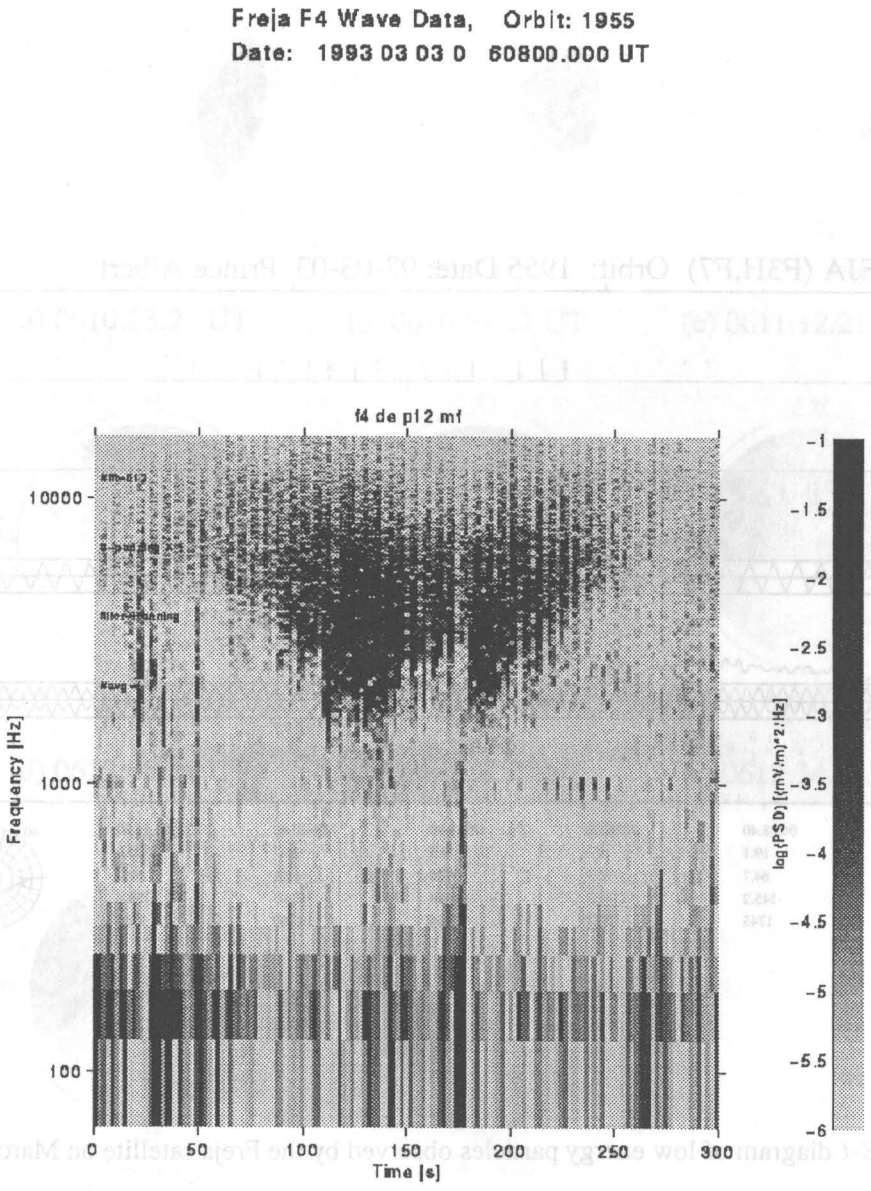

Figure 5.20: An f-t diagram of the V-shaped hiss observed by the Freja satellite on March 3, 1993.

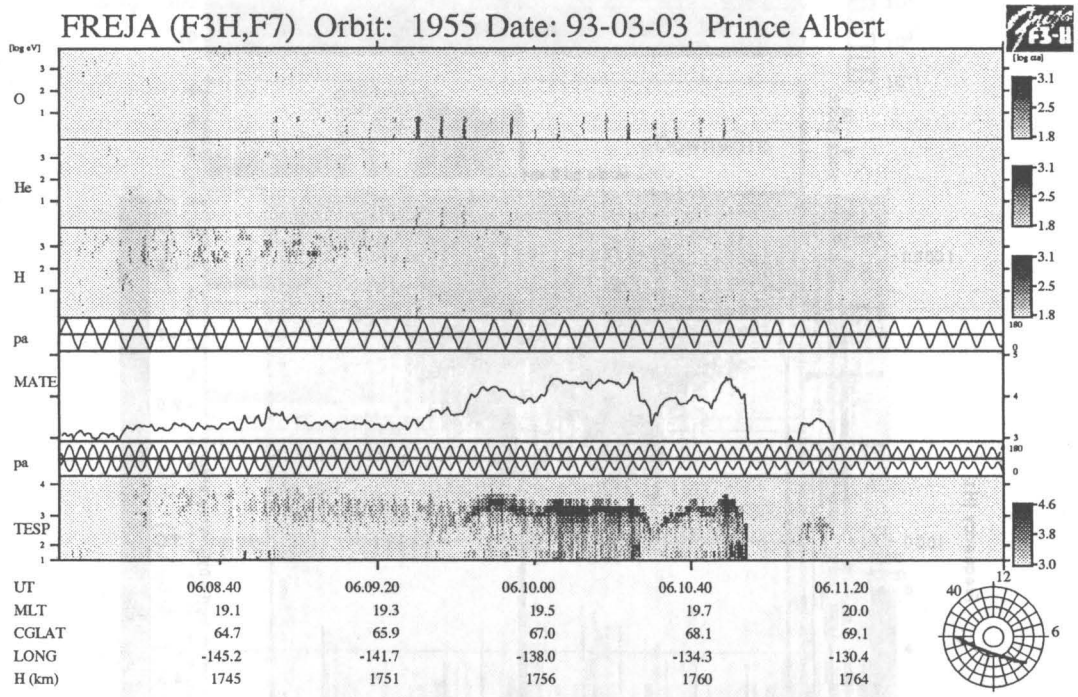

Figure 5.21: An E-t diagram of low energy particles observed by the Freja satellite on March 3, 1993.

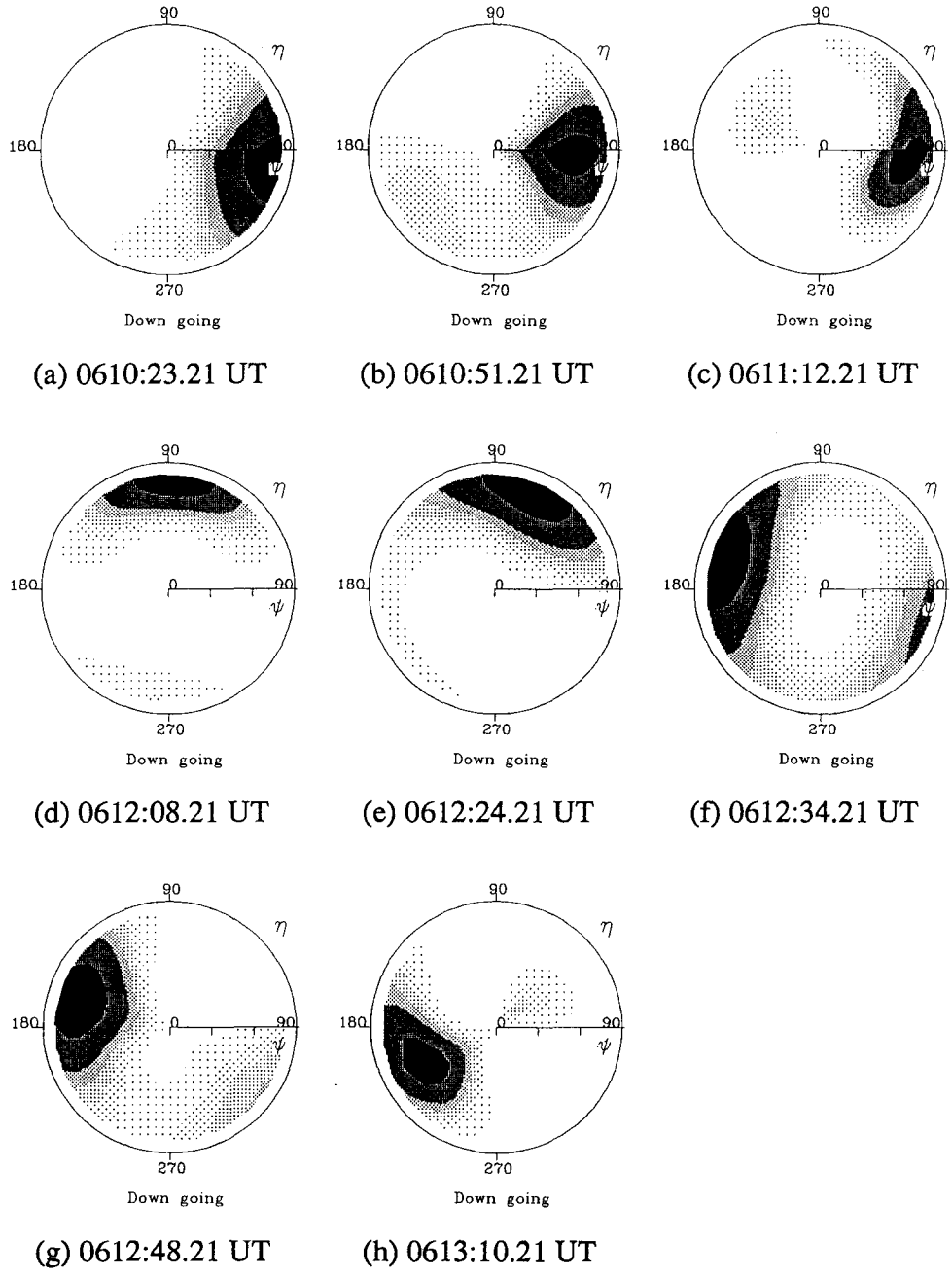

(a) 0610:23.21 UT (b) 0610:51.21 UT (c) 0611:12.21 UT

(d) 0612:08.21 UT (e) 0612:24.21 UT (f) 0612:34.21 UT

(g) 0612:48.21 UT (h) 0613:10.21 UT

Figure 5.22: The wave normal directions at 10.2 kHz of the V-shaped hiss observed by the Akebono satellite on March 3, 1994.

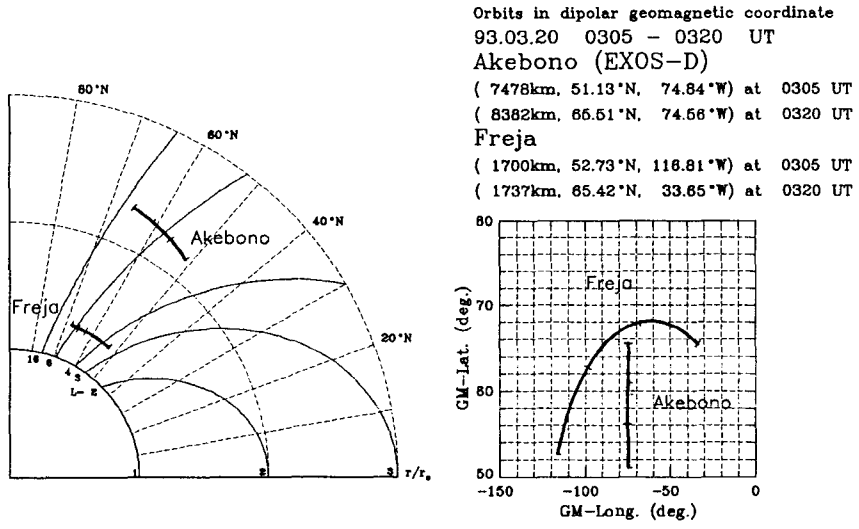

Figure 5.23: Trajectories of the Akebono satellite and the Freja satellite on March 20, 1993.

the Freja satellite. In Figure 5.21, upper three panels show energy-time spectrograms for O^+, $He^+$and H^+, respectively. The fourth panel gives the pitch angle of the ion observations. Fifth panel shows electron flux, and the last panel shows energy-time spectrogram for electrons. It is remarkable that the accelerated electrons in the energy range around 1 keV were observed from 0609:40 UT to 0610:50 UT, when the minimum of the V-shaped frequency was observed. Comparing those data observed by the both satellites, we can find that there is a spatially localized structure along the magnetic field line which extends from more than 7,300 km down to 1,700 km.

The wave normal directions of the V-shaped hiss observed by the Akebono satellite are determined (Figure 5.22), when the PFX were tuned at 10.2 kHz. We can find the same propagation characteristics as shown in Figure 5.4 and Figure 5.5, that is, 1) the wave was propagating downward with their wave normal angle (ψ) always very close to resonanse angle, 2) the azimuthal angle (η) is outward (0°) in the geomagnetic meridian plane at the lower latitude side (Figures 5.22 (a)-(c)), becomes nearly 90° around the frequency minimum of the V-shape (Figures 5.22 (d)-(f)), and finally turns to inward (180°) in the meridian plane (Figures 5.22 (g) and (h)).

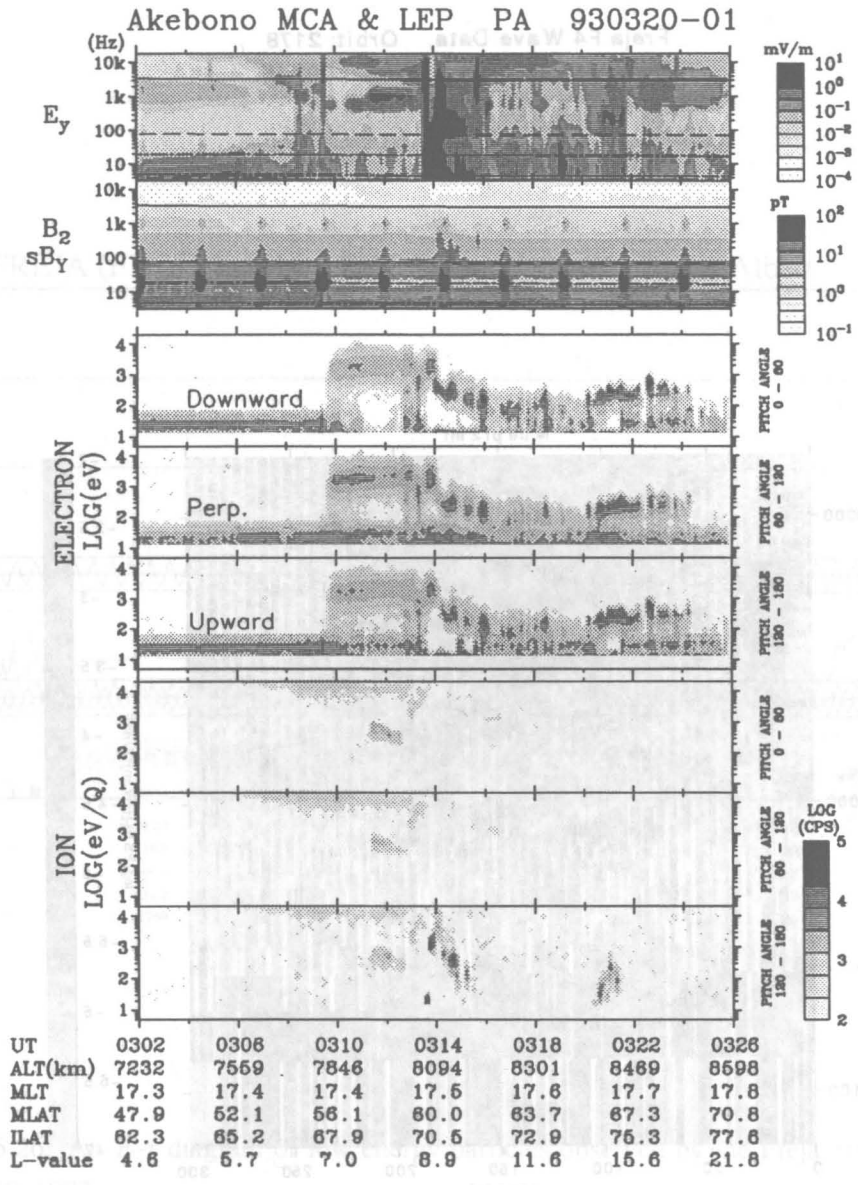

Figure 5.24: An f-t diagram of the V-shaped hiss and an E-t diagram of low energy particles observed by the Akebono satellite on March 20, 1993.

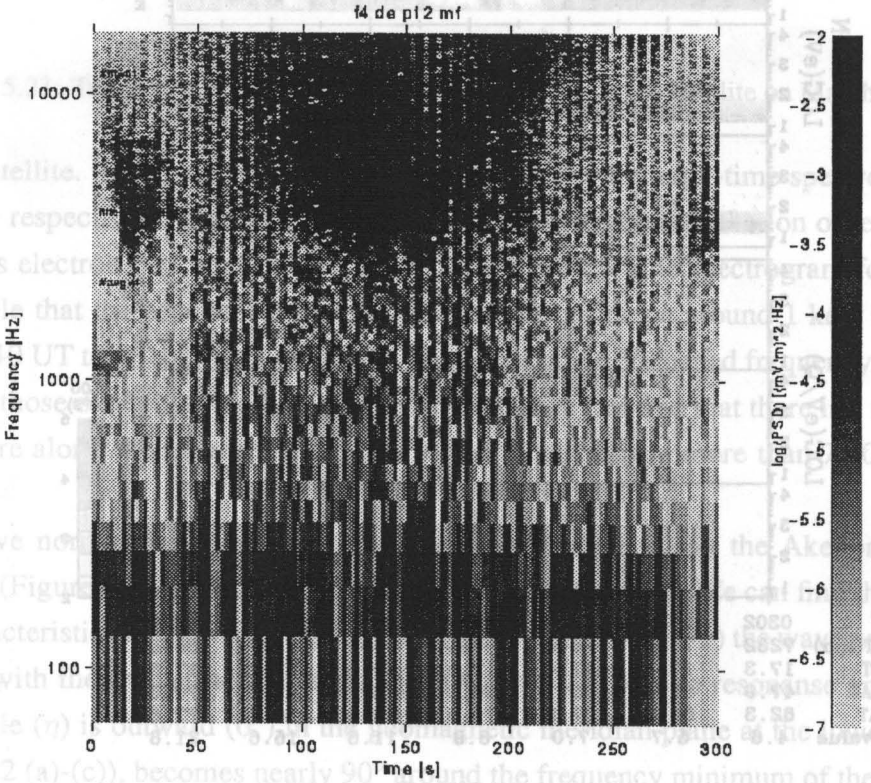

Figure 5.25: An f-t diagram of the V-shaped hiss observed by the Freja satellite on March 20, 1993.

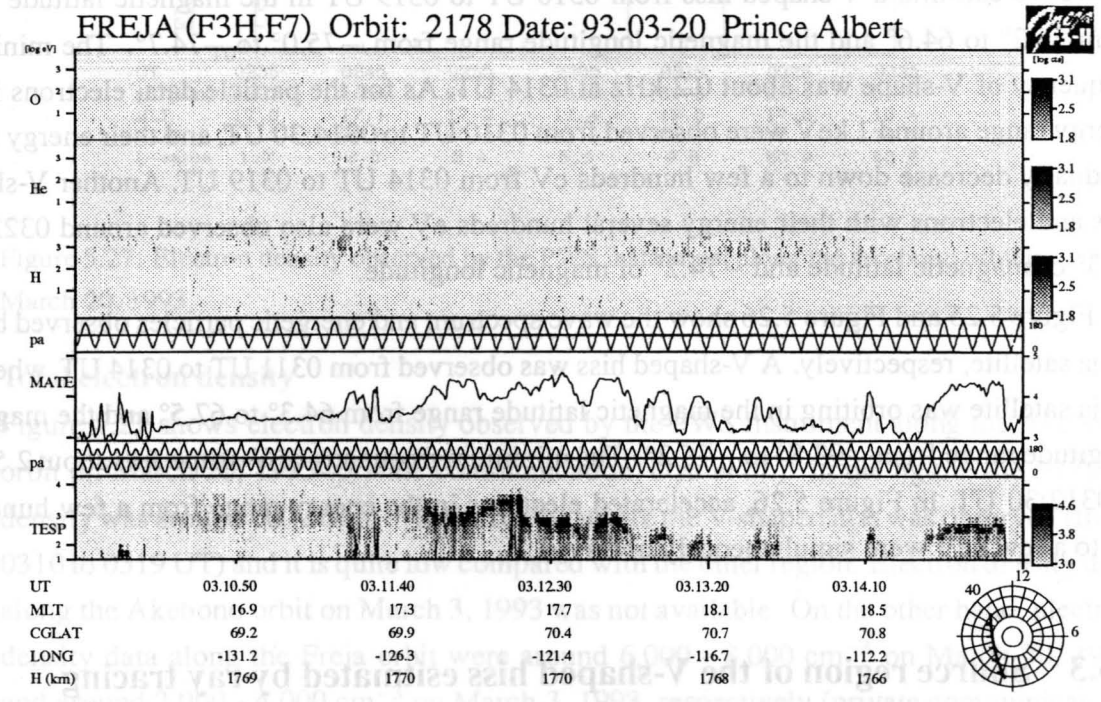

Figure 5.26: An E-t diagram of low energy particles observed by the Freja satellite on March 20, 1993.

March 20, 1993

Two trajectories of the Akebono and Freja satellites from 0305 UT to 0320 UT on March 20, 1993 is shown in Figure 5.23. The conjunction time in this case was at 0312 UT, when the Akebono satellite was orbiting along the geomagnetic meridian plane toward the higher latitude at an altitude of 8,000 km and the Freja satellite was traversing the meridian plane eastward at an altitude of 1,770 km. The magnetic local time was 17.5 hrs.

Spectra of wave and particle observed by the Akebono satellite are shown in Figure 5.24, where we can find a V-shaped hiss from 0310 UT to 0319 UT in the magnetic latitude range from 56.2° to 64.6° and the magnetic longitude range from −75.0° to −74.7°. The minimum frequency of V-shape was about 0.2 kHz at 0314 UT. As for the particle data, electrons in the energy range around 1 keV were observed from 0310 UT to 0314:30 UT, and their energy range gradually decrease down to a few hundreds eV from 0314 UT to 0319 UT. Another V-shaped hiss and electrons with their energy several hundreds eV were also observed around 0322 UT, 67.3° of magnetic latitude and −74.2° of magnetic longitude.

Figure 5.25 and Figure 5.26 show the wave spectrum and energetic particles observed by the Freja satellite, respectively. A V-shaped hiss was observed from 0311 UT to 0314 UT, when the Freja satellite was orbiting in the magnetic latitude range from 64.3° to 67.5° and the magnetic longitude range from −93.8° to −75.2°. The minimum frequency of V-shape was about 2.5 kHz at 0312:30 UT. In Figure 5.26, accelerated electrons in the energy range from a few hundreds eV to a few keV were simultaneously observed.

5.6.3 Source region of the V-shaped hiss esitmated by ray tracing

Elctron density profile

Using ray tracing method, we will try to reconstruct the spectrum of the V-shaped hiss observed by both the Akebono and Freja satellite. As the Akebono satellite was orbiting latitudinal direction and the Freja was orbiting longitudinally in both conjunction cases, the size and location of the source region of the V-shaped hiss can be estimated in three dimensional extent.

In the previous study, we used the electron density profile for ray tracing shown in Figure 5.9. As it was made from electron density data observed by the PWS instrument for several trajectories in the geomagnetic latitude range between 60° and 70° in the magnetic local time range between 6 hrs and 18 hrs, it is assumed to be a typical density profile. However, this is not apporopriate for the present case, because of the following two reasons.

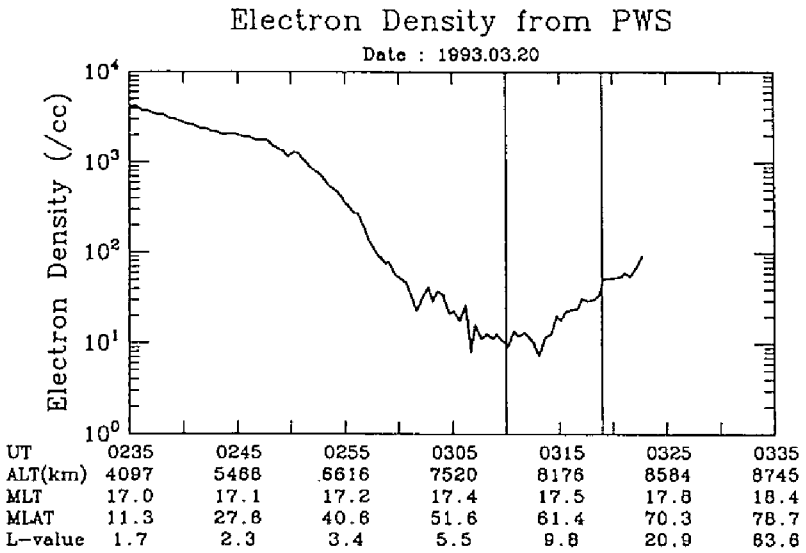

Figure 5.27: Electron density observed by the PWS instrument along the Akebono orbit on March 20, 1993

1. **Total electron density**

   Figure 5.27 shows electron density observed by the PWS instrument along the Akebono orbit on March 20, 1993 (private communication, *Oya et al.*). In the figure, the electron density was around 10 - 50 cm^{-3} in the region where the V-shaped hiss was observed (from 0310 to 0319 UT) and it is quite low compared with the other region. Electron density data along the Akebono orbit on March 3, 1993 was not available. On the other hand, electron density data along the Freja orbit were around 6,000 - 8,000 cm^{-3} on March 20, 1993 and around 2,000 - 4,000 cm^{-3} on March 3, 1993, respectively (private communication, *Stasiewicz*). These electron density observed by both the Akebono and Freja satellites were much lower than the profile shown in Figure 5.9.

2. **Ion constituents**

   The frequency minimum of the V-shaped hiss is assumed to be the upper limit of the local LHR frequency of whistler mode (which is denoted by Ω_{LHR1}). For example, the frequency minimums of the V-shaped hiss were 0.5 kHz at an altitude of 7,300 km and 2 kHz at an altitude of 1,750 km for the conjunction case on March 3, 1993, whereas they become 1.7 kHz and 14 kHz respectively according to the electron density profile shown in Figure 5.9.

Therefore we used an alternative electron density profile shown in Figure 5.28, which is

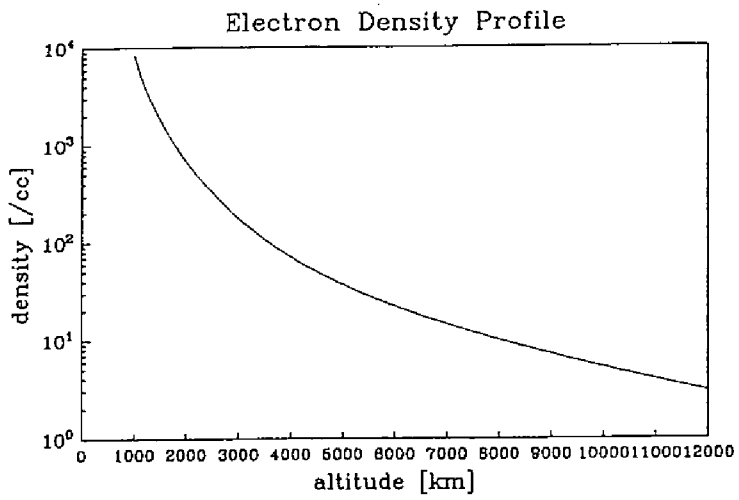

Figure 5.28: The electron density profile used for ray tracing.

fitted by the collisionless (CL) model. In the model, we assumed two species of ions, that is, H^+ and O^+. He^+ ions were neglected in order to simplify the model. The parameters used in the model were 0.01% of H^+, 99.9% of O^+ and 11,500 cm^{-3} of the electron density at the reference altitude of 1,000 km, and the ion temperature of 2,900°. Ω_{LHR1} in the exsistence of multiple ions is approximated by the following equation,

$$\Omega_{LHR1} = \sqrt{\sum_{\alpha} \frac{C_{i_\alpha} m_e}{m_{i_\alpha}} \times \left(\frac{\Pi_e^2 \Omega_e^2}{\Pi_e^2 + \Omega_e^2} \right)} \tag{5.1}$$

where C_{i_α} and m_{i_α} are the relative constituent and mass of α-th ion, respectively. m_e, Π_e and Ω_e are mass, plasma frequency and cyclotron frequency of electron.

In the CL model shown in Figure 5.28, ion constituents become (1.4% H^+, 98.6% O^+) and (70% H^+, 30% O^+) at altitudes of 1,700 km and 8,000 km, respectively. The LHR frequency of whistler mode calculated by (5.1) becomes 1,840 Hz and 550 Hz at each altitude.

Ray tracing

March 3 Event In order to simulate the March 3 event, the three dimensional ray tracing of hiss is performed. Each ray path is initiated along geomagnetic field lines in the invariant latitude range of 68°±1° at an altitude from 7,000 km and 11,000 km, and geomagnetic longitude range between −81.0° and −94.0° (cf. Figure 5.18). Initial wave normal direction (ψ) is set to be the

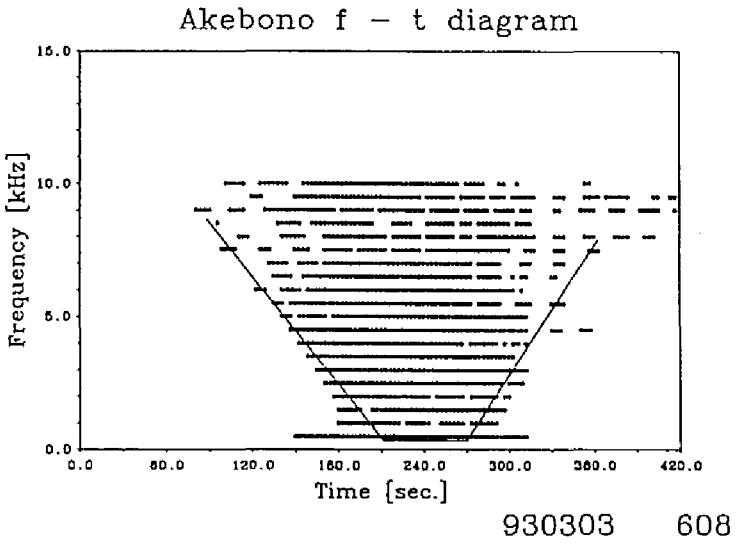

Figure 5.29: Frequency versus time curve to be observed along the Akebono orbit on March 3, 1993 estimated by ray tracing. Solid line shows the observed V-shaped hiss by the Akebono satellite.

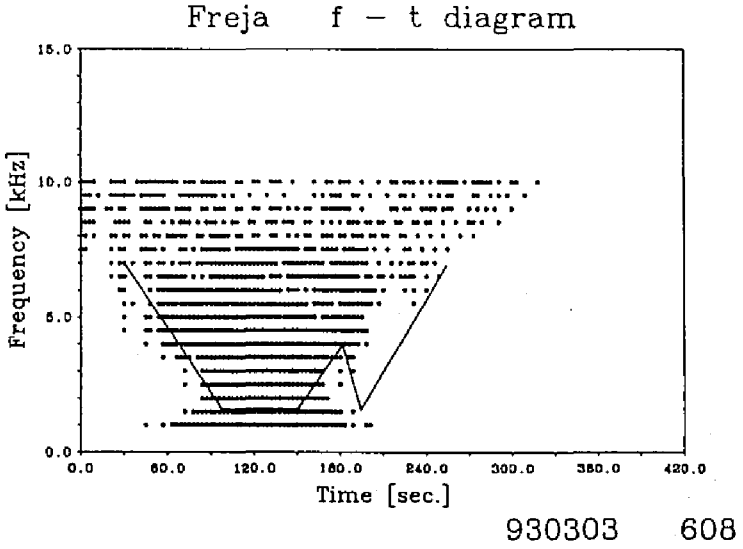

Figure 5.30: Frequency versus time curve to be observed along the Freja orbit on March 3, 1993 estimated by ray tracing. Solid line shows the observed V-shaped hiss by the Freja satellite.

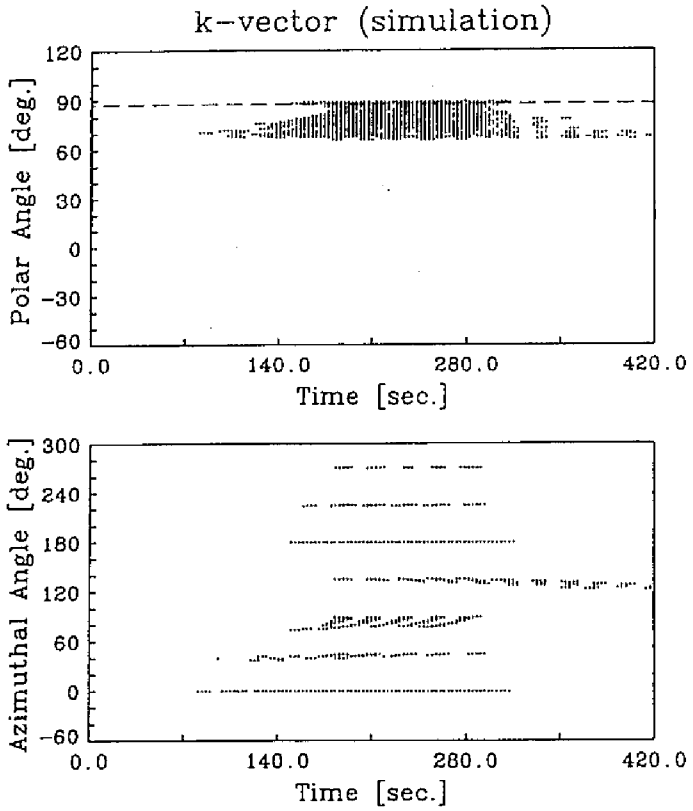

Figure 5.31: Wave normal directions along the Akebono orbit as a result of ray tracing for the V-shaped hiss observed on March 3, 1994.

resonance cone angle at the start point and the azimuthal angle of the wave normal vector (η) is directed every 45° (0°, 45°, $\cdots$, 315°).

Frequency versus time curves to be observed along the Akebono and Freja orbits are shown in Figure 5.29 and Figure 5.30, respectively. The transverse axis indicates relative time (second) from 0608 UT. In the figures, solid lines indicate the observed V-shaped hiss by the Akebono (Figure 5.29) and Freja (Figure 5.30) satellites, respectively. In the lower frequency ranges near the frequency minimum of V-shape in both cases, the reconstructed spectra are widely distributed than the observation results. It is bacause some ray paths calculated by ray tracing still reach downward region where their frequencies become lower than local LHR frequency. It should be examined in detail whether these wave can propagate downward into such region without damping by hot plasma ray tracing as a further study. As for the higher frequency range, spectra reconstructed by the ray tracing are almost the same as the observation in both cases.

Figure 5.31 shows the wave normal directions along the Akebono orbit as a result of ray tracing. In the figure, all wave normal angles (ψ) of rays to be observed along the Akebono orbit are more than 70° and this is consistent with result shown in Figure 5.22.

March 20 Event In the same way, the March 20 event was also simulated by ray tracing. Each ray path is initiated along geomagnetic field lines in the invariant latitude range of 70.5°±1° at an altitude from 7,000 km and 11,000 km, and geomagnetic longitude range between −75.0° and −88.0° (cf. Figure 5.23).

Frequency versus time curves to be observed along the Akebono and Freja orbits are shown in Figure 5.32 and Figure 5.33, respectively. The transverse axis indicates relative time (second) from 0311 UT. In the figures, solid lines indicate the observed V-shaped hiss by the Akebono (Figure 5.32) and Freja (Figure 5.33) satellites, respectively. Although there still remains a disagreement between the observation and the ray tracing results in the latter part in Figure 5.32, spectra reconstructed by the ray tracing are almost the same as the observed spectra in both cases for the Akebono and Freja satellites. Figure 5.34 shows the wave normal directions along the Akebono orbit as a result of ray tracing.

5.7 Conclusions

In this study, we have analyzed the Akebono VLF data especially for V-shaped hiss and saucer emissions. Using 696 orbit data in 1992, occurrence rate of V-shaped hiss and saucer emissions are surveyed on the dependence upon local time, altitude and magnetic latitude. These results show good agreement with the previous reports by *Ondoh* [1990] and *Hoffman and Lin* [1981].

So far upward or downward direction of Poynting flux for V-shaped hiss and saucer emissions was identified by Injun-5 [*Gurnett et al.*, 1971], however, our observation enabled us to determine the wave normal direction of these emissions in detail using 5 components of electric and magnetic field wave data. It is found that the V-shaped hiss come down to the spacecraft in the altitude range from 3,000 km to 5,000 km and the saucer emissions are going up to the spacecraft. Those results are consistent with the Injun-5 observation. We could also find a detailed feature on the wave normal vector of the V-shaped hiss, that the wave normal vector is directed radially outward in the lower latitude side of the emissions with respect to the location when the frequency of lowest border of hiss emission becomes minimum, whereas in the higher latitude side, it is directed radially inward.

The frequency versus time characteristics as well as the above features on their wave normal

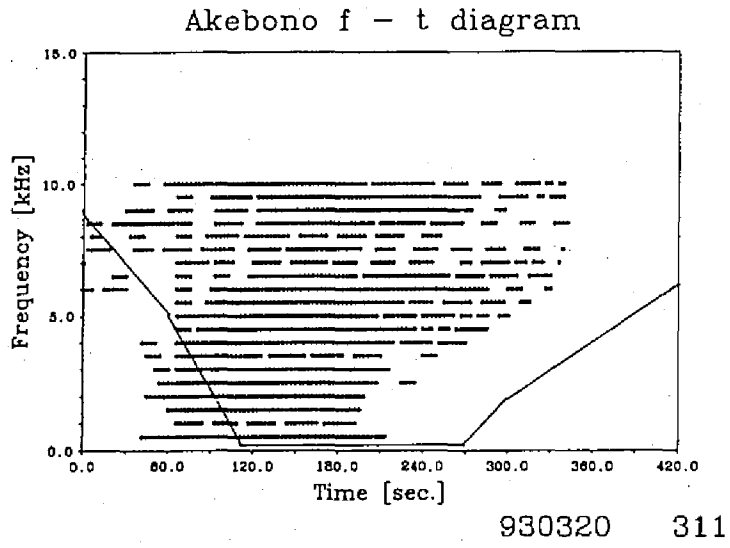

Figure 5.32: Frequency versus time curve to be observed along the Akebono orbit on March 20, 1993 estimated by ray tracing. Solid line shows the observed V-shaped hiss by the Akebono satellite.

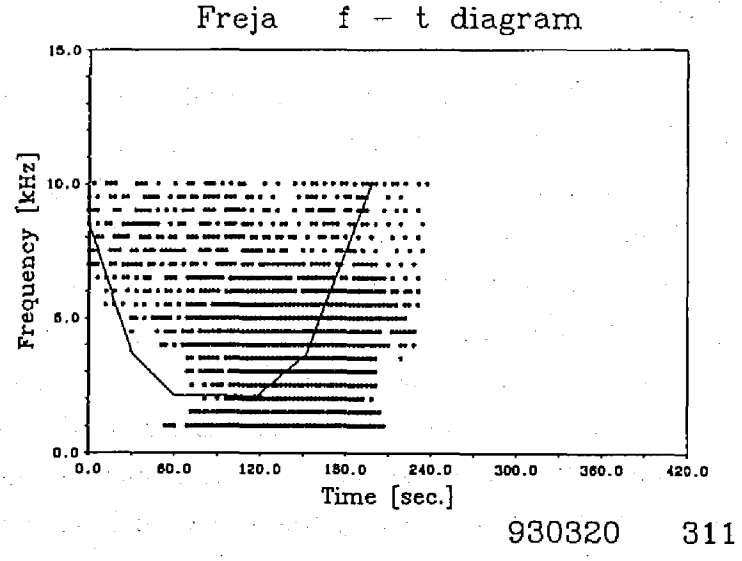

Figure 5.33: Frequency versus time curve to be observed along the Freja orbit on March 20, 1993 estimated by ray tracing. Solid line shows the observed V-shaped hiss by the Freja satellite.

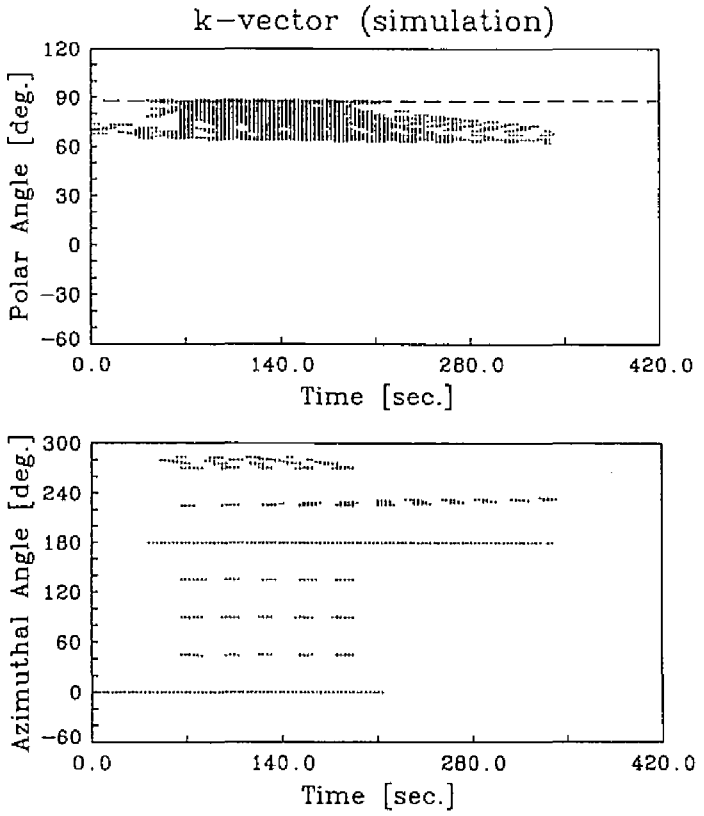

Figure 5.34: Wave normal directions along the Akebono orbit as a result of ray tracing for the V-shaped hiss observed on March 20, 1994.

vector are interpreted by ray tracing. The size and location of the source region of the V-shaped hiss and saucer emissions are also quantitatively estimated by calculating the ray paths for each satellite trajectory. It is found that the V-shaped hiss is generated in a line source region with an altitude range from more than 10,000 km down to a few 1,000 km, and the non-sharpness of the V-shape is explained by the deviation distance of the satellite trajectory from the source region. As to the saucer emissions, the band width of the emission can be explained by the relative position between the line source and the satellite trajectory.

Same analyses are also applied for the V-shaped hiss simultaneously observed by the Akebono and Freja satellites at their conjunction points. We analyzed two conjunction cases. Those waves are closely correrated with electrons in the energy range around 1 keV and they indicated a similar trend of change of wave normal vector with the other cases. Ray tracing study was made to reconstruct the observed spectra along the Akebono and Freja satellites in order to esti-

mate the three dimensional extent of the source region. It is found that the source region of the V-shaped hiss was assumed to be in the electron cavity and the wave propagated downward in the lower altitude region.

In order to discuss the generation mechanism of the V-shaped hiss and saucer emissions, the relation between the wave and particle observed on the satellite are studied. The clear correlation between the V-shaped hiss and precipitating electron beams with energies at least from a few tens to a few hundreds eV is found. This fact show good agreement with the generation mechanism that the wave is generated by Cérenkov radiation and coherent amplification mechanism by beaming electrons, although we have not yet examine the validity from the view point whether the wave intencty is also consistent with the observed particles on the assumption that they are generated by the above mentioned mechanism. On the other hand, as for the saucer emission, any upgoing electron beam correlated with are not found in the energy range above a few tens eV, and further research for the generation mechanism is needed.

Chapter 6

Concluding Remarks

In the present paper, we have studied ELF/VLF waves observed by the Akebono satellite. It is found that these wave phenomena are closely connected with the plasma structure in the Earth's magnetosphere; plasma density and its gradient, ion constituents of H^+, He^+, O^+ and the other particles such as alpha particles, and so on. We could clarify the characteristics of the waves, and furthermore had a lot of clues to know the structure of the magnetosphere by using those characteristics.

In Chapter 2, we introduced two main techniques, that is, wave distribution function (WDF) method as a data analysis technique and three-dimensional ray tracing method as a theoretical technique. Both methods were developed in order to apply them for the waves associate with ions. Our ray tracing program was applicable both in cold and hot plasma models, thus we can obtain not only ray paths of the wave but also the various parameters such as propagation time, wave normal direction and total growth/damping of the wave.

On the other hand, the WDF method is used for determining the wave normal direction from wave data observed by a satellite. Since all the ELF/VLF emissions studied in the present paper are natural wave phenomena, their energy source may distribute in rather wide area and thus multiple waves can coexist simultaneously at the observation point. The WDF is derived from the concept that observed signals consist of a number of elementary plane waves, that is useful for our purpose. The performance of the WDF was evaluated by computer simulation and we confirmed that the results are almost agreeable.

In Chapter 3, and 4, we introduced bands of ELF emissions type A and type B respectively, which are often observed in the vicinity of the geomagnetic equator by the Akebono satellite. The frequency range of the ELF instrument covers the local cyclotron frequencies of proton (H^+), helium (He^+), and oxygen (O^+) ions, and these wave phenomena are found to be associated with

ion constituents.

As for the type A emissions, they are usually observed below the local proton cyclotron frequency (f_{cH^+}) with a clear cutoff above the local cyclotron frequencies of heavy ions such as helium or oxygen. From statistical study and estimation of the refractive index of the emissions, they are identified as electromagnetic ion cyclotron waves (ICW) which might have been generated in the geomagnetic equatorial plane. It is important to note that the existence of those emissions requires an existence of rather high concentration of He^+ and/or O^+ ions. We introduced a different type of ion cyclotron wave which may be related to alpha particles. This fact may reflect a high solar activity in 1989 and 1990 and a strong evidence that a lot of alpha particle originated from the solar wind were pervaded into the magnetosphere.

The wave normal direction of the H^+ mode emission is determined and it is found that the wave normal vector is in the meridian plane, and the wave normal angle between the geomagnetic field is rather large. The result was consistent with those of three-dimensional ray tracing for ion mode waves using both a cold and a hot plasma model. According to our ray path calculation, these ICW mode waves propagate along the geomagnetic field lines, and are trapped within a limited geomagnetic latitude range with multiple bounces by the LHR reflection.

Sufficiently large growth of the wave was obtained along the ray path by our hot plasma ray tracing method on the assumption that the ion cyclotron resonant instability due to the temperature anisotropy of the hot H^+ ions causes the generation of the ICW mode wave. Although low energy ions could not be measured within the geomagnetic latitude of $\pm 60°$, where the ion mass spectrometer and low-energy particle analyzer were turned off to prevent high counts due to radiation particles, an abundant energy source for the ion cyclotron resonant instability may possibly exist since the trajectories of the Akebono satellite around the geomagnetic equator is within the inner radiation belt.

In Chapter 4, we discussed the characteristics of type B emission. Type B emission is observed not only below but also above the local proton cyclotron frequency, has a multiband structure in frequency, and has no dependence upon the local cyclotron frequencies. The refractive index estimated by the observed wave data satisfied a dispersion relation of whistler mode wave. Wave normal directions were determined by the WDF method, and were nearly perpendicular to the geomagnetic meridian plane. That is, they were propagating in the azimuthal direction nearly on the equatorial plane. Our ray tracing study revealed that the propagation perpendicular to the geomagnetic meridian plane is possible as a result of a density gradient such as plasmapause. Around the plasmapause region, waves with their frequencies below f_{LHR} are trapped between the edges of a density gradient and propagate around the plasmapause in a low

latitude region.

Our results are also consistent with the generation mechanism suggested by *Curtis and Wu* [1979]. They suggested that several kinds of MeV ions which have strong pitch angle anisotropy can generate emissions at frequencies near the harmonics of the ion cyclotron frequencies, and only waves which propagate under the condition of constant geomagnetic field intensity can take reasonable amplification. In this sense, the most favorable propagation condition is an azimuthal propagation.

Auroral hiss, especially V-shaped hiss and saucer emissions, were studied in Chapter 5. So far upward or downward direction of Poynting flux for V-shaped hiss and saucer emissions was identified in the previous study [*Gurnett et al.*, 1971], our observation enabled us to determine the wave normal direction of these emissions in detail using 5 components of electric and magnetic field wave data. It was found that the V-shaped hiss come down to the spacecraft in the altitude range from 3,000 km to 5,000 km and the saucer emissions are going up to the spacecraft. We could also find that the wave normal vector is directed radially outward in the lower latitude side of the emissions with respect to the location when the frequency of lowest border of hiss emission becomes minimum, whereas in the higher latitude side, it is directed radially inward.

The frequency spectra of the emissions were also interpreted by ray tracing. It is important that the size and location of the source region of the V-shaped hiss and saucer emissions are quantitatively estimated by calculating the ray paths for each satellite trajectory. It is found that the V-shaped hiss is generated in a line source region with an altitude range from more than 10,000 km down to a few 1,000 km, and the non-sharpness of the V-shape is explained by the deviation distance of the satellite trajectory from the source region. As to the saucer emissions, the band width of the emission can be explained by the relative position between the line source and the satellite trajectory.

Same analyses are also applied for the V-shaped hiss simultaneously observed by the Akebono and Freja satellites at their conjunction points. Those waves are closely correlated with electrons in the energy range around 1 keV and they indicated a similar trend of change of wave normal vector with the other cases. Ray tracing study was made in order to estimate the three dimensional extent of the source region. We found that the source region of the V-shaped hiss was assumed to be in the electron cavity and the wave propagated downward in the lower altitude region than usual cases.

In conclusion, we have studied ELF/VLF emissions observed by the Akebono satellite in a multicomponent plasma model. It should be emphasized that our contribution of the present

study is not only clarifying the generation mechanism and propagation characteristics of ELF/VLF waves but also giving a clue to investigate the global plasma distribution especially for the plasma density distribution and ion constituents in the magnetosphere by using the propagation characteristics of the plasma wave in a multicomponent plasma. Especially in the equatorial region, the ion mass spectrometer and low-energy particle analyzer on board the Akebono satellite cannot measure these quantities correctly because the trajectories of the Akebono satellite are within the inner radiation belt, however, it may be possible to infer the plasma environment from wave observation.

Finally, some suggestions will be presented for further work. As described in Chapter 5, it is difficult to tell a physical phenomenon from observed data by one satellite whether it is a temporal change, a spatial change or mixture of them. In order to study the spatial structure of the magnetosphere, simultaneous observation by multi-satellites is indispensable. In the present study, we briefly introduced the conjunction study between the Akebono and Freja satellites. As was described in Chapter 1, since more than 15 of scientific satellites will be orbiting in the near future associated with ISTP, such kind of collaborative study will be made more and more actively. We hope our study play a significant role to this international collaboration.

Acknowledgments

The author would like to express his sincere and hearty appreciation to Professor Iwane Kimura for his continual guidance, stimulating and helpful discussions throughout the present work, and for his careful reading of the manuscript and useful suggestions for revision. The author wishes to express his deep appreciation to Professor Hiroshi Matsumoto, and Professor Kozo Hashimoto for their fruitful discussions and suggestions throughout the present work and for their careful and critical reading of the manuscript.

The author also wishes to express his deep appreciation to Dr. Yoshiharu Omura for his comments and constructive suggestions throughout the present work. The author wishes to express his thank to Professor Isamu Nagano in Kanazawa University and Dr. Toshimi Okada in Toyama Prefectural University for their useful discussions and enlightening criticism on the methods of research.

In the present data analyses, the data by the PWS, MGF, LEP and TED were indispensable. The author is grateful to Professors Hiroshi Oya and Hiroshi Fukunishi in Tohoku University, Professor Toshifumi Mukai and Dr. Koichiro Oyama in the Institute of Space and Astronautical Science, Dr. Takumi Abe in Aoyama Gakuin University and their colleagues. He also would like to thank Professor Koichiro Tsuruda, who is the project manager of the Akebono satellite, the Akebono tracking team members and the staff of the Akebono tracking station at Kagoshima Space Center, Syowa Base in Antarctica, Prince Albert in Canada and Esrange in Sweden for continual data acquisition of the Akebono telemetry.

The wave and particle data observed by the Freja satellite were provided from the science groups of the Swedish Institute of Space Physics at Uppsala and Kiruna, respectively. The author greatly appreciates Dr. Kristof Stasiewicz, Dr. Lars Eliasson and Dr. Masatoshi Yamauchi for the fruitful suggestions and discussions in addition to providing those data. The author also appreciate Professor Kjell Rönnmark, Dr. Mats André and Dr. Tord Oscarsson in Umeå University for the stimulating comments and suggestions.

The author is grateful to Dr. Kazuaki Takao, Dr. Toru Sato and Mr. Toshio Matsuo for their helpful suggestions and encouragement. The author is deeply indebted to Mr. Masayuki Yamamoto for his helpful advice and continuous encouragement.

The author wishes to thank Mr. Akira Sawada for his invaluable advice in completing the analyses system of the Akebono VLF data and ray tracing program with the effect of ions. Many figures in the preset thesis are drawn by graphic software package named "YACG" developed by him.

The author appreciates Mr. Hideki Kenmochi, Mr. Ken-ichiro Yoshida and Mr. Daiji Ido for their collaborative works and discussions. Thanks are due to the colleagues of Kimura's Laboratory and Radio Atmospheric Science Center for their discussions and suggestions. Especially the author thanks Mr. Katsuhiko Tsunehara and Mr. Tomohisa Hosoda for their help in completing the present thesis.

The author also wishes to express his thank to Dr. Masao Kitano, Dr. Toshio Wakayama and many other persons for constructing and maintaining the computers and network system in Kimura's Laboratory. Part of the numerical calculation was executed on the KDK systems at Radio Atmospheric Science Center, Kyoto University. K_p index was referred to a data base on geomagnetic activity archived at the Data Processing Center of Kyoto University.

The present work was financially supported by the Grant-in-Aid for Scientific Research, project (#63420016), Ministry of Education, Science and Culture of Japan, and is also financially supported by the Japanese STEP program. The collaborative study between the Freja and Akebono satellites was financially supported by the International Science Research Program (#06044110) of the Ministry of Education, Science and Culture of Japan, and the Kyoto University Foundation.

Bibliography

Abe, T., K. Oyama, H. Amemiya, S. Watanabe, T. Okuzawa, and K. Schlegel, Measurements of temperature and velocity distribution of thermal electrons by the Akebono (EXOS-D) satellite - Experimental setup and preliminary results -, *J. Geomagn. Geoelectr., 42*, 537-554, 1990.

Aikyo, K., and T. Ondoh, Propagation of nonducted VLF waves in the vicinity of the plasmapause, *J. Radio Res. Lab. Jpn., 18*, 153-182, 1971.

André, M., H. Koskinen, G. Gustafsson, and R. Lundin, Ion waves and upgoing beams observed by the Viking satellite, *Geophys. Res. Lett., 14*, 463-466, 1987.

Angerami, J. J., and J. O. Thomas, The distribution of ions and electrons in the Earth's exosphere, *J, Geophys. Res., 69*, 4537-4560, 1964.

Boehm, M., G. Paschmann, J. Clemmons, H. Höfner, R. Frenzel, M. Ertl, G. Haerendel, P. Hill, H. Lauche, L. Eliasson, and R. Lundin, The TESP electron spectrometer and correlator on Freja, *The Freja Mission* ed. by R. Lundin et al., Kluwer Academic Publishers, The Netherlands, 105-136, 1994.

Buchalet, L. J., and F. Lefeuvre, One and two direction models for VLF electromagnetic waves observed on-board GEOS 1, *J, Geophys. Res., 86*, 2377-2383, 1981.

Curtis, S. A., and C. S. Wu, Gyroharmonic emissions induced by energetic ions in the equatorial plasmasphere, *J. Geophys. Res., 84*, 2597-2607, 1979.

Eliasson, L., O. Norberg, R. Lundin, K. Lundin, S. Olsen, H. Borg, M. André, H. Koskinen, P. Riihelä, M. Boehm, and B. Whalen, The Freja hot plasma experiment - Instrument and first results, *The Freja Mission* ed. by R. Lundin et al., Kluwer Academic Publishers, The Netherlands, 159-172, 1994.

Eviatar, A., A. M. Lenchek, and S. F. Singer, Distribution of density in an ion-exosphere of a non rotating planet, *Phys. Fluid, 7*, 1775, 1964.

Fukunishi, H., R. Fujii, S. Kokubun, K. Hayashi, T. Tohyama, Y. Tonegawa, S. Okano, M. Sugiura, K. Yumoto, I. Aoyama, T. Sakurai, T. Saito, T. Iijima, A. Nishida, and M. Natori, Magnetic field observations on the Akebono (EXOS-D) satellite, *J. Geomag. Geoelectr., 42*, 385-409, 1990.

Gendrin, R., General relationships between wave-amplification and particle diffusion in a magnetoplasma, *Rev. Geophys. Space Phys., 19*, 171-184, 1981.

Gendrin, R., M. Ashour-Abdalla, Y. Omura, and K. Quest, Linear analysis of ion cyclotron interaction in a multicomponent plasma, *J. Geophys. Res., 89*, 9119-9124, 1984.

Gomberoff, L., and P. Vega, Effect of He^+ temperature and thermal anisotropy on the electromagnetic ion cyclotron instability in the geosynchronous region of GEOS 2, *J. Geophys. Res., 92*, 7728-7732, 1987.

Gurnett, D. A., S. R. Mosier, and R. R. Anderson, Color spectrograms of very-low-frequency Poynting flux data, *J. Geophys. Res., 76*, 3022-3033, 1971.

Gurnett, D. A., and L. A. Frank, VLF hiss and related plasma observations in the polar magnetosphere, *J. Geophys. Res., 77*, 172-190, 1972.

Gurnett, D. A., Plasma wave interactions with energetic ions near the magnetic equator, *J. Geophys. Res., 81*, 2765-2770, 1976.

Gurnett, D. A., S. D. Shawhan, and R. R. Shaw, Auroral hiss, Z mode radiation and auroral kilometric radiation in the polar magnetosphere: DE 1 observations, *J. Geophys. Res., 88*, 329-340, 1983.

Haselgrove, J., Ray theory and a new method for ray tracing, in *Proceedings of the Cambridge Conference on Physics of the Ionosphere, p. 355, Physical Society*, London, 1955.

Hashimoto, K., and I. Kimura, Oblique whistler mode propagation in a hot plasma, *Rep. Ionos. Space Res. Japan, 27*, 73-78, 1973.

Hashimoto, K., I. Kimura, and H. Kumagai, Estimation of electron temperature by VLF waves propagating in directions near the resonance cone, *Planet. Space Sci., 25*, 871-877, 1977.

Hashimoto, K., K. Yamaashi, and I. Kimura, Three-dimensional ray tracing of electrostatic cyclotron harmonic waves and Z mode electromagnetic waves in the magnetosphere, *Radio Sci.*, *22*, 579-594, 1987.

Hoffman, R. A., and C. S. Lin, Study of inverted-V auroral precipitation events, *Physics of Auroral Arc Formation* ed. by S. I. Akasofu and J. R. Kan, *AGU Monograph 25*, 80-90, 1981.

Holback, B., S.-E. Jansson, L. Åleén, G. Lundgren, L. Lyngdal, S. Powell, and A. Meyer, The Freja wave and plasma density experiment, *The Freja Mission* ed. by R. Lundin et al., Kluwer Academic Publishers, The Netherlands, 173-188, 1994.

Hultqvist, B., The Viking project, *Geophys. Res. Lett.*, *14*, 379-382, 1987.

International Association of Geomagnetism and Aeronomy Division I Working Group 1 (IAGA), International geomagnetic reference field revision 1985, *J. Geomagn. Geoelectr.*, *37*, 1157-1164, 1985.

Ito, Y., Measurements of the wave normal and Poynting vector of VLF signals in the magnetosphere observed by the Akebono satellite (in Japanese), *Master thesis*, Faculty of Engineering, Kyoto University, 1990.

James, G., VLF saucers, *J. Geophys. Res.*, *81*, 501-514, 1976.

Kasahara, Y., Three-dimensional ray tracing of the waves including the effects of ions (in Japanese), *Graduation thesis*, Faculty of Engineering, Kyoto University, 1989.

Kasahara, Y., A. Sawada, M. Yamamoto, I. Kimura, S. Kokubun, and K. Hayashi, Ion cyclotron emissions observed by the satellite Akebono in the vicinity of the magnetic equator, *Radio Sci.*, *27*, 347-362, 1992.

Kasahara, Y., H. Kenmochi, and I. Kimura, Propagation characteristics of the ELF emissions observed by the satellite Akebono in the magnetic equatorial region, *Radio Sci.*, *29*, 751-767, 1994.

Kasahara, Y., K. Yoshida, T. Matsuo, I. Kimura, and T. Mukai, Propagation Characteristics of Auroral Hiss Observed by Akebono Satellite, *J. Geomag. Geoelectr.*, *47*, 509-525, 1995.

Kimura, I., Effects of ions on whistler-mode ray tracing, *Radio Sci.*, *1*, 269-283, 1966.

Kimura, I., Cerenkov instability and VLF emissions generated outside the plasmapause, *Rep. Ionos. Space Res. Japan, 25(4)*, 360-368, 1971.

Kimura, I., T. Matsuo, K. Tsuruda and H. Yamagishi, Measurements of the directions of propagation vector and Pointing flux of aurolal hiss by means of the S-310JA-5 rocket, *Mem. Natl. Inst. Polar Res. Special Issue, No.18*, 439-452, 1981.

Kimura, I., and T. Matsuo, Wave normal direction of auroral hiss observed by the S-310JA-5 rocket, *Mem. Natl. Inst. Polar Res. Special Issue, No.22*, 185-195, 1982.

Kimura, I., H. Matsumoto, T. Mukai, K. Hashimoto, T. F. Bell, U. S. Inan, R. A. Helliwell, and J. P. Katsufrakis, EXOS-B/Siple station VLF wave-particle interaction experiments: 1. General description and wave-particle correlations, *J. Geophys. Res.*, *88*, 282-294, 1983.

Kimura, I., K. Hashimoto, I. Nagano, T. Okada, M. Yamamoto, T. Yoshino, H. Matsumoto, M. Ejiri, and K. Hayashi, VLF observations by the Akebono (EXOS-D) satellite, *J. Geomagn. Geoelectr.*, *42*, 459-478, 1990.

Kokubun, S., M. Takami, K. Hayashi, H. Fukunishi, I. Kimura, A. Sawada, and Y. Kasahara, Triaxial search coil measurements of ELF waves in the plasmasphere: initial results from EXOS-D, *Geophys. Res. Lett.*, *18*, 301-304, 1991.

Koskinen, H. E. J., P. M. Kintner, G. Holmgren, B. Holback, G. Gustafsson, M. André, and R. Lundin, Observations of ion cyclotron harmonic waves by the Viking satellite, *Geophys. Res. Lett.*, *14*, 459-462, 1987.

Kumagai, H., K. Hashimoto, H. Matsumoto, and I. Kimura, Computer simulation of a Cerenkov interaction between obliquekly propagating whistler mode waves and an electron beam, *Phys. Fluids, 23(1)*, 184-193, 1980.

Laakso, H., H. Junginger, A. Roux, R. Schmidt, and C. de Villedary, Magnetosonic waves above $f_c(H^+)$ at geostationary orbit: GEOS 2 results, *J. Geophys. Res.*, *95*, 10,609-10,621, 1990.

Lefeuvre, F., and C. Delannoy, Analysis of random electromagnetic wave field by a maximum entropy method, *Ann. Telecommun.*, *34*, 204-213, 1979.

Lefeuvre, F., M. Parrot, and C. Delannoy, Wave distribution function estimation of VLF electromagnetic waves observed on-board GEOS 1, *J. Geophys. Res.*, *86*, 2359-2375, 1981.

Lotko, W., and J. E. Maggs, Damping of electrostatic noise by warm auroral electrons, *Planet. Space Sci., 27*, 1491-1506, 1979.

Lotko, W., and J. E. Maggs, Amplification of electrostatic noise in cyclotron resonance with an adiabatic auroral beam, *J. Geophys. Res., 86*, 3449-3458, 1981.

Lundin, R., G. Haerendel, S. Grahn, The Freja science mission, *The Freja Mission* ed. by R. Lundin et al., Kluwer Academic Publishers, The Netherlands, 1-16, 1994.

Maeda, K., and I. Kimura, *Contemporary theory of electromagnetic waves (in Japanese)*, Ohm, Japan, 1984.

Maggs, J. E., Coherent generation of VLF hiss, *J. Geophys. Res., 81*, 1707-1724, 1976.

Maggs, J. E., Electrostatic noise generated by the auroral electron beam, *J. Geophys. Res., 83*, 3173-3188, 1978.

Maggs, J. E., and W. Lotko, Altitude dependence model of the auroral beam and beam-generated electrostatic noise, *J. Geophys. Res., 86*, 3439-3447, 1981.

Matsumoto, H., S. Miyatake, K. Tsuruda, A. Morioka, J. Ohtsu, H. Oya, and I. Kimura, VLF wave observation by satellite Jikiken (EXOS-B), *J. Geomag. Geoelec., 33*, 63-72, 1981.

Matsumoto, H., K. Hashimoto, M. Morikura, I. Kimura, and T. Mukai, Correlation between VLF plasma waves and energetic electrons simultaneously observed by satellite Jikiken (EXOS-B), *J. Geomag. Geoelectr., 33*, 73-87, 1981.

Mauk, B. H., C. E. McIlwain, and R. L. Mcpherron, Helium cyclotron resonance within the Earth's magnetosphere, *Geophys. Res. Lett., 8*, 103-106, 1981.

Means, J. D., Use of the three-dimensional covariance matrix in analyzing the properties of plane waves, *J. Geophys. Res., 77*, 5551-5559, 1972.

Menietti, J. D., and J. L. Burch, "Electron conic" signatures observed in the nightside auroral zone and over the polar cap, *J. Geophys. Res., 90*, 5345-5353, 1985.

Miyamoto, K., *Plasma physics for nuclear fusion*, Cambridge, 1980.

Mukai, T., N. Kaya, E. Sagawa, M. Hirahara, W. Miyake, T. Obara, H. Miyaoka, S. Machida, H. Yamagishi, M. Ejiri, H. Matsumoto, and T. Itoh, Low energy charged particle observations in the "auroral" magnetosphere: First results from the Akebono (EXOS-D) satellite, *J. Geomagn. Geoelectr., 42*, 479-496, 1990.

Omura, Y., M. Ashour-Abdalla, R. Gendrin, and K. Quest, Heating of thermal helium in the equatorial magnetosphere: A simulation study, *J. Geophys. Res., 90*, 8281-8292, 1985.

Omura, Y., H. Usui, H. Matsumoto, Parallel heating associated with interaction of forward and backward electromagnetic cyclotron waves, *J. Geomagn. Geoelectr., 40*, 949-961, 1988.

Ondoh, T., Polar occurrence map of broad-band auroral hiss observed by ISIS satellite, *J. Radio Res. Lab., 35*, 1-14, 1988.

Ondoh, T., Broad-band auroral hiss and inverted-V electrons precipitated from the boundary plasma sheet, *J. Radio Res. Lab., 37*, 15-28, 1990.

Oya, H., and K. Oyama, Data from TAIYO satellite, *report, Inst. of Space and Astronaut. Sci.*, Kanagawa, 1985.

Oya, H., A. Morioka, K. Kobayashi, M. Iizima, T. Ono, H. Miyaoka, T. Okada, and T. Obara, Plasma wave observation and sounder experiments (PWS) using the Akebono (EXOS-D) satellite – Instrumentation and initial results including discovery of the high altitude equatorial plasma turbulence, *J. Geomagn. Geoelectr., 42*, 411-442, 1990.

Perraut, S., A. Roux, P. Robert, R. Gendrin, J. Sauvaud, J. Bosqued, G. Kremser, and A. Korth, A systematic study of ULF waves above F_{H^+} from GEOS 1 and 2 measurements and their relationships with proton ring distributions, *J. Geophys. Res., 87*, 6219-6236, 1982.

Radio Research Laboratories, Ministry of Posts and Telecommunications, Summary plots of ionospheric parameters obtained from Ionosphere Sounding Satellite-b, *report, vol.4*, Tokyo, 1985.

Rauch, J. L., and A. Roux, Ray tracing of ULF waves in a multicomponent magnetospheric plasma: Consequences for the generation mechanism of ion cyclotron waves, *J. Geophys. Res., 87*, 8191-8198, 1982.

Roux, A., S. Perraut, J. L. Rauch, C. de Villedary, G. Kremser, A. Korth, and D. T. Young, Wave-particle interactions near Ω_{He^+} observed on-board GEOS 1 and 2, 2, Generation of ion cyclotron waves and heating of He^+ ions, *J. Geophys. Res., 87*, 8174-8190, 1982.

Russell, C. T., R. E. Holzer, and E. J. Smith, OGO 3 observations of ELF noise in the magnetosphere, 2, The nature of the equatorial noise, *J. Geophys. Res., 75*, 755-768, 1970.

Sakamoto, K., Y. Kasahara, and I. Kimura, K-vector determination of whistler mode signals by using amplitude data obtained by a spacecraft borne instrument, *IEEE Trans. Geoelectr. and Remote Sensing, 33(3)*, 528-534, 1995.

Samson, J. C., and J. V. Olson, Some comments on the descriptions of the polarization states of waves, *Geophys. J. R. Astron. Soc., 61*, 115-129, 1980.

Sawada, A., Three-dimensional ray tracing of electromagnetic and electrostatic waves in the magnetosphere, *Master thesis*, Faculty of Engineering, Kyoto University, 1988.

Sazhin, S. S., K. Bullough, and M. Hayakawa, Auroral hiss: A review, *Planet. Space Sci., 41*, 153-166, 1993.

Stix, T. H., *The Theory of Plasma Waves*, McGraw-Hill, New York, 1962.

Storey, L. R. O., and F. Lefeuvre, The analysis of 6-component measurements of a random electromagnetic wave field in a magnetoplasma, 1, The direct problem, *Geophys. J. R. Astron. Soc., 56*, 255-269, 1979.

Storey, L. R. O., and F. Lefeuvre, The analysis of 6-component measurements of a random electromagnetic wave field in a magnetoplasma, 2, The integration kernels, *Geophys. J. R. Astron. Soc., 62*, 173-194, 1980.

Yamaguchi, M., K. Hattori, N. Iwama, and M. Hayakawa, A new direction finding method of magnetospheric VLF/ELF radio waves using regularization and generalized cross validation, in *Proceedings of the 1992 International Symposium on Antennas and Propagation (ISAP), vol. 4*, pp. 1165 - 1168, IEICE, Japan, 1992.

Yamaguchi, M., K. Hattori, N. Iwama, S. Shimakura, and M. Hayakawa, A new ground-based direction finding method using a linear reconstruction of wave distribution function of magnetospheric VLF/ELF radio waves (in Japanese), *Trans. IEICE, J76-B-II(11)*, 880-889, 1993.

Yamamoto, T., On the amplification of VLF hiss, *Planet. Space Sci., 27*, 273-284, 1979.

Young, D. T., S. Perraut, A. Roux, C. de Villedary, R. Gendrin, A. Korth, G. Kremser, and D. Jones, Wave-particle interactions near Ω_{He^+} observed on GEOS 1 and 2, 1, Propagation of ion cyclotron waves in He^+-rich plasma, *J. Geophys. Res.*, *86*, 6755-6772, 1981.